

Dynamic Model and Design of an Integrated Flywheel Energy Storage System

A Thesis

Presented in Partial Fulfillment of the Requirements for the

Degree of Master of Science

with a

Major in Electrical Engineering

in the

College of Graduate Studies

University of Idaho

by

Bridget T. Wimer

May 2014

Major Professor: Joseph D. Law, Ph.D.

Authorization to Submit Thesis

This thesis of Bridget T. Wimer, submitted for the degree of Master of Science with a major in Electrical Engineering and titled “Dynamic Model and Design of an Integrated Flywheel Energy Storage System,” has been reviewed in final form. Permission, as indicated by the signatures and dates given below, is now granted to submit final copies to the College of Graduate Studies for Approval.

Major Professor _____ Date _____

Joseph D. Law

Committee

Members _____ Date _____

Christine A. Berven

_____ Date _____

Brian K. Johnson

Department

Administrator _____ Date _____

Fred Barlow

Discipline's

College Dean _____ Date _____

Larry Stauffer

Final Approval and Acceptance by the College of Graduate Studies

_____ Date _____

Jie Chen

Abstract

To support human colonization and exploration of the lunar surface, NASA needs a way to store energy generated by various possible sources to meet demand that varies with the time of the lunar day. Flywheels provide a reliable, efficient and low-maintenance way to provide continuous energy on demand. In general, a Flywheel Energy Storage (FES) system includes an electric machine to convert between mechanical and electric energy, power electronics to provide an interface between the machine and the electric distribution and generation system, and a flywheel to store energy. This thesis investigates and designs an integrated hubless flywheel and electric machine designed for low rotational speeds. To properly predict the response of the FES system to external imbalances, a dynamic model of the integrated system is developed in this thesis. The dynamic model is useful in developing the control algorithm for the FES system.

Acknowledgments

Without the help from my colleagues, professors, family, and friends, this thesis and project would not have been possible. I would like to start by thanking my fiancé, Jeremy, for supporting and consoling me anytime I struggled with completing my thesis and graduate school. Without my family, especially my parents Burnell and Arlene, and his encouragement, I would not have had the motivation needed to complete my thesis.

The flywheel project involved multiple professors and students, and without each of their individual contributions, the project would not have advanced this far. I would like to especially thank my major professor, Dr. Joseph Law, for giving me the opportunity to work on the flywheel project and for always being there anytime I had questions. His constant mentoring and dedication always motivated me to want to be a better student. In addition to Dr. Law, I would like to thank the other professors and students involved with the project.

Specifically, I would like to thank Juliet Petersen for her help in designing the Field Regulated Reluctance Machine. Also, I would like to thank the two other electrical engineering graduate students, Kevin Ramus and Brent Kisling, for all of their collaborative work over the past two years. Since all of our work was interrelated, my portion of the project would not have been completed without them successfully completing their work. They were both always available for guidance and willing to help me with any of my design calculations and questions.

Lastly, I would like to thank the NASA Idaho Space Grant Consortium for providing me with a fellowship to fund my project. I would also like to thank the NASA Ralph Steckler Space Grant for providing our team with the opportunity to pursue our flywheel research by funding the University of Idaho for two phases.

Table of Contents

Authorization to Submit Thesis	ii
Abstract	iii
Acknowledgments.....	iv
Table of Contents	v
List of Figures	viii
List of Tables.....	x
List of Abbreviations.....	xi
Chapter 1. Introduction	1
1.1 Background and Motivation	1
1.2 Flywheel Energy Storage System Overview and Advantages	2
1.3 University of Idaho's Flywheel Energy Storage System Components	5
1.4 Dynamic Model of the FES System	7
Chapter 2. Thesis Objectives	8
Chapter 3. Scope	9
Chapter 4. Literature Review.....	11
4.1 Review of Sources for the FRRM Selection and Design Process	11
4.2 Review of Sources for the Rotor Dynamic Model	13
Chapter 5. The Field Regulated Reluctance Machine Theory and Design.....	16
5.1 Machine Selection	16
5.2 Machine Design Considerations and Operation	18
5.2.1 Machine Specifications and Topology	18
5.2.2 Principle of Operation.....	19
5.2.3 Rotor Saliency and Chevron Design.....	21
5.2.4 Machine Laminations	22
5.2.5 Machine Height.....	23
5.3 Machine Design Calculations.....	23
5.3.1 Impacts based on the Number of Poles.....	24

5.3.2 Basic Machine Calculations.....	24
5.3.3 Stator Dimensions.....	25
5.3.4 Rotor Design Calculations	29
5.3.5 Determining the Quadrature and Direct Axis Flux.....	30
5.3.6 Determining Turns and the Field Current.....	34
5.3.7 Determining Power Losses and Efficiency.....	34
5.3.8 Machine Optimization	36
5.3.8.1 Optimizing Rotor Chevron Geometry	36
5.3.8.2 Optimizing Stator Windings.....	37
5.4 Final Machine Dimensions.....	38
 Chapter 6. Passive and Active Magnetic Bearings	41
6.1 Active Magnetic Bearing Control Loop Design Considerations.....	41
6.2 Active Magnetic Bearing Design Considerations for the Stability of the Rotor	43
 Chapter 7. Drive and Stabilizing Bearing Force Derivations	48
7.1 Electromagnetic Force Derivation.....	48
7.2 Stabilizing Bearing Electromagnetic Forces	52
7.2.1 Stabilizing Bearing Mechanical Stiffness.....	55
7.2.2 Stabilizing Bearing Force/Current Factor.....	57
7.3 Drive Bearing Electromagnetic Forces	58
7.3.1 Winding Theory Derivation.....	59
7.3.2 Modified Winding Function Approach.....	63
7.3.3 Modified Winding Approach Applied to the Drive Bearing	66
7.3.3.1 Drive Bearing Mechanical Stiffness.....	72
7.3.3.2 Drive Bearing Force/Current Factor.....	73
7.3.4 Inclusion of both Axial and Radial Non-uniformities	75
7.3.5 Magnetic Circuit Model Verification for the Drive Bearing	77
7.4 Finite Element Analysis Verification	81
7.4.1 Drive Bearing Static Force Model Verification.....	82

7.4.2 Drive Bearing Bias Current Selection Process	84
7.4.3 Stabilizing Bearing Static Force Model Verification	86
Chapter 8. Dynamic Model of the FES System.....	88
8.1 Rigid Body Model Introduction and Assumptions.....	88
8.2 General Radial Dynamic Equations of Motion	92
8.3 Equations of Motion for the Simulink® Rotor Dynamic Model	95
8.4 Simulink® Model – Radial Dynamics	102
8.4.1 Open-Loop Dynamic Model.....	102
8.4.1.1 Stationary to Rotational Transformation	108
8.4.2 Closed-Loop Dynamic Model with Active Control	112
8.5 Axial Dynamic Model Components.....	116
Chapter 9. Summary, Conclusions, and Recommendations	118
9.1 Summary	118
9.2 Conclusions	119
9.3 Recommendations for Future Work	122
9.3.1 Low-Speed FES System Proof-of-Concept Recommendations	122
9.3.2 High-Speed FES System Recommendations	124
References	125
Appendix A: Field Regulated Reluctance Machine Design Calculations	127
Appendix B: Rotor Assembly Moment of Inertia Calculations.....	141
Appendix C: Modified Winding Approach Calculations	156
Appendix D: Bearing Stiffness and Current/Force Graphs.....	178
Appendix E: Magnetic Circuit Model – Drive Bearing Calculations	184
Appendix F: CATIA Model Outputs	193
Appendix G: Rotor Dynamic Simulink® Model	197

List of Figures

Figure 1: Energy Density Comparison for Energy Storage Systems (Modified Version of Comparison in [5])	4
Figure 2: UI's Complete FES System Setup (without Power Electronics Pictured)	7
Figure 3: FRRM Rotor and Stator Laminations with d and q Axes Labeled.....	21
Figure 4: Initial FRRM Rotor Lamination Chevron Shaped Design	22
Figure 5: M-36 Grade Electrical Steel BH Characterization Curve, from [19]	26
Figure 6: Stator Tooth and Slot Dimensions for the FRRM	28
Figure 7: Unwound FRRM Stator Laminations pressed onto Shaft	29
Figure 8: Quadrature Axis Magnetic Circuit including the FRRM Stator, Rotor and Airgap Reluctances	30
Figure 9: Flux Linkage for One Fully-Pitched Coil versus Electrical Angle	33
Figure 10: Total Winding Power Losses versus the Number of Poles for the FRRM	36
Figure 11: FRRM Wound Stator Laminations Completed by Strom Electric	38
Figure 12: Final FRRM Rotor and Stator Dimensions	39
Figure 13: Rotor Assembly Components (Top Plate, SB, Spacer, DB, and Magnet Plate)	44
Figure 14: Simple Magnetic Circuit, from [7]	50
Figure 15: Force for a Radial Bearing Geometry, from [7]	52
Figure 16: Stabilizing Bearing Stator Winding Schematic and Flux Paths	53
Figure 17: Negative Stabilizing Bearing Stiffness (N/mm) for the Linearized Bearing Force Equation	57
Figure 18: Force/Current Factor for the Linearized Stabilizing Bearing Force Equation	58
Figure 19: Doubly-Cylindrical Machine with Windings Placed in the Airgap, from [6]	60
Figure 20: Salient-Pole Machine with Rotor Eccentricities, from [18]	64
Figure 21: Drive Bearing Stator Winding Schematic	67
Figure 22: DB Airgap Function with or without Radial Eccentricities	68
Figure 23: Total DB MMF for the Operating Point (1mm Airgap and 1.75A Bias Currents)	70
Figure 24: Total DB Flux Density about the Operating Point (1mm Airgap and 1.75A Bias Currents).....	71

Figure 25: Negative Drive Bearing Stiffness (N/mm) for the Linearized Bearing Force Equation	73
Figure 26: DB Force/Current Factor for the Linearized Bearing Force Equation	74
Figure 27: Symmetrical Inclined Eccentricity between the DB Stator and Rotor	77
Figure 28: Equivalent Magnetic Circuit Model for the DB with 8 D-Axis Coils Energized... ..	78
Figure 29: DB Mechanical Stiffness for 8 Energized Coils – MCM Approach	80
Figure 30: DB Negative Stiffness for 8 D-Axis Coils Energized using the MWA Calculations	81
Figure 31: Flux Density Plot for 16 Direct Axis Coils on the DB Energized at 1.75A	83
Figure 32: Flux Density Plot for 16 Direct Axis Coils on the DB Energized at 4.38 A	85
Figure 33: Flux Density Plot for SB Coils Energized at 2.6 Amps	87
Figure 34: Rigid Rotor Model for the FES System’s Rotor Assembly	89
Figure 35: FES System’s Rigid Rotor with Four Position Sensor Locations	98
Figure 36: Eddy Current Position Sensor Physical Hardware Setup	99
Figure 37: Y-Z Plane – CCW Rotation of the Rotor Assembly for the angle β about the X-Axis	100
Figure 38: X-Z Plane – CW Rotation of the Rotor Assembly for the angle $-\alpha$ about the Y-Axis	101
Figure 39: Summation of X-Forces for the FES System Modeled in Simulink	103
Figure 40: Initial Sensor Measurement Transformation Subsystem in Simulink	105
Figure 41: Total X force and X COM Displacement versus Time for an Initial Translation ..	106
Figure 42: Summation of Moments about the X-Axis for the FES System Modeled in Simulink	107
Figure 43: Alpha and Beta versus Time for a Rotating Rotor with Initial Rotor Tilt.....	108
Figure 44: Stationary to Rotational Transformation for the Rotating Rotor Assembly.....	110
Figure 45: X and Y DB Rotating Displacements versus Theta for a Rotating Rotor	111
Figure 46: Stationary DB and SB Forces versus Time with Equal Bearing Parameters	112
Figure 47: PID Controllers (sensor displacements – inputs and control currents – outputs). ..	114
Figure 48: COM Displacements in the Closed-Loop Model for an Unconstrained Case.....	115
Figure 49: Tilt Angles in the Closed-Loop Model for an Unconstrained Case	115
Figure 50: Closed-loop Rotor Dynamic Model Flow Chart for the Simulink Model.....	116

List of Tables

Table 1: FRRM Final Machine Design Parameters and Results.....	40
Table 2: Final Design Parameters based on MOI and Moment Calculations	47
Table 3: Potential DB Bias Current and Corresponding Stator Teeth Flux Density	86
Table 4: CATIA Outputs used in the Rotor Dynamic Model	90
Table 5: Radial Dynamic Model .m File Inputs.....	104

List of Abbreviations

A_a	Airgap Area
AMB	Active Magnetic Bearing
Area_Pole_d	Direct Axis Pole Area
Area_Pole_q	Quadrature Axis Pole Area
B	Flux Density
B_a	Airgap Flux Density
B_{dairgap}	Direct Axis Flux Density in the Airgap
B_{Total}	Total Airgap Flux Density
CCW	Counterclockwise
COM	Center of Mass
CW	Clockwise
d	Direct Axis
DB	Drive Bearing
FEA	Finite Element Analysis
FEMM	Finite Element Method Magnetics
FES	Flywheel Energy Storage
FRRM	Field Regulated Reluctance Machine
F_{x Total}	Total X Force
G	Center of Gravity
H	Field Intensity
H_a	Airgap Field Intensity
HTS	High Temperature Superconductor
I_d	Direct Axis or Field Current
I_P	Polar Moment of Inertia
I_q	Quadrature Axis or Armature Current
I_T	Transverse Moment of Inertia
I_x	Moment of Inertia about the Rotational Axis
I_z	Moment of Inertia about the Axis Orthogonal to the Rotational Axis
k_i	Force/Current Factor
k_s	Negative Bearing Stiffness
L₁	Axial Distance from the Drive Bearing's Center to the Rotor's Center of Gravity
l₁	Axial Distance from the Sensor Plane #1 to the Rotor's Center of Gravity
L₂	Axial Distance from the Stabilizing Bearing's Center to the Rotor's Center of Gravity
l₂	Axial Distance from the Sensor Plane #2 to the Rotor's Center of Gravity
L_d	Direct Axis Inductance
L_q	Quadrature Axis Inductance
M(ϕ)	Modified Winding Function
MCM	Magnetic Circuit Model
m_d	Direct Axis Coils per Pole
MMF	Magnetomotive Force
MMF_{Airgapd}	MMF Drop in the Direct Axis Airgap
MMF_{Totald}	MMF Drop in the Direct Axis
MOI	Moment of Inertia
m_q	Quadrature Axis Coils per Pole

m_{total}	Total Number of Coils per Pole
MWA	Modified Winding Approach
N	Number of Turns
n(ϕ)	Turns Function
N(ϕ)	Winding Function
PID	Proportional Integral Derivative
PMB	Passive Magnetic Bearing
PMSM	Ironless Permanent Magnet Synchronous Machine
Pole_Arc_d	Pole Arc in the Direct Axis
q	Quadrature Axis
r_{ir}	Inner Radius of the FRRM's Rotor
r_{os}	Outer Radius of the FRRM's Stator
R_x	Airgap Reluctances
s	Airgap
SB	Stabilizing Bearing
SRM	Synchronous Reluctance Machine
UI's	University of Idaho's
UPS	Uninterruptible Power System
V_a	Volume of the airgap
W_a	Field Energy Stored in the Airgap
WFA	Winding Function Approach
x₁	X-axis Sensor Coordinate for Sensor Plane #1
x₂	X-axis Sensor Coordinate for Sensor Plane #2
x_G	X-axis Center of Gravity Displacement
y₁	Y-axis Sensor Coordinate for Sensor Plane #1
y₂	Y-axis Sensor Coordinate for Sensor Plane #2
y_G	Y-axis Center of Gravity Displacement
z	Axial Length
α	Azimuthal Angle (Chapter 7) & Rotor Tilt Angle about the y-axis (Chapter 8)
β	Rotor Tilt Angle about the x-axis
Δi_x	Change in Coil Current
δ_s	Static Eccentricity Coefficient
ζ_{xx}	Shifting Variable of the Stabilizing or Drive Bearing
θ	Rotor Position Angle
σ	Radial Bearing Angle
ϕ	Azimuthal Angle (Section 7.4.2) & Flux (elsewhere)
ϕ_d	Direct Axis Flux
ϕ_{dAirgap}	Direct Axis Flux in the Airgap
ϕ_{dStatorTooth}	Direct Axis Flux in the Stator Teeth
ω	Angular Rotor Velocity

Chapter 1. Introduction

1.1 Background and Motivation

To support human colonization and exploration of the lunar surface, NASA needs a way to effectively store either solar or nuclear-generated power. These, and other energy sources, require storage to enable them to meet demand that varies throughout the day while the source generating capacity simultaneously varies. Flywheels provide a reliable, efficient and low-maintenance way to provide continuous energy on demand.

Since the moon cycles through 14 earth days of sunlight and 14 earth days of darkness, the intermittent energy methods (such as solar panels) cannot serve as a constant source. Also, nuclear generation must be reduced during the day to prevent overheating due to high lunar day-time temperatures. One feasible solution is to use a flywheel energy storage (FES) system to provide continuous energy for life support and scientific instruments. A FES system requires a lighter payload for installation than batteries, NASA's current alternative. In addition, a FES system has a broad operating temperature range and can withstand elevated radiation levels experienced on the lunar surface.

Basic flywheel energy storage is a well-known technology, currently being marketed in ratings up to hundreds of kilowatt-hours of energy storage with power ratings up to hundreds of kilowatts [1]. High speed flywheels provide safe, reliable and convenient energy storage for intermittent energy generation technologies, such as solar and wind. As a result, FES systems are also a reasonable energy storage alternative on earth. Boeing has worked with the Department of Energy to deploy a FES system in a commercial uninterruptible power system (UPS) environment [2]. With reasonable modification, they hold great promise in the unique characteristics of the lunar environment.

The remainder of this chapter discusses the University of Idaho's (UI's) proof-of-concept FES system and how each component enables this proof-of-concept FES system to achieve high efficiency. To move energy in a bidirectional fashion efficiently and effectively, electromagnetic motor-generators (or machines) are needed. Various machine topologies are explored and outlined in the literature review. To effectively design a controller that prevents instability, a dynamic model is useful and is introduced in this chapter. In addition, the advantages and basic operation of FES technology are discussed.

1.2 Flywheel Energy Storage System Overview and Advantages

Flywheels are not a new technology and date back to the Industrial Revolution. During the Industrial Revolution, flywheels were purely mechanical and were used to maintain smooth machine operation [3]. During the 1960s and the 1970s, NASA proposed using flywheels as a source of energy storage for future space missions; flywheels were also a primary candidate for electric vehicle and stationary backup-power applications. Flywheel technology was not ready for space applications until the 1980s when magnetic bearings, power electronics, carbon fiber constructed flywheels, and machines with high power densities were introduced [3]. Current applications of flywheels include electric vehicles, supplementary UPS storage, providing storage for renewable energy generation (such as wind), and to improve power quality issues with the electric grid [4].

A flywheel operates by storing kinetic energy in the form of a rotating mass. As the speed of a flywheel is increased, the amount of energy stored significantly increases. The kinetic energy in a flywheel is directly related to the inertia and rotational speed of the flywheel as shown below:

$$\text{KE} = \frac{1}{2} I \omega^2 \quad (1.1)$$

where **KE** is the kinetic energy stored in the flywheel, **I** is the moment of inertia, and **ω** is the angular velocity of the flywheel [4]. The moment of inertia depends on the shape and mass of the flywheel.

In general, a FES system includes an electric machine to convert between mechanical and electric energy, power electronics to control the machine and power flow, and a flywheel to store energy. A FES system may also include a vacuum chamber to reduce windage losses, and magnetic bearings to eliminate friction.

The electric machine can be operated as either a motor or a generator to transfer energy into and out of the flywheel. If the machine is being operated as a motor, electric energy is supplied to the stator windings, which then applies torque to the rotor, causing a faster rotational speed and an increase in stored kinetic energy. When the machine is operated as a generator, the stored kinetic energy is converted to electrical energy [4]. The power electronics are used to operate the electric machine as either a motor or generator.

In addition to FES systems, there are other viable energy storage systems including batteries (lead-acid and nickel- and lithium-based), compressed air, pumped hydroelectricity, and supercapacitors. Compared to these alternative energy storage systems, the advantages of flywheels include [4]:

- Long life expectancy (20+ years)
- High energy and power density (energy density comparison shown in Figure 1 for current and theoretical energy storage systems) [1], [5]
- High energy conversion and storage efficiency on the order of 85-95% [1]
- Reliable - no periodic maintenance is required
- Low environmental impact (no hazardous materials)

- Operate in extreme environments (wide operating temperatures compared to batteries)
- Easily measure the state of charge based on rotational velocity
- Rapid discharge rates without degradation

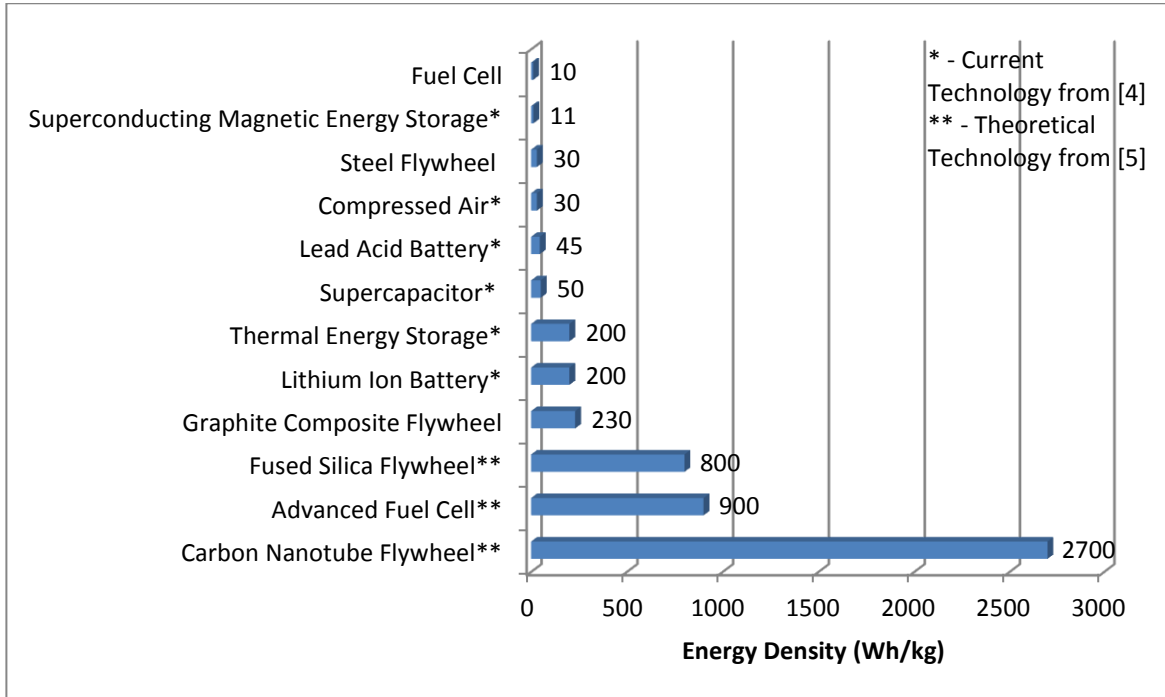


Figure 1: Energy Density Comparison for Energy Storage Systems (Modified Version of Comparison in [5])

To obtain a highly energy efficient FES system, system losses such as windage and friction can be reduced by using a vacuum system and magnetic bearings. To further reduce FES system losses, the hysteresis and eddy current losses must also be eliminated. These are commonly referred to as core losses, since they result from changing magnetic fields in the iron core of the electric machine. Although no magnetomotive force is being applied to the machine during idling periods, flux still exists in the machine and does not passively return to zero, thus a magnetic field (known as residual flux) is left in the core [6]. To eliminate the

residual flux in the machine, a machine topology must be selected that can be degaussed; i.e., eliminate, or greatly reduce, the residual flux in the machine.

1.3 University of Idaho's Flywheel Energy Storage System Components

The UI's FES system consists of various subsystems designed to reduce any inherent machine losses and improve efficiency. This FES system includes a field regulated reluctance machine (FRRM), a passive magnetic bearing levitation system, liquid nitrogen and water cooling systems, a vacuum and containment system, power electronics for control, and an active magnetic bearing. Various machine topologies are explored for the machine component of the FES system and are explained in the literature review. The FRRM's purpose is to efficiently convert electrical energy applied to the stator windings into kinetic energy stored in the spinning rotor. To prevent the stator windings from overheating, a water cooling system runs through the center shaft. The vacuum system minimizes windage losses by achieving vacuum conditions of approximately 10^{-4} Torr. It also serves as the containment system in the case of system failure at low rotational speeds.

Instead of using a mechanical bearing with high friction losses and required maintenance, magnetic bearings are used to lift the machine vertically via repelling magnetic forces. The magnetic levitation system results in minimal friction due to the lack of contact with the center shaft. In general, there are two forms of magnetic bearings: passive and active. Passive magnetic bearings do not require any control to maintain stability, whereas active magnetic bearings require active control to achieve stability [7].

The magnetic levitation system is a passive magnetic bearing (PMB) and, therefore, position control or electricity are not required. The PMB is composed of high temperature superconductors (HTS) and a permanent magnet Halbach array. When the HTS are cooled to

a sufficiently low temperature, less than 90 K for YBCO [8], almost all of the magnetic flux is expelled from the HTS. A repulsive force results that acts against the magnetic flux and the magnet array that create flux, thus resulting in contactless levitation of the rotor. The HTS bearing technology has the potential to reduce idle losses to less than 0.1% of stored energy per hour [9]. Although the HTS do not require active control, the HTS will need to be cryogenically cooled with liquid nitrogen to 77 K to exhibit the superconducting properties. Therefore, the HTS are mounted on top of a copper plate and liquid nitrogen is continually moved through a channel in the copper plate to provide cooling.

In addition to the PMB, there is also a dedicated active magnetic bearing (AMB) which uses active control based on feedback from eddy current sensors. The purpose of the AMB is to prevent collision between the stator and rotor. The AMB controls the horizontal and tilting forces acting on the rotor in coordination with the FRRM. The FRRM is a self-bearing and serves two purposes: as an active magnetic bearing to control the rotor's position and as a machine to provide rotation. To actively control the bearing forces, a feedback control loop and eddy current sensors are used to measure rotor displacements. A microprocessor then transforms these measurements into a control signal, and an amplifier converts these signals into currents that provide corrective magnetic forces [7]. The assembled FES system is shown in Figure 2.

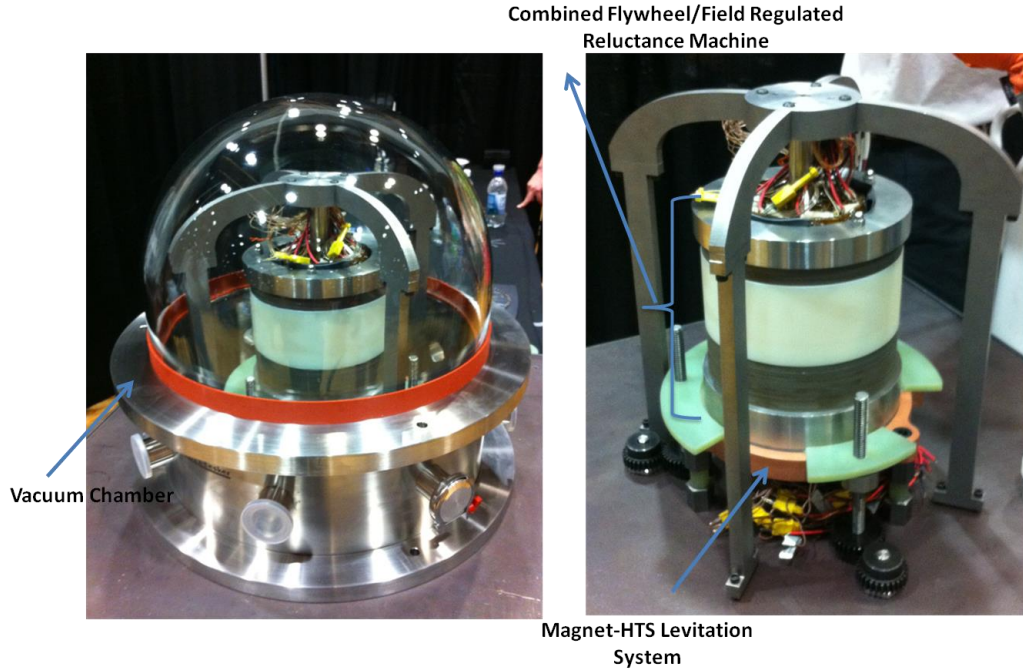


Figure 2: UI's Complete FES System Setup (without Power Electronics Pictured)

1.4 Dynamic Model of the FES System

As was discussed previously, the AMB in combination with the self-bearing is necessary to provide corrective forces to control the rotor's position. To actively control the horizontal and tilting forces acting on the rotor, a dynamic model is needed to predict rotor responses to imbalances without the use of a control-scheme. To properly design a controller, the rotor is modeled as a symmetric and uniform rigid body, and rotor displacements are modeled in terms of translational and angular motion about the rotor's center of mass. Based on a few key assumptions, the axial and radial dynamics are modeled separately, and the inherently nonlinear rotor dynamic equations are linearized about an operating point. In future chapters, the dynamic model for the FES system is described. The dynamic model described here is used by the other graduate student researchers who worked on the project to aid in development of a control algorithm for the FES system to prevent collisions between the rotating and non-rotating portions of the electric machine.

Chapter 2. Thesis Objectives

The first objective of this thesis is to discuss the iterative design process used to design the FRRM given a set of operating conditions. Although there are various machine topology options, the FRRM is an ideal candidate to serve as the motor-generator portion of the FES system. One of the advantages of the FRRM is that it can be used as a proof-of-concept to verify and compare degaussing algorithms in the future. The integrated flywheel and machine design described here are optimized for low rotational speeds.

The next primary objective of this thesis is to model the dynamic behavior of the rotor. The AMB and self-bearing control the horizontal and tilting forces acting on the rotor in conjunction with the passive HTS bearing. An open-loop rotor dynamic model is created to show how imbalances affect the forces and moments acting on the rotor without active control. Then a dynamic model is used to aid the development of the linear controller algorithm to prevent dynamic instability. A rigid body model is created in Simulink® to simulate the decoupled radial and axial dynamics of the rotor.

The last objective is to derive the electromagnetic bearing force expressions that model the forces acting on the rotor's center of mass. These bearing forces are inherently nonlinear and are linearized about an operating point to reduce computation time. These bearing forces are derived based on magnetic circuit model approach and modified winding theory approach. After modeling the linear bearing forces in Simulink®, a closed-loop dynamic model is simulated with active control to ensure dynamic stability. The closed-loop dynamic model is a tool that will be used for the future design of the rotational controller algorithm.

Chapter 3. Scope

Before discussing the layout of this thesis, the objectives and accomplishments of the UI's NASA funded, multi-phase project are outlined. Phase I provided analytical and experimental proof that iron energy losses could be reduced during idling periods. In addition, various machine topologies were explored during Phase I, and the FRRM was selected for the FES system. The work completed in this thesis is part of Phase II. The goal of Phase II was to design and build a proof-of-concept low-speed, integrated, hubless flywheel and machine. This proof-of-concept FES system will be used in future work to verify and compare degaussing algorithms. If Phase III funding is received, future work will include the design, construction, and testing of a high-speed FES system adapted to the lunar environment.

During Phase II, the design and implementation of the FES system proof-of-concept relied on collaboration with two other electrical engineering graduate students. This thesis primarily covers the FRRM design process and the rotor dynamic model, whereas the thesis written by Brent Kisling [10] describes the AMB controller algorithm, design and implementation. The thesis written by Kevin Ramus [11] contains the sensors, printed circuit boards, and power amplifier designs necessary to implement the controller algorithms.

Chapter 4 contains a literature review that was used to design the machine and model the rotor dynamics. Chapter 5 discusses why the FRRM was selected for the machine portion of the FES system. In addition, this chapter explains the major design decisions and the equations used to select the final design. Chapter 6 describes the basic operation and design of the passive and active magnetic bearings. Chapter 7 explains the derivation of the FRRM and the AMB linearized electromagnetic force models, where the modified winding and magnetic circuit approaches are used to obtain expressions for the radial bearing forces. This chapter

also includes a finite element verification of the FRRM and AMB designs. Chapter 8 develops the radial and axial rotor dynamic equations and models these using Matlab's Simulink® environment. Lastly, Chapter 9 presents a summary and conclusions reached from the dynamic model and machine design, along with recommendations for future work.

Chapter 4. Literature Review

A literature review was conducted to determine the most effective FRRM design and rotor dynamic model used in research and in the field. This literature review explored the major equations and assumptions used to design a functional FRRM. A primary source was used to develop the UI's FRRM design, while additional sources were reviewed to confirm that the FRRM was the ideal machine for this project. Most of the sources consulted in this thesis were used for the design of the rotor dynamic model. Assumptions were then taken from these sources to simplify the dynamic model and provide a linear bearing force model for both bearings.

4.1 Review of Sources for the FRRM Selection and Design Process

At the beginning of the project, multiple machines were considered for the machine component of the FES system. The top contenders were then selected based on the expected machine force density and its ability to be degaussed [12], where force density was defined as a “measure of how effectively a machine uses the airgap area to create beneficial force” [13]. Force density was a metric used to compare the following four machines [12]:

- 1) Synchronous Reluctance Machine (SRM)
- 2) Field Regulated Reluctance Machine (FRRM)
- 3) Ironless Permanent Magnet Synchronous Machine (PMSM)
- 4) Iron-on-Rotor Permanent Magnet Synchronous Machine

The SRM is a synchronous machine with salient poles that lack field windings. The SRM can be degaussed by applying decaying modulated voltage waveforms to the stator windings [12]. Due to the absence of brushes and slip rings, the SRM can also operate in vacuum conditions.

The FRRM is a modified synchronous machine with the field windings located on the stator. The FRRM's stator coils operate in a time-share mode and constantly alternate their function between field and armature windings; varying the coil's function permits independent control of torque and rotor flux [13]. The FRRM also has the ability to be degaussed and can achieve the highest force and power densities by optimizing the control of individual stator windings [13].

The ironless PMSM operates similarly to an excited-field synchronous machine, with the exception of having permanent magnets connected to the rotor to produce a majority of the field flux [12]. Instead of an iron rotor, the rotor is composed of permanent magnets, either in an array or one solid magnet. Unlike the ironless PMSM, the iron-on-rotor PMSM includes magnets to create the field flux. Since the iron-on-rotor PMSM removes the iron from the stator, the residual flux normally produced by the sinusoidal stator currents is eliminated [12].

After comparing machine force densities and other metrics, the FRRM was selected as the ideal candidate for the UI's FES system. Since the FRRM could not be purchased from vendors, it was designed in house. The primary machine design equations were derived by Law in [13] and were modified for the UI's FRRM design. Law validated the machine design procedure and successfully operated a six-phase, 28-kW, 500 RPM FRRM [13]. This procedure included equations to select the number of phases, stator teeth and slot dimensions, the number of poles, along with other parameters. One major modification made to the equations taken from Law's work was to neglect the magnetomotive force drops across the rotor and stator iron, since these were negligible in comparison to the drops across the airgap.

Additional papers were also used to develop the FRRM design equations. The paper written by Law and Lipo in [14] was used to establish an understanding of the basic operation of a FRRM. In addition, this paper presented a design equation used to relate the flux linking one full-pitch turn to the electrical angle. Using this equation, a relationship between the machine's voltage and flux linkages was derived. The magnetic circuit model for the FRRM presented in [15] was also used to develop the governing equations for the FRRM.

4.2 Review of Sources for the Rotor Dynamic Model

After the FES system was designed and constructed, a dynamic model was created to assist in developing the controller algorithm. The controller was responsible for maintaining the rotor's position and preventing dynamic instability. In order to reduce computation time and simplify the controller design, a linear control scheme was desirable. To design the controller, the equations of motion for the rotor assembly were necessary. The equations of motion for the rotational and translational motion of the rotor assembly were then linearized to simplify the dynamic model.

The equations of motion for two radial bearings were derived by Schweitzer [7]. The key assumptions made in this work were also used for the UI's dynamic model to decouple the radial and axial dynamics. Based on the physical rotor dimensions and constraints, and the assumption that the airgap displacements were small in comparison to the rotor dimensions, the radial equations of motion could then be linearized [7]. An additional assumption was made to describe the angular and translational displacements of the rotor by the position of the rotor-fixed system with respect to the inertially fixed coordinate system [7]. This assumption, along with an assumed constant angular velocity, led to characterizing the Euler's angles as

inclinations about the stationary x and y axes, where Euler's angles were used to describe the angular motion of the rotor.

The equations of motion derived in [7] were successfully implemented in the work completed by Kascak in [16]. Kascak used a linear form of the equations of motion to describe the radial dynamics for a fully levitated rotor that was magnetically suspended by two separated conical motors. The rotor was modeled as a rigid body in Matlab's Simulink® environment and combined with PID controllers to merge the mechanical dynamic system with the linear controller. Kascak successfully used the dynamic model to rotate the motors at low speeds and prevent instability.

The electromagnetic bearing force expressions were needed to model the forces acting on the rotor in the dynamic model, where the bearing forces were nonlinear due to the squared relationships with the coil current and airgap. It was found that a linear control scheme has been successfully implemented to control these inherently nonlinear bearing forces for various applications [7]. To reduce computation time, Schweitzer linearized the bearing's force/displacement and force/current relationships about an operating point (the equilibrium position of the system) and used these as approximations for the bearing forces [7]. A linear bearing force model has limits of applicability that must be avoided, such as contact between the rotor and stator, severe flux saturation, or low coil currents [7]. To determine the force/displacement and force/current relationships for the UI's FES system, an electromagnetic model for both bearings was developed.

Methods used in literature to develop electromagnetic models included a magnetic equivalent circuit method, finite element analysis, and the winding function method. The magnetic equivalent circuit method was selected for the UI's AMB, but would not be

sufficient for the FRRM due to the complexity of the machine geometry. Previous work completed by Lipo in [17] was initially used to derive the FRRM's electromagnetic model using the winding function method. However, this method assumed that the airgap was uniform, which was not the case for eccentric rotors. Since the force/displacement relationship was desired for the FRRM, radial eccentricities were needed to calculate the resulting bearing forces. Therefore, Lipo's approach was insufficient, and the modified winding approach [18] that incorporated airgap eccentricities into the flux and force distribution calculations was used instead.

Chapter 5. The Field Regulated Reluctance Machine Theory and Design

This chapter discusses why the FRRM was selected, the decisions made to design the machine and a summary of the final design parameters. There were various machine candidates, but the FRRM was selected as the final machine primarily due to the high potential energy density and independent coil control. The FRRM utilizes coils that are continuously varying whether they are being operated as a torque or field producing coil. This can result in a highly efficient machine as long as the controller design is implemented successfully. The machine design was an iterative process where various poles, stator tooth and slot dimensions, rotor dimensions, airgap sizes, etc. were explored to result in an optimal design. The chapter concludes with a summary of the final machine design, along with a table highlighting the major dimensions.

5.1 Machine Selection

As was discussed in the introduction, the project specifications and goals reduced the number of viable machine options. One initial project specification was to eliminate machine options that utilized field windings on the rotor. Field windings on the rotor were undesirable since slip rings and brushes required continual maintenance, introduces additional machine power losses, and would not work in a vacuum. In addition, removing field windings from the rotor eliminated rotor conduction losses. There were only a few machines that could operate without field windings on the rotor, such as the synchronous reluctance machine and the FRRM [12].

To maximize the FES system efficiency, minimization of the energy losses was required. Windage and mechanical friction losses were greatly reduced by operating the FES system in a vacuum and using magnetic bearings, respectively. Another source of energy loss

was due to the residual magnetic flux in the rotor, as was explained in Section 1.2. This criteria eliminated a permanent magnet synchronous machine because there would be inherent hysteresis losses in the stator due to the permanent magnetic field [13]. Whereas the FRRM is a non-permanent magnet design and could thus be degaussed.

The FRRM was selected due to the following advantages it had for FES system applications:

- 1) No field windings located on the rotor: Because slip rings and brushes do not operate in vacuum and introduce additional machine losses, a FRRM has both the field and torque producing windings located on the stator. In addition, by removing the field windings from the rotor, the rotor conduction losses are eliminated.
- 2) Ability to be degaussed: Since the residual magnetic flux in the rotor produces undesirable energy losses, the FRRM design allows degaussing to reduce the idling iron losses.
- 3) Independently controlled coils: allow for independent control of the torque and field regulation (i.e. magnetizing) flux [14] since each coil's function (armature versus field winding) varies with the rotor's position. Independent control also makes it possible to use the FRRM as an AMB to actively control the rotor's position.
- 4) High potential force density: reduces material and machining costs and produces a more efficient machine [12]. Compared to other machine topologies, the FRRM has the highest potential force density [12].

Unlike other machine options, the FRRM could not be ordered from a vendor, and was designed and constructed at the UI.

5.2 Machine Design Considerations and Operation

Prior to discussing the specific steps taken to design the machine, the principle machine operation and design considerations are explained. The machine design process was iterative and various parameters were changed to optimize the design. The major parameters that were varied include the number of poles, number of coils per pole (direct and quadrature) and the airgap between the rotor and the stator. To better understand how the FRRM operates, the direct (d) and quadrature (q) axis coils are explained. This section also includes the initial design considerations for the rotor's shape, height, and material. To begin the design process, the flywheel team determined a list of desired operating conditions.

5.2.1 Machine Specifications and Topology

The team involved with designing the FES system developed initial specifications for a low-rotational speed machine. As was discussed previously, the chosen machine had to be able to be degaussed, operate in vacuum conditions, and provide a high force density. In addition to these specifications, the following desired operating conditions were specified: output power (400 Watts), voltage (12 Volts), force density (1.5 kN/m^2), operating speed (1800 RPM), d-axis airgap flux density (B_{dairgap}) (0.33 T), as well as the machine dimensions. For machines, the force density is equal to the tangential force (rotation force) per airgap area and shows how well a machine can produce forces with a given airgap [14]. The B_{dairgap} was set equal to the ratio of the tooth width to the slot cord. The outer rotor radius was limited by the size of the lathe-chucks available in the UI's machine shop.

The machine topology selected was an “inside-out” or open core topology, so the rotor was positioned outside of the stator. The spinning rotor also served as the flywheel. In accordance with Equation (1.1), the open core topology allowed for a larger moment of inertia

and increased the angular velocity of the flywheel, thus increasing the energy stored. In addition, the “inside-out” design resulted in a smaller airgap between the rotor and stator, which increased electromagnetic forces. Before explaining the design optimization process, the basic operation of the FRRM is described.

5.2.2 Principle of Operation

When current is applied to the stator windings, a rotating magnetic field is produced that causes the rotor to spin. This rotating magnetic field can be represented as two magnetic poles: a north pole where the flux leaves the rotor and a south pole where the flux enters the rotor. For a two pole machine (meaning a single north and south pole), the electrical and mechanical frequencies are the same. However, for a four pole machine, there are two north poles and two south poles. Thus, in one electrical cycle, the rotor only moves halfway around the stator. This results in an electrical frequency that is twice as fast as the mechanical frequency of rotation:

$$\omega_e = \frac{P}{2} \omega_m \quad (5.1)$$

where ω_e is the electrical frequency, P is the number of poles and ω_m is the mechanical frequency. As the number of poles increase, the electrical frequency required for the rotor to perform one mechanical rotation also increases.

The ferromagnetic rotor is essentially a large electromagnet that is composed of magnetic poles. For the FRRM, the rotor’s poles are salient, meaning they protrude out from the cylindrical surface of the rotor [6]. A cylindrical rotor (i.e. non-salient rotor) has a uniform distribution of flux around it. The rotor’s saliency alters how the flux is distributed around the machine. Saliency results in a different amount of flux (and therefore inductance) for the pole and interpole regions of the rotor. The FRRM efficiency increases as the ratio of the

inductances, also known as the saliency ratio, between the axis aligned with the poles (the d-axis) and the axis aligned with the interpoles (the q-axis) is maximized.

The torque and field producing windings (q-axis and d-axis coils) are both on the stator and eliminate field windings on the rotor. Each of the stator coils are controlled independently in the FRRM and the function of each coil (i.e. armature versus field winding) is constantly varying with rotor position. The FRRM is essentially a synchronous machine with all of the windings located on the stator operating in a time-share mode between field and armature windings. The time-share mode is advantageous since the rotor's flux and torque production can be independently controlled [13]. Since the function of each coil varies with time, a controller is needed to vary the current and voltage in each coil. H-bridges are used to vary the coil current based on the location of the coil. The controller algorithm and methodology are not explained in this thesis and are discussed in [10].

The d-axis coils' purpose is to produce the main magnetic field in the FRRM, similar to the field windings in a synchronous machine [6]. In a synchronous machine, the rotor's magnetic field is supplied by a dc current applied to the rotor windings. The dc current is supplied by either an external dc source via slip rings and brushes or by mounting a dc power source to the shaft [6]. As was previously mentioned, brushes and slip rings require maintenance and the brushes introduce additional power losses that are undesirable for this project.

The rotating magnetic field induces the voltage within the stator's armature windings. The purpose of the q-axis coils is to provide torque, similar to the armature windings in a synchronous machine where the main voltage is induced [6]. The q-axis coils (m_q) are located opposite of the rotor pole faces and the d-axis coils (m_d) are located in the interpole regions.

The physical placement of these coils is offset 90 electrical degrees from the d- and q- axes shown in Figure 3.

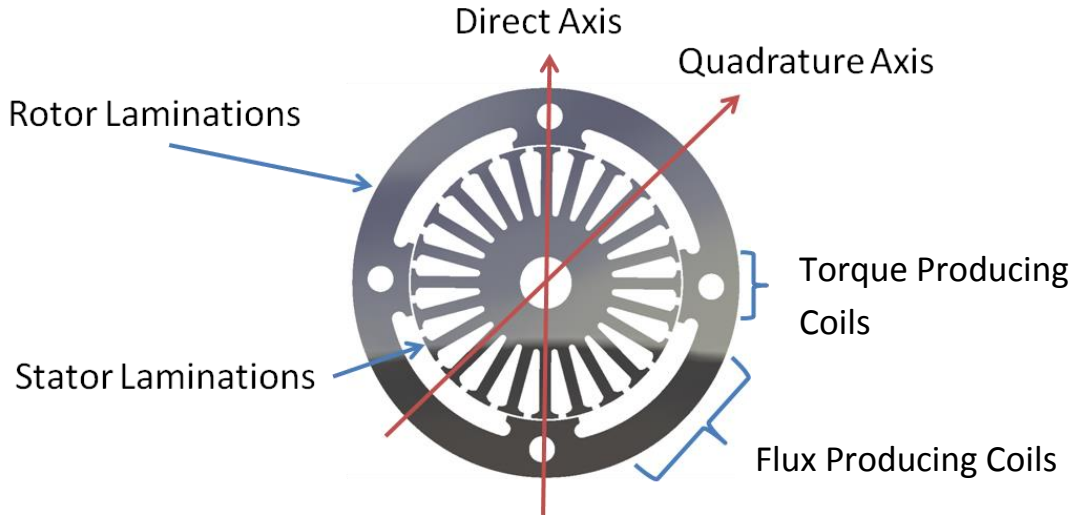


Figure 3: FRRM Rotor and Stator Laminations with d and q Axes Labeled

5.2.3 Rotor Saliency and Chevron Design

To determine the number of poles, the ideal shape for the rotor poles and interpole regions (also referred to as rotor chevrons) were investigated in order to maximize the saliency ratio, which is a ratio of the inductance in the d-axis to the q-axis (L_d/L_q). If L_d was equal to L_q , no torque would be produced. As the saliency ratio is increased, the torque produced also is increased. The saliency ratio was dependent on the airgap and therefore the shape of the rotor chevrons. In the initial rotor design, the chevrons were shaped like clovers as shown in Figure 4, and the clover dimensions were varied to analyze the impact on the saliency ratio. To optimize the chevron design, the airgap function and its inverse were calculated; these functions modeled the airgap between the rotor and the stator. A Fourier series approximation was developed for the inverse airgap function to calculate the mutual and self inductances of the stator and the resulting saliency ratio.

Next, the height and width of the rotor chevrons were varied in order to determine the ideal shape. If the iron was not saturated, increasing the depth of the slot in the rotor chevrons had no impact on the saliency ratio; however, changing the width of the chevrons did. Extending the chevron width too far led to increasing q-axis flux, and making the chevron too narrow, causing an undesirable decrease in the d-axis flux. From these calculations, the optimal arc lengths for the rotor chevrons (sixty electrical degrees) were determined.

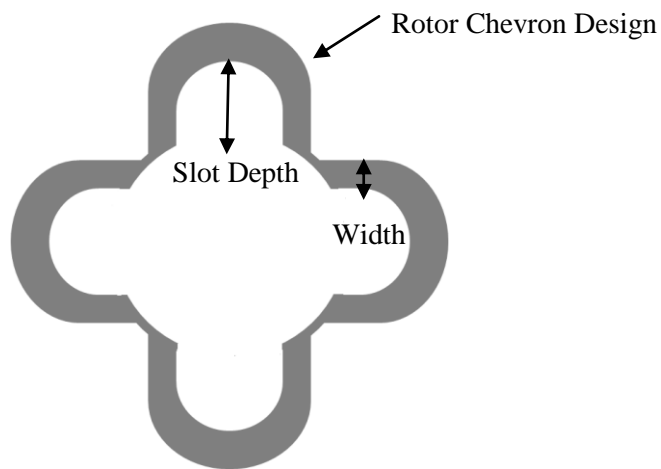


Figure 4: Initial FRRM Rotor Lamination Chevron Shaped Design

5.2.4 Machine Laminations

The rotor and stator were composed of iron laminations rather than a solid block of iron to reduce the eddy current losses. According to Faraday's law, time-changing flux induces a voltage within the core, thereby causing current to circulate within the core. These circulating currents, also known as eddy currents, cause heating and therefore losses in the core [6]. Constructing the iron core out of laminations reduces the eddy current losses by breaking the ferromagnetic core into strips. Since eddy current losses are proportional to the current path length, breaking the iron core material into strips reduces these losses. An oxide coating was also applied to the laminations to further reduce the current paths in the UI's design.

There were two types of laminations that were considered: vertical and horizontal orientations. Vertically oriented laminations were ruled out due to the difficulty of fabrication. The horizontally orientated laminations were made out of 26 gauge, M-36 grade silicon electrical steel sheets. The M-36 grade was selected due to its ideal magnetization curve, which was ideal due to the curve's saturation point. The electrical steel sheets were only available in certain sizes from the supplier, which determined their thickness (0.0185 inches). These electrical steel sheets were cut using water jetting at Northwest EDM in Spokane, WA. These were not machined in-house due to cost and the desired tolerances (0.002 inches).

5.2.5 Machine Height

When the machine was initially being designed, the HTS were approximated as being able to provide a total force of 2 N/cm^2 radially and 3.3 N/cm^2 axially to the rotor. If there was no active control and the rotor was off-center, the HTS radial forces were intended to exceed the electromagnetic forces between the rotor and stator (to maintain the rotor's ideal position). Since electromagnetic force is proportional to surface area, the lamination height of the machine was selected to prevent the electromagnetic machine forces from exceeding the HTS radial forces to prevent a rotor and stator collision.

5.3 Machine Design Calculations

This section outlines the design process and calculations (found in Appendix A) used to select final machine dimensions. These calculations included determining the stator and rotor dimensions, the number of poles, the direct and quadrature axis currents and flux, the number of turns per coil, the total Magnetomotive Force (MMF) for the d- and q- axes, power losses due to the stator windings and the overall efficiency. The machine design equations were a function of the airgap, inner radius of the rotor, number of poles, and number of

quadrature versus direct axis coils. These were varied until an optimized machine design was obtained.

5.3.1 Impacts based on the Number of Poles

The FRRM design was analyzed over a range of two to eight poles to see how the number of poles impacted efficiency. Since the predefined machine dimensions result in a relatively small machine, a maximum of eight poles was considered. By incorporating more than eight poles, the stator slots would be too small and would not leave adequate room for the stator coils.

The design calculations were performed as a function of poles to show how the number of poles impacted other dimensions and outputs. As the number of poles increased, the L_d/L_q ratio increased because the flux path length in the d-axis decreased. The shorter path length resulted in a smaller MMF drop across the rotor chevrons. By applying Ampere's Law, the MMF can be shown to be equal to the product of the magnetic field intensity (\mathbf{H}) and the length (\mathbf{l}) of the path traveled by the flux:

$$\mathbf{MMF} = \mathbf{HI} \quad (5.2)$$

For an unsaturated machine, the majority of the MMF drop was across the airgap versus the iron core. For a higher pole count machine, the disadvantage of having more airgaps for the flux to overcome offset the advantages of having a shorter d-axis flux path. This geometry also resulted in smaller end winding losses, since the stator coils were wound about a smaller coil pitch.

5.3.2 Basic Machine Calculations

The first step in the design process was to calculate the outer radius of the stator (r_{os}) and rotor (r_{or}) based on a given inner radius of the rotor (r_{ir}). These dimensions varied as a

function of the airgap between the rotor and stator and the given r_{ir} . Using these dimensions, the effective length of the machine could be determined, where the effective length is equal to the total height of the iron laminations. As was explained previously, the rotor and stator consist of stacked laminations, each coated with a specialized oxide to reduce eddy current losses. To take into account the ratio of iron versus oxide, a stacking factor of 0.96 was defined based on prior machine designs [13]. The actual height of the machine is equal to the effective length divided by the stacking factor. To determine the effective length, the equations for force density ($\frac{\text{Force}}{\text{Area}}$) and power (Torque * ω_m) were combined and resulted in (where the lateral area of the machine is $2\pi r_{os} \text{EffectiveLength}$):

$$\text{EffectiveLength} = \frac{(\text{Power})(\text{StackingFactor})}{(2\pi)(r_{os}^2)(\omega_m)(\text{ForceDensity})} \quad (5.3)$$

The pole pitch, the angular distance between two adjacent poles, was calculated in mechanical degrees and was used to determine the spacing between the coils and the aspect ratio. The pole pitch can also be expressed as a distance if the angular pole pitch was multiplied by r_{os} . The aspect ratio is the ratio between two sizes (the effective length and pole pitch), and if between 0.5-2, is considered desirable and improves machine stability. The next step was to determine the more detailed stator dimensions (such as the stator teeth and slot dimensions).

5.3.3 Stator Dimensions

The stator teeth and slot dimensions were designed to reduce power losses in the stator windings and to avoid saturation in the stator teeth. A larger slot area was desirable since power losses decreased as a function of increasing slot area, where the slot area represented the open space between two stator teeth. The slot area was increased as the width of the teeth decreased, and as the slot depth increased. The slot depth was set equal to the difference

between r_{os} and 1.35 inches, which left adequate room for the center shaft and maintained structural integrity. The minimum tooth width was limited by manufacturing capabilities and the prevention of saturation within the stator teeth. The stator tooth flux density was set to 1.0 T to avoid saturation, where 1.0 T was well below the knee of the BH curve for the M-36 material and was in the linear region of the BH curve. By avoiding saturation, the MMF drops in iron can be neglected. The BH curve is shown in Figure 5.

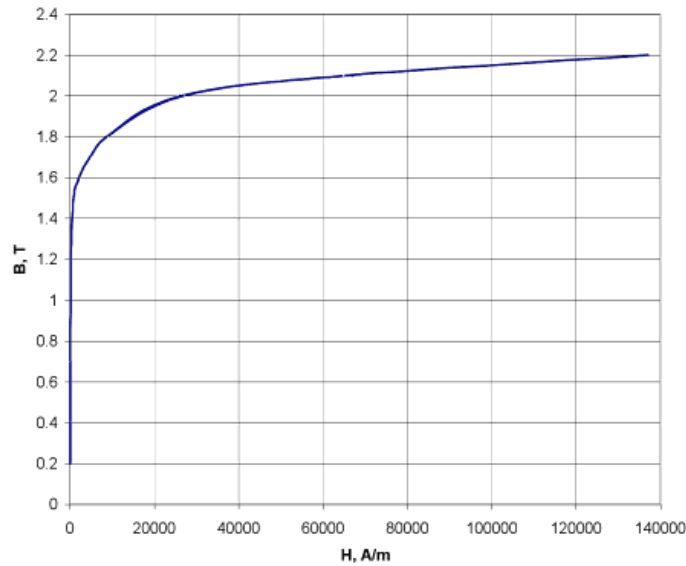


Figure 5: M-36 Grade Electrical Steel BH Characterization Curve, from [19]

To maximize the slot area, thus reducing power losses, the tooth width was computed by setting the d-axis fluxes equal in the tooth ($\phi_{dStatorTooth}$) and the airgap ($\phi_{dAirgap}$). The relationship between the flux density and flux ($\Phi = BA$) was used to find $\phi_{dAirgap}$ and $\phi_{dStatorTooth}$, as shown in equations (5.4) and (5.5). Based on the final design, two stator teeth were always located opposite from the rotor pole face. Therefore, the stator tooth area included the width of two stator teeth. Initially, a different method was used to find the width of the stator teeth, but this resulted in a wide tooth that did not maximize the slot area. Instead, the equations below were used to maximize the slot area.

$$\Phi_{d\text{StatorTooth}} = 2(B_{d\text{StatorTooth}})(\text{EffectiveLength})(\text{ToothWidth}) \quad (5.4)$$

$$\Phi_{d\text{Airgap}} = (B_{d\text{Airgap}})(\text{EffectiveLength})(\text{PolePitch}_d) \quad (5.5)$$

where the **PolePitch_d** is equal to the width of the poles. Equation (5.4) was then set equal to equation (5.5), which resulted in the following equation for the tooth width:

$$\text{ToothWidth} = (\text{PolePitch}_d)(B_{d\text{Airgap}})/(2B_{d\text{StatorTooth}}) \quad (5.6)$$

As the number of poles increased, the width of the tooth decreased, thereby limiting the maximum number of poles. The top of the tooth was designed to be wider than the remainder of the tooth to minimize pulsating torque on the rotor (as shown in Figure 6). The width of the top of the stator tooth allowed for a slot width opening equal to five times the wire diameter to minimize stator winding complexity. In order to evenly distribute flux to the rotor without reducing the slot area, the height of the top of the tooth was determined to be 0.079 in.

Next, the slot area was calculated which required the determination of the slot cord length. The slot cord length is the distance between the middle of two adjacent stator teeth as shown in Figure 6. The slot arc is the angle between these two teeth and is equal to:

$$\text{SlotArc} = \frac{2\pi}{(\text{Poles})(m_{\text{total}})} \quad (5.7)$$

where **m_{total}** is equal to the total number of direct and quadrature axis coils per pole. Using basic geometry, the slot cord was defined as:

$$\text{Slot_Cord} = 2(r_{os})(\sin \frac{\text{SlotArc}}{2}) \quad (5.8)$$

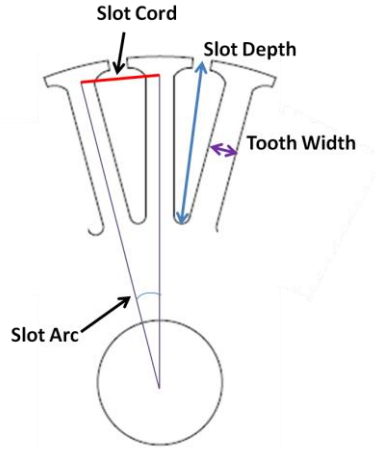


Figure 6: Stator Tooth and Slot Dimensions for the FRRM

Using the slot cord length, the slot opening top width ($\text{slot}_{\text{widthtop}}$) was defined as the difference between the slot cord length and the tooth width. Next, the slot opening bottom width ($\text{slot}_{\text{widthbottom}}$) was defined by calculating the slot cord length at the bottom of the slot. The total slot opening area was defined as the slot depth multiplied by the average slot width ($(\text{slot}_{\text{widthtop}} + \text{slot}_{\text{widthbottom}})/2$). Since a two layer winding design had been selected, meaning there were two windings per slot, the slot opening area was designed to fit both windings.

The maximum wire gauge was determined based on the slot area and the desired number of turns (N). The fill factor took into account that the slot area included the copper windings in addition to the wire insulation, and was defined as the fraction of the cross-sectional area of copper to the slot area; this was necessary to determine the wire gauge. The maximum wire gauge was determined by setting the total area of the coil wiring equal to the slot opening area multiplied by the fill factor, as shown below:

$$(\text{FillFactor})(\text{SlotOpeningArea}) = 2(N) \left(\frac{\pi}{4}\right) (\text{WireDiameter}^2) \quad (5.9)$$

Based on the final slot area, the selected conductor was AWG 18, which corresponded to a conductor diameter of 0.0403 in. It was decided to fully-pitch the coils so

that the coils could be operated as a field or torque producing coil. If the coils were fully-pitched, then the angular distance between the sides of each stator coil was the same as the pole pitch. After the stator teeth and slot dimensions were finalized, the stator laminations were fabricated and pressed onto the shaft. Figure 7 shows the top view of the unwound stator.

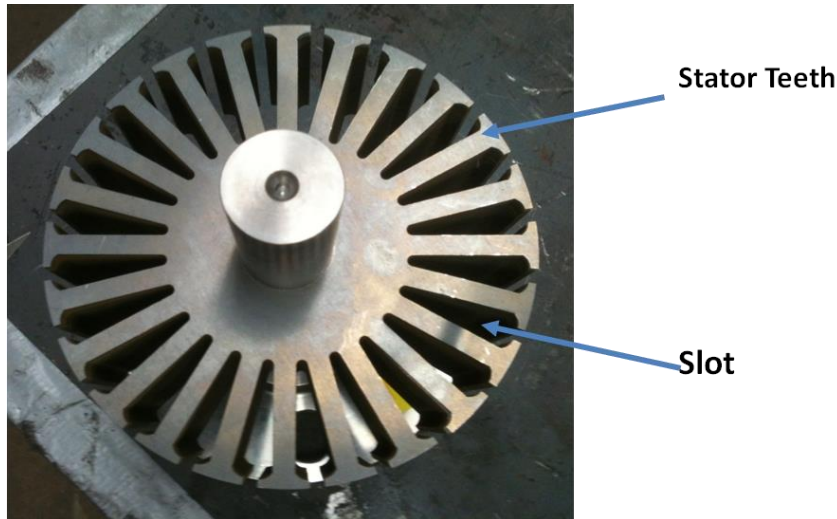


Figure 7: Unwound FRRM Stator Laminations pressed onto Shaft

5.3.4 Rotor Design Calculations

Due to the saliency on the rotor, the rotor pole and interpole regions had different dimensions. To determine these dimensions, the ratio of m_q to m_d per pole was investigated to maximize efficiency. The number of q- and d- axis coils affected the pole and interpole face arc dimensions. The d-axis pole arc (Pole_Arc_d) was defined as the region under the d-axis of the machine (or rotor poles) and the Pole_Arc_d was defined as the ratio of m_q/m_{total} multiplied by the pole arc. The interpole face arc (or the q-axis arc) was defined as the ratio of m_d/m_{total} multiplied by the pole arc. These arcs were also expressed as pole pitches for the d- and q-axes (Pole_Pitch_d and Pole_Pitch_q respectively) by multiplying each ratio by the pole pitch,

where the pole pitches were necessary to find the cross-sectional area of the pole and interpole regions.

As was explained previously, a larger number of d-axis versus q-axis coils was desired. The final machine design resulted in four d-axis coils and two q-axis coils per pole. Therefore, the d-axis pole arc was 30 mechanical degrees, and the q-axis pole arc was 60 mechanical degrees. Next, the width of the rotor chevrons (labeled in Figure 12) in the interpole region was determined. The rotor chevron width was defined as one-half of the pole face width to ensure that there would be a lower MMF drop across the airgap in the interpole regions. The cross-sectional areas of the d and q axis paths ($\text{Area}_{\text{Pole}_d}$ and $\text{Area}_{\text{Pole}_q}$) were then determined. The $\text{Area}_{\text{Pole}_d}$ was defined as the $\text{Pole}_{\text{Pitch}_d}$ multiplied by the effective length. The $\text{Area}_{\text{Pole}_q}$ was defined as one-fourth of the $\text{Area}_{\text{Pole}_d}$, based on the q axis flux path for one coil.

5.3.5 Determining the Quadrature and Direct Axis Flux

The rotor dimensions were used to calculate the q-axis current and the change in flux due to the armature reaction by solving the q-axis magnetic circuit shown in Figure 8. The iron reluctances shown in Figure 8 were neglected since the iron was not saturated.

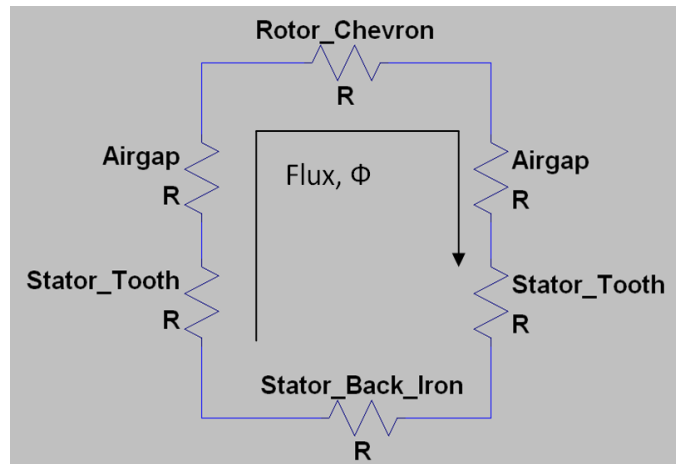


Figure 8: Quadrature Axis Magnetic Circuit including the FRRM Stator, Rotor and Airgap Reluctances

The total q-axis current (I_q) per coil was defined as:

$$I_q = \text{Power}/((\text{Voltage})(m_q)(\text{Poles})) \quad (5.10)$$

where I_q is related to the desired output power and voltage of the machine (since these coils are responsible for the torque production). Next, the direct axis flux (Φ_d) was determined:

$$\Phi_d = (B_{dairgap})(\text{Area})(\text{Pole}_d) \quad (5.11)$$

The MMF drop in the d-axis airgap ($MMF_{Airgapd}$) was calculated by applying Ampere's law (5.2) to the Φ_d path. In addition, the Carter factor was used to account for the difference in the flux distribution along the stator teeth and slot openings. Since the flux density decreased at the slot openings, it was difficult to define an average flux density over the slot pitch; therefore, the Carter factor was needed. The slot pitch was defined as the distance from the edge of one tooth to the edge of the next tooth, which included one stator tooth and the slot opening. The Carter factor is defined as (where the **SlotOWT** is the width at the top of the slot opening) [13]:

$$\text{CarterFactor} = \frac{\text{SlotPitch}}{(\text{SlotPitch} - \frac{2}{\pi}(\text{SlotOWT} \tan(\frac{\text{SlotOWT}}{2\text{airgap}}) - \text{airgap} \ln(1 + (\frac{\text{SlotOWT}}{2\text{airgap}})^2)))} \quad (5.12)$$

The $MMF_{Airgapd}$ was then calculated using the Carter factor correction value:

$$MMF_{Airgapd} = (\text{CarterFactor})(2)(\text{Airgap})(H_{Airgapd}) \quad (5.13)$$

If the stator and rotor laminations were saturated, the MMF drops in the iron (including the stator back iron, stator teeth, and rotor laminations) would need to be included in the total d-axis MMF (MMF_{Totald}) calculation. Initially, these MMF terms were included in the total MMF calculation; however the MMF drops in the iron were found to be much smaller than the drops in the airgap, and were neglected. Thus, the MMF_{Totald} was equal to the $MMF_{Airgapd}$.

Using MMF_{Totald}, the q-axis flux was determined using an iterative approach, which was necessary because there were two nonlinear equations and two unknowns involving N and the q-axis flux. The first equation was derived using the relationship between the machine's voltage (V_q) and flux linkages (λ) (Faraday's Law: $V_q = \frac{d\lambda}{dt}$), where the stator leakage inductance and resistance were neglected. According to Faraday's law, when flux flows through a winding, voltage is induced proportionally to the flux rate-of-change, with respect to time [6]. Faraday's law was rewritten by separating variables as follows:

$$V_q = \frac{d\lambda}{dt} = \frac{d\lambda}{d\theta_e} \frac{d\theta_e}{dt} \quad (5.14)$$

where $\frac{d\theta_e}{dt}$ is the electrical frequency (ω_e), which is related to the mechanical frequency (refer to equation (5.1)), and $\frac{d\lambda}{d\theta_e}$ is the rate-of-change in flux linkages with respect to the electrical angle. The flux linking one fully-pitched coil over the electrical angle is based on the FRRM operation. When the coil is operated as a q-axis coil, there is a q-axis current and voltage present, and when the coil is operated as a d-axis coil, d-axis current is present and the voltage is reduced to zero.

Based on Figure 9, $\frac{d\lambda}{d\theta_e} = \frac{2\lambda m}{\pi m_q}$ where m is the total number of coils per pole and λ is the total flux linkage, which is defined as the total d- and q- axis flux per pole ($\Phi_d + \Phi_q$) multiplied by one-half of the number of turns (N_{cp}) per coil pair.

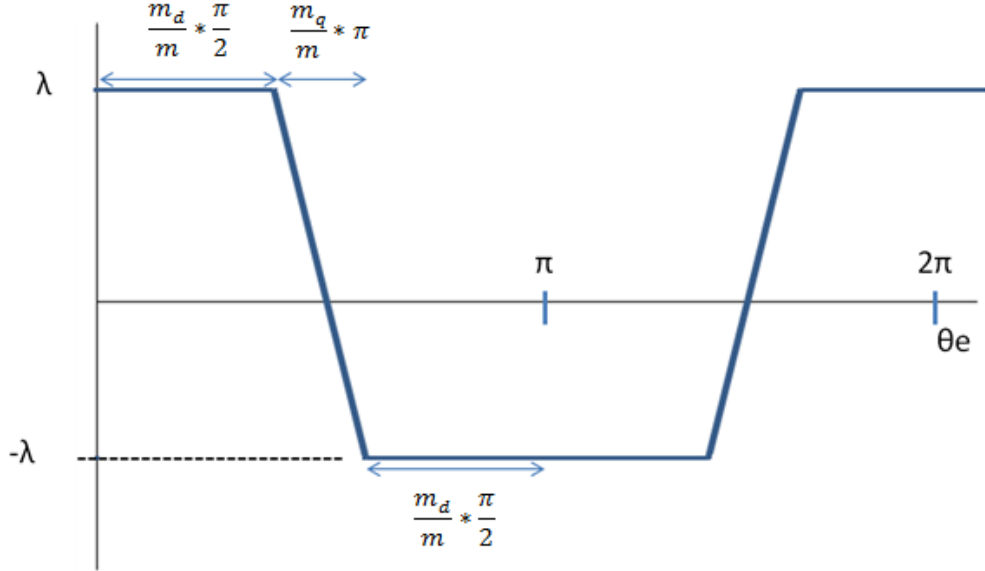


Figure 9: Flux Linkage for One Fully-Pitched Coil versus Electrical Angle

The rate-of-change in flux linkages with respect to the electrical angle was then substituted into equation (5.14), which resulted in the following equation for the machine's voltage:

$$\text{Voltage} = \frac{N(\varphi_q + \varphi_d)\omega_m \text{Poles}}{2\pi \frac{m_q}{m_{\text{total}}}} \quad (5.15)$$

Next, Ampere's law was applied to the q-axis flux path, which resulted in:

$$\text{MMF}_q = \sum H_q I_q = \frac{(m_q)(N)(I_q)}{2} \quad (5.16)$$

where \mathbf{H}_q is the airgap field intensity for the q-axis and I_q is the q-axis flux path, which includes two airgaps. Equation (5.16) represents the q-axis MMF drop per airgap and is corrected by the Carter factor in Appendix A.

While increasing I_q could maximize torque, there was a limit due to saturation, thus, a q-axis current of 4.17 A was selected. Equations (5.15) and (5.16) were rearranged to solve for N, and were set equal to one another. Using a solve block in MathCAD, the number of turns and the q-axis flux were calculated.

5.3.6 Determining Turns and the Field Current

Once the q-axis flux was determined, the next step was to solve for N (using equation (5.15)) and the d-axis current per coil (I_d). Initially, the machine operating voltage was set to 120 V; however, this resulted in 550 turns per coil. In order to fit that many turns in a small slot area, the wire gauge would have to be microscopic. Therefore, 120 V was not a feasible option and the specified voltage was decreased until a reasonable number of turns were reached.

To determine I_d , MMF_{Total_d} was set equal to the total number of d-axis turns enclosed by the d-axis flux path:

$$I_d = \frac{\text{MMF}_{\text{Total_d}}}{(N)(m_d)} \quad (5.17)$$

where I_d was used to determine the appropriate ratio of q-axis to d-axis coils. In order to minimize power losses, the minimum RMS current was desired, which was obtained by setting I_d (4.38 A) approximately equal to I_q (4.17 A).

5.3.7 Determining Power Losses and Efficiency

The final design step was to calculate the power losses and efficiency of the machine. The power losses were due to resistances in the stator windings, and were a primary concern because overheating the windings reduced the lifetime of the insulation. Therefore, a water cooling system was designed to remove the heat from the stator and protect the winding insulation. The stator end and slot resistances were defined as (resistance was inversely proportional to area and increased with the number of poles):

$$\text{Resistance} = \frac{(\rho)(l)}{\text{AreaWire}} = \frac{(N^2)(\rho)(l)}{(\text{SlotOpeningArea})(\text{FillFactor})} \quad (5.18)$$

where l is the length of either the wire in the slot (twice the length of the machine) or the end winding (accounts for an additional 0.025m since the wire cannot be bent at right angles)

multiplied by N , the **AreaWire** is equal to: $(\text{SlotOpeningAreaFillFactor}/N)$, and ρ is the resistivity of the conductor ($2.1 \times 10^{-8} \Omega\text{m}$ [13]).

To determine power losses, the RMS current that flowed through the windings was necessary. The RMS current was used to select the appropriate wire gauge and the ratings for the power electronics. The RMS current was calculated by finding the current density for the q- and d- axis coils and taking the square root of the total current density.

$$I_{\text{RMS}} = \left(\frac{m_q}{m_{\text{total}}} I_q^2 + \frac{m_d}{m_{\text{total}}} I_d^2 \right)^{0.5} \quad (5.19)$$

The total power loss was the sum of the d- and q- axis losses in the slot and end windings.

These power losses take the generic form of equation (5.18):

$$\text{Power Loss} = (m_x)(\text{Poles})(\text{Resistance})(I_x^2) \quad (5.20)$$

where m_x is equal to m_d or m_q and I_x is equal to I_d or I_q depending on the power loss being computed. To minimize the power losses, a four pole machine design was selected. While the two pole design had the least amount of losses, at least four poles were needed to actively control the rotor position along the x-y plane (two poles for the x-axis and two poles for the y-axis). For a smaller machine, the airgap was more significant, so a smaller number of poles resulted in reduced power losses. Figure 10 shows the total power losses as a function of the number of poles.

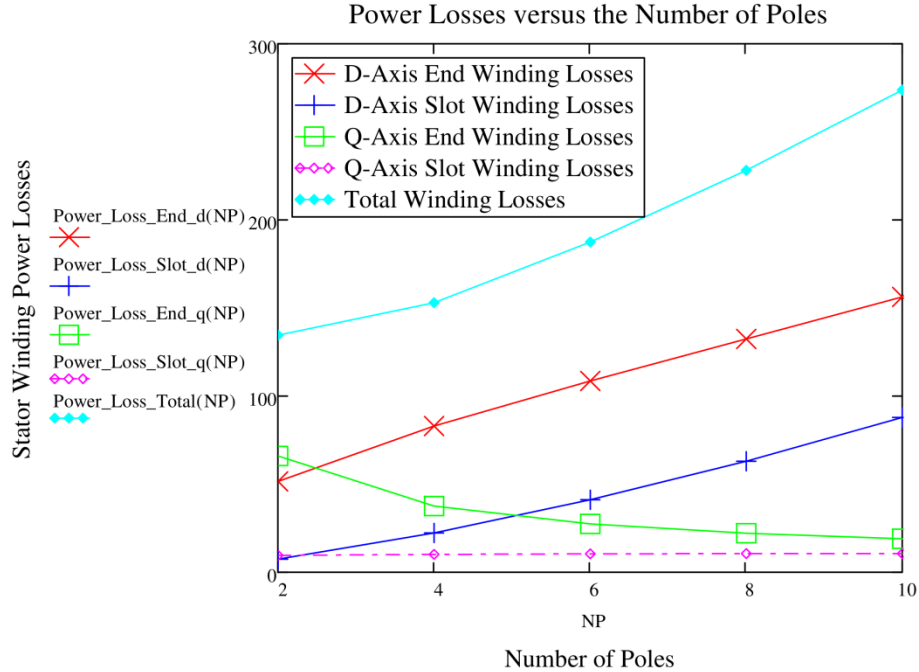


Figure 10: Total Winding Power Losses versus the Number of Poles for the FRRM

The next step was to determine the efficiency of the machine (where power is the desired output power):

$$\text{Efficiency} = \frac{P_{\text{out}}}{P_{\text{in}}} = \frac{\text{Power}}{\text{Power} + \text{Total Power Losses}} \quad (5.21)$$

To maximize efficiency, parameters (such as the rotor pole and interpole dimensions, airgap, m_q , and m_d) were adjusted.

5.3.8 Machine Optimization

After the number of poles was determined and the power losses and efficiency were calculated, the rotor and stator geometries were optimized. The machine design inputs were varied to observe the effects on efficiency.

5.3.8.1 Optimizing Rotor Chevron Geometry

Once the number of poles was determined, the airgap was decreased in the d-axis (the rotor pole region) and increased in the q-axis (the rotor interpole region) to improve machine

efficiency. By decreasing the airgap in the d-axis, larger electromagnetic forces were possible, but a minimum size was necessary due to fabrication limitations.

In the original rotor design, the chevrons were shaped as concentric semicircles. A more effective design was to have a uniform, large airgap beneath the interpole regions. Therefore, the rotor chevron design was changed to rectangles as opposed to circles. In addition, the area of the pole face was increased (thus decreasing power losses), by eliminating the airgap between the chevrons. The resulting rotor shape contained four pole faces, all connected by an outer ring, as previously shown in Figure 3.

5.3.8.2 Optimizing Stator Windings

After finalizing the shape of the rotor, the next consideration was the total number of coils per pole. Multiples of three were considered so that, if desired, the FRRM could be rewound as a three phase machine. Six coils and nine coils were considered. In both cases, one third of the coils were designated as q-axis coils, and two thirds of the coils were designated as d-axis coils.

The total number of coils per pole selected was six. A larger slot area resulted from selecting six coils, which reduced power losses and left adequate room to physically wind the machine. However, the benefit of using nine coils was a smoother output torque because there was less space between the slots, which resulted in a smaller flux change from coil-to-coil.

After the total number of coils was selected, a winding schematic for the stator was completed and provided to Strom Electric of Troy, ID. Each lead was brought out separately and labeled with a red or black wire to denote the polarity of the coils. Strom was able to shorten the end winding length, which would decrease power losses and improve efficiency. The wound stator is shown in Figure 11.



Figure 11: FRRM Wound Stator Laminations Completed by Strom Electric

5.4 Final Machine Dimensions

After comparing various options and optimizing parameters, a four pole machine with an airgap of 1mm was selected. The optimal number of coils per pole was six, with two of these designated as the q-axis coils and four as the d-axis coils. The force density and desired output power were adjusted to improve efficiency. In order to decrease the force density, the length of the machine was increased. To compensate for this, the rated output power was decreased to 400W, which allowed for levitation. Based on the designed operating speed of 1800 RPMs and the final rotor dimensions, the energy stored in the rotor would be equal to 2.04 kJ. The final FRRM design is shown in Figure 12 and can be found in Appendix A.

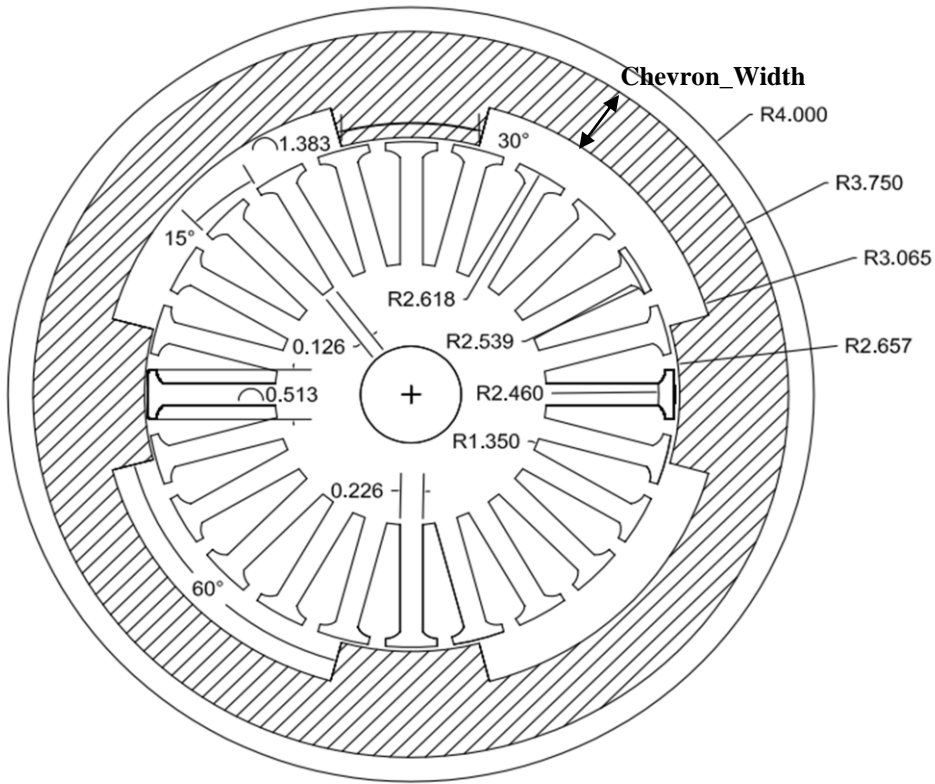


Figure 12: Final FRRM Rotor and Stator Dimensions

Table 1 contains a list of the final stator and rotor dimensions, and the major results from the machine design calculations. The dimensions were used to manufacture the FRRM, and the calculated results must be verified in future work. The final machine design parameters were derived based on the initial design operating conditions, such as the desired voltage, output power, and speed. These operating conditions will change and need to be revisited when the machine is operated, since the d- and q- axis currents will be reduced in Chapter 7 to prevent saturation in the stator teeth.

Table 1: FRRM Final Machine Design Parameters and Results

Machine Parameter	Value
Number of Poles	4
Desired Output Power (Watts)	400
Desired Operating Speed (RPM)	1800
Energy Stored (J)	2.04×10^3
Rotor Outer Radius (in.)	3.75
Rotor Inner Radius (in.)	2.657
Stator Outer Radius (in.)	2.618
Airgap (mm)	1
Coils per Pole	6
Direct Axis Coils per Pole	4
Quadrature Axis Coils per Pole	2
Pole Face Arc (deg.)	30
Desired Force Density (kN/m ²)	1.5
Effective Length (in.)	2
Pole Face Width (in.)	1.062
Slot Pitch (in.)	0.685
Slot Arc (deg.)	15
Tooth Width (in.)	0.226
Slot Opening Top Width (in.)	0.457
Slot Opening Bottom Width (in.)	0.126
Slot Depth (in.)	1.268
Number of Turns	55
Wire Gauge (AWG)	18
Calculated Power Loss (Watts)	153
Calculated Efficiency (%)	72.33

Chapter 6. Passive and Active Magnetic Bearings

The UI FES system includes two types of contactless magnetic bearings: passive magnetic bearings (PMB) and active magnetic bearings (AMB). Magnetic bearings suspend the rotor without contact, and therefore, eliminate frictional losses due to the contact between mechanical bearings and the rotor. The term active implies that the bearing actively requires a control feedback loop to maintain stable suspension. Both types of bearings have been successfully employed in industrial applications to support a rotor for high speeds [7].

One advantage of AMBs is the ability to actively adjust the bearing's capabilities with control, whereas, the PMB's capabilities are limited based on the bearing size and mechanical design. The AMB's parameters are adjusted to actively add dynamic and static stiffness, damping, and unbalance force attenuation to a rotating system [7]. A PMB can provide damping, but this is typically very low and is not adjustable [7]. Depending on the application, a PMB can provide a standalone solution.

The UI FES system initially only relied on the passive HTS bearing, but later incorporated an AMB to ensure stable rotor suspension. Different vertical levitation forces cause the rotor to tilt if the superconductors are not homogenous. If the rotor is tilted, there is no way to return the rotor to its nominal position without an AMB. The AMB design is not extensively covered in this thesis [10], but the basic design considerations of the AMB system are explained and necessary for the dynamic model derivation.

6.1 Active Magnetic Bearing Control Loop Design Considerations

A “standard” AMB system includes a bearing electromagnet and a rotor, a contactless position sensor to measure rotor displacements, a controller to maintain the rotor's position, and an amplifier to convert position command signals into an electric current in the bearing

coils [7]. To simplify the controller design, a linear control scheme is used for the UI's AMB system. Despite the nonlinear magnetic bearing forces, linear control schemes have been successfully implemented to control AMBs [7]. The magnetic bearing forces can be linearized by operating the bearing around a bias point. The linear approximations for the magnetic forces produced by the AMB are explained in Chapter 7.

To design the linear control scheme, multiple controller options were considered. This thesis includes the high level design considerations, but an in-depth explanation is described in [10]. The controller returns the rotor to an equilibrium position by providing restoring forces. The controller is designed with a stiffness coefficient, similar to that of a mechanical spring, and a damping coefficient, to attenuate oscillations about the operating point [7], to provide controlled restoring forces. The controller determines the command current necessary to return the rotor displacements to zero. PID controllers were selected for the UI's bearings since they were easy to design and implement.

The controller assumes the magnetic bearing current can instantaneously track the commanded current. Unless a large internal amplifier voltage is available, the coil inductance resists instantaneous current changes [7]. An electrical coil model, in addition to the controller model, is necessary to accurately model the behavior of the AMB system and are modeled in [10]. The electrical properties of the coil, the coil's inductance and resistance, in addition to the total amplifier voltage, are included in the electric coil model. The bearing current is now a system state that impacts the overall dynamics of the system. A complete AMB system model also includes a mechanical dynamic model of the system, which is derived in Chapter 8.

A current controlled scheme rather than a voltage controlled scheme was selected for the UI's controllers, which simplified the controller design. When a current controlled scheme is used, the underlying current control loop is necessary to model the system dynamics introduced by the coil inductance. The underlying current control loop can be designed and implemented in hardware and performs faster than the rest of the system dynamics [7]. The UI's controller contains an underlying current control loop, in addition to the outer position control loop. PID controllers are used locally for each bearing unit, which is referred to as decentralized control.

6.2 Active Magnetic Bearing Design Considerations for the Stability of the Rotor

The stabilizing bearing (SB) is the dedicated AMB and was added to the UI FES system to correct for rotor tilt. The FES system includes two magnetic bearings to provide radial forces: the SB, located on the top, and the drive bearing (DB), which refers to the FRRM, and is located on the bottom. Since the SB was designed after the DB was already fabricated, the SB needed to conform to the preexisting system design.

The SB was designed to provide corrective forces and moments to return the rotor to its nominal position. The SB stator design is derived in [10] and briefly explained in this thesis. The SB stator geometry was designed to maximize corrective electromagnetic forces and to minimize winding power losses. The outer and inner radii of the SB stator and rotor were set equal to the preexisting dimensions of the DB.

The SB and spacer heights were then varied to prevent dynamic instability of the rotor. The rotor assembly, shown in Figure 13, includes the SB rotor laminations, spacer, DB rotor laminations, top plate, and the bottom magnet plate. The spacer was incorporated in the system design to allow adequate spacing between the two bearing's windings.

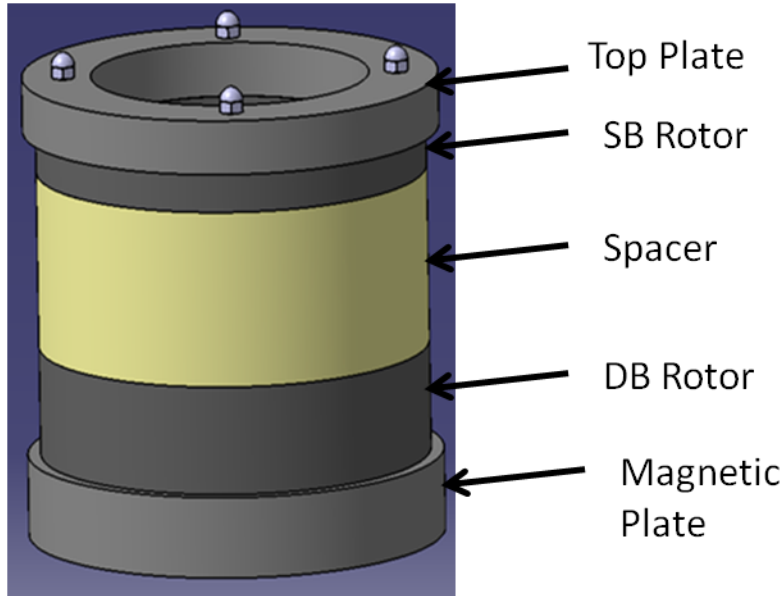


Figure 13: Rotor Assembly Components (Top Plate, SB, Spacer, DB, and Magnet Plate)

The final spacer dimensions and material, and the SB height, were determined based on rotor assembly's moment of inertia (MOI) ratio. The MOI ratio impacted the stability of the rotor assembly and was used to determine the final spacer and SB dimensions. In addition, a static case was analyzed for the worst case rotor tilt scenario to ensure that the combination of the DB and SB could provide the corrective moment necessary to return the rotor to the nominal position. The bearing coil currents were adjusted to provide the corrective forces and were limited to avoid saturation.

The MOI ratio is the ratio between the MOI about the rotational axis (I_z) and the axis orthogonal to it (I_x).

$$\text{MOI Ratio} = I_z/I_x \quad (6.1)$$

To avoid dynamic instability and a state of permanent resonance, the MOI ratio should not equal one. As the MOI ratio approaches one, the rotor becomes more sensitive to dynamic unbalances, which excite rotational resonance modes [7], [20]. To provide smooth operation

of the rotor for low rotational speeds, a MOI ratio between 0.9 – 1.1 was avoided. The rotor assembly's dimensions, such as the rotor's radius and height, affected the MOI ratio.

The MOI ratio for the rotor assembly was calculated by determining I_x and I_z . The following steps were taken to calculate the rotor assembly's I_x and I_z , as shown in more detail in Appendix B:

- 1) Determine the area for each cylindrical component of the rotor assembly, where Area = πr^2 .
- 2) Calculate each component's mass(Volume * ρ = Area * Height * ρ), where the spacer's density (ρ) and the SB and spacer heights were varied.
- 3) Determine the center of mass (COM) location of the rotor assembly:

$$\mathbf{m}_{\text{total}} \mathbf{X}_{\text{COM}} = \sum_{i=1}^N \mathbf{m}_i \mathbf{x}_i \quad (6.2)$$

where $\mathbf{m}_{\text{total}}$ is the total mass of the rotor assembly, \mathbf{m}_i is the mass of each particle in the system, \mathbf{x}_i represents the coordinate of each particle in the system, and \mathbf{X}_{com} is the COM location for the system of particles (the rotor assembly).

- 4) Calculate the MOI ratio using equation (6.1) for the rotor assembly. To find the rotor assembly's MOI ratio, I_x and I_z are necessary for each individual component. Each of the components are treated as thick-walled cylindrical tubes with open ends, and the following equations were applied [21]:

$$I_z = \frac{1}{2}(\rho)(\text{Area})(\text{Height})(r_{\text{inner}}^2 + r_{\text{outer}}^2) \quad (6.3)$$

$$I_x = \frac{1}{12}(\rho)(\text{Area})(\text{Height})[3(r_{\text{inner}}^2 + r_{\text{outer}}^2) + \text{Height}^2] \quad (6.4)$$

The total I_x and I_z were then determined for the rotor assembly by adding the individual component's I_x and I_z . To determine the total I_x , the parallel axis theorem was used to transfer the MOI of each body from the axis passing through the individual body's center of gravity to

a parallel axis passing through the rotor assembly's center of gravity. The MOI ratio was then calculated and was a function of the spacer and SB heights and the spacer's density. These parameters were varied to ensure a desirable MOI ratio was obtained. The heights of the DB (2 in.) and magnet plate (1.5 in.) were taken from the preexisting UI FES system design. The top plate height was set to 1 in. to provide sufficient target material for the sensors.

After the MOI ratio was calculated, the SB and DB moments were determined for a static case where the rotor assembly was symmetrically inclined (refer to Appendix B). A dynamic case was not explored until after the SB had been designed and built due to project time constraints. The DB and SB forces were calculated along the height of each bearing and were necessary for the moment calculations. The bearing forces were a function of the airgap between the stator and rotor, which varied axially for the inclined rotor scenario. A programming loop was used in MathCAD to determine the total bearing forces and moments. The SB and spacer heights impacted where the rotor assembly's COM was located and the lever arms used for the moment calculations.

The ideal rotor assembly's COM location was in the spacer due to the minimum spacer and SB heights necessary to prevent winding clearance issues and maximize the bearing's output force capabilities, respectively. When the SB and spacer heights were adjusted, the rotor assembly's MOI ratio and COM location were checked. Then the bearing's forces and resultant moments were determined. The resultant moment for the worst case rotor tilt scenario was -25.52 Nm.

To return the rotor to its nominal position and prevent translation, a positive resultant moment and total force of zero were desired. The currents in both bearings' windings were varied until a positive resultant moment was obtained, while ensuring the bearings were not

saturated. The final SB and spacer heights were simultaneously varied to obtain a desirable MOI ratio and positive resultant moment, while ensuring the rotor assembly's mass was below 40 lbs to allow for levitation. The final spacer height was defined as the sum of the DB and SB end winding heights, and 0.5 in. to avoid interference issues. The height of the SB was selected to maximize the output bearing force and to maintain the desired MOI ratio. Nylon was selected for the spacer material since it had a desirable material density, lower cost, and was easier to machine. Table 2 includes the final design dimensions, along with any major results from the MOI and moment calculations.

Table 2: Final Design Parameters based on MOI and Moment Calculations

Parameter	Designed Value	Design Constraints
Spacer_Height	3.25 in	Minimum Height = 2.8 in.
SB_Height	0.75 in	Minimum Height = 0.5 in.
Spacer_Density	0.05 lb/in ³	
Rotor_Assembly_COM	3.96 in	Above DB (exceed 3.5 in)
MOI_Ratio	0.77	Avoid 0.9 – 1.1
Rotor_Assembly_mass	36.05 lb	Below 40 lbs for levitation
Moment_Sum	1.40 Nm	Positive Moment
Force_Sum	0.21 N ≈ 0 N	Total Force = 0 N (No Translation)
Required SB Current Change (ΔI_{SB})	1.35 A	Maximum of 2.2 A
Required DB Current Change (ΔI_{DB})	0.65 A	Maximum of 0.7 A
Radius_inner_Spacer	2.657 in	
Radius_outer_Spacer	3.75 in	Based on DB dimensions
Radius_inner_SB	2.657 in	Based on DB dimensions
Radius_outer_SB	3.75 in	Based on DB dimensions

The SB and spacer final dimensions were added to the UI FES system's 3D CAD model. The CAD model was used as an alternative method to determine the rotor assembly's: MOI ratio = 0.80, COM = 3.98 in., and mass = 36.09 lb. While the CAD model results did not match the MathCAD results perfectly, these were close and varied due to assumptions in the MathCAD model made to simplify the calculations.

Chapter 7. Drive and Stabilizing Bearing Force Derivations

The purpose of this chapter is to introduce how the electromagnetic force expressions for the DB and SB are derived. The magnetic bearings provide forces in two different x-y planes and are located at two different heights along the z-axis. The DB is located on the bottom and is a self-bearing since it is a machine and an AMB. The SB is located on the top and is a dedicated AMB.

The SB and DB are used to correct for radial or axial eccentricities and provide corrective forces and moments about the x and y axes. Machine eccentricities occur when there is an unequal airgap (either axially or radially) between the rotor and the stator, and result in imbalanced forces. If there is a radial eccentricity, the airgap length varies in the radial direction and the airgap is axially uniform. If the rotor and stator axes are not parallel, there is axial eccentricity present [22]. When eccentricities occur, the controller needs to provide restoring forces to return the FES system to the ideal state without eccentricities.

The electromagnetic bearing force expressions are necessary for the rotor dynamic model. The bearing force expressions are determined from the electromagnetic bearing models. There are various approaches to develop the electromagnetic bearing models including a magnetic equivalent circuit method, finite element analysis (FEA), and the winding function method [22]. The modified winding function method was used to model the DB and the magnetic equivalent circuit method was used to model the SB. A FEA program was also used to verify these approaches.

7.1 Electromagnetic Force Derivation

The electromagnetic force for a simplified magnetic circuit, shown in Figure 14, is first derived. Energy conversion occurs in a machine through magnetic fields. A magnetic

field is produced around a coil carrying current. When the coil carries current in the presence of a magnetic field, the coil has forces induced on it [6]. Ampere's law is used to describe the magnetic field produced by the current in the coil:

$$\oint \mathbf{H} \cdot d\mathbf{l} = I_{\text{net}} \quad (7.1)$$

where \mathbf{H} is the magnetic field intensity, I_{net} is the current, and $d\mathbf{l}$ is the length of the integration path. A coil of N turns is wrapped around the leg of a rectangular ferromagnetic core (Figure 14 without the airgaps) and Ampere's law is applied to this magnetic circuit. If the core is made out of iron, a majority of the magnetic field produced by the coil remains in the core. Therefore, the path of integration ($d\mathbf{l}$) is the mean path length of the iron core (l_{fe}). The net current is equal to Ni , since the current flows through the path of integration N times. Ampere's law is then expressed as (where \mathbf{H} is the magnitude of the field intensity):

$$Hl_{\text{fe}} = Ni \quad (7.2)$$

Next, Ampere's law is applied to the simple magnetic circuit shown in Figure 14. The integration path now includes two airgaps. An assumption is that the flux flows entirely through the iron and the airgap, and thus, there is no leakage flux. The permeability of the iron is much larger than the air, causing the magnetic field lines to leave the iron perpendicularly to its surface [7]. To find the flux density (B), the assumption is the flux flows completely through the magnetic loop, consisting of equal and uniform airgap and iron cross-sectional areas ($A_{\text{fe}} = A_a$ and $\phi = B_{\text{fe}}A_{\text{fe}} = B_aA_a$). A_{fe} is the cross-sectional area of the iron, A_a is the cross-sectional area of the airgap, ϕ is the flux, B_{fe} is the magnetic flux density within the iron, and B_a is the magnetic flux density within the air. Since the field is assumed to be homogenous in the iron and airgap, the mean path length of the iron (l_{fe}) and the airgap length ($2s$) are used [7].

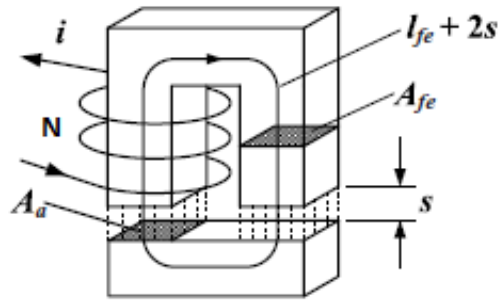


Figure 14: Simple Magnetic Circuit, from [7]

For the simple magnetic circuit, Ampere's law results in:

$$\oint \mathbf{H} \cdot d\mathbf{l} = I_{fe} H_{fe} + 2sH_a = Ni \quad (7.3)$$

The flux densities are then substituted into equation (7.3), where $B_a = B_{fe}$. Since the permeability of iron ($\mu_r \gg 1$) is much larger than the permeability of air (μ_0) and the iron is not saturated, the iron MMF terms are neglected and results in:

$$\mathbf{B} = (\mu_0 NI)/2s \quad (7.4)$$

Neglecting the iron, the magnetic forces are then determined for the simple magnetic circuit. Unlike the Lorentz force, where the forces act on a conductor in a magnetic field, the magnets exhibit an attractive force that is produced at the boundaries between the materials with differing permeability [7]. In Figure 14, there is an attractive force between the U-shaped bar and the bottom rectangular shaped bar that pulls the rectangular bar towards the U-shaped bar. The magnetic force is calculated based on the field energy (W_a) stored in the volume of the airgap and is equal to [7]:

$$W_a = \frac{1}{2} B_a H_a V_a \quad (7.5)$$

where V_a is the volume of the airgap and H_a is the field intensity of the airgap.

For the magnetic circuit above, the volume of the airgap is equal to $V_a = A_a 2s$. The magnetic force is produced when there is a change in the energy stored in V_a , which varies as

the airgap changes. If the airgap displacements (Δs) are small, the magnetic flux ($B_a A_a$) remains constant and no energy is produced. As the airgap (s) increases by Δs , this leads to an increase in the field energy (ΔW_a). The energy produced is provided mechanically, so an attractive force must be overcome [7].

Based on the principle of virtual displacement, the magnetic force is equal to the partial derivative of W_a taken with respect to s . The magnetic force equation contains a negative sign to denote that the attractive force is being applied on the bottom rectangle by the electromagnet:

$$f = -\frac{\partial W_a}{\partial s} = \frac{1}{2} B_a H_a A_a 2s = B_a H_a A_a \quad (7.6)$$

The force equation is then written in terms of flux density:

$$f = (B_a^2 A_a) / \mu_0 \quad (7.7)$$

Using the result from equation (7.7), the magnetic force is then written as a function of s and coil current (i):

$$f = A_a / \mu_0 (N_i / 2s)^2 \quad (7.8)$$

A_a is the projected area of the pole face instead of the curved surface area [7]. The magnetic force is inherently nonlinear with respect to the current and the airgap. The magnetic force is directly proportional to current squared and inversely proportional to the airgap squared. For a nonlinear system, a linear controller can be designed for a linear set of equations determined around an operating point. The magnetic force expressions for the UI FES system are linearized for both bearings.

For a real radial magnetic bearing (shown in Figure 15), the forces at the magnetic poles affect the rotor with an angle σ , unlike the U-shaped magnet [7]. The angle σ depends on the number of pole pairs and the given bearing geometry. For the radial bearing below, σ is

equal to 22.5 degrees. The total magnetic force is the sum of the resultant forces along the bearing pole faces:

$$f = \frac{A_a}{\mu_0} * \left(\frac{Ni}{2s}\right)^2 * \cos \sigma \quad (7.9)$$

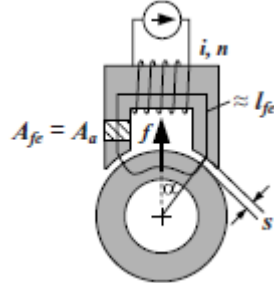


Figure 15: Force for a Radial Bearing Geometry, from [7]

The force equations derived above are then applied to the SB and DB. The geometry of the bearings and the airgap volume impact the magnetic force expressions for both bearings.

7.2 Stabilizing Bearing Electromagnetic Forces

The SB is an eight-pole bearing and can produce forces in the x and y directions. An eight-pole design allows for decoupling the x and y bearing forces, since two pole pairs can be assigned to each Cartesian axis (two for the x-axis and two for the y-axis). The SB provides corrective forces in the x and y directions to correct for airgap eccentricities. The SB is configured with an “inside-out” topology, where stator is located on the inside and the rotor is located on the outside. The airgap between the SB rotor and stator is equal to 1 mm (same as the DB).

The SB winding schematic is shown in Figure 16. The blue arrows represent the flux paths generated by the pole pairs (where flux enters the rotor at the South pole and exits the rotor at the North pole). The SB is operated in pole pairs and this is accomplished by connecting the pole pairs’ windings in series (i.e. windings 7 & 8, 5 & 6, 1 & 2, and 3 & 4 are connected in series). The polarity of the current for each winding is denoted by either an ‘X’

or a ‘•’. The ‘X’ represents turns carrying current into the page and is positive. Whereas, the ‘◦’ denotes turns carrying current out of the page and is negative. Pole pairs 7 & 8 and 3 & 4 are used to produce forces along the y-axis and pole pairs 5 & 6 and 1 & 2 produce forces along the x-axis. The attractive forces for the pole pairs associated with the y-axis are shown in Figure 16 and pull the rotor towards the stator.

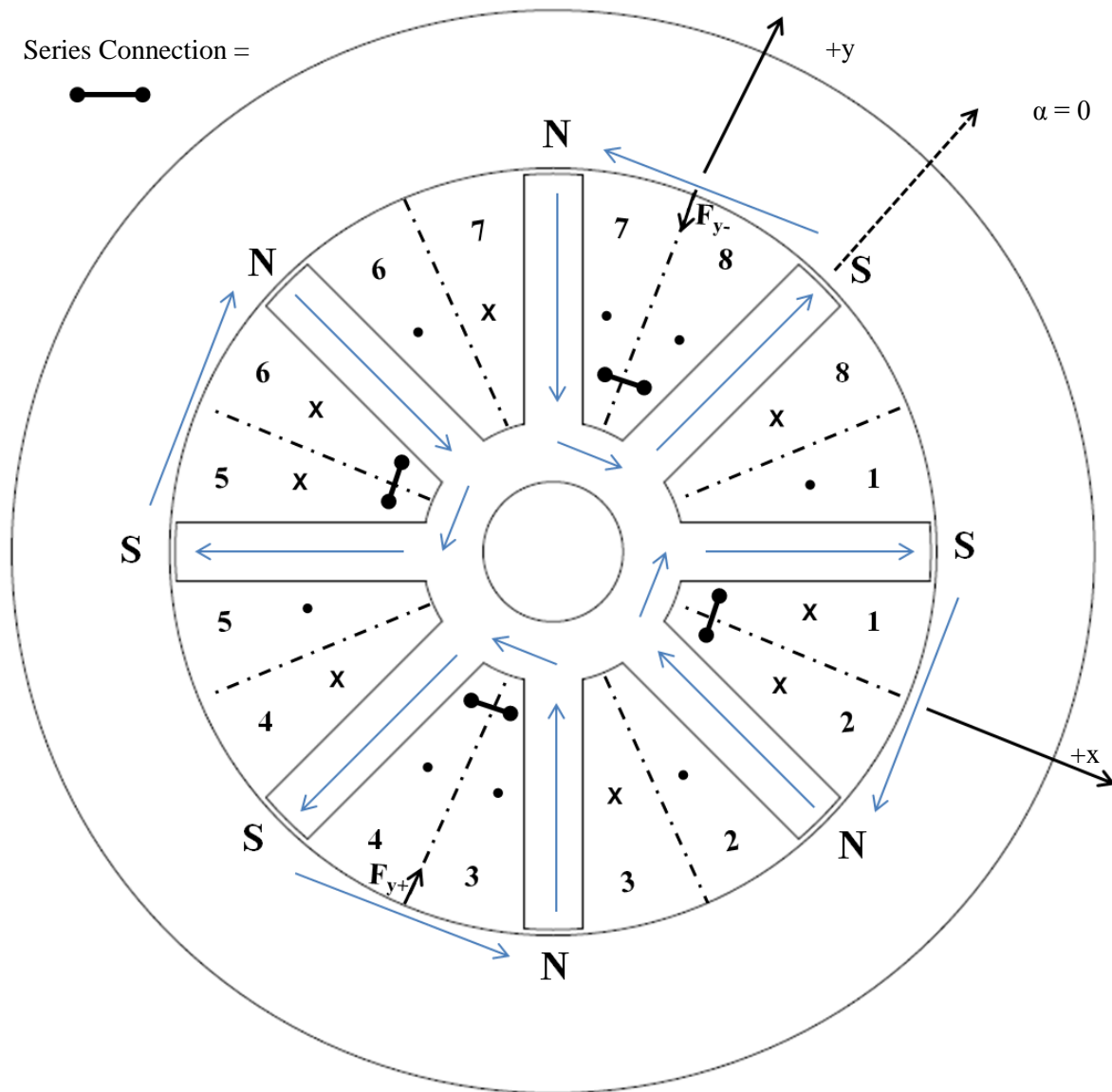


Figure 16: Stabilizing Bearing Stator Winding Schematic and Flux Paths

The x and y forces for the SB are then determined using the derivations from Section 7.1. The same assumptions from Section 7.1 are still valid including no leakage flux and the permeability of iron is infinite. The airgap B for each of the pole pairs is found by applying Ampere's law to one of the flux paths and is equal to:

$$\mathbf{B} = (2NI\mu_0)/(s_1 + s_2) \quad (7.10)$$

where N is equal to the number of turns per winding (183), I is equal to the bias current (2.6 A) for each coil, and s_1 and s_2 are equal to the airgap lengths. For the ideal case, s_1 is equal to s_2 . Since Ampere's law includes the total number of windings enclosed in the integration path, the two is needed in equation (7.10) to account for the total SB windings enclosed.

The x and y forces for each pole pair are derived based on the W_a stored in the V_a (as shown in Section 7.1). For each pole pair, the attractive forces between the two rotor poles and the stator are found using equation (7.6) (the principle of virtual displacement). The field energy is a function of the energy stored in the volume of one airgap, resulting in $V_a = 1s_xA_a$ (where s_x is the airgap between the rotor pole and stator). Equation (7.6) is applied and the SB magnetic force is equal to:

$$\mathbf{f} = (B_a^2 A_a)/2\mu_0 \quad (7.11)$$

where A_a is the cross-sectional area of the SB pole face and B_a is the airgap flux density. Ultimately, the total attractive force for each pole pair is desired. As shown in Section 7.1, for a real radial magnetic bearing, the force of the magnetic poles is affected by the angle σ . The total resultant force for each pole pair is determined by combining the attractive forces between the two rotor poles and stator. The SB total force is then written as a function of coil current and airgap as:

$$f_{SB_Pole_Pair} = \left(\frac{2NI\mu_0}{s_1 + s_2} \right)^2 \frac{A_a}{\mu_0} \cos \sigma \quad (7.12)$$

The SB force expressions were defined in MathCAD and were a function of airgap and coil current (see Appendix C). To incorporate radial airgap eccentricities into the force calculations, an airgap function was defined as:

$$\text{gap}_{\text{devSB}}(\alpha) = \text{g}_{\text{SB}}(\alpha) - (\text{Radial_Shift}) \sin(\alpha + \xi_{\text{SB}}) \quad (7.13)$$

where g_{SB} is the ideal airgap between the stator and rotor (1mm), **Radial_Shift** is the radial eccentricity coefficient, ξ_{SB} is the angle where the eccentricity is placed, and α is the azimuthal angle. The radial shift coefficient is multiplied by either a sine or cosine to model how the radial eccentricity affects the airgap circumferentially between the SB stator and rotor. To apply an eccentricity along the SB x or y axes, ξ_{SB} is set equal to 67.5 degrees. The eight airgaps are defined as the airgap function for a given α , where α depends on the pole location (i.e. the airgap for the pole associated with winding 1 is located at $\alpha = 315$ deg).

Using the force and airgap equations, the total x and y forces are determined by combining each pole's contributions. To verify the calculations, all of the airgaps are set equal to the ideal airgap of 1mm, and the total x and y forces are zero. Next, a radial eccentricity is introduced along the y-axis (where Radial_Shift equals 0.2mm and ξ_{SB} equals 67.5 degrees). The total x force equals zero since the eccentricity is not affecting the airgaps along the x-axis. The positive radial shift causes the airgap to decrease at $\alpha = 22.5$ deg (which increases the negative force along the positive y-axis) and the airgap to increase at $\alpha = 202.5$ deg (which decreases the positive force along the negative y-axis). This scenario resulted in a total y force of -41.6 N.

7.2.1 Stabilizing Bearing Mechanical Stiffness

As was previously mentioned, the nonlinear bearing forces are linearized about an operating point, and the linear force/current and force/displacement relationships are

necessary for each bearing. The linear force/displacement relationship for the SB is derived based on the inverse relationship between the magnetic bearing force and the airgap. Radial eccentricities result in an unequal airgap circumferentially between the rotor and stator, causing an imbalance in the magnetic bearing forces. To analyze how the magnetic bearing forces vary with changes in the airgap, the current in the SB windings is held constant and equals the bias current of 2.6 A. As the airgap decreases, the SB magnetic force significantly increases, causing an unstable open-loop relationship between the SB rotor and stator.

Unlike the magnetic bearing, a mechanical spring provides a restoring force to oppose a decrease in the airgap and maintain rotor stability around a bias point. Therefore, the magnetic bearing has a negative stiffness. The bearing stiffness is found by taking the negative derivative of the suspension force (f_s) with respect to the airgap displacement [7]:

$$k_{\text{mechanical}} = - \frac{df_s}{dx} \quad (7.14)$$

For small airgaps, the magnetic flux in the bearing becomes saturated; limiting how much the magnetic bearing force increases. Although these nonlinearities exist in a magnetic bearing, the magnetic bearing forces can be linearized around an operating point and controlled with a linear control scheme [7]. The operating point is the desired equilibrium position of the rotor.

The negative bearing stiffness for the SB was found and remained valid for small deviations around the operating point. To remain in the linear operating region, the SB stiffness was determined over an airgap displacement of ± 0.2 mm around the nominal airgap of 1mm. Based on this range of displacements, the total resultant x force (in intervals of 0.025 mm) was calculated and plotted, as shown in Figure 17. Based on the definition of the mechanical bearing stiffness, the slope of the line below is equal to the SB negative stiffness (-2.03×10^5 N/m) and is found in Appendix D.

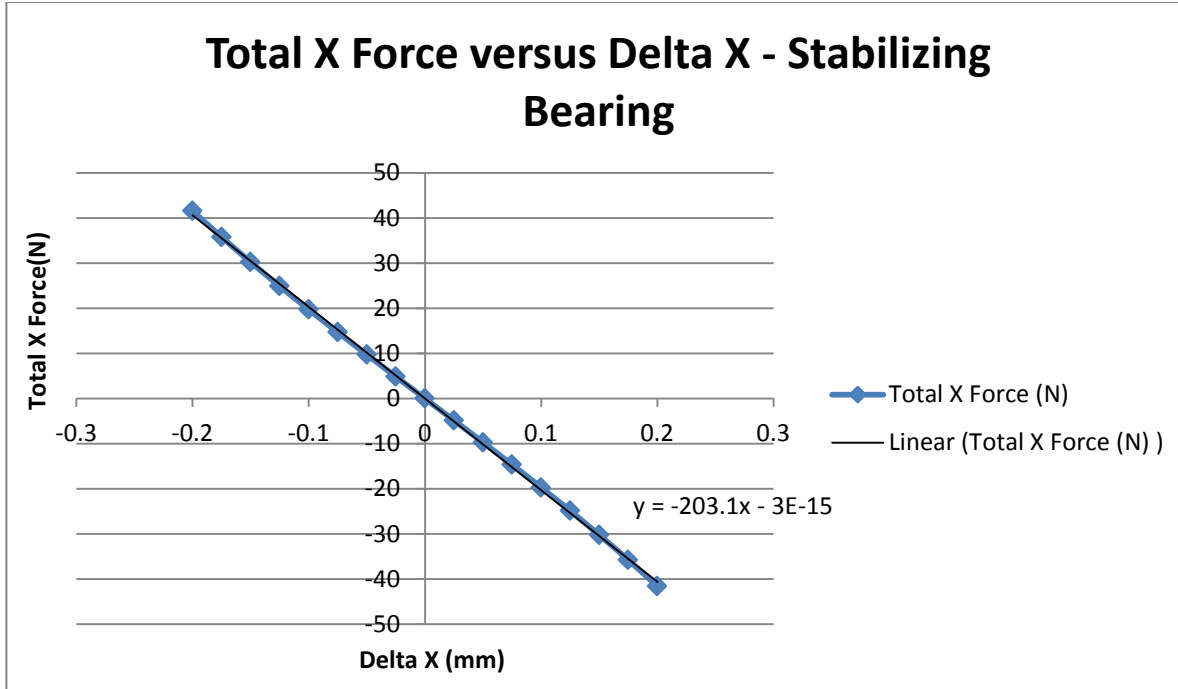


Figure 17: Negative Stabilizing Bearing Stiffness (N/mm) for the Linearized Bearing Force Equation

7.2.2 Stabilizing Bearing Force/Current Factor

The bearing also has a nonlinear force/current relationship. To correct for radial airgap eccentricities, the controller varies the coil currents to produce restoring forces, similar to that of a mechanical spring, to return the rotor to the ideal position. To design the controller, the force/current relationship is linearized around the operating point, and the airgap is held constant at the nominal position of 1mm. The nonlinear force/current relationship is linearized since linear relations are preferable for computation and control design [7]. For large coil currents, the magnetic flux in the bearing becomes saturated, limiting the maximum bearing force.

To avoid saturation and maintain a linear force/current relationship, the command current (Δi_x) is limited to ± 1.0 A around the SB bias current of 2.6 A. Since the x and y forces are decoupled for the SB design, the currents in the two pole pairs associated with each axis is varied independently. The pole pairs are operated in a differential driving mode, where the

windings associated with the positive x-axis are driven with a sum of Δi_x and the bias current, and the windings associated with the negative x-axis are driven with the difference of Δi_x and the bias current. The total resultant x force was determined over a Δi_x range in intervals of 0.1 A and is shown in Figure 18. From Figure 18, the force/current relationship is -80.69 N/A and the corresponding data is found in Appendix D. This is the force/current factor that is used in linear magnetic bearing force equation for the rotor dynamic model.

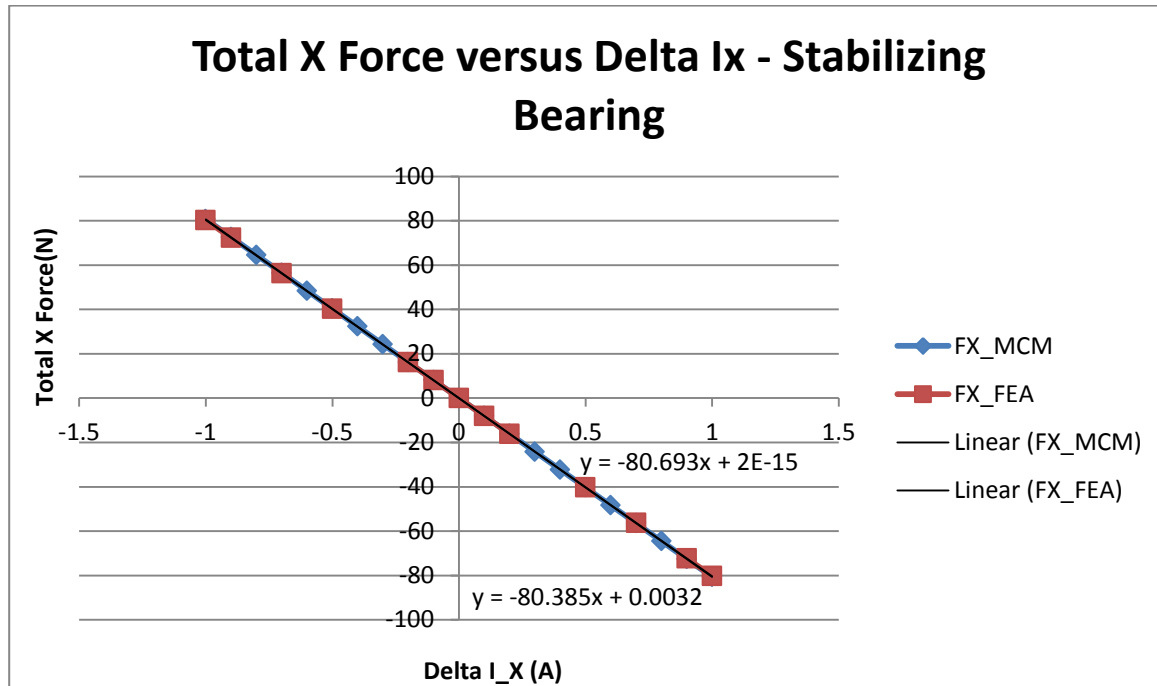


Figure 18: Force/Current Factor for the Linearized Stabilizing Bearing Force Equation

To validate the magnetic circuit model (MCM) approach, FEA analysis was used and is discussed in Section 7.4. The percentage error between the FEA program and the MCM approach was less than 1%. Since the Δi_x range avoided saturating the bearing's iron, the two methods should result in similar factors.

7.3 Drive Bearing Electromagnetic Forces

The electromagnetic model for the DB is necessary to determine the DB force expressions. While the MCM approach could be used for the DB, a different electromagnet

model was used for the DB due to the bearing's complex geometry. A modified version of the winding function approach (WFA) is used to derive the electromagnetic model for the DB. The WFA is based on the geometry of the machine and winding layout. This approach gives a complete model for how the flux is distributed in the interpole and pole regions of the rotor. To verify the results derived using the modified winding approach (MWA), an equivalent MCM is also used for a simplified case. The next two sections discuss winding theory and how it is modified to determine the resulting electromagnetic bearing forces.

7.3.1 Winding Theory Derivation

Unlike other electromagnetic model approaches, winding theory only requires the geometry of the machine and the corresponding winding layout. Windings are placed on the stator and rotor to create a distributed magnetic field. The magnetic flux density is distributed between the rotor and the stator in the airgap. When the windings are correctly excited, this causes the field to rotate relative to the stator. The flux interaction between the rotor and stator causes forces and torque. The torque and forces can be determined by knowing how the flux is distributed. Instead of modeling the machine in terms of the magnetic fields, winding theory is used to develop coupled magnetic circuit models [17].

To develop the winding theory fundamentals, a doubly-cylindrical machine is used and is shown in Figure 19. A few general assumptions are made and include [17]:

- 1) The stator and rotor shapes are cylindrical and are axially aligned.
- 2) The permeability of the stator and rotor iron cores is infinite compared to the airgap permeability. Due to the infinite permeability of the iron cores, these reluctances are equal to approximately zero and are not included in the MMF calculations.

- 3) The windings are not associated with either the stator or the rotor and are located in the airgap. Also, the windings are not skewed or tilted. The FRRM windings, like most machines, are placed in slots to reduce the airgap and the forces impressed on them when the coils are excited [6]. Even though these are placed in slots, the windings are still modeled in the airgap.
- 4) There is a uniform airgap between the rotor and the stator and the airgap is assumed to be small in relation to the rotor's outer radius.

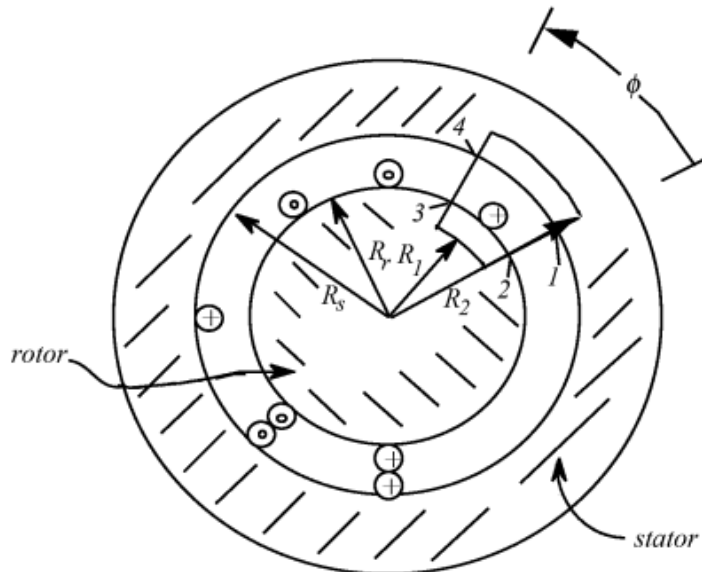


Figure 19: Doubly-Cylindrical Machine with Windings Placed in the Airgap, from [6]

A reference point is selected at an arbitrary point along the airgap to denote $\phi = 0$, which is the starting point for path 1-2. The azimuthal angle, ϕ , increases in the counterclockwise (CCW) direction until an arbitrary point ϕ ($0 \leq \phi \leq 2\pi$) where path 3-4 ends. Assume there is a single wire carrying current between the rotor and stator a number of times equal to N. Ampere's law is applied along the closed path 12341, which encloses the surface (S), and results in:

$$\oint_{12341} \mathbf{H} \cdot d\mathbf{l} = \int_S \mathbf{J} \cdot d\mathbf{s} \quad (7.15)$$

where \mathbf{H} is the magnetic field intensity and $d\mathbf{l}$, by definition, lies along the flux lines originating or terminating at two points of the closed path 12341 [18]. If all the windings carry the same current, this equation reduces to:

$$\oint_{12341} \mathbf{H} \cdot d\mathbf{l} = n(\phi) i \quad (7.16)$$

where $n(\phi)$ is the turns function, which represents the total number of turns enclosed by the closed path 12341. When the turns function is plotted versus ϕ , it has a magnitude equal to the total number of turns (N) enclosed by the path. By the right hand convention, turns carrying current into the page have a positive polarity and turns carrying current out of the page have a negative polarity. Ampere's law is expressed in terms of the MMF drops ($MMF = HI$) that are included in path 12341:

$$MMF_{12} + MMF_{23} + MMF_{34} + MMF_{41} = n(\phi) i \quad (7.17)$$

Since the permeability of iron is assumed to be infinite compared to the permeability of air, the iron MMF drops are negligible, and result in:

$$MMF_{12} + MMF_{34}(\phi) = n(\phi) i \quad (7.18)$$

Next, the MMFs are expressed in terms of H , where ϕ is a particular, but arbitrary point, around the airgap:

$$MMF_{12} = - \int_{r_rotor}^{r_stator} H_r(r, 0) dr \quad (7.19)$$

$$MMF_{34} = \int_{r_rotor}^{r_stator} H_r(r, \phi) dr \quad (7.20)$$

Assuming the airgap (s) remains small in comparison to the rotor's radius, the rotor field intensity (H_r) is assumed to remain constant, and results in: $MMF_{12} = -H_r(r, 0)s$ & $MMF_{34} = H_r(r, \phi)s$. Gauss's law for magnetic fields is then applied, which states that the net flux leaving any closed surface is equal to zero [17]:

$$\oint_S \mathbf{B} \cdot d\mathbf{S} = 0 \quad (7.21)$$

B is the flux density and **S** is the closed cylindrical surface encompassing the rotor that is located in the airgap of the machine, before the stator inner radius. Gauss's law is expressed in terms of H:

$$\int_0^{2\pi} \int_0^{L_{\text{eff}}} \mu_0 H(\phi) r dl d\phi = 0 \quad (7.22)$$

where L_{eff} is the effective length of the rotor and r is the stator inner radius. The rotor's B, and therefore H, is assumed to be independent of the axial direction. Equations (7.20) and (7.22) are combined and result in:

$$\int_0^{2\pi} MMF_{34}(\phi) d\phi = 0 \quad (7.23)$$

Next, the terms in equation (7.18) are integrated from 0 to 2π , which one term is equal to zero as shown in equation (7.23). This results in the following equation, where $\langle n \rangle$ is equal to the average value of the turns function:

$$MMF_{12} = i \frac{1}{2\pi} \int_0^{2\pi} n(\phi) d\phi = i \langle n \rangle \quad (7.24)$$

The MMF for any point along the airgap is determined by substituting the result from equation (7.24) into equation (7.18):

$$MMF_{34}(\phi) = i[n(\phi) - \langle n \rangle] \quad (7.25)$$

The winding function is represented by $N(\phi)$, which is equal to: $n(\phi) - \langle n \rangle$. The field distribution in the airgap of the machine is known if the winding function and current is known for each winding. From here, the MMF at any point can be determined. The turns and winding functions depend on where the reference point ($\phi = 0$) is selected but will result in the same outcome [17].

Winding theory cannot be used to create the electromagnetic model for the DB, since winding theory [17] assumes the airgap is uniform and is for a doubly-cylindrical machine.

Winding theory has been modified for a salient-pole machine, where the airgap is no longer independent of the angle ϕ . The stator is assumed to have a non-uniform cross section and it is assumed that each pole has an identical shape so that symmetry can be applied [17]. Unlike the previous case, there rotor now includes saliency. For the salient-pole machine, Ampere's law and Gauss's law are applied where the integration paths are defined along the flux lines. The major assumption is the airgap is identically shaped over the regions 0 to π and π to 2π . Since the windings are identically placed over the two regions, this results in the same flux (but in opposing directions), over the two regions [17].

The salient-pole and doubly-cylindrical machine both result in the same equations, implying that saliency has no impact on the winding function. When radial airgap eccentricities occur, the airgap for the FRRM is not identically shaped over the two regions. Therefore, the winding theory must be modified to incorporate radial airgap eccentricities into the electromagnetic machine model.

7.3.2 Modified Winding Function Approach

The MWA revises the previously discussed winding theory to account for non-symmetrical airgaps in a salient-pole machine. The same major assumptions (cylindrical stator, infinite iron permeability in the stator and rotor, and windings not associated with the rotor and the stator) hold for the MWA [18]. This approach assumes axial uniformity. An extended method is later introduced in this chapter to include non-uniformity axially. Unlike the winding theory derivation, the airgap is longer uniform, as shown in Figure 20.

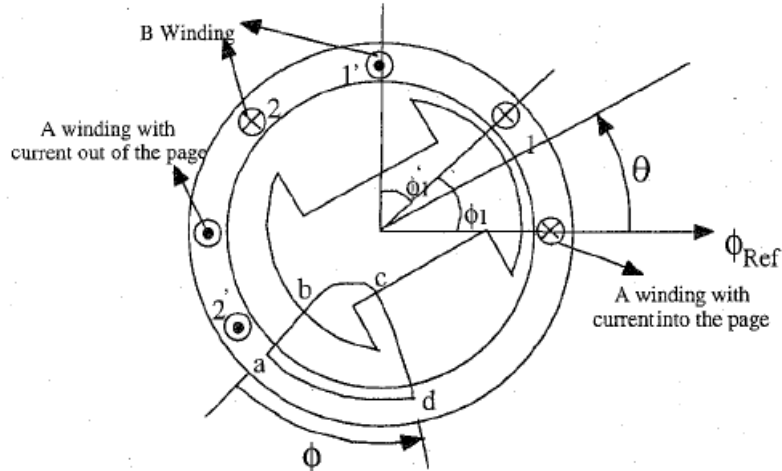


Figure 20: Salient-Pole Machine with Rotor Eccentricities, from [18]

The winding theory derivation steps are repeated for the MWA. Ampere's law is applied to the closed path abcd, where b and c are positioned on the rotor and a and d are on the stator. For a salient-pole machine, the flux lines in the airgap are irregular, but the flux lines intersect the rotor and stator at right angles [18]. Therefore, paths a-b and c-d are defined along the flux lines, even though these cannot be uniquely defined without plotting the flux. Using Gauss's law, b and c are uniquely defined, since two flux lines never originate from the same point if points a and d are fixed on the stator [18].

Ampere's law is applied to the closed path abcd and results in equation (7.16), where the turns function is a function of ϕ and can be a function of the rotor position angle (θ) if the coil is not stationary. Initially, the rotor is assumed to be stationary, so the subsequent derivations are not a function of θ . Next, the MMF drops (neglecting iron) for the path are expressed and result in equation (7.18). Gauss's law is then used to find the MMF at the reference point $\phi = 0$.

Since the flux density does not vary with the axial length, the MMF is defined as the flux radial length multiplied by H (MMF = HI). Gauss's law as a function of H, equation (7.22), is used to derive the equation (7.26). The MMF divided by the airgap function ($g(\phi)$) is

substituted into equation (7.22) for H and the rest of the constant terms are eliminated. Since the machine does not have a uniform airgap, a function is necessary to model the airgap circumferentially around the machine from 0 to 2π and can no longer be eliminated:

$$\int_0^{2\pi} \text{MMF}(\phi)/g(\phi) d\phi = 0 \quad (7.26)$$

Next, equation (7.18) is divided by the airgap function and integrated from 0 to 2π to result in:

$$\int_0^{2\pi} [\text{MMF}_{ab}(0) + \text{MMF}_{cd}(\phi)]/g(\phi) d\phi = \int_0^{2\pi} [n(\phi)i]/g(\phi) d\phi \quad (7.27)$$

By Gauss's law, the second term ($\text{MMF}(\phi)/g(\phi)$) is equal to zero, and results in:

$$\int_0^{2\pi} \text{MMF}_{ab}(0)/g(\phi) d\phi = \int_0^{2\pi} [n(\phi)i]/g(\phi) d\phi \quad (7.28)$$

Since the $\text{MMF}(0)$ term does not vary with the angle ϕ , it can be taken outside of the integral. The left hand side of the equation (7.28) is multiplied by a factor of one, or $2\pi/2\pi$. The equation is then a function of the average value of the inverse airgap function

$(\frac{1}{2\pi} \int_0^{2\pi} g(\phi)^{-1} d\phi)$. To apply the MWA, the average value of the inverse airgap function

$(\langle g^{-1}(\phi) \rangle)$ is determined. Next, the MMF at the reference position ($\phi=0$) is determined:

$$\text{MMF}_{ab}(0) = \frac{1}{2\pi * \langle g^{-1}(\phi) \rangle} \int_0^{2\pi} [n(\phi)i]/g(\phi) d\phi \quad (7.29)$$

Equation (7.29) is substituted into (7.18) and the MMF at the angle ϕ is determined:

$$\text{MMF}_{cd}(\phi) = n(\phi)i - \frac{1}{2\pi * \langle g^{-1}(\phi) \rangle} \int_0^{2\pi} n(\phi)g^{-1}(\phi)i d\phi = M(\phi)i \quad (7.30)$$

Equation (7.30) represents the MMF for an angle ϕ and contains the modified winding function. The modified winding function ($M(\phi)$) is equal to the following [18]:

$$M(\phi) = n(\phi) - M_{\text{Comp}} \quad (7.31)$$

$$M_{\text{Comp}} = \frac{1}{2\pi * \langle g^{-1}(\phi) \rangle} \int_0^{2\pi} n(\phi)g^{-1}(\phi)d\phi \quad (7.32)$$

The modified winding function takes into account rotor radial airgap eccentricities. If there are no eccentricities and the airgap is symmetric, then $M(\phi)$ reduces to the winding

function found in Section 7.3.1. When there are no airgap eccentricities, the modified winding component (M_{comp}) only has even harmonics, including a dc value, and reduces to $\langle n \rangle$ [18]. The MWA is used to find the MMFs circumferentially around the airgap between the DB's rotor and stator.

7.3.3 Modified Winding Approach Applied to the Drive Bearing

When radial airgap eccentricities occur, the MWA is necessary to derive the DB magnetic forces. The steps taken in the Section 7.3.2 are used to derive the MMFs for the DB. To begin, the DB stator geometry and winding layout are explained. The DB is a four-pole machine with 24 coils, which are all fully-pitched and each has 55 turns. Unlike the previous winding theory derivations, the DB is an inside-out machine (where the rotor is on the outside and the stator is on the inside), which does not alter the MWA derivations.

The winding layout of the DB, in reference to the bottom of the DB, is shown Figure 21. The polarity of the current flowing through the 24 coils was predefined and results in a clockwise (CW) rotation of the rotor from the perspective of the bottom of the stator. Note that 'X' denotes turns carrying current into the page and is positive and '•' denotes turns carrying current out of the page and is negative. Based on the right hand rule, at the south poles, the flux enters the rotor and leaves the stator and at the north poles, the flux exits the rotor to the stator. As shown in Figure 21, the reference position for the azimuthal angle (now denoted as α since ϕ represents flux) is located halfway between the North and South poles ($\alpha = 0$).

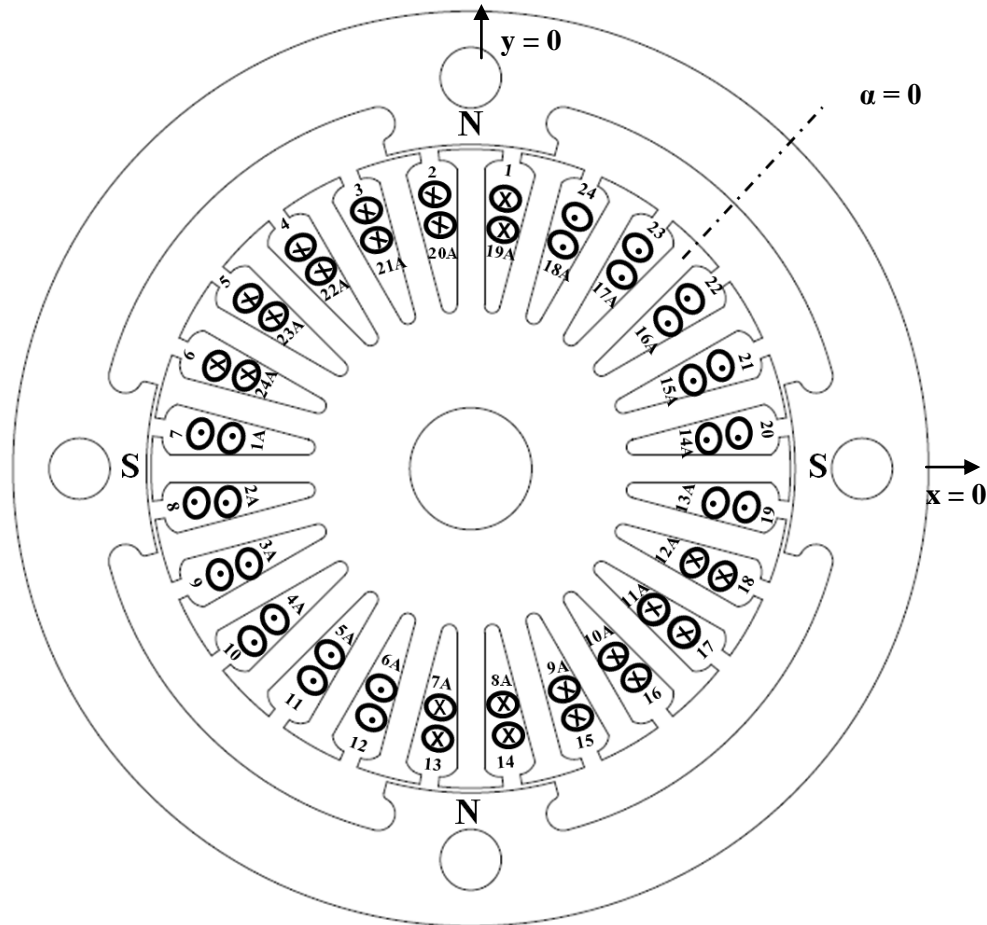


Figure 21: Drive Bearing Stator Winding Schematic

Using DB's stator winding layout and geometry, the MWA steps are used to develop a DB electromagnetic model. The MWA calculations take into account radial airgap eccentricities and a more in-depth derivation is in Appendix C. The first step in the MWA calculations is to define the turns function for the 24 coils. For example, the turns function for coil #1 ($n_1(\alpha, \zeta)$) is defined as a function of the shifting variable angle (ζ) and the azimuthal angle (α). The remainder of the turns functions are defined as the turns function for coil #1 and are shifted by the appropriate ζ . Since the turns functions represent the total N enclosed by the integration path, the coils' turns functions have a magnitude of N between the coil's ends and are zero elsewhere.

Next, the airgap function is defined for a symmetric rotor and includes radial airgap eccentricities. The DB's ideal airgap ($g_1(\alpha)$) is a function of α and is equal to 1mm under the pole regions and 11mm in the interpole regions, due to the rotor's geometry. Although the rotor poles are curved, these are approximated as straight edges to simplify the calculations. The ideal airgap function is modified to include radial airgap eccentricities:

$$\text{gap}_{\text{dev}(\alpha)} = g_1(\alpha) - \text{Radial_Shift} \cos(\alpha + \xi) \quad (7.33)$$

where **Radial_Shift** is the radial eccentricity coefficient and ξ is the angle where the eccentricity occurs. Radial_Shift is multiplied by either a sine or cosine to model how the radial eccentricity affects the airgap circumferentially between the DB stator and rotor. To make the MWA results easier to analyze, ξ equals 45 degrees, thus, the airgap eccentricity is placed along the DB x and y axes. If the radial shift coefficient is positive, the airgap decreases along the positive x or y axes. Figure 22 shows the ideal airgap function versus the modified airgap function for a radial shift of 0.2mm placed at $\xi = 45$ degrees.

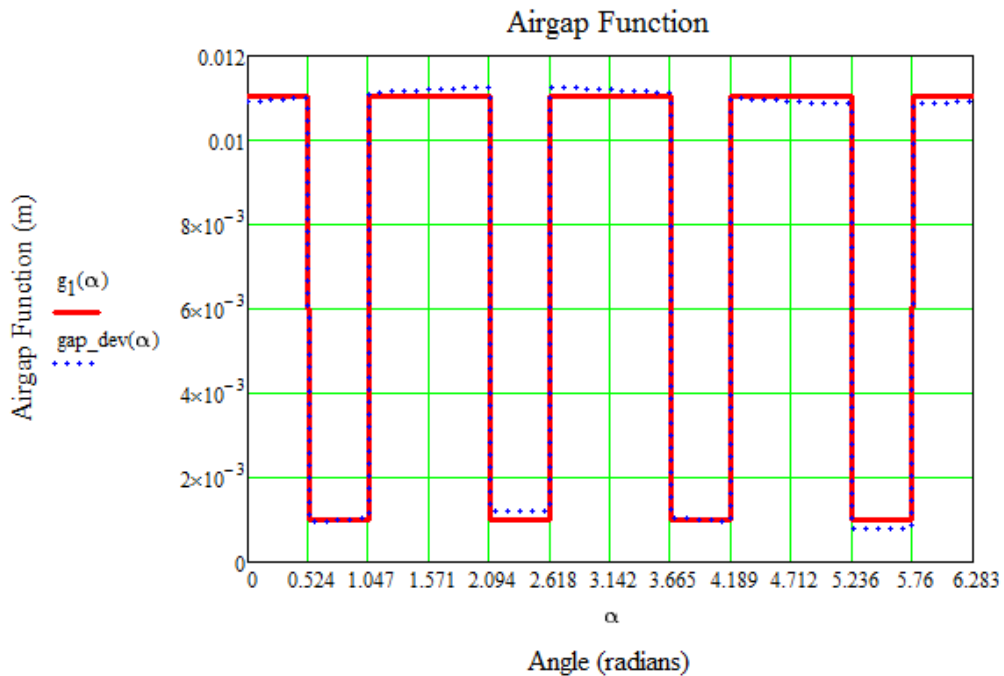


Figure 22: DB Airgap Function with or without Radial Eccentricities

Next, the inverse airgap function ($g_{1_inv}(\alpha) = \text{gap_dev}(\alpha)^{-1}$) and average inverse airgap function ($g_{1_inv_avg}$) are defined. The average value of the inverse airgap function is equal to:

$$\frac{1}{2\pi} \int_0^{2\pi} g(\phi)^{-1} d\phi \quad (7.34)$$

Then the modified winding function component (M_{comp_x} , where x is the coil number) was defined for each coil using equation (7.32). If there were no airgap eccentricities, the M_{comp_x} was found to be equal to the average turns function. A radial shift of 0.2mm was then placed along the y-axis, which caused the airgap at $\alpha = 45$ deg to decrease and the airgap at $\alpha = 225$ deg to increase. The modified components varied inversely with the airgap. The M_{comp_x} increased for coils located around $\alpha = 45$ deg, and decreased for coils located around $\alpha = 225$ deg.

The modified winding function ($M_x(\alpha)$) and the magnetomotive force ($MMF_x(\alpha)$) for each coil were then determined using equations (7.31) and (7.30) respectively. The d- and q-axis currents were defined separately. The q-axis coils (1&2, 7&8, 13&14, and 19&20) were defined as 0A, since these are responsible for torque production and do not cause magnetic forces between the rotor and stator. To determine the DB's negative bearing stiffness, the currents in the d-axis coils were held constant and were equal to the coil's bias current of 1.75 A. The DB bias current was selected to maintain an equilibrium position and avoid saturation.

Since the magnetic force has a relationship with flux density, the total MMF ($MMF_{Total}(\alpha)$) due to the d-axis coils was necessary. The total MMF was determined by summing the individual coils' MMFs and is plotted versus α in Figure 23 for the ideal case.

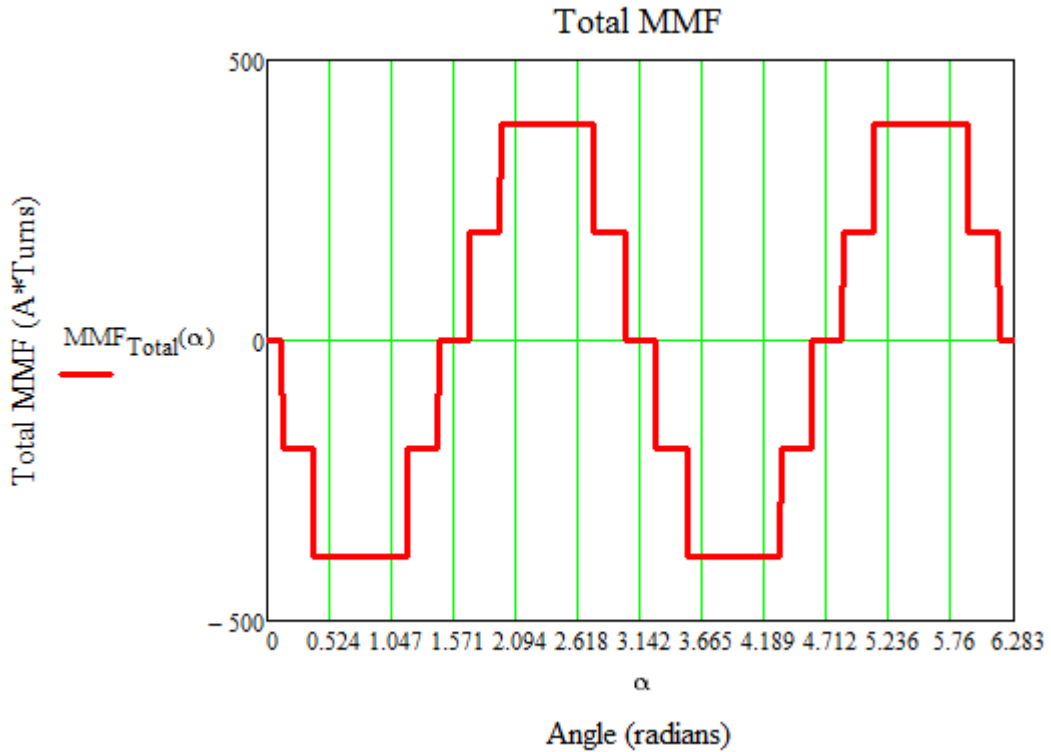


Figure 23: Total DB MMF for the Operating Point (1mm Airgap and 1.75A Bias Currents)

When the d-axis coils were energized with the DB bias current and the rotor was in the equilibrium position, the coils combined to produce equal but opposite MMF along the positive and negative x and y axes. The pole regions had the largest MMF magnitude, since the airgap was smaller in these regions, and was where a majority of the d-axis flux flowed.

Before solving for the total x and y forces, the total field intensity ($H_{Total}(\alpha) =$ $MMF_{Total}(\alpha)g_{1_inv}(\alpha)$) and the total flux density ($B_{Total}(\alpha) = H_{Total}(\alpha)\mu_0$) were determined. Since the magnetic force expressions are a function of B, B_{Total} was needed and is shown in Figure 24.

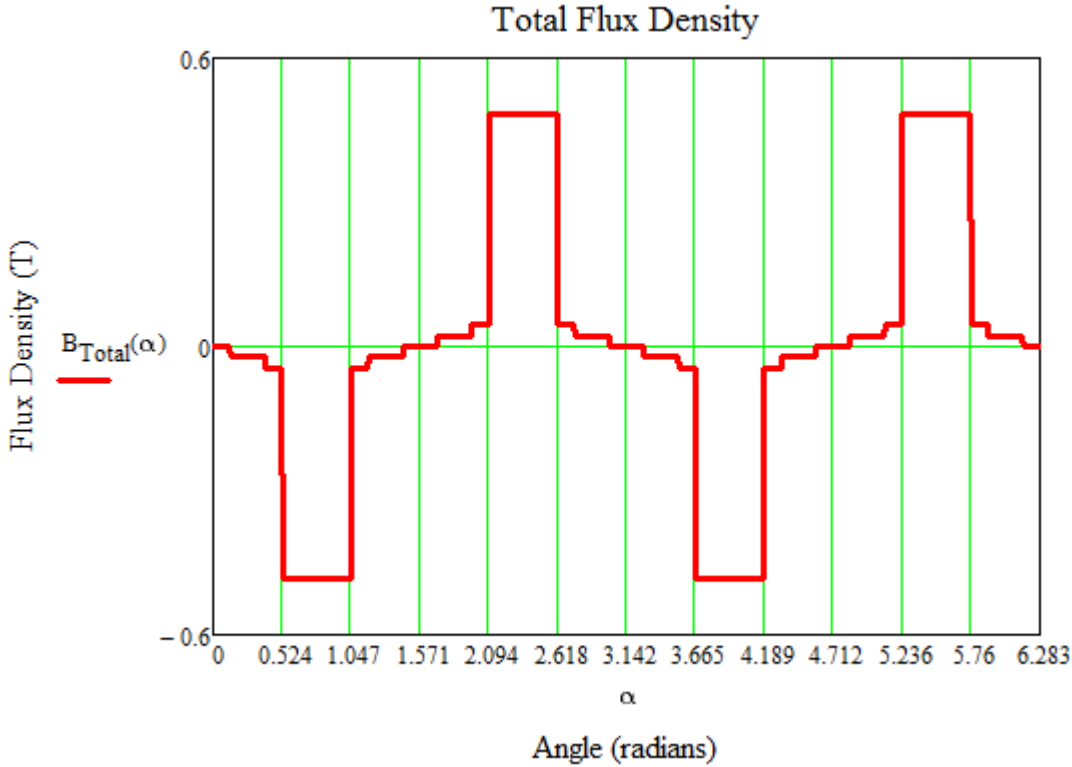


Figure 24: Total DB Flux Density about the Operating Point (1mm Airgap and 1.75A Bias Currents)

The MWA is applied using Ampere's law and Gauss's law. To ensure that Gauss's law was satisfied (i.e. the net flux leaving any closed surface is zero), equation (7.21) was utilized and resulted in:

$$\int_0^{2\pi} H_{\text{Total}}(\alpha) \mu_0 d\alpha = 0 \quad (7.35)$$

The total x and y forces ($F_{x,\text{Total}}$ and $F_{y,\text{Total}}$) were then found and were based on the force expressions derived in Section 7.2 for the SB. The resulting force expression for the SB, shown in equation (7.6), was used for the DB. Since B_{Total} was defined circumferentially around the machine, instead of only under the pole regions, the total x and y forces were determined by integrating B_{Total} from $0 < \alpha < 2\pi$. Geometry was then used to resolve the total force into the x and y components:

$$F_{x,\text{Total}}(\varepsilon) = - \int_0^{2\pi} \left(\frac{B_{\text{Total}}(\alpha)^2 r_{os} L_{\text{eff}}}{2\mu_0} \right) \cos(\alpha + \varepsilon) \quad (7.36)$$

$$\mathbf{F}_{Y\text{Total}}(\boldsymbol{\varepsilon}) = - \int_0^{2\pi} \left(\frac{B_{\text{Total}}(\alpha)^2 r_{os} L_{\text{eff}}}{2\mu_0} \right) \sin(\alpha + \boldsymbol{\varepsilon}) \quad (7.37)$$

where the cross-sectional area from equation (7.6) is equal to the outer stator radius (r_{os}) multiplied by the effective length (L_{eff}), and $\boldsymbol{\varepsilon}$ is the angle used to resolve the total DB force into the x and y components. The total x and y forces were determined for the ideal case, using the ideal airgap and DB bias currents, which resulted in total forces of zero. For this scenario, the total x and y forces should equal 0N since the x and y forces should cancel for the bearing's equilibrium position.

To check the force calculations, a radial airgap eccentricity was placed along the y-axis (where Radial_Shift was defined as 0.2mm and ξ was 45 deg). This scenario resulted in $F_{x\text{Total}} = 0\text{N}$ and $F_{y\text{Total}} = -135.24\text{N}$. These results were correct for the given airgap eccentricity, since the airgap decreased at $\alpha = 45$ deg, which increased the negative y force, and the airgap increased at $\alpha = 225$ deg, which decreased the positive y force. Unlike the ideal case, the eccentricity caused an imbalance in flux and the magnetic forces.

7.3.3.1 Drive Bearing Mechanical Stiffness

To find the force/displacement relationship for the DB, the d-axis coils were energized with the DB bias current (1.75 A). The same approach was used to find the stiffness for the DB as was previously done for the SB (see Appendix D for more information). To maintain a linear force/displacement relationship, the negative bearing stiffness was determined for a maximum airgap displacement of ± 0.2 mm around the ideal airgap of 1mm. Based on this range of displacements, the total resultant y force (in intervals of 0.025 mm) was determined and plotted, as shown in Figure 25. Based on the definition of the bearing stiffness, the slope of the line in Figure 25 is equal to the DB negative stiffness ($-6.65 \times 10^5 \text{ N/m}$).

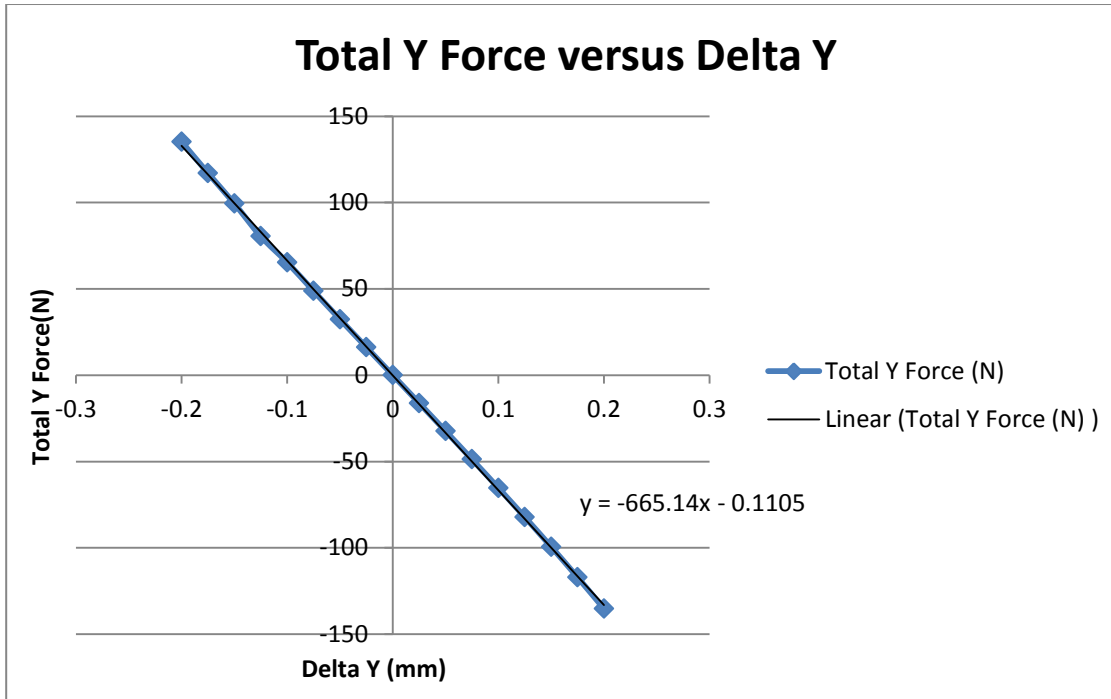


Figure 25: Negative Drive Bearing Stiffness (N/mm) for the Linearized Bearing Force Equation

The negative bearing stiffness for the DB and SB were necessary to aide in designing the PID controller gains. The controller compensates for the negative bearing stiffness by producing a restoring force, similar to that of a mechanical spring. Since the x and y forces are decoupled for both bearings, the same process is used to find the stiffness associated with the opposing axis. Since the bearings are symmetrical, the negative bearing stiffness for the x and y axes are the same.

7.3.3.2 Drive Bearing Force/Current Factor

The force/current relationship for the DB was then determined by holding the airgap constant at 1mm. To avoid saturation and maintain a linear force/current relationship, the change in the command currents (Δi_x) was limited to ± 0.7 A around the DB bias current of 1.75 A. This relationship was found independently for the x and y axes since eight d-axis coils are associated with each axis. A differential driving operating mode was used for the DB, where a positive Δi_x caused the currents in coils 3-6 to decrease, and the currents in coils 15-

18 to increase. For each Δi_x , the total resultant x force was determined and plotted as shown in Figure 26. The force/current relationship, using the MWA, is equal to -366.84 N/A.

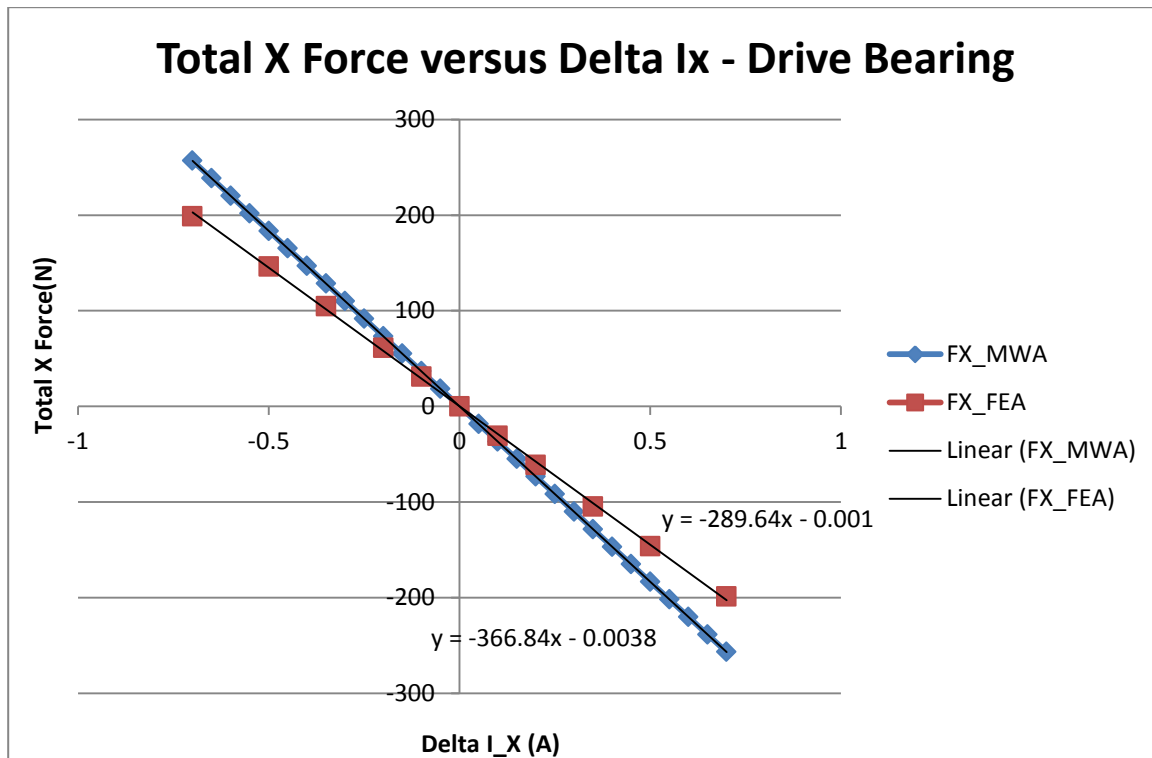


Figure 26: DB Force/Current Factor for the Linearized Bearing Force Equation

To validate the MWA, a FEA program was used to determine the force/current relationship, and the two methods resulted in a percent error of 21%. A higher percentage error occurred in the DB versus the SB, since the stator teeth were more heavily saturated for the Δi_x extremes. The MWA neglected the iron MMF drops, since this method assumed that the iron permeability was infinite compared to air. For the larger Δi_x values, this assumption was not valid since the stator teeth were saturated. The FEA program included the iron MMF drops and was more accurate. Regardless, the percentage error between the two methods was small enough to use the MWA for the aforementioned calculations.

7.3.4 Inclusion of both Axial and Radial Non-uniformities

The MWA was extended to include both axial and radial airgap non-uniformities. The MWA equations were adjusted to include axial variations, but the remainder of the MWA assumptions still applied. Inclined eccentricities occur when the rotor and stator axes are not parallel [22]. Inclinations cause an uneven airgap axially and radially between the rotor and stator, causing different magnetic forces axially between the rotor and stator. The same basic steps and equations from the MWA were used to find the resulting forces in the x and y directions.

Since the DB windings were not skewed, the turns function for the DB coils were not redefined to vary with the axial length (z), as was done in [22]. The work completed in [22] modified the MWA equations to include the axial variations. Since the airgap varies axially, the MWA airgap function was made a function of z . The remaining equations were also made a function of z , and integrated with respect to z , in addition to α . The effective length was not a constant anymore and could not be divided through in the equations for M_{compX} and $g_{1_inv_avg}$. Ampere's law and Gauss's law were used, as was done in the MWA, to determine the total flux density.

A symmetrical inclined eccentricity (i.e. the eccentricity is symmetrical to the midpoint of the machine shaft) [22] was assumed to determine the modified airgap function. There were two different functions presented in [22] that modeled the airgap function, one for the range $0 < z < L/2$ and the other for the range $L/2 < z < L$ (where L is the total height of the rotor that overlaps with the stator). Since these calculations were for the DB, the function defined over the range $0 < z < L/2$ was necessary. The height of the DB is equal to 1.97 in.,

which is below one-half of the total rotor assembly height (including the SB, spacer, and the DB).

The ideal airgap function was modified to include axial airgap eccentricities. A static eccentricity coefficient (δ_s) was defined as a function of z . For the symmetrically inclined rotor assembly, δ_s was derived for a given tilt angle (θ_{tilt}), as shown in Figure 27. The tilt angle was physically constrained since there is a maximum airgap of 2 mm between the rotor and stator, at which point the rotor and stator have collided. To avoid a collision and maintain adequate control for any radial or axial airgap eccentricities, the maximum airgap displacements considered were ± 0.2 mm around the ideal airgap of 1mm. Based on this constraint, the maximum tilt angle was calculated and equals 0.152 degrees (where $\delta_s = 0.2$ mm and the total rotor assembly height is 5.92 in.). Then the static eccentricity coefficient was derived using the tilt angle and was defined as:

$$\delta_s(z) = \left| z - \frac{L_{\text{TotalHeight}}}{2} \right| \sin \theta_{\text{tilt}} \quad (7.38)$$

The remainder of the steps were outlined in [22] and were contained in the extended MWA calculations. These calculations were not used to design the force/current or force/displacement relationships for the DB. In the future, these calculations could be revisited and incorporated into the dynamic model to fine tune the controller design. The relationships used in the dynamic model were determined for radial airgap eccentricities and were deemed acceptable for this phase of the project.

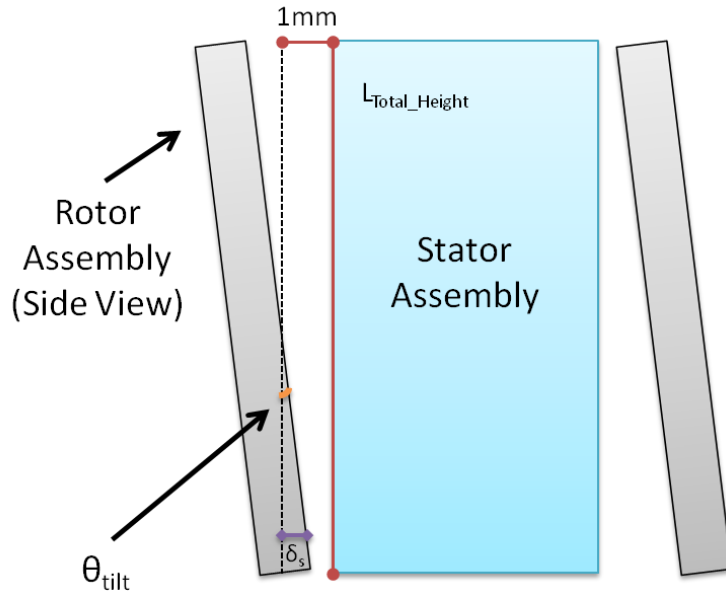


Figure 27: Symmetrical Inclined Eccentricity between the DB Stator and Rotor

7.3.5 Magnetic Circuit Model Verification for the Drive Bearing

To verify the MWA, an equivalent MCM with eight d-axis coils energized (either the eight coils producing forces in the x or y directions) was created. Ampere's law and Gauss's law were used to determine the flux flowing through the airgap reluctances. The bearing stiffness was found using the MCM approach.

An equivalent MCM was created for the eight d-axis coils associated with producing forces in the x direction. To simplify the analysis, all of the 16 d-axis coils were not energized. The same current polarity (where 'X' is positive and '•' is negative) was used from the winding schematic in Figure 21. Based on right hand convention, there were four d-axis flux paths between the rotor's North and South poles for the equivalent circuit. As assumed in winding theory, the permeability of the iron was infinite in comparison to the permeability of air. Therefore, the reluctances of the iron in the stator and rotor were essentially zero and were treated as short circuits. The interpole airgaps were large in comparison to the pole airgaps

and were therefore neglected. Similar to an electrical circuit with resistances, the magnetic circuit had airgap reluctances between the rotor and stator for each pole region (represented by R_a , R_b , R_c and R_d). The equivalent magnetic circuit for these airgap reluctances is shown in Figure 28.

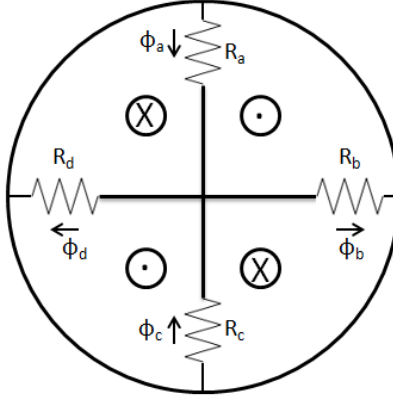


Figure 28: Equivalent Magnetic Circuit Model for the DB with 8 D-Axis Coils Energized

The equivalent MCM also included branch fluxes (represented by ϕ_a , ϕ_b , ϕ_c and ϕ_d) and eight d-axis coils (each circle represented four coil ends denoted with the appropriate polarity).

The branch fluxes represented the total flux flowing through each of the airgap reluctances. To solve for the branch fluxes, Ampere's law was applied to the four flux path loops. If the four loop equations were used, this led to an overconstrained problem. Therefore, Gauss's law was also necessary and provided a relationship between the branch fluxes. By using both Gauss's and Ampere's law, the same governing equations from the MWA were used. Ampere's law was applied to three of the loops to determine the enclosed MMF:

$$\Phi_a R_a + \Phi_b R_b = 4NI \quad (7.39)$$

$$\Phi_c R_c + \Phi_b R_b = 4NI \quad (7.40)$$

$$\Phi_d R_d + \Phi_c R_c = 4NI \quad (7.41)$$

where N represents turns and I represents the DB bias current. Gauss's law was then applied to the magnetic circuit to determine the total flux at the center node. To satisfy Gauss's law, the total flux entering the center node should equal the total flux exiting the node:

$$\Phi_a + \Phi_c = \Phi_d + \Phi_b \quad (7.42)$$

These four equations were combined into a matrix, and then the unknown branch fluxes were determined. The airgap reluctances were defined and substituted into these equations. Reluctance is a function of the mean path length (I_c), the cross-sectional area (A) and the magnetic permeability of the material (μ).

$$R = I_c / (\mu A) \quad (7.43)$$

Since eccentricities were introduced in the x direction, the mean airgap path lengths for the reluctances R_a and R_c were always equal to the ideal airgap of 1mm. Whereas, the reluctances R_b and R_d mean path lengths included radial airgap eccentricities. Using the four governing equations, the branch fluxes were determined. For the ideal case, with no airgap eccentricities, the branch fluxes were equal in magnitude, since the airgap reluctances were equal. To determine the magnetic forces, B was determined using each of the branch fluxes:

$$B = \Phi / A \quad (7.44)$$

Using B , the total force in the x direction was found using equation (7.11). For a case with no eccentricities, the total x force was equal to 0N, since the flux was balanced. The bearing stiffness was determined by calculating the total resultant force (F_x) due to displacements in the airgap along the x -axis (Δx). The negative DB stiffness, for the simplified case, was equal to -1.64×10^5 N/m, as shown in Figure 29. These calculations are found in Appendix E.

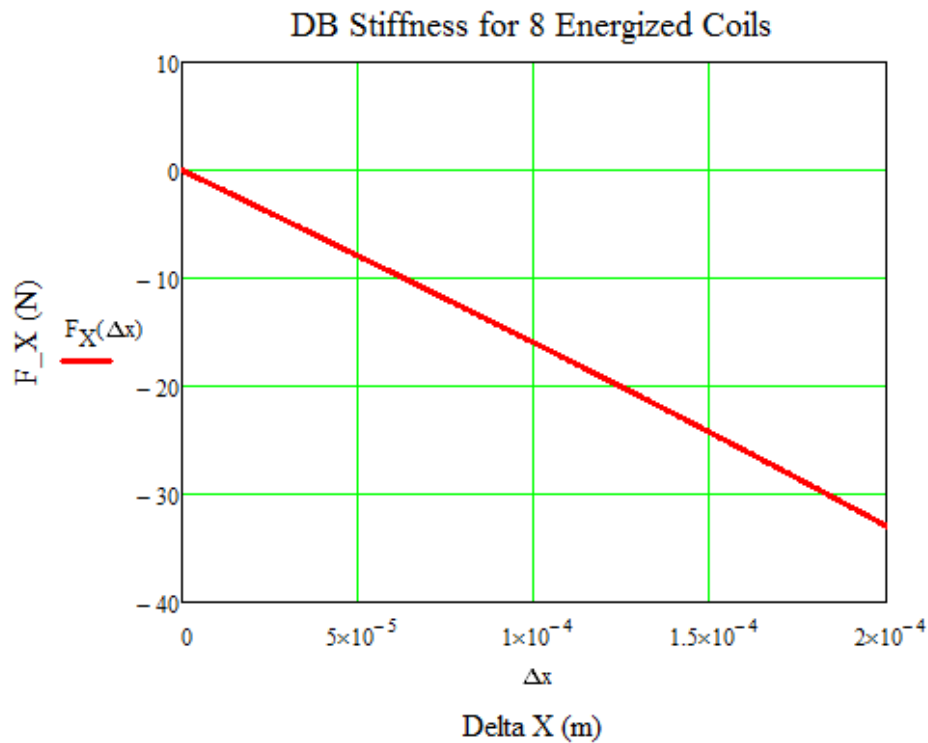


Figure 29: DB Mechanical Stiffness for 8 Energized Coils – MCM Approach

Since the MCM approach was used with eight d-axis coils energized, the MWA was constrained by setting the eight d-axis coils associated with producing forces in the y-direction to 0 A. The DB stiffness was then determined using the same approach for the 16 energized coil case. Using the MWA, the DB stiffness is equal to -1.67×10^5 N/m and is shown in Figure 30 below (see Appendix D).

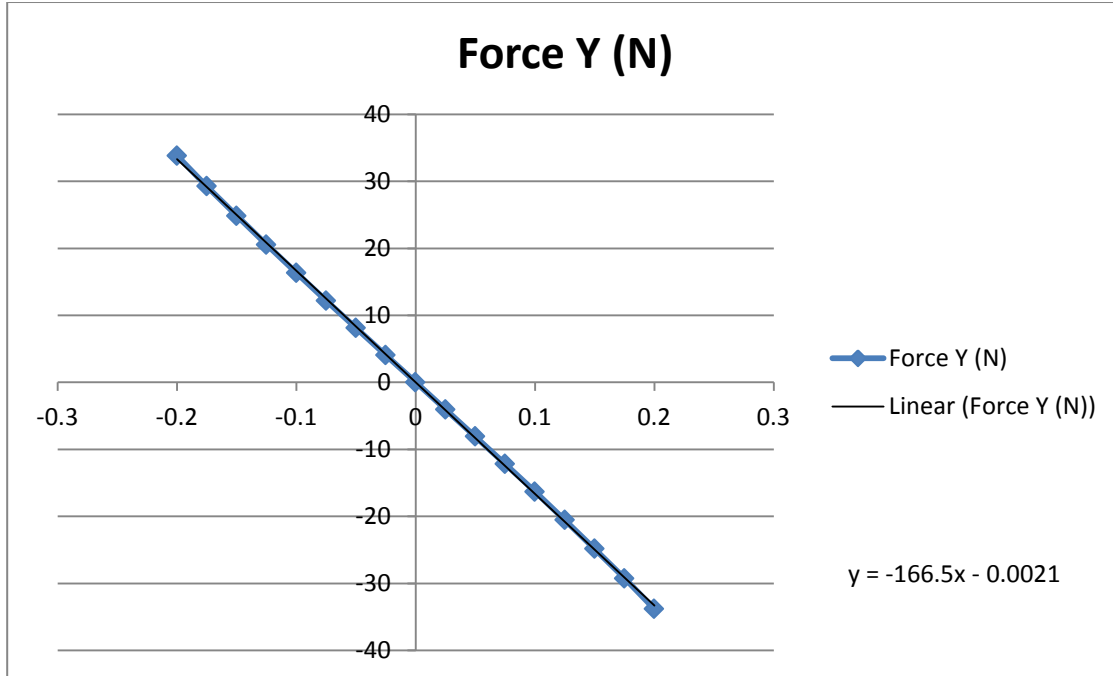


Figure 30: DB Negative Stiffness for 8 D-Axis Coils Energized using the MWA Calculations

The MCM and MWA methods resulted in percentage error of 2%. The MCM approach did not include the flux paths for interpole regions. Therefore, the MWA would be expected to predict a higher force, and therefore bearing stiffness.

7.4 Finite Element Analysis Verification

As the project progressed, the team acquired a FEA program created by David Meeker, known as Finite Element Method Magnetics (FEMM) [23]. FEMM was used to validate the accuracy of the static bearing force calculations using the MWA and MCM methods. The program was selected for this project since it interfaced well with Autocad, was available for free, and was easy to use.

The program was used to verify the flux density and forces for both the SB and DB. The MWA and MCM methods assumed that the iron MMF drops could be neglected. FEMM was used to test if this assumption was valid, and if not, where and when saturation occurred.

The FEA program was limited to calculating static forces and was not used for the complete rotor dynamic analysis presented in Chapter 8.

7.4.1 Drive Bearing Static Force Model Verification

To begin the analysis, the dxf files for the DB were imported into FEMM and then the bearing materials and boundary conditions were defined. The 16 d-axis coils were energized with the bias current of 1.75 A in FEMM. Using the MWA, the B_a was equal to approximately 0.5 T. FEMM was used to plot the flux density and showed how it was distributed around the machine, as shown in Figure 31. Based on the flux density plot, B_a was approximately equal to 0.6 T. These two methods varied since FEMM included the iron MMF drops in both the stator and rotor.

The flux density plot showed larger flux densities in the stator teeth than designed for, up to 1.2 T. As the current in the DB coils was increased, saturation occurred in the stator teeth. Therefore, the MWA was not valid and was limited by the stator teeth design. When saturation occurred, the calculated forces using FEMM were lower than the MWA. Saturation limited the range of possible DB command currents and will be limited when the command currents are realized with the actual machine.

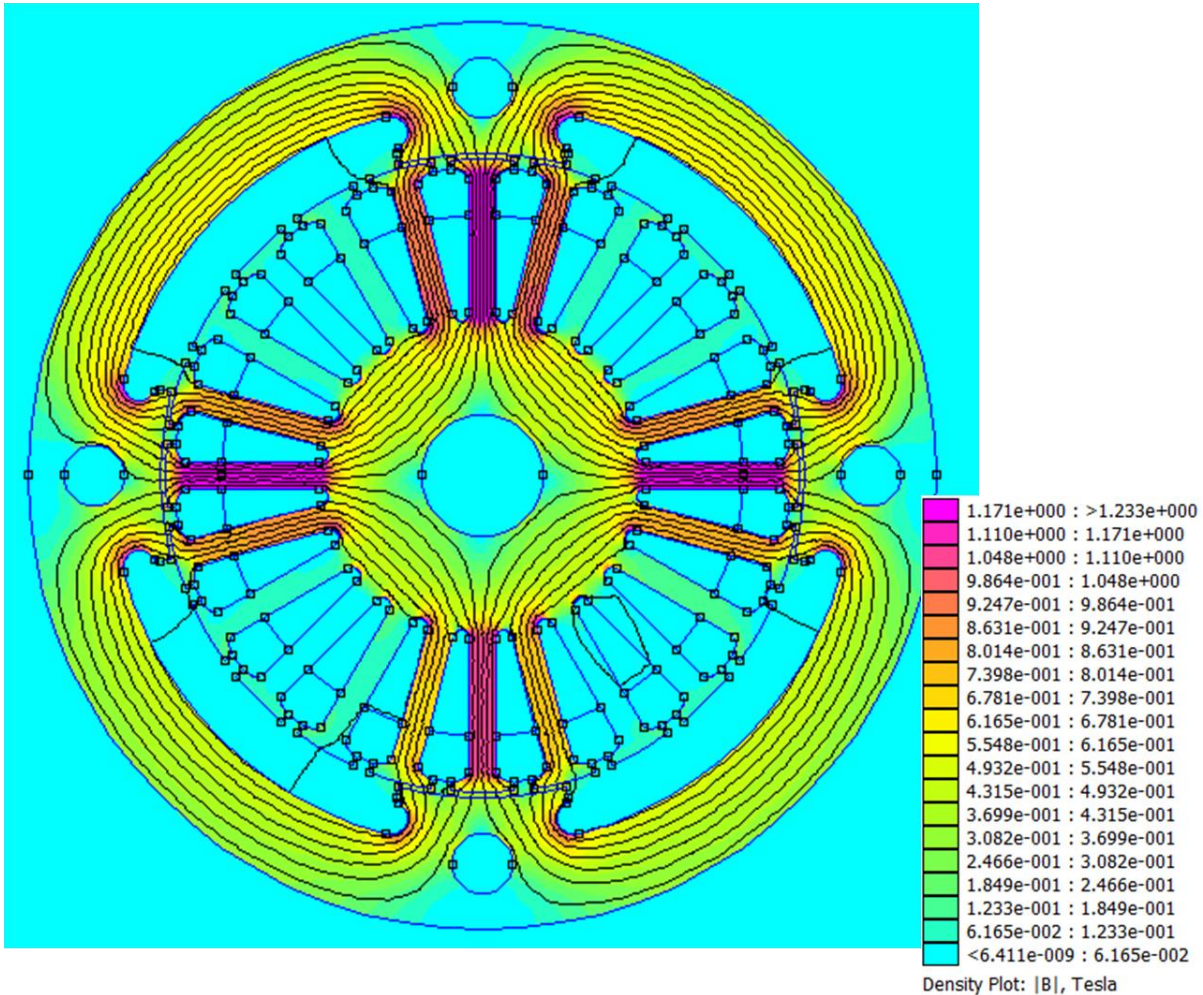


Figure 31: Flux Density Plot for 16 Direct Axis Coils on the DB Energized at 1.75A

FEMM was used to calculate the resulting magnetic forces when the d-axis currents were adjusted. The force/current relationship was determined for the DB using FEMM and was plotted in Section 7.4.4. A percentage error of approximately 20% occurred between the MWA and FEMM approaches, due to the saturated stator teeth. If the DB coil currents were adjusted by more than ± 0.7 A, the FEMM magnetic forces leveled off due to saturation. For the case when the DB bias currents were adjusted by 0.7 A, the three stator teeth under the pole face had flux densities ranging from 1.2 – 1.5 T. The stator teeth were saturated and caused the calculated magnetic forces to be smaller than the MWA.

7.4.2 Drive Bearing Bias Current Selection Process

The DB was initially designed with the d-axis bias currents of 4.38 A (as shown in chapter 5). Initially, the DB force/displacement and force/current factors were determined for this design, since the FEA program was not obtained until later in the project. For the initial design case, where the DB 16 d-axis coils were energized with the designed bias current of 4.38 A, severe saturation occurred, as shown in Figure 32. The flux density in the three stator teeth opposite the rotor pole faces ranged from 1.7-1.8 T, resulting in extreme saturation. If severe saturation occurred at the equilibrium operating point, this limited the ability to command different DB currents and provide the necessary restoring forces. Therefore, the DB bias currents were lowered to 1.75 A to prevent saturation for the equilibrium case and to increase the possible range of controller command currents. By reducing the d-axis currents, this will reduce the rotor's potential restoring forces, operating speed, and therefore, the energy stored in the flywheel.

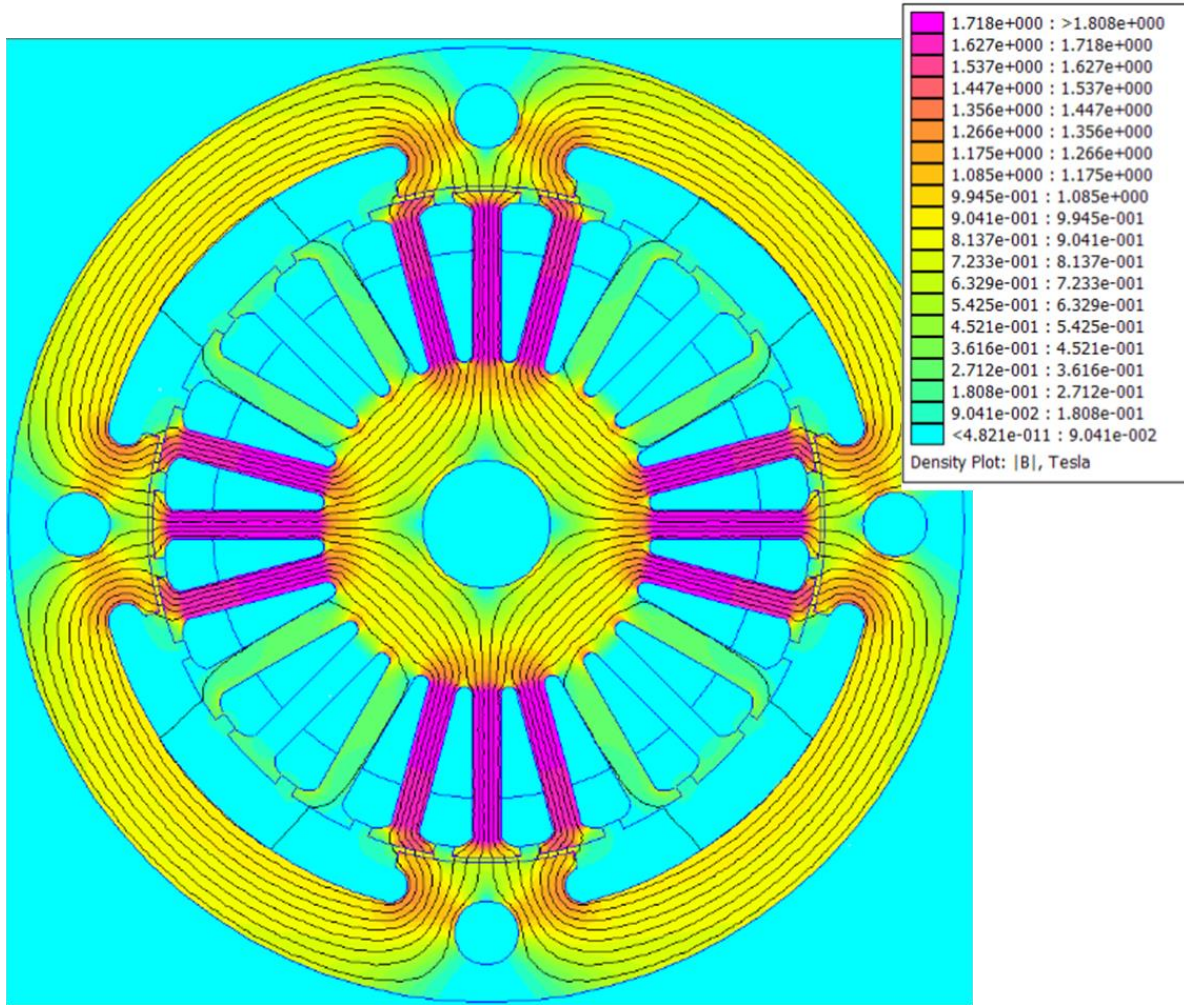


Figure 32: Flux Density Plot for 16 Direct Axis Coils on the DB Energized at 4.38 A

To reach this design decision, various cases were simulated in FEMM until the saturation in the stator teeth was below approximately 1.2 T. Table 3 includes the range of DB bias currents that were explored and the corresponding stator teeth flux density. The flux density was only recorded for the stator teeth that were near the saturation point of the M-36 material's BH curve (between approximately 1.2 – 1.5 T, depending on the M-36 BH curve source). For the purpose of optimizing the control scheme, the DB should be operated in the linear range of the BH curve (between approximately 0.1 T and 1.2 T) [7]. The best options for the DB bias current were either 1.5 A or 1.75 A. By reducing the DB bias current, this

reduced the desired output power, force density, and other operating conditions that were calculated in Chapter 5.

Table 3: Potential DB Bias Current and Corresponding Stator Teeth Flux Density

I_d Bias – 16 DB Coils (A)	B_{StatorTeeth} (T)	# of Stator Teeth Saturated (under one pole face)
4.3	1.7 – 1.8	3
3.0	1.55-1.6	3
2.5	1.48 - 1.56	3
2.0	1.2-1.4	1 (middle)
1.5	1.1	1 (middle)
1.75	1.1 – 1.2	1 (middle)

Since the DB is used as an AMB, the bias current of 1.75 A was selected to increase the range of DB command currents necessary to provide restoring forces, while avoiding severe iron saturation. The command currents were limited to ± 0.7 A to maintain operation in the linear region of the lamination material's BH curve. Since the d-axis bias current was altered, the q-axis current was also reduced to 1.67 A to maintain the same ratio between the currents from Chapter 5. This is an important design feature that may need to be reconsidered when the machine is rotated. If the machine is redesigned, the stator teeth could be altered to reduce saturation.

7.4.3 Stabilizing Bearing Static Force Model Verification

Figure 33 shows the flux density plot for the S, where all the coils were energized with the bias current of 2.6 A. For this case, the saturation was very minimal and only occurred around the stator teeth. The SB command current range was ± 1.0 A, since the SB was designed to operate well below saturation. A further explanation of the FEMM simulation results are included in [10].

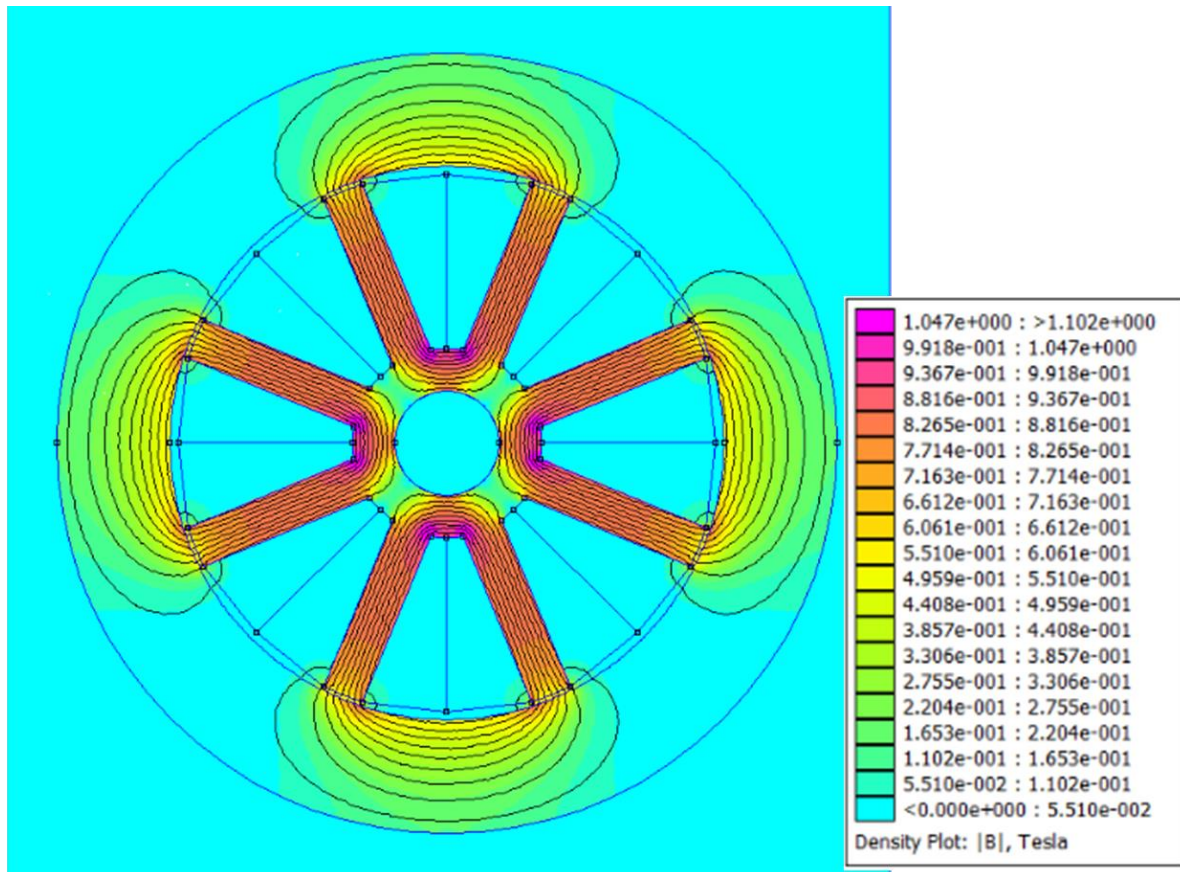


Figure 33: Flux Density Plot for SB Coils Energized at 2.6 Amps

Chapter 8. Dynamic Model of the FES System

This chapter introduces how the rotor dynamic model was derived for the UI's FES system. Rotor dynamics is a branch of mechanics that studies the behavior of the dynamics and stability of rotating machinery. Rotor dynamics analyzes the impact of the gyroscopic moments, cross-coupled forces and potential whirling instabilities caused by the rotating rotor [24]. While rotor dynamic analysis is useful for the design stage, it also supplies a deeper insight when the machine is operated and tested [20]. The rotor is free to rotate about an axis fixed in space and has six degrees of freedom of motion. A dynamic model of the UI FES system simulates the behavior of the system using MATLAB's Simulink® environment.

The rotor dynamic model predicts how the rotor responds to disturbances in an open-loop environment, or an environment without active control. The rotor assembly includes the DB and SB. The dynamic behavior of the rotor is dependent on the force/displacement and force/current linear relationships for both bearings that were derived in Chapter 7. When disturbances occur, the controller responds with restoring forces to return the system to the ideal state. The dynamic model aides in the development of the controller algorithms, and the controllers are responsible for controlling the rotor's motion. The controller's inputs are the rotor's displacements measured from the position sensors. In response to those measurements; the controller determines the command current necessary to provide restoring forces and return the rotor to the ideal state. This chapter concludes with combining the rotor dynamic model with the controller to simulate the closed-loop behavior of the system.

8.1 Rigid Body Model Introduction and Assumptions

To simplify the equations of motion for the rotor assembly, a few initial assumptions are made. The rotor is assumed to be a rigid and symmetric body. To describe the inertial

properties of a rotating rigid rotor, the moments of inertia (I_x , I_y , and I_z) and products of inertia (I_{yx} , I_{xy} , and I_{zx}) are found for a body-fixed reference system and combined into an inertia matrix [7]. For a special coordinate axes, known as the principal axes of inertia, the inertia matrix is diagonal and the non-zero moments of inertia are the principal moments of inertia. If the rigid body has geometrical symmetries, then the axes of symmetry are the principal axes of inertia [7]. This is the case for the UI's rotor assembly shown in Figure 34. For a symmetrical rotor, the moments of inertia about the x-axis (I_x) and y-axis (I_y) are equal.

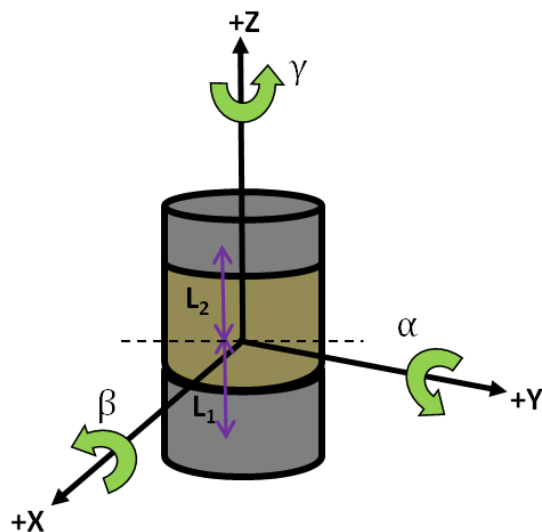


Figure 34: Rigid Rotor Model for the FES System's Rotor Assembly

The shape of the rotor (disk-like versus elongated) impacts the relationship between the moment of inertia about the rotational axis and the axis orthogonal to it. If these moments of inertia are equal ($I_x = I_z$), then the rotor becomes increasingly sensitive to dynamic imbalances. This design should be avoided to ensure smoother rotor operations with low-level vibrations [7]. As discussed in Chapter 6, the rotor assembly was designed to avoid equal moments of inertia, and therefore, dynamic instability. The rotor assembly was modeled using 3D-CAD software, known as CATIA. Using this software, the principal moments of inertia were determined and are found in Appendix F. Table 4 includes the CATIA outputs that were

used in the dynamic model (where I_{oxG} , I_{oyG} and I_{ozG} are the principal moments of inertia about the x-, y- and z- axes respectively and G_z is the center of mass location in the z-direction for each component).

Table 4: CATIA Outputs used in the Rotor Dynamic Model

Component	I_{oxG}/I_{oyG} (lb*in ²)	I_{ozG} (lb*in ²)	G_z (in)
Rotor Assembly	509.28	406.69	3.98
Top Plate	42.03	82.88	7.96
Magnetic Plate	54.09	105.27	0.85
SB Rotor	24.40	48.36	7.08
DB Rotor	54.77	103.44	2.50

To simplify the rotor dynamic model, the axial and radial dynamics can be decoupled for the mechanical representation of this system. The key assumptions necessary to decouple the axial and radial dynamics include [7],[25]:

- 1) The rotor assembly is symmetric and rigid.
- 2) When the rotor is at rest, the center of gravity (G) coincides with the stationary coordinate system. This represents the rotor's reference nominal position.
- 3) Deviations from the reference position of the rotor are small in comparison to the physical dimensions of the rotor. Since the deviations from the reference position (represented by Δx and Δy) are small, the equations of motion can be linearized, thereby decoupling the axial and radial dynamics.
- 4) The angular velocity of the rotor (represented by ω) about the longitudinal rotor-fixed axis z_0 is assumed to be constant.
- 5) The angular and translational displacements represent the position of the rotor. This position is characterized by the position of the rotor-fixed coordinate system ($x_0y_0z_0$), also known as the principal axes of inertia, with respect to the stationary coordinate system ($x_sy_sz_s$) that is inertially fixed.

Euler's angles (α , β , and γ) describe the angular motion of the rigid rotor about the rotor's spin axis. Right hand convention is used, where CCW represents a positive rotation and CW represents a negative rotation, as shown in Figure 34. The origin of the coordinate system is located at the rotor's G. As was previously stated, the angular velocity $\dot{\gamma} = \omega$ is assumed to be constant, therefore $\ddot{\gamma} = 0$. To ensure this assumption is valid for the FES system in the future, the controller needs to control the rate at which the machine's speed is adjusted.

Since the equations of motion are linearized, the angles β and α are characterized as inclinations about the inertially fixed coordinate system (x_s and y_s respectively) [7], [25]. The linearization of the equations of motion requires that the angles β and α remain small to be characterized as inclinations about x_s and y_s . Due to this constraint, these are no longer proper Euler angles [25]. For the UI's rotor assembly, these inclinations are small in comparison to the rotor dimensions. In addition, these inclinations are physically constrained since the rotor and stator collide when the airgap is 2 mm. To avoid collision and maintain adequate control, the maximum inclination angle is 0.152 degrees, as was previously determined in Section 7.3.4 . To determine this angle, the rotor was symmetrically inclined with a maximum radial shift of 0.2 mm and was found using the following equation:

$$\text{MaxTilt} = \text{atan}\left(\frac{\text{AirgapShift}}{\text{RotorHeight}/2}\right) = \text{atan}\left(\frac{0.2 \text{ mm}}{5.92 \text{ in}/2}\right) = 0.152^\circ \quad (8.1)$$

Due to these small inclinations, the small angle approximations were valid and utilized, where $\sin(x) = x$, $\cos(x) = 1$, and $\tan(x) = \frac{\sin(x)}{\cos(x)} = x$. The translational motion of the rotor assembly was represented by the displacements x_G and y_G from G. Since the axial and

radial dynamics were decoupled, the next section derives the basic equations of motion for the rotor's radial motion.

8.2 General Radial Dynamic Equations of Motion

The radial equations of motion for the rigid rotor are described by the translational and angular motion about the G. When a rigid body model is used, only the rigid body modes of the rotor assembly can be predicted: cylindrical (center of gravity whirl) and conical (tilt whirl) [25]. To predict the rigid body modes and overall dynamic behavior of the rotor assembly, the equations of motion for the translational and angular displacements (x_G , y_G , α , and β) are determined using Lagrange's equations [25]:

$$\frac{d}{dt} \left(\frac{\partial L}{\partial \dot{\theta}_n} \right) - \left(\frac{\partial L}{\partial \theta_n} \right) = Q_n \quad (8.2)$$

where L is the Lagrangian function ($L = T - V$; where T is the kinetic energy and V is the potential energy), the coordinates have a motion represented by θ_n , and the non-conservative torques on the n^{th} coordinate are equal to Q_n . Lagrange's equations result in differential equations that describe the equations of motion for a given system. By taking the Lagrangian of a spinning disk, the differential equations of motion for a rigid disk are derived and equal to [25]:

$$L = T = \frac{1}{2} m (\dot{x}^2 + \dot{y}^2) + \frac{1}{2} I_T (\dot{\alpha}^2 + \dot{\beta}^2) + \frac{1}{2} I_P (\omega^2 - 2\omega\dot{\alpha}\beta) \quad (8.3)$$

where ω is the constant rotational speed, m is the mass of the spinning disk or rotor, I_T is the transverse moment of inertia about the x or y axis (for a symmetric rotor), and I_P is the polar mass moment of inertia of the disk about the z axis. Equation (8.3) represents the kinetic energy of the rotor and is expressed in terms of Euler's angles (α and β), which must remain small.

The right hand side of Lagrange's equation (8.2) is replaced with the forces that act on the disk, since these are considered as part of the virtual work. The coordinates θ_n from equation (8.2) are replaced with x_G , y_G , α , and β . The virtual work (ΔW), from all the forces acting on the disk, is equal to [25]:

$$\Delta W = \sum F_x \Delta x_G + \sum F_y \Delta y_G + \sum M_Y \Delta \alpha + \sum M_X \Delta \beta \quad (8.4)$$

From Lagrange's equation (8.2), the generalized forces and moments are equal to:

$$Q_1 = \sum F_x, Q_2 = \sum F_y, Q_3 = \sum M_Y, \text{ and } Q_4 = \sum M_X \quad (8.5)$$

where $\sum F_x$ and $\sum F_y$ represent the sum of forces acting on the disk's center of mass in the x and y directions, and $\sum M_x$ and $\sum M_y$ represent the sum of moments about the x and y axes. Equations (8.3) and (8.5) are substituted into Lagrange's equation (8.2) and outcomes in the following four general differential equations of motion [25]:

$$m\ddot{x}_G = \Sigma F_x \quad (8.6)$$

$$m\ddot{y}_G = \Sigma F_y \quad (8.7)$$

$$I_T \ddot{\beta} + I_P \omega \dot{\alpha} = \Sigma M_x \quad (8.8)$$

$$I_T \ddot{\alpha} - I_P \dot{\beta} \omega = \Sigma M_y \quad (8.9)$$

Due to the simplifications that were made, these linearized equations are used to model the system. These equations retain the basic features of the dynamic behavior of the rotor and provide an accurate system representation [20]. These equations can also be determined by using vector equations, without introducing a set of coordinates, to describe the rotation of a rigid body as shown in [26].

Equations (8.6) and (8.7) describe the translation motion of the rotor in terms of the acceleration of the body's center of mass. Equations (8.8) and (8.9) describe the rotational motion of the rotor in terms of Euler's angles. The terms involving I_P represent the gyroscopic

moments. The gyroscopic moments tend to stiffen the rotor in the forward whirl and destiffen it in the backward whirl, thus altering the natural frequencies and critical speeds of the rotor [25]. The system's natural frequencies are frequencies where the system oscillates and encounters resonances, which can cause system vibration due to small disturbances. When the natural frequency of the rotor system coincides with the frequency of an excitation source, the rotor is being operated at a critical speed [7]. This leads to high levels of vibrations, which are undesirable and should be avoided. The SB and DB can be used to actively dampen the rotor's vibrations, which is important when passing through critical speeds.

These rotational equations of motion are inherently nonlinear and cross-coupled due to the angular velocity terms ($\dot{\alpha}$ and $\dot{\beta}$). Therefore, an angular velocity about the y axis produces a moment about the x axis when the rotor is rotating. The effect of the gyroscopic moments is determined by the ratio of I_p/I_t , which is the MOI ratio that was determined in Chapter 6. If the MOI ratio is equal to one, the natural frequency will coincide with the rotor's frequency, which could lead to a permanent state of resonance.

The moments and forces on the left hand side of equations (8.6)-(8.9) are due to electromagnetic bearing forces between the rotor and stator for the DB and SB. In addition, if the rotor is imbalanced; the distribution of the mass imbalance along the rotor also produces a force and can cause synchronous whirl. The rotor assembly was not mechanically balanced and these imbalance forces should be included in the dynamic model. When the rotor is rotated at higher speeds, the machine should be mechanically balanced to prevent dynamic instability. For a complete rotor dynamic model, the radial and vertical levitation forces should also be modeled. At this point in the project, these forces were not completely understood or characterized, and were therefore, not included.

8.3 Equations of Motion for the Simulink® Rotor Dynamic Model

The general equations of motion derived in Section 8.2 are tailored to the UI FES system's rotor assembly. These equations provide a model of the rotating rigid rotor, including gyroscopic effects. This section combines the rigid rotor model with the bearing and controller models. Initially, only the linearized electromagnetic forces produced by the SB and DB are considered. These bearing forces are proportional to the displacements at the bearing sites (x_{DB} , y_{DB} , x_{SB} , and y_{SB}). The bearing forces are modeled as a conventional linear mechanical spring with a negative bearing stiffness ($k_{DB} = -6.65 \times 10^5 \text{ N/m}$ & $k_{SB} = -2.03 \times 10^5 \text{ N/m}$). The bearings have a negative stiffness since they are unstable in an open-loop system. The negative stiffness for both bearings was determined over a range of $\pm 0.2 \text{ mm}$ around the ideal airgap of 1mm in Chapter 7.

Since the bearing forces are “active” forces, or controlled electromagnetic forces, the bearing forces are described as a linearized function of the coil currents in addition to the bearing displacements [7]. To model both bearings, the bearing force equations are linearized about an operating point, and the linear force/current and force/displacement relationships are determined. The bearing displacements and command currents must be small deviations around the operating point to use the linear bearing force approximations [7]. The following linearized equation represents the DB and SB forces in the x and y directions:

$$\mathbf{F}_B = -\mathbf{k}_s \mathbf{x}_B + |\mathbf{k}_i| \mathbf{i}_B \quad (8.10)$$

where \mathbf{k}_s is the negative bearing stiffness [N/m], \mathbf{x}_B is the rotor displacement for each bearing [m], \mathbf{k}_i is the force/current factor [N/A], and \mathbf{i}_B is the individual coil currents for each bearing [A].

Equation (8.10) is a linear approximation of the actual force -current or -displacement relationships and is only accurate for small deviations about the operating point. This approximation has successfully been implemented for a wide variety of applications, but is limited for the following cases: rotor and stator collision, flux saturation, and low bias currents [7]. The force/current factors for the SB and DB were determined in Chapter 7. Since the bearings are symmetric, k_i for both bearings are the same in the x and y directions. These factors equal: $k_{i_DB} = -366.84 \text{ N/A}$ and $k_{i_SB} = -80.69 \text{ N/A}$. To operate both bearings in the linear region of the BH curve, k_i is accurate over a range of $\pm 1 \text{ A}$ for the SB and $\pm 0.7 \text{ A}$ for the DB.

The forces and moments on the right hand side of the four differential equations derived in Section 8.3 are replaced with the linearized bearing force equations and the other external system forces are neglected. The first two equations represent the translational movement of the rotor. The DB and SB forces were derived using equation (8.10) and the mass (m) of the rotor assembly is equal to 16.34 kg.

$$m\ddot{x}_G = \Sigma F_x = F_{DBx} + F_{SBx} \quad (8.11)$$

$$m\ddot{y}_G = \Sigma F_y = F_{DBy} + F_{SBy} \quad (8.12)$$

The next two equations describe the angular motion of the rotor. The bearing forces are modeled as point forces applied at the center of both bearings. The center of the DB is a fixed axial distance of L_1 from G, while the SB is a distance L_2 from G, as shown in Figure 34. These distances were determined from the CATIA outputs given in Table 3 and are equal to: $L_1 = 0.038 \text{ m}$ and $L_2 = 0.079 \text{ m}$. The moments of inertia were also determined from Table 3 and are equal to: $I_T = 0.149 \text{ kg*m}^2$ and $I_P = 0.119 \text{ kg*m}^2$, and ω is 188.5 rad/s (1800 RPMs).

Equations (8.8) and (8.9) were modified to match the previously defined motion of the rotor assembly derived above (where $-\alpha$ is a CW rotation).

$$\mathbf{I}_T \ddot{\beta} - \mathbf{I}_P \omega \dot{\alpha} = \Sigma \mathbf{M}_x = \mathbf{L}_1 \mathbf{F}_{DBy} - \mathbf{L}_2 \mathbf{F}_{SBx} \quad (8.13)$$

$$\mathbf{I}_T \ddot{\alpha} + \mathbf{I}_P \dot{\beta} \omega = \Sigma \mathbf{M}_y = \mathbf{L}_1 \mathbf{F}_{DBx} - \mathbf{L}_2 \mathbf{F}_{SBx} \quad (8.14)$$

The equations of motion describe the displacement of the rotor in terms of the translational and angular motion about G. Therefore, the bearing and sensor coordinates must be related to the G coordinates, so that only one set of coordinates is used to describe the rotor's motion. To derive these relationships, the location of the position sensors, in relation to the rotor's G, is shown in Figure 35. For a rigid body, the bearing and sensor locations are a scaled distance from G. The sensor x and y coordinates are represented by x_1 , x_2 , y_1 , and y_2 (where 1 refers to the sensors located closest to the DB and 2 to the SB). These sensor coordinates are measured distances between the sensor location and the rotor assembly. The position sensors are located at a fixed axial distance l_1 (0.08m) and l_2 (0.101m) from the rotor's G. If the sensor locations change, these two parameters will need to be adjusted in the dynamic model.

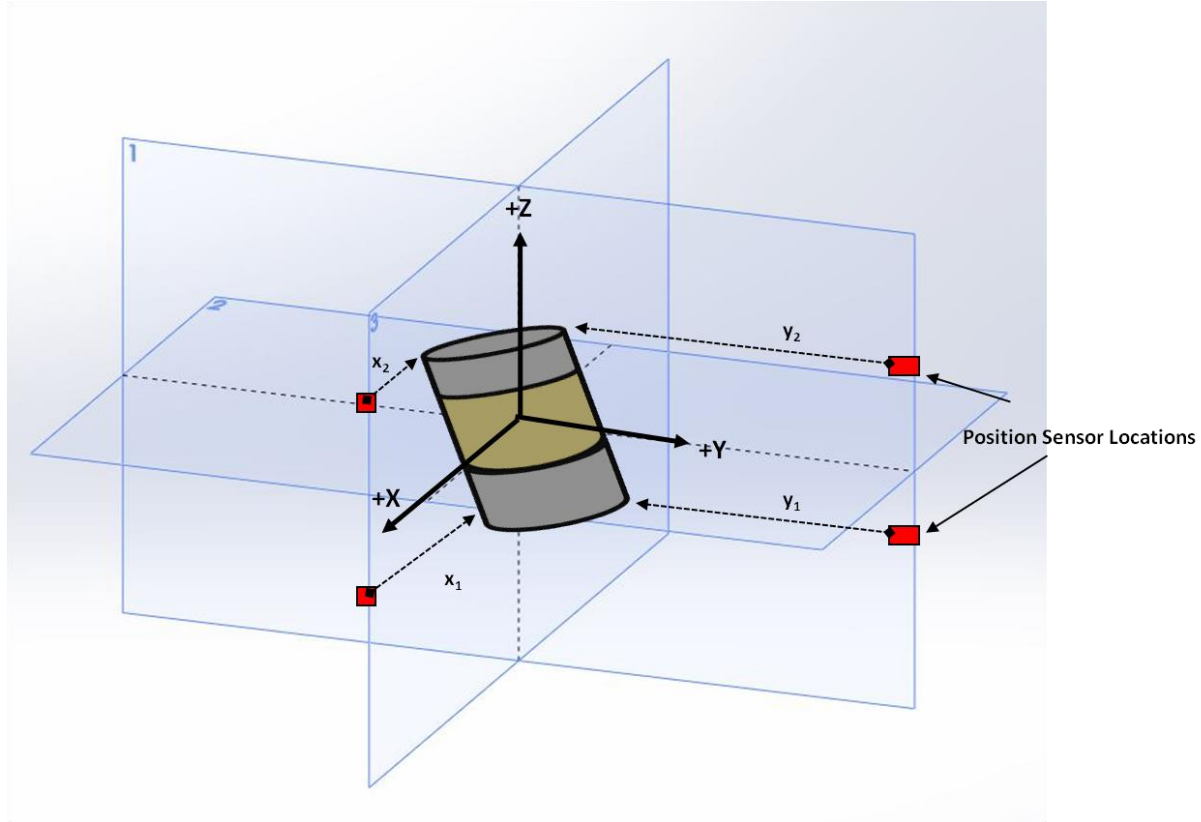


Figure 35: FES System's Rigid Rotor with Four Position Sensor Locations

Before developing the relationships between the various coordinate systems, the four position sensors are briefly explained. A more detailed description is given in [11]. A KD2306 sensing system was purchased from Kaman Precision Products for the four eddy current sensors. The 9U eddy current sensor probe uses an AC waveform to induce eddy currents in the target material of the rotor assembly. To ensure adequate target material for optimal sensor operation, the bottom sensors were axially positioned at the center of the magnet plate and the top sensors were positioned at the center of the top plate. The sensor uses the eddy currents to determine a distance 'd' (outputted as a voltage) between the sensor and the rotor. Figure 36 shows the hardware associated with each sensor. An electronic box was required to linearize the signal transmitted from the sensor. The electronic box outputs a

voltage between 0-10V that has a linear relationship with a set of distances that range between 0-3mm (where \mathbf{d} is in mm and \mathbf{V}_{out} is in Volts).

$$\mathbf{d} = 0.2988\mathbf{V}_{\text{out}} + 0.0044 \quad (8.15)$$

The output voltage is scaled down to 0-3V for the analog to digital converter (ADC) sampling by a TI Delfino series microcontroller. The initial distance between the sensors and the rotor assembly is 1 mm. The actual range of readings will be between 0.5mm-2.5mm, with either extreme resulting in a collision between the rotor and stator.

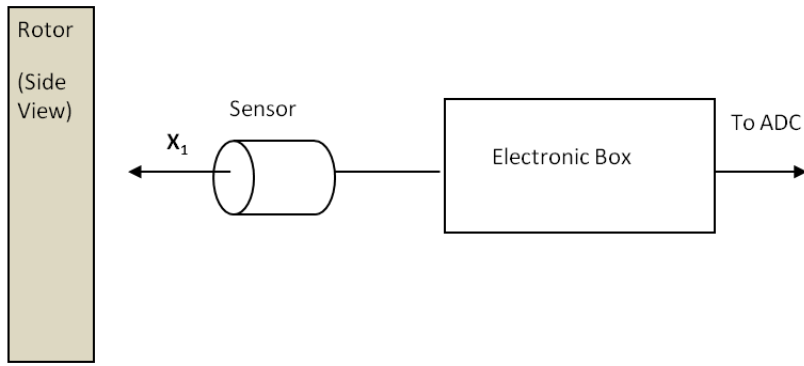


Figure 36: Eddy Current Position Sensor Physical Hardware Setup

The sensor and bearing displacements were related to the center of gravity displacements for the differential equations of motion. To derive these relationships, two tilt angles were defined as a function of the measured sensor coordinates [16]:

$$\mathbf{X}' = \frac{\Delta x}{\Delta z} \text{ and } \mathbf{Y}' = \frac{\Delta y}{\Delta z} \quad (8.16)$$

where Δz is the separation between the two sensor planes ($l_1 + l_2$) and Δx and Δy are the differences between the x and y sensor coordinates for both sensor planes ($x_2 - x_1$ and $y_2 - y_1$ respectively). Since the tilt angles are small, the small angle approximation is used to derive equation (8.16). If Δx and Δy are equal to zero, the rotor is perfectly upright and is not tilted. The tilt angles are equal to the angles β and α used in the equations of motion:

$$\alpha = \mathbf{X}' \text{ and } \beta = \mathbf{Y}' \quad (8.17)$$

Using these angles, a relationship between the sensor and center of gravity displacements was derived. To derive this relationship, a y-z plane depicting a CCW inclination of β about the x-axis, based on a right handed coordinate system, is shown in Figure 37.

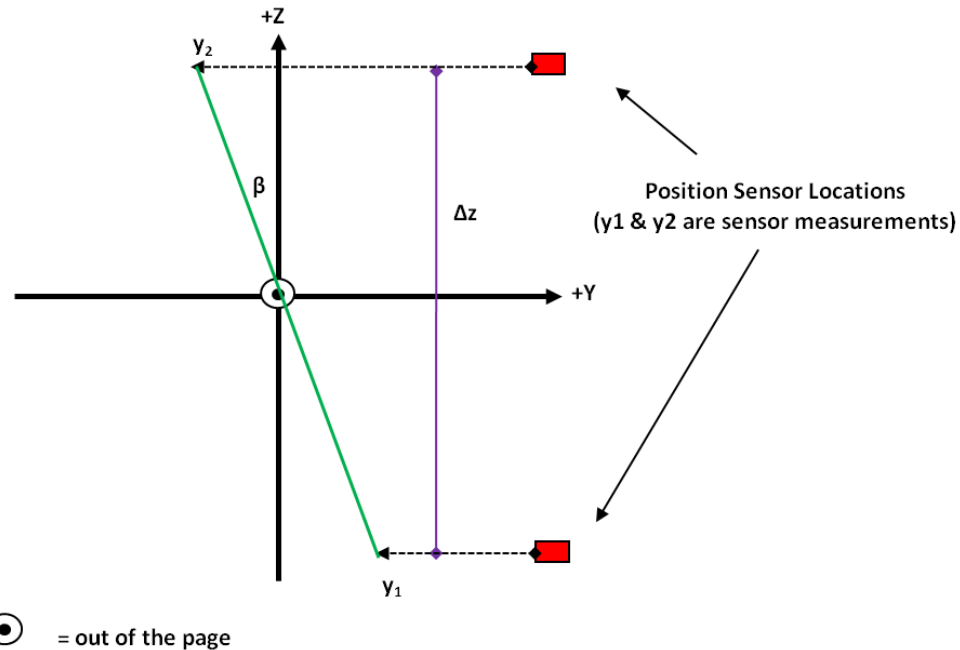


Figure 37: Y-Z Plane – CCW Rotation of the Rotor Assembly for the angle β about the X-Axis

Since the equations of motion are a function of displacements, the sensor coordinates are converted to sensor displacements ($x_{1\Delta}$, $x_{2\Delta}$, $y_{1\Delta}$, and $y_{2\Delta}$), where x_{offset} is the initial distance between the sensors and the rotor when it is perfectly centered:

$$x_{1\Delta} = x_{\text{offset}} - x_1 \quad (8.18)$$

Using the equation of a line, a relationship between the sensor and center of gravity displacements (x_G and y_G) is derived. For a given distance 'z' from G, the y sensor displacement is derived using the equation of a line:

$$y_\Delta(z) = -mz + b = -\frac{\Delta y}{\Delta z}z + y_G \quad (8.19)$$

where m is the slope of the line, and is equal to the tilt angle Y' ($\Delta y/\Delta z$) or β , and b is the y-intercept, and is equal to y_G (as shown in Figure 37). Equation (8.19) is used to express the

measured rotor displacements $y_{1\Delta}$ and $y_{2\Delta}$ in terms of the center of gravity displacements for $z = -l_1$ and l_2 .

$$y_{1\Delta} = Y'l_1 + y_G \quad (8.20)$$

$$y_{2\Delta} = -Y'l_2 + y_G \quad (8.21)$$

To derive a relationship between the x sensor displacements and the tilt angle X' , the rotor is inclined $-\alpha$ degrees about the x-axis, and is shown in Figure 38. A CCW rotation is defined as a positive angle and a CW rotation is defined as a negative angle.

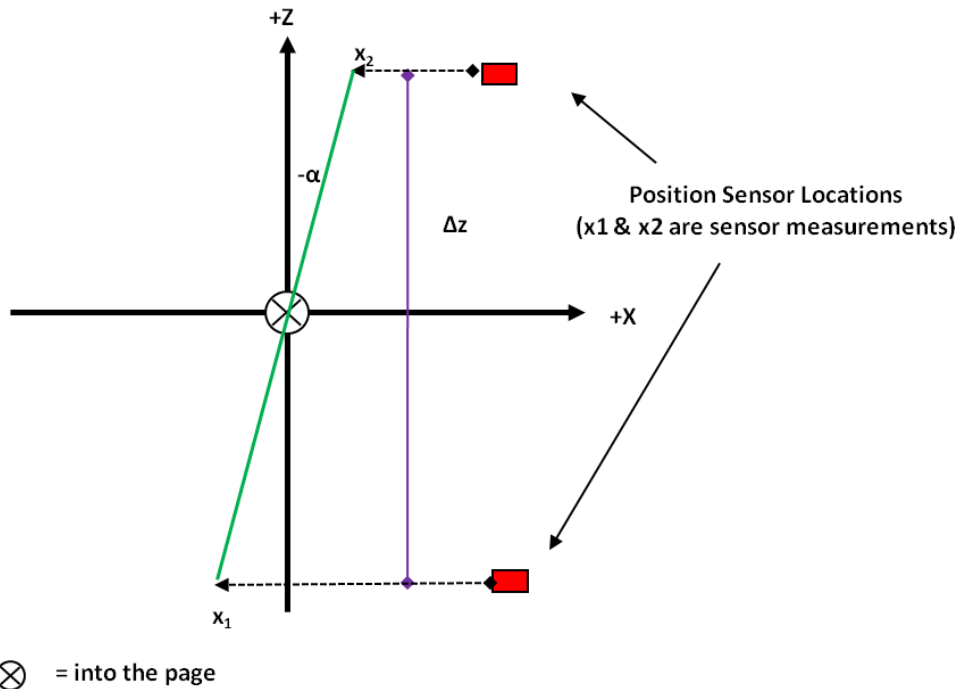


Figure 38: X-Z Plane – CW Rotation of the Rotor Assembly for the angle $-\alpha$ about the Y-Axis

Equation (8.19) was modified for the x-z plane to express the measured rotor displacements, $x_{1\Delta}$ and $x_{2\Delta}$, in terms of the center of gravity displacements:

$$x_{1\Delta} = X'l_1 + x_G \quad (8.22)$$

$$x_{2\Delta} = -X'l_2 + x_G \quad (8.23)$$

The sensor displacement equations were rearranged to solve for the center of gravity displacements. These relationships were used in the Simulink® model to calculate the initial center of gravity displacements, given various sensor displacement measurements.

$$x_G = \frac{x_2 \Delta * l_1 + x_1 \Delta * l_2}{l_2 + l_1} \quad (8.24)$$

Using a similar approach, a relationship between the bearing and center of gravity displacements was derived. As was previously explained, the centers of the DB and SB are located at a fixed axial distance L_1 and L_2 from the rotor's G. The bearing stiffness and forces are dependent on the rotor displacement in the bearings and therefore these are necessary [7]. These displacements were determined using a linear transformation matrix:

$$\begin{bmatrix} x_{DB} \\ x_{SB} \\ y_{DB} \\ y_{SB} \end{bmatrix} = \begin{bmatrix} 1 & -L_1 & 0 & 0 \\ 1 & L_2 & 0 & 0 \\ 0 & 0 & 1 & -L_1 \\ 0 & 0 & 1 & L_2 \end{bmatrix} * \begin{bmatrix} x_G \\ -\alpha \\ y_G \\ -\beta \end{bmatrix} \quad (8.25)$$

The equations of motion were then modeled in Simulink® to investigate the stability of the FES system for an open-loop system.

8.4 Simulink® Model – Radial Dynamics

The equations of motion are modeled and simulated in Simulink®. The Simulink® model was initially modeled as an open-loop system, without any active control, and is found in Appendix G. Due to the negative bearing stiffness, the system is inherently unstable when airgap displacements occur. Next, the system was combined controllers to actively maintain system stability. The controller algorithm design was not included in this thesis and is found in [10].

8.4.1 Open-Loop Dynamic Model

The open-loop Simulink® dynamic model includes four main subsystems that model the four differential equations of motion, (8.11) – (8.14). Two of these subsystems describe

the translational motion of the rotor and model the linear DB and SB forces expressed in terms of k_i and k_s . Figure 39 contains a snapshot of the subsystem for the summation of forces in the x-direction (the y force subsystem is very similar and is included in Appendix G). The linearized bearing force equations for the SB and DB are the inputs to the x force subsystem. Equation (8.11) is used to find x_G , denoted as x_{com} in Figure 39. The sensor and bearing displacements are then derived from x_G , and these transformations are included in the ‘Transform COM: Bearing, Sensor Displacements’ subsystem block.

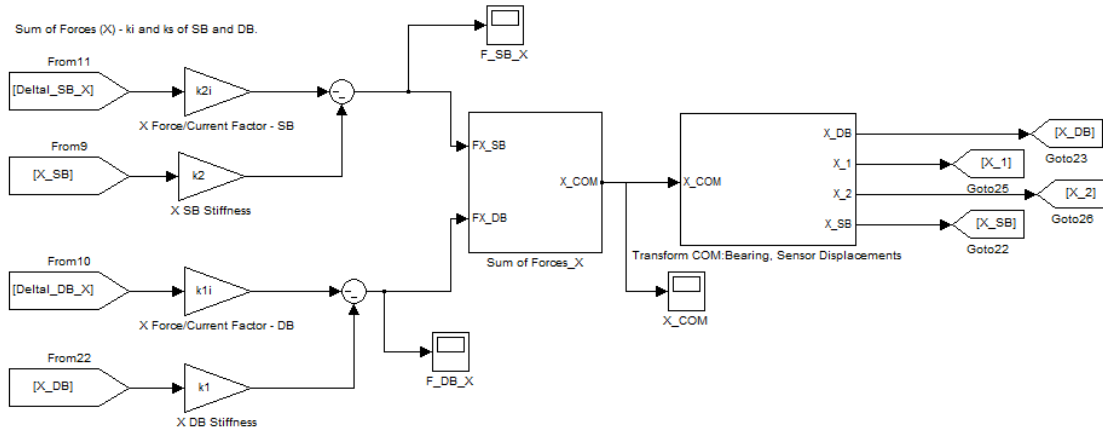


Figure 39: Summation of X-Forces for the FES System Modeled in Simulink

MATLAB script is also used and includes the model inputs and the measured sensor coordinates (x_1 , x_2 , y_1 , and y_2) needed to simulate the Simulink® model. While the sensor coordinates are not physical measurements from the sensors, these are used to introduce radial and axial airgap eccentricities into the system to predict how the rotor will respond to disturbances. Table 5 includes the dynamic model inputs for an unconstrained case without airgap eccentricities.

Table 5: Radial Dynamic Model .m File Inputs

Model Input	Input Value
I_T	$0.149 \text{ kg}^*\text{m}^2$
I_P	$0.119 \text{ kg}^*\text{m}^2$
m	16.343 kg
l_1	0.08 m
l_2	0.101 m
L_1	0.038 m
L_2	0.079 m
$k_1 (\text{DB})$	$-6.65*10^5 \text{ N/m}$
$k_2 (\text{SB})$	$-2.03*10^5 \text{ N/m}$
$k_{1i} (\text{DB})$	-366.84 N/A
$k_{2i} (\text{SB})$	-80.69 N/A
$x1_m$	1 mm (ideal)
$x2_m$	1 mm (ideal)
$y1_m$	1 mm (ideal)
$y2_m$	1 mm (ideal)
ω	$188.5 \text{ rad/s (1800 RPMs)}$

The Simulink® model includes a coordinate transformation function, shown in Figure 40, to transform the sensor measurements into the initial G displacements (x_{Gi} and y_{Gi}) and rotor tilt angles (β_i and α_i). These initial displacements and angles are the initial conditions used for the integrators associated with the four equations of motion involving x_G , y_G , β , and α . If the rotor is perfectly centered and upright, these initial angles and displacements are equal to zero, and no disturbances are introduced into the system.

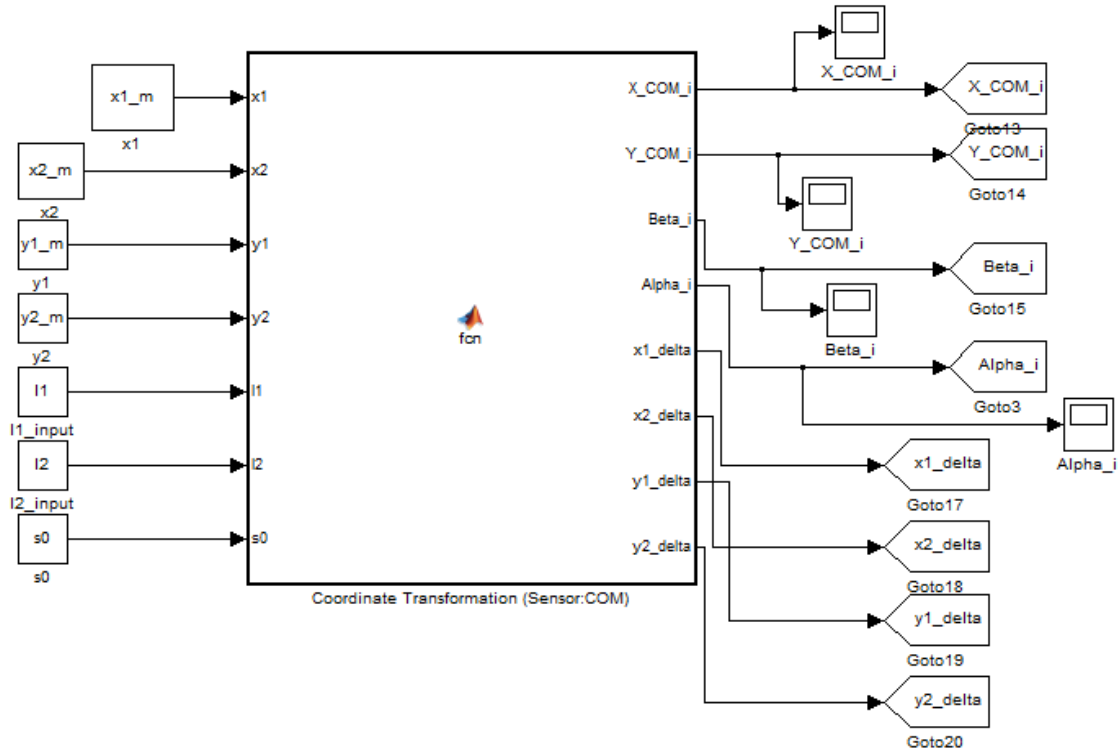


Figure 40: Initial Sensor Measurement Transformation Subsystem in Simulink

The rotor dynamic model was initially constrained to ensure that the summation of x and y force subsystems were behaving as expected. These constraints included modeling both bearings as the SB (with equal k_i and k_s factors), arranging the sensors and bearings symmetrically ($I_2 = I_1 = 0.08$ m and $L_2 = L_1 = 0.038$ m), and inhibiting rotor rotation ($\omega = 0$). For a non-rotating rotor, the rotational and translational motions are decoupled. For case #1, the sensor measurements were set to: $x_1 = x_2 = 0.8$ mm and $y_1 = y_2 = 1$ mm and were introduced into the model at a time of $t = 0.5$ ms, which resulted in $x_{Gi} = 0.2$ mm and $y_{Gi} = 0$ mm.

For this case, the rotor assembly moved closer to the sensors, which caused the airgap to decrease along the rotor's negative x-axis, and the force to increase. Since there was no active control, $\sum F_x$ and x_G continued to increase with time, as shown in Figure 41. When x_G

exceeds 1 mm, the rotor and stator would collide. This collision was not included in the model, therefore, $\sum F_x$ and x_G continued to increase with time. No angular motion ($\beta=\alpha=0$) occurred, since the angular and translational motion were decoupled for this case.

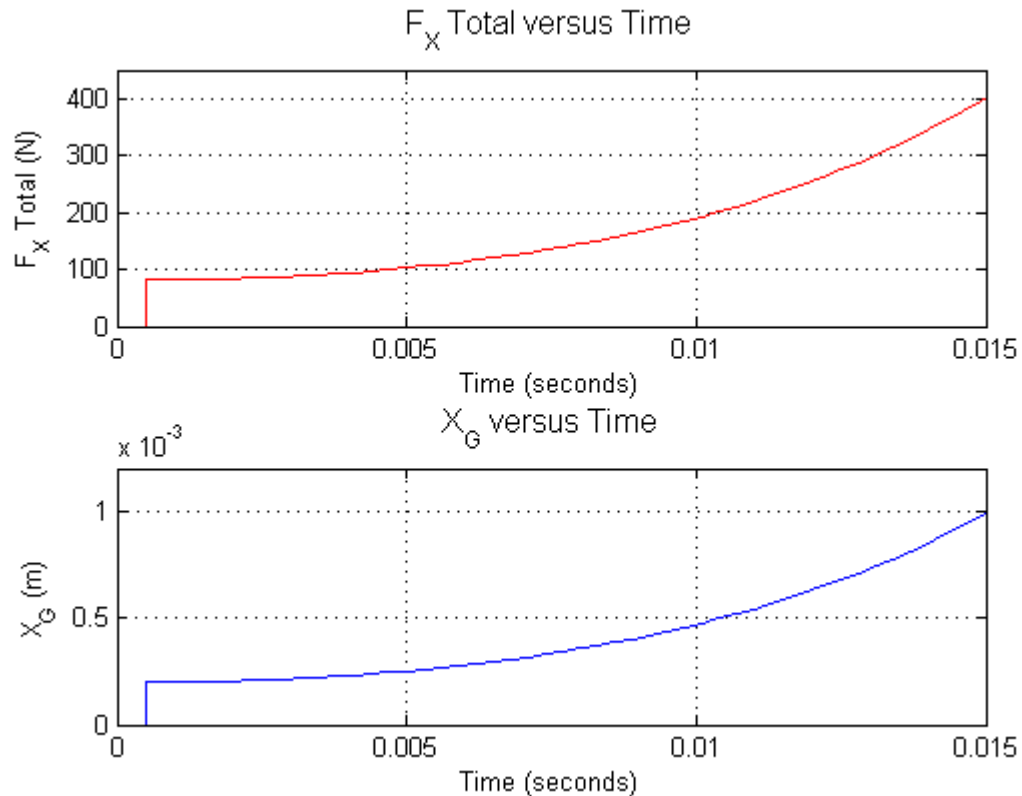


Figure 41: Total X force and X COM Displacement versus Time for an Initial Translation

The other two subsystems describe the rotational motion of the rotor. Figure 42 includes a snapshot of the summation of moments about the x-axis subsystem (the moments about the y-axis subsystem is very similar and is in Appendix G). The SB and DB moment equations and the gyroscopic moment term are the inputs to the x moments subsystem. Equation (8.13) is used to determine β , denoted as beta in Figure 42, and is represented by the 'Sum of Moments_X' subsystem block.

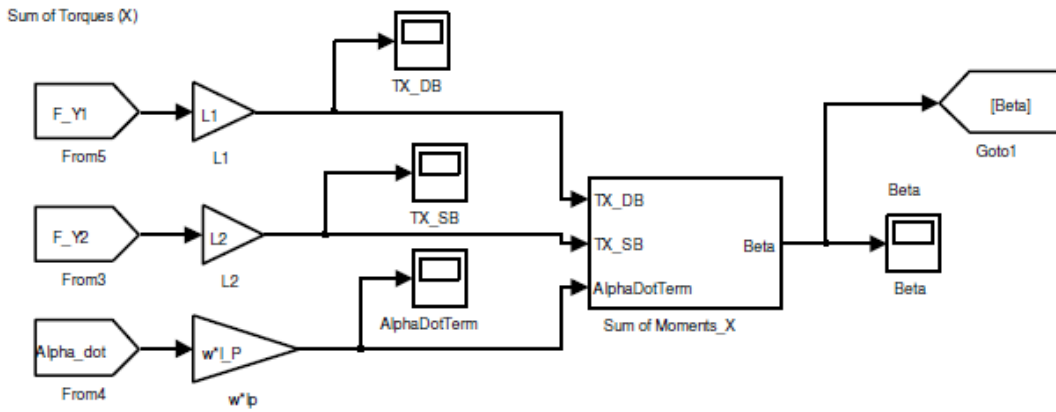


Figure 42: Summation of Moments about the X-Axis for the FES System Modeled in Simulink

The same constraints from case #1 were used to ensure the summation of moment subsystems were correct. For case #2, the sensor measurements were defined as: $x_1 = x_2 = 1$ mm and $y_1 = 0.9$ mm and $y_2 = 1.1$ mm and were introduced into the model at a time of $t = 0$ s, which resulted in $\beta_i = 1.25 \times 10^{-3}$ and $\alpha_i = 0$. For this case, the rotor assembly rotated in the CCW direction about the center of gravity, which caused β to increase until collision occurred between the rotor and stator. The rotor continued to rotate in the CCW direction since the moments produced by the SB and DB were both in the CCW direction.

Additional cases were simulated to verify the dynamic model. The last case included rotation ($\omega \neq 0$), and thus, the translation and angular motions were not decoupled. The remainder of the constraints and sensor measurements from case #2 applied to case #3. As expected, β initially increased in the CCW direction, and due to cross-coupling, $-\alpha$ increased in the CW direction. Since there was no active control, the rotor assembly continued to oscillate and is shown in Figure 43.

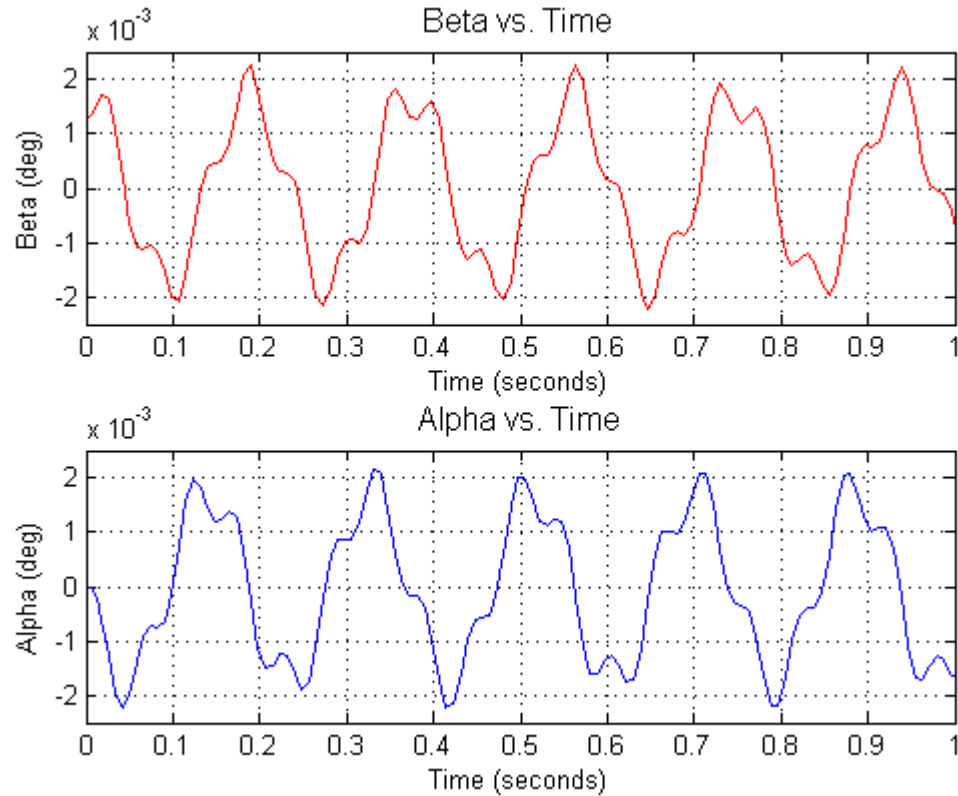


Figure 43: Alpha and Beta versus Time for a Rotating Rotor with Initial Rotor Tilt

8.4.1.1 Stationary to Rotational Transformation

There was one more function that was included in the open-loop dynamic model. Due to the non-cylindrical DB rotor, the stationary sensor displacements were transformed into the bearing displacements located underneath the four rotor poles, which are necessary for the magnetic force equations. A rotational sensor will need to be purchased in the future to detect the DB rotor's pole locations, and sensor recommendations are found in [11]. Using the relationship between the rotor's angular velocity and angle ($\omega = \frac{d\theta}{dt}$), the angle of the rotating rotor, which is the angle between the stationary fixed axes and rotating axes, was determined and used in the open-loop model.

The rotor angle (θ_r) is the angular distance between the stationary sensor x- and y-axes (x_{DB_S} and y_{DB_S}) and the rotating DB x- and y- axes (x_{DB_R} and y_{DB_R}). The DB's stationary axes are aligned axially with the SB axes; where the sensors are located. The following transformation converts the DB displacements at the sensor locations to the DB displacements underneath the rotor's poles:

$$\begin{bmatrix} x_{DB_R} \\ y_{DB_R} \end{bmatrix} = \begin{bmatrix} \cos(\theta_r) & \sin(\theta_r) \\ -\sin(\theta_r) & \cos(\theta_r) \end{bmatrix} \begin{bmatrix} x_{DB_S} \\ y_{DB_S} \end{bmatrix} \quad (8.26)$$

The displacements (x_{DB_R} and y_{DB_R}) are multiplied by the DB stiffness, k_1 , to determine DB x and y magnetic forces present between the rotating rotor's poles and stator. The forces between the rotating rotor's poles and stator are then transformed, using the inverse transformation matrix from equation (8.26), to the magnetic forces present between the rotor and stator at the stationary axes. These stationary magnetic bearing forces are the inputs for the rotor's four governing equations of motion. The rotating to stationary transformation is shown in Figure 44.

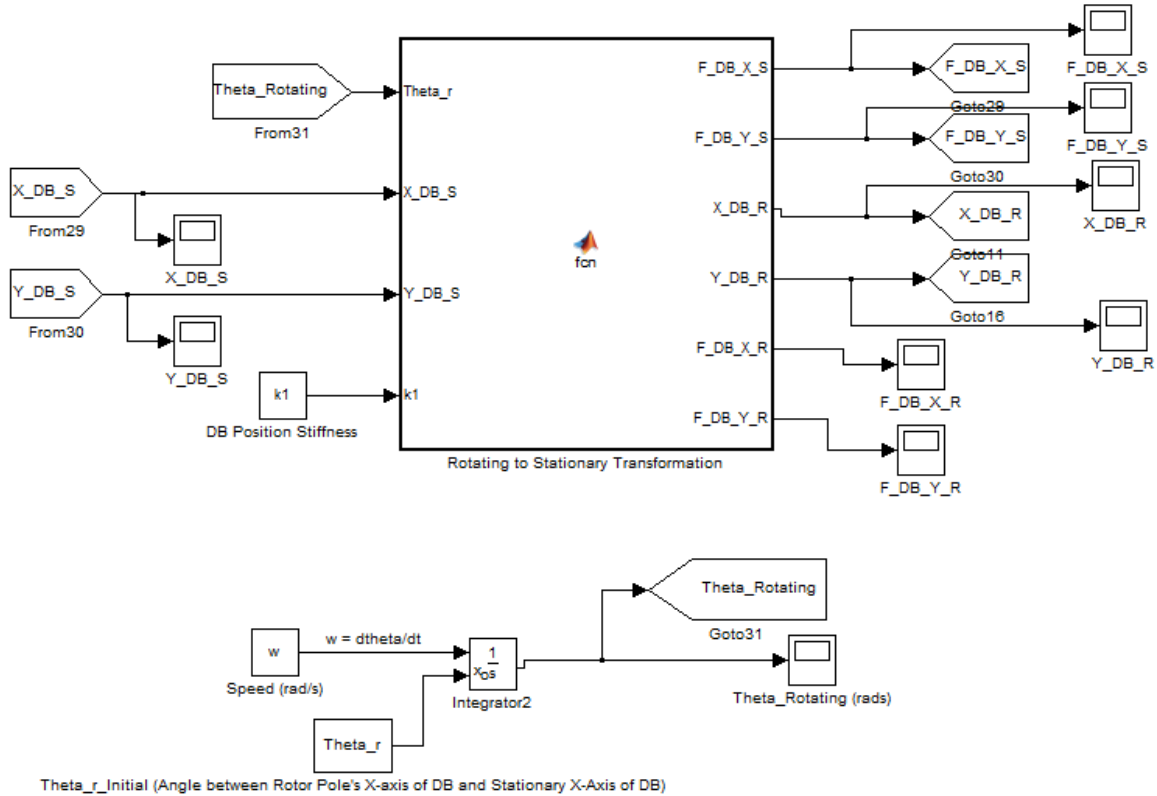


Figure 44: Stationary to Rotational Transformation for the Rotating Rotor Assembly

An additional case was simulated using the constraints from case #3 (where $\omega = 188.5$ rad/s), but the sensor measurements were defined as: $x_1 = x_2 = 1$ mm and $y_1 = y_2 = 1.2$ mm. As done in case #3, both bearings were identically modeled using the SB parameters to make the simulation easier to analyze. The DB displacements (x_{DB_R} and y_{DB_R}) under the rotating rotor's poles were plotted versus the rotational angle for one period, as shown in Figure 45. Since the bearing displacements varied with the rotor's angle, the DB rotating forces were also a function of the rotor's angle.

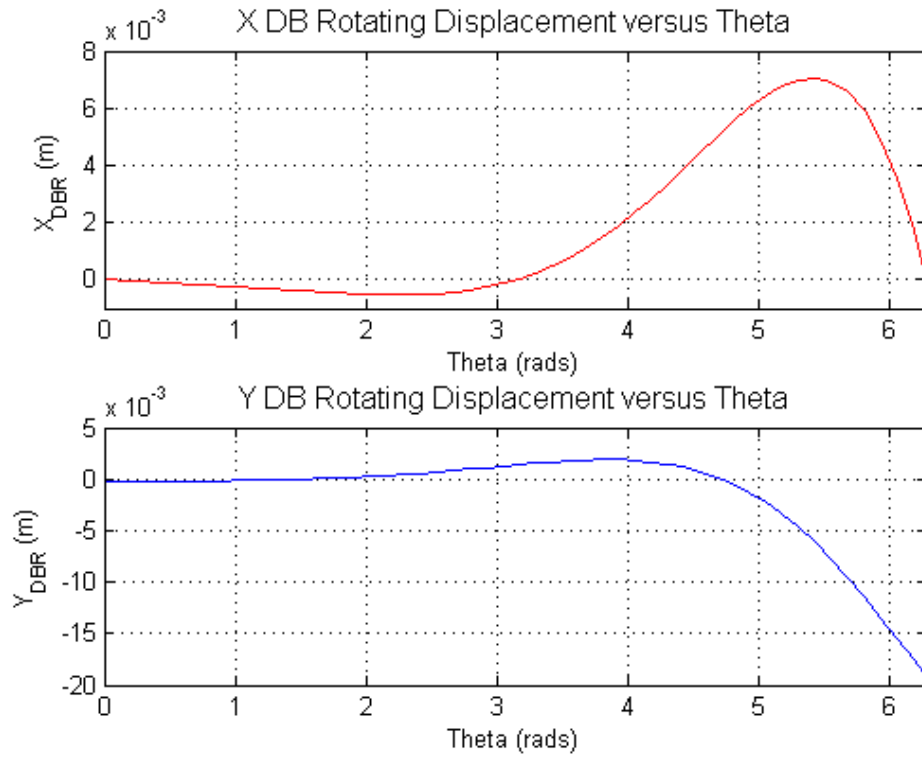


Figure 45: X and Y DB Rotating Displacements versus Theta for a Rotating Rotor

The rotating forces were then transformed into the forces at the stationary axes using the inverse transformation matrix from equation (8.26). Since the DB is symmetric, k_1 was taken out of the matrix multiplication operation, and resulted in the identity matrix. The total stationary y forces for the DB and SB are shown in Figure 46 and are identical. Therefore, the rotational to stationary transformation was not a necessary step for the current version of the dynamic model equations.

While the stationary to rotating transformation was included in Appendix G, this was not included in the closed-loop model. The transformation will be needed in the future when the complete controller model is completed, as discussed in [10]. While the PID controller models were completed, the electrical coil models were not completed and will require these transformations.

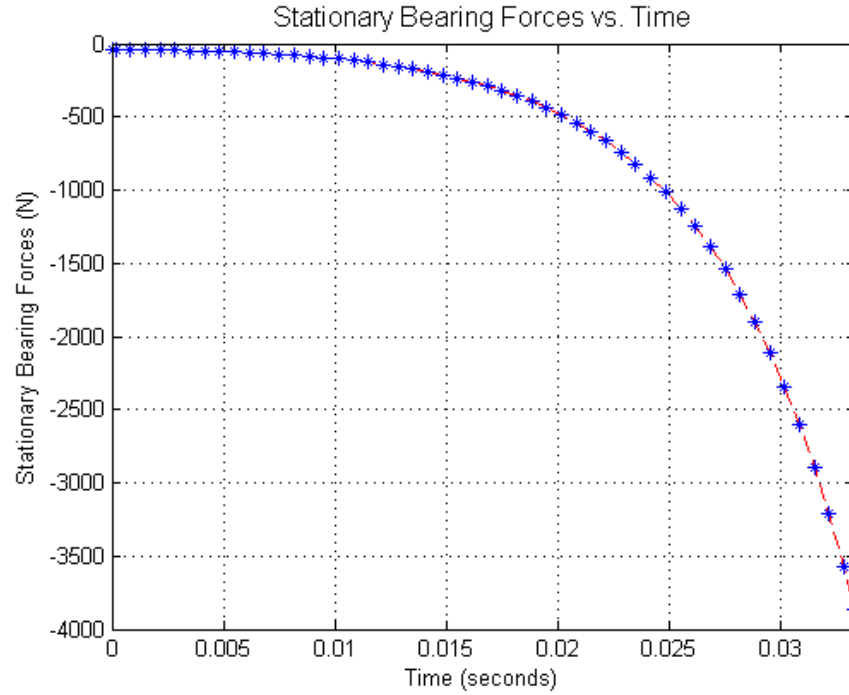


Figure 46: Stationary DB and SB Forces versus Time with Equal Bearing Parameters

8.4.2 Closed-Loop Dynamic Model with Active Control

PID controllers were implemented locally for each bearing and the bearing axes were controlled separately, which is known as decentralized control [7]. While this control scheme is simpler to design, it does not allow for communication between the bearing controllers. Therefore, the angular and translational displacements of the rotor cannot be calculated, since these displacements require the sensor displacements for both bearings. Decentralized control neglects that the sensors and bearings are non-collocated (i.e. their axes differ by an axial distance) [7]. The closed- and open- loop dynamic models in this thesis assume that the sensor measurements can be communicated between the two bearing's controllers. In the future, this assumption will need to be revisited before simultaneous bearing control is implemented.

The bearing controllers use the sensor measurements and determine the necessary command current to control the rotor's position. The PID controller transmits the command to

an amplifier, which transforms the signal into the actual coil currents. The dynamics of the sensors and amplifiers were not included in this thesis. The PID controller actively provides stiffness and damping to compensate for the negative bearing stiffness and maintain system stability [7]. A PID controller contains three feedback terms: a proportional feedback control parameter (P), a differential feedback control parameter (D), and an integrator feedback control parameter (I). These parameters are selected to provide the desired controller stiffness and damping to the closed-loop system.

The closed-loop dynamic model actively controls the position of the rotor with the PID controllers. The small command currents are inputs for the dynamic model equations of motion. The inputs to the PID controllers are the sensor displacements ($x_{1\Delta}$, $x_{2\Delta}$, $y_{1\Delta}$, and $y_{2\Delta}$), and the outputs are the command currents, which provide x and y restoring forces (Δi_{x_SB} , Δi_{y_SB} , Δi_{x_DB} , and Δi_{y_DB}). The PID controllers for the SB and DB are shown in Figure 47.

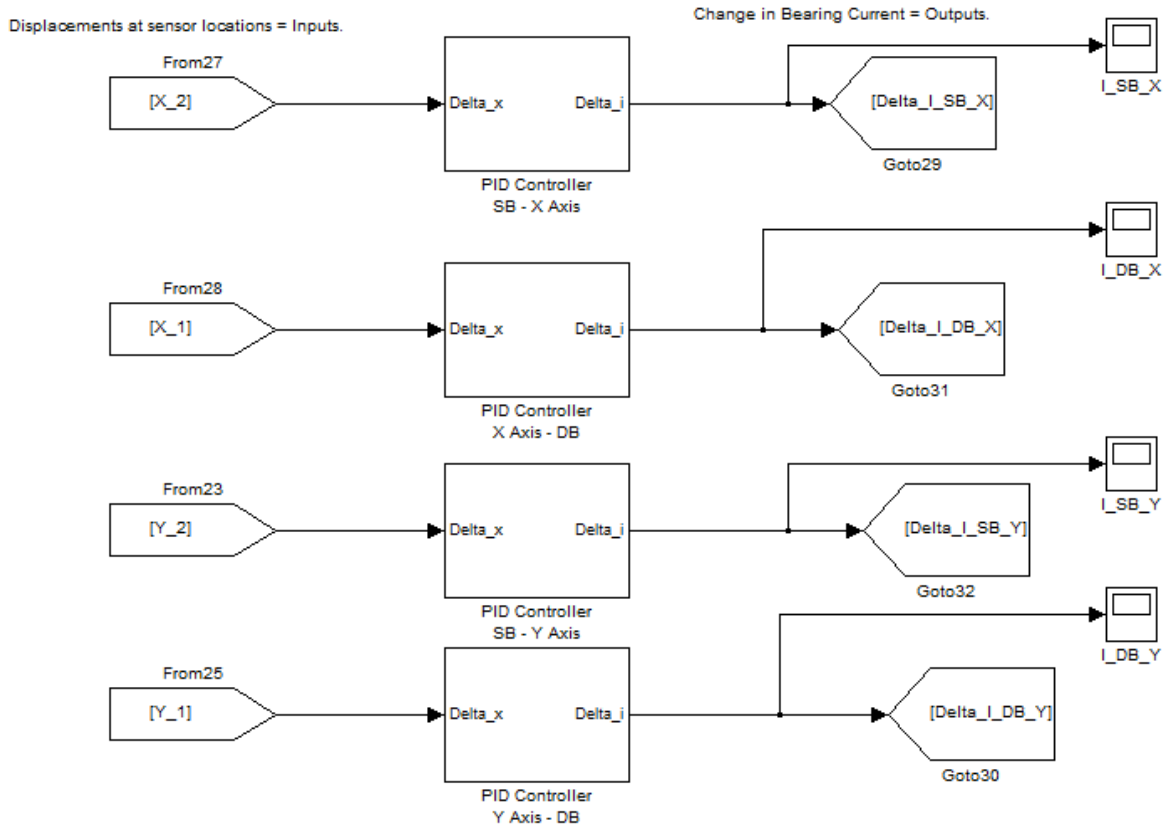


Figure 47: PID Controllers (sensor displacements – inputs and control currents – outputs)

The closed-loop dynamic model is the last model in Appendix G. The closed-loop Simulink® model was simulated for various cases to ensure that the controllers were maintaining the desired rotor's position. For one of these cases, the sensor measurements were defined as: $x_1 = 0.8 \text{ mm}$ and $x_2 = 1.2 \text{ mm}$ and $y_1 = y_2 = 1.1 \text{ mm}$, and were introduced into the model at a time of $t = 9 \text{ ms}$. The model was unconstrained, where the bearings were modeled with different k_i and k_s values and $\omega = 188.5 \text{ rad/s}$. For this case, the PID controllers returned the rotor to its ideal position, where the tilt angles and center of mass displacements were returned to zero, as shown in Figures 48 and 49. The PID controllers used in the closed-loop dynamic model were also used to control the bearings in the actual hardware setup and are included in [10].

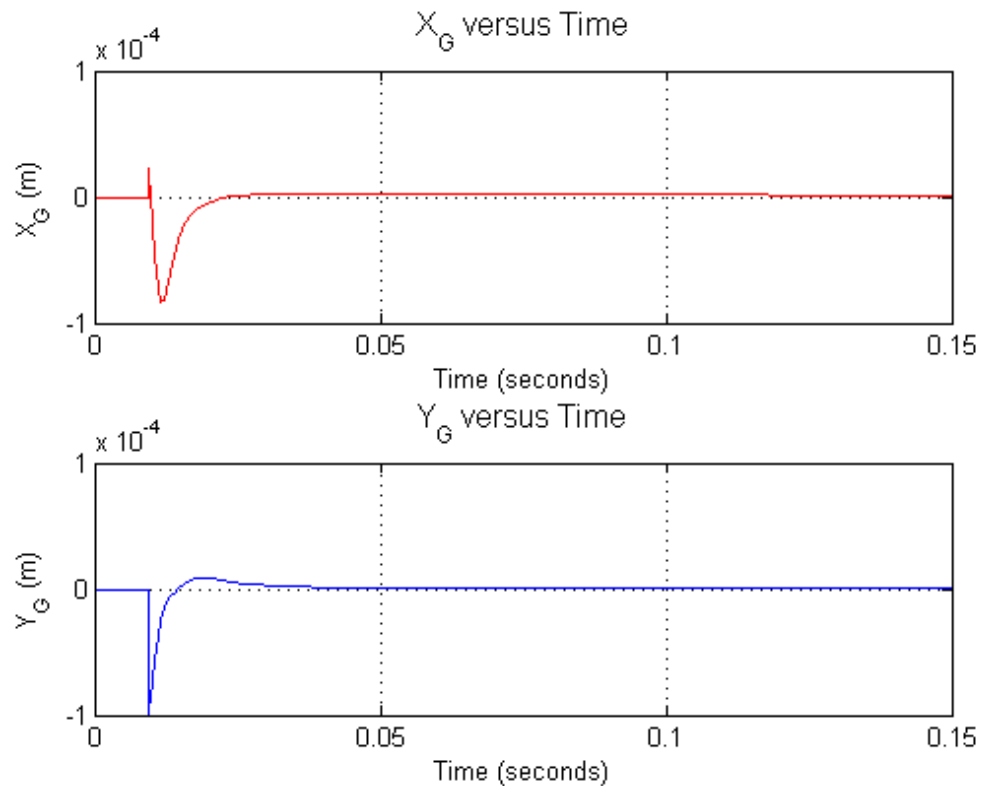


Figure 48: COM Displacements in the Closed-Loop Model for an Unconstrained Case

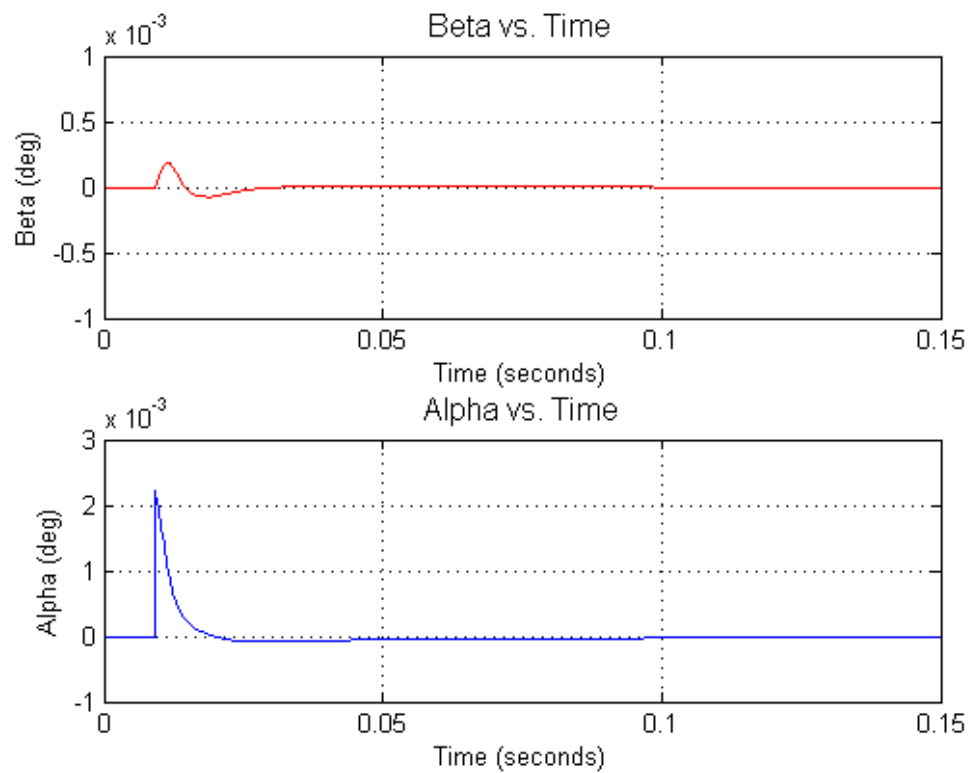


Figure 49: Tilt Angles in the Closed-Loop Model for an Unconstrained Case

Figure 50 includes a flow chart of the radial dynamic model and displays the steps taken in the closed-loop dynamic model. The PID controller steps could be eliminated from the flow chart and this revised flow chart would represent the open-loop dynamic model.

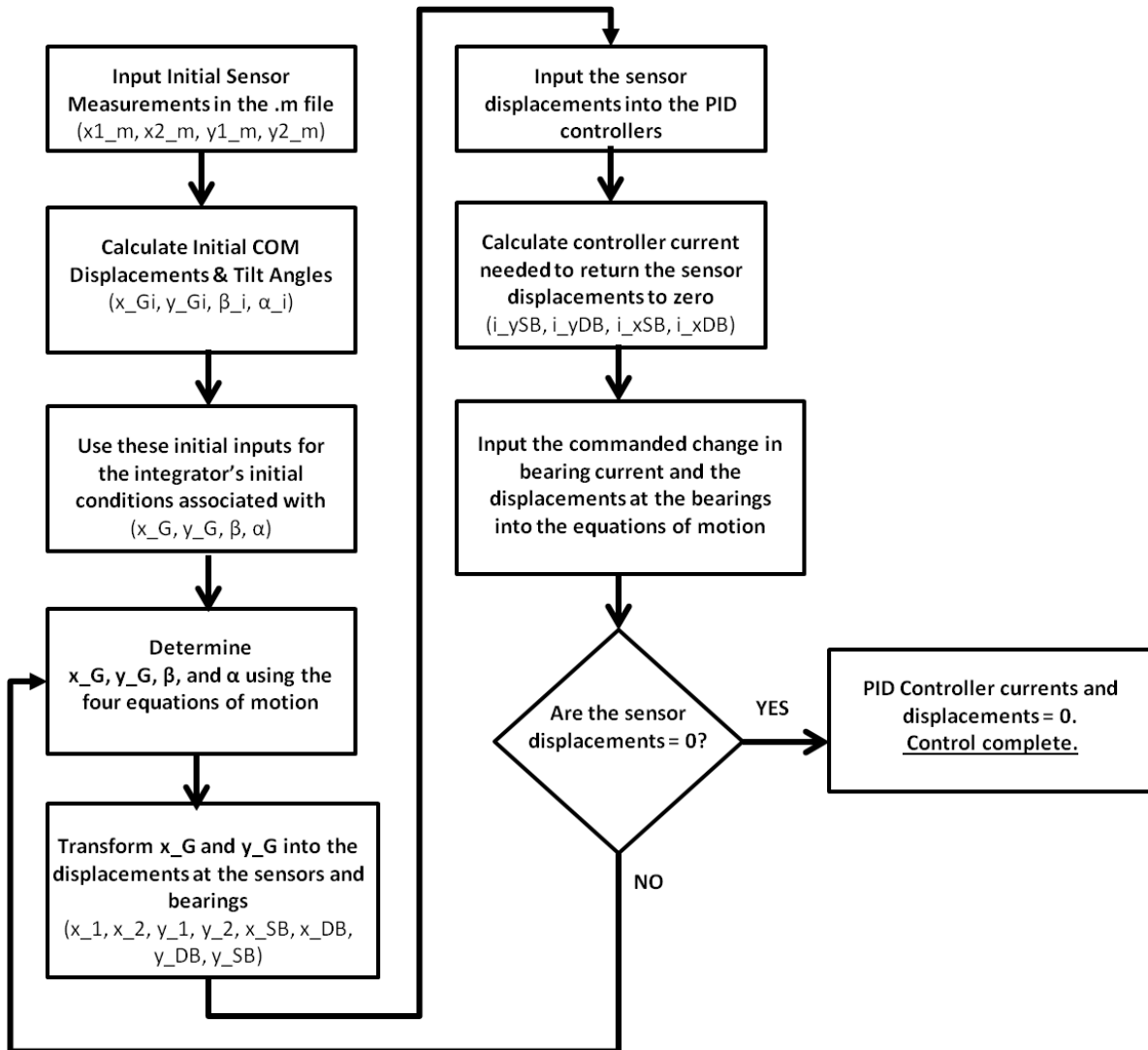


Figure 50: Closed-loop Rotor Dynamic Model Flow Chart for the Simulink Model

8.5 Axial Dynamic Model Components

Since the radial and axial dynamics were decoupled, the previous sections were dedicated to deriving the radial dynamic model. The axial dynamics are simpler and are modeled as though the rotor assembly is a simple point mass. The only axial forces are due to

gravity and levitation, where the total levitation force could be approximated using the average levitation height. The individual HTS are not homogenous and provide different vertical levitation forces. Therefore, the levitation force approximation should be revisited in the future.

Experiments are currently being conducted at the UI to determine the average levitation height, which is needed to model the vertical levitation force. The UI's rotor assembly has been successfully levitated, but future experimentation is required to completely characterize the levitation forces. The following equation was included in the axial dynamic model for a levitation height of 5 mm:

$$F_{ZLev} = 21 * \frac{2026}{101.97} * e^{-\frac{z}{4.7}} \quad (8.27)$$

where F_{ZLev} [N] is the vertical levitation force and z [mm] is the average levitation height. After experimentation is completed, a new levitation height should be incorporated into the axial dynamic model.

Chapter 9. Summary, Conclusions, and Recommendations

9.1 Summary

This thesis presented the derivations and equations for designing the machine component of the FES system. An iterative design process was used to optimize the FRRM design by varying the number of poles, q- versus d- axis coils, and other physical machine dimensions. A given set of operating conditions, such as the desired speed and output power, were used as inputs for the machine design. Using these conditions and additional design constraints, various design options were explored for a static machine model, until the maximum efficiency was achieved. An expression was developed for the power losses to evaluate the impact the number of poles and airgap had on the conduction losses. The final machine design provided the dimensions for the rotor and stator, operating d- and q- axis currents, and the winding layout for the stator coils.

In addition to deriving equations for the FRRM design, a rigid rotor dynamic model was developed and simulated in Matlab's Simulink® environment. The radial equations of motion for the dynamic model were linearized to simplify the model and reduce computation time. There were four primary equations of motion that were linearized to describe the angular and translation motion of the rotor. An open-loop dynamic model was created in Simulink® to predict the rotor's behavior to disturbances. The open-loop dynamic model was then combined with PID controllers to close the loop. A closed-loop dynamic model was also created by combining the open-loop dynamic model with control to actively maintain the rotor's position.

To develop the rotor dynamic model, the electromagnetic bearing force expressions were derived for the SB and DB. These electromagnetic forces were intrinsically nonlinear

due to the squared relationship with the coil current and airgap. The nonlinear bearing forces were approximated with linearized bearing force equations, which required finding the force/current and force/displacement bearing relationships around an equilibrium operating point. For the linearized force expressions to remain valid, the changes in currents and airgap displacements were kept in close proximity to the operating point. The magnetic bearing force expressions were derived using an equivalent MCM approach for the SB and the MWA for the DB, both of which neglected the MMF drops across the iron. These force equations were used in the rotor dynamic model, and this dynamic model serves as a tool for designing the rotational controller algorithm in the future.

9.2 Conclusions

This thesis presented an iterative machine design process used to design and construct the FRRM. In addition, a rotor dynamic model was developed and modeled in Simulink®. Several conclusions were reached in this thesis and are outlined below:

- The final FRRM design parameters were selected to optimize the efficiency of the machine by reducing power losses. It was found that the power losses decreased as the number of poles decreased. While the two pole machine option resulted in the highest efficiency, a four pole option was needed such that the x and y forces could be decoupled for simplifying the controller design. The iterative design process was a successful approach used for determining the final number of poles. Since the FRRM will be used for controlling the rotor's position, the machine was designed to maximize the d-axis magnetic force capabilities. To maximize the output bearing forces, the airgap length was reduced to a minimum length that could be physically machined. Six coils per pole were selected for the final design, since this amount

reduced power losses and allowed adequate space for winding the stator. The MMF drops in iron were found to be negligible in comparison to the MMF airgap terms, and were neglected in the MCM equations.

- A linear instead of a nonlinear model was selected for the rotor dynamic model. The equations of motion were linearized to describe the angular and translational motion of the rotor. Linearization is widely used in industry to simplify rotor dynamic analysis, and was therefore used for the UI's dynamic model [7]. A number of assumptions were necessary for developing a linearized model that correctly described the dynamic behavior of the rotor [20]. Various constrained cases were simulated, and verified that linearization was an appropriate assumption for the UI's rotor dynamic model. For example, both bearings were modeled the same, with equal lever arms, and rotation was enabled. Tilt was introduced into the system and resulted in the angles α and β continually oscillating for the open-loop model. This case showed that the tilting motion is a function of the rotational speed, and that these angles are coupled due to the gyroscopic moment terms as discussed in [7]. In the future, these cases can be used to verify results implemented in hardware.
- The small angle approximation used for the static and dynamic models were determined to be valid assumptions. A maximum rotor tilt angle of 0.152 degrees was calculated for worst case tilt scenario. This angle was small enough that the small angle approximations, such as $\sin(x) = x$, hold. This is an important conclusion since it is an assumption necessary for characterizing Euler's angles, α and β , as inclinations about the rotor's stationary x and y axes.

- The rigid body model of the rotor was developed in Simulink® and simulated with the proposed PID controllers for both bearings. Simulink® was a useful tool for combining various models, such as the rotor dynamic model with the controllers, since these models were all interrelated and designed by different students. The PID controllers successfully returned an assortment of translational and angular displacements to zero for low-speed rotation. The PID controller gains were selected based on the linear force/current and force/displacement relationships derived in this thesis.
- The SB was shown to be controllable using the PID gains, which were determined using the linear bearing force relationships derived in this thesis. Step functions were used to introduce disturbances in the actual hardware setup and the results can be found in the work completed by Kisling in [10]. The PID controllers successfully returned the rotor to the equilibrium position since saturation and rotor and stator collision were avoided. Successfully controlling the rotor's position with a linear control scheme verified that a linear versus nonlinear force model was sufficient, as long as the airgap displacements and command currents were in close proximity to the operating point.
- To develop the linear bearing force relationships, the bearing electromagnetic force expressions were derived as part of this thesis. The MWA and MCM approach were used to model the static bearing forces. These approaches were shown to be valid by comparing the force/current relationships for both bearings with the results from the FEMM program. The maximum error between the two methods was 20% due to iron saturation in the DB's stator teeth. The MWA and MCM approach neglected the

MMF drops in the iron and were valid approaches as long as severe saturation was avoided.

9.3 Recommendations for Future Work

Before moving to a high-speed FES system design, work still needs to be completed on the low-speed FES system proof-of-concept. Due to project time constraints, the majority of the work presented in this thesis is theoretical and needs to be experimentally validated. In addition, the dynamic model for the low-speed FES system could be further improved. The sections below are divided into recommendations for the low- versus high- speed systems.

9.3.1 Low-Speed FES System Proof-of-Concept Recommendations

To complete the rotor dynamic model for low-speeds, the levitation forces need to be experimentally characterized and incorporated into the radial and axial models. Although the rotor assembly has been successfully levitated, there has not been a way to measure the vertical levitation and radial restoring forces. In addition, the radial dynamic model does not include rotor unbalances due to not having the rotor mechanically balanced. In the future, the rotor should be mechanically balanced but, even then, unbalances will still exist and should be modeled as discussed in [16].

Since the rotor assembly was not levitated and rotated with active control, the dynamic model could not be compared to experimental results. Therefore, tests should be conducted in the future to experimentally verify the force/current and force/displacement bearing relationships. Step responses could be used in the hardware setup to introduce disturbances and the system response could be compared with the closed-loop model responses simulated in Simulink®. Recommendations were made in [7] and [16] on how to conduct the force/current and force/displacement experiments.

In addition, the iron MMF drops could be included in the bearing force models for the SB and DB if the bias currents are adjusted. Including the effects of iron saturation will improve the accuracy of the bearing force models. If the iron is saturated, the MWA would not be a valid way to model the DB. If any changes are made to the bearings' operating points, a FEA program should be used to validate the static force models before these are included in the dynamic model.

Since the DB d- and q- axis currents were lowered after the FRRM was already designed and built, the desired operating conditions for the FRRM are no longer valid. These operating conditions, such as the desired output power and speed, were optimized for the initial d- and q- axis currents. These were reduced to prevent saturation for active control, and will lead to de-rating the machine. These new operating conditions were not determined in this thesis, but should be reevaluated and determined before the FRRM is rotated. Since the FRRM serves as a proof-of-concept, de-rating the machine is acceptable and it can still be used to rotate and actively control the rotor's position.

The dynamic model is a tool that should be used to design the speed controller algorithm for the low-speed FES system. As mentioned above, the rotor unbalances should be incorporated in the rigid rotor's equations of motion. The effects of the rotor unbalances can be determined by modeling these unbalances. Rotor unbalances can excite the rotor and lead to a state of resonance. Therefore, these unbalances should be modeled and understood. In addition, the behavior of the rotor at high speeds can be predicted by analyzing the behavior of the eigenvalues as a function of the angular velocity. By doing this analysis, the nutation and precession frequencies can be distinguished, which vary with the speed of the rotor [7]. The current model can be used to predict the critical speeds of the rotor and the system

resonant frequencies, but a more advanced model would be needed to determine the body-harmonic frequencies of the rotor itself. A more advanced model will be important for the high-speed FES system.

9.3.2 High-Speed FES System Recommendations

When the high-speed FES system is designed, a parallel/conical decomposition control methodology will be used. Therefore, the PID controllers will control the rotor's center of mass displacements and tilt angles as discussed in [7] and [16], instead of the sensor coordinates. For the high-speed FES system, the rigid rotor dynamic model could be improved by moving to a flexible rotor model. A flexible rotor model would allow the user to predict the vibrational frequencies of the rotor, since the rigid body model assumes no deformations and does not allow one to predict the vibrational frequencies of the free-free spinning body.

The FRRM will need to be adapted to the lunar environment and adjusted for higher rotational speeds. The future design will not have an integrated machine and flywheel design. The flywheel should be made out of carbon fiber, or a similar material, to increase the potential energy stored. The selected machine should have a high efficiency and the ability to be degaussed. A FEA program should be used to verify the static machine design before it is constructed to avoid any design errors. If the FRRM is selected for the machine, the machine design calculations in Chapter 5 can be used to some extent to design the machine, but with caution, since the assumptions made may not be valid.

References

- [1] F. A. Bhuiyan and A. Yazdani, “Energy storage technologies for grid-connected and off-grid power system applications,” in *2012 IEEE Electrical Power and Energy Conference (EPEC)*, 2012, pp. 303–310.
- [2] M. Strasik, P. E. Johnson, A. C. Day, J. Mittleider, M. D. Higgins, J. Edwards, J. R. Schindler, K. E. McCrary, C. R. McIver, D. Carlson, J. F. Gonder, and J. R. Hull, “Design, Fabrication, and Test of a 5-kWh/100-kW Flywheel Energy Storage Utilizing a High-Temperature Superconducting Bearing,” *IEEE Trans. Appl. Supercond.*, vol. 17, no. 2, pp. 2133–2137, Jun. 2007.
- [3] J. G. Bitterly, “Flywheel technology past, present, and 21st Century projections,” in *Energy Conversion Engineering Conference, 1997. IECEC-97., Proceedings of the 32nd Intersociety*, 1997, vol. 4, pp. 2312–2315 vol.4.
- [4] H. B. Björn Bolund, “Flywheel energy and power storage systems,” *Renew. Sustain. Energy Rev.*, no. 2, pp. 235–258, 2007.
- [5] G. Roe, “Boeing Flywheel Energy Storage Technology.” 2012.
- [6] S. J. Chapman, *Electric machinery fundamentals*. New York, NY: McGraw-Hill Higher Education, 2005.
- [7] G. Schweitzer, H. Bleuler, E. H. Maslen, M. Cole, P. Keogh, R. Larsonneur, E. Maslen, R. Nordmann, Y. Okada, G. Schweitzer, and A. Traxler, *Magnetic Bearings: Theory, Design, and Application to Rotating Machinery*. Springer, 2009.
- [8] R. Yang, *Time-resolved Magnetic Flux and AC-current Distributions in Superconducting Yttrium Barium Copper Oxide Thin Films and Multifilaments*. ProQuest, 2008.
- [9] A. C. Day, J. R. Hull, M. Strasik, P. E. Johnson, K. E. McCrary, J. Edwards, J. A. Mittleider, J. R. Schindler, R. A. Hawkins, and M. L. Yoder, “Temperature and frequency effects in a high-performance superconducting bearing,” *IEEE Trans. Appl. Supercond.*, vol. 13, no. 2, pp. 2179–2184, Jun. 2003.
- [10] B. Kisling, “Active Magnetic Bearing Control for an Experimental Flywheel Energy Storage System,” University of Idaho, 2014.
- [11] K. Ramus, “Power Electronic Components and Hardware for an Experimental Flywheel Energy Storage System,” University of Idaho, 2014.

- [12] I. M. Higginson, *Force Density and Radial Stiffness Development for Low Idle Loss Machine Topologies*. University of Idaho, May 14, 2011.
- [13] J. D. Law, *Modeling of Field Regulated Reluctance Machines*. University of Wisconsin--Madison, 1991.
- [14] J. D. Law, A. Chertok, and T. A. Lipo, “Design and performance of field regulated reluctance machine,” *IEEE Trans. Ind. Appl.*, vol. 30, no. 5, pp. 1185–1192, 1994.
- [15] J. D. Law, T. J. Busch, and T. A. Lipo, “Magnetic circuit modelling of the field regulated reluctance machine. Part I: model development,” *IEEE Trans. Energy Convers.*, vol. 11, no. 1, pp. 49–55, Mar. 1996.
- [16] P. E. Kascak, “Fully Levitated Rotor Magnetically Suspended by Two Pole-Pair Separated Conical Motors,” Case Western Reserve University, 2010.
- [17] T. A. Lipo, *Analysis of synchronous machines*. Boca Raton, FL: CRC Press, 2012.
- [18] N. A. Al-Nuaim and H. A. Toliat, “A novel method for modeling dynamic air-gap eccentricity in synchronous machines based on modified winding function theory,” *IEEE Trans. Energy Convers.*, vol. 13, no. 2, pp. 156–162, 1998.
- [19] J. F. Gieras, *Advancements in electric machines*. [New York]: Springer, 2008.
- [20] G. Genta, *Dynamics of Rotating Systems*. Springer, 2007.
- [21] “List of moments of inertia,” *Wikipedia, the free encyclopedia*. 09-Mar-2014.
- [22] H. Akbari, H. Meshgin-Kelk, and J. Milimonfared, “Extension of winding function theory for radial and axial nonuniform air gap in salient pole synchronous machines,” *Prog. Electromagn. Res.*, vol. 114, pp. 407–428, 2011.
- [23] D. Meeker, *Finite Element Method Magnetics*. 2011.
- [24] J. M. Vance, F. Y. Zeidan, and B. Murphy, *Machinery Vibration and Rotordynamics*, 1 edition. Wiley, 2010.
- [25] J. M. Vance, *Rotordynamics of turbomachinery*. New York: Wiley, 1988.
- [26] K. R. Symon, *Mechanics*. Reading, Mass.: Addison-Wesley Pub. Co., 1971.

Appendix A: Field Regulated Reluctance Machine Design Calculations

Last Date Modified: January 23, 2012. **Title:** Field Regulated Reluctance Machine Design Calculations.
Authors: Juliet Petersen and Bridget Wimer. **Page Count:** 13

I. Define the Situation

Field Regulated Reluctance Machine, FRRM

Determine number of poles to optimize efficiency NP := 2, 4.. 10

A. Desired Flux Densities

B_{d_Airgap} := 0.33·T *Direct axis airgap flux density*

B_{d_Chevron} := 0.66T *Direct axis chevron flux density*

B_{d_Tooth} := 1.00T *Direct axis stator tooth flux density*

B. Geometry

Poles := 4 *Number of magnetic pole*

Airgap := 1·mm *Airgap distance between the stator and rotor* Airgap = 0.039·in

D_Inner_Rotor := 13.5·cm *Inner Diameter of the rotor* D_Inner_Rotor = 5.315·in

Stacking_Factor := 0.96 *Fraction of the length of iron length to the actual length of the machine*

C. Windings

Fill_Factor := 0.40 *Fraction of the cross-sectional area of copper to the slot area*

m_{total} := 6 *Number of coils per pole*

m_q := 2 *Number of q-axis/armature coils per pole*

m_d := m_{total} - m_q *Number of d-axis/field coils per pole*

II. Desired Operating Conditions

Force_Density := 1.5· $\frac{\text{kN}}{\text{m}^2}$ *Circumferential force per airgap area*

Power := 400 W *Power converted from electrical to mechanical operating as a motor*

Voltage := 12·V *Quadrature axis voltage per coil*

ω_m := 188.5· $\frac{\text{rad}}{\text{sec}}$ *Rotor angular frequency*

III. Solution

A. Frequency Calculations

Speed := ω_m

Speed = 1800.0·rpm

$\omega_e(\text{Poles}) := \omega_m \cdot \frac{\text{Poles}}{2}$

$\omega_e(\text{Poles}) = 377 \cdot \frac{\text{rad}}{\text{sec}}$

$$f_e(\text{Poles}) := \frac{\omega_e(\text{Poles})}{2\pi}$$

$$f_e(\text{Poles}) = 60.001 \cdot \text{Hz}$$

B. Geometry Calculations

1) Determining Diameters and Radii

$$D_{\text{Outer_Stator}} := D_{\text{Inner_Rotor}} - 2 \cdot \text{Airgap}$$

$$D_{\text{Outer_Stator}} = 5.236 \cdot \text{in}$$

$$R_{\text{Inner_Rotor}} := \frac{D_{\text{Inner_Rotor}}}{2}$$

$$R_{\text{Inner_Rotor}} = 2.657 \cdot \text{in}$$

$$R_{\text{Outer_Stator}} := \frac{D_{\text{Outer_Stator}}}{2}$$

$$R_{\text{Outer_Stator}} = 2.618 \cdot \text{in}$$

2) Determining Lengths, Arcs, and Pitches:

Note: Arcs are defined as angles, and pitches are defined as lengths

$$\text{Effective_Length} := \frac{\text{Power}\cdot\text{Stacking}\cdot\text{Factor}}{(2\cdot\pi\cdot R_{\text{Outer_Stator}}^2\cdot\omega_m\cdot\text{Force}\cdot\text{Density})}$$

$$\text{Effective_Length} = 1.924 \cdot \text{in}$$

Convert length from Effective to Real:

$$\text{Length} := \frac{\text{Effective_Length}}{\text{Stacking_Factor}}$$

$$\text{Length} = 2.004 \cdot \text{in}$$

$$\text{Pole_Arc}(\text{Poles}) := \frac{2\cdot\pi}{\text{Poles}}$$

$$\text{Pole_Arc}(\text{Poles}) = 90 \cdot \text{deg}$$

$$\text{Pole_Pitch}(\text{Poles}) := \text{Pole_Arc}(\text{Poles}) \cdot R_{\text{Outer_Stator}}$$

$$\text{Pole_Pitch}(\text{Poles}) = 4.113 \cdot \text{in}$$

$$\text{Aspect_Ratio}(\text{Poles}) := \frac{\text{Effective_Length}}{\text{Pole_Pitch}(\text{Poles})}$$

$$\text{Aspect_Ratio}(\text{Poles}) = 0.468$$

3) Determining Pitch, Widths and Depths of Slots, Teeth, and Slot Openings

- a. Slot: The slot pitch is the distance from the edge of one tooth to the edge of the next, it includes one tooth and one opening.

$$\text{Slot_Pitch(Poles)} := \frac{2 \cdot \pi \cdot R_{\text{Outer_Stator}}}{\text{Poles} \cdot m_{\text{total}}} \quad \text{Slot_Pitch(Poles)} = 0.685 \cdot \text{in}$$

$$\text{Slot_Arc(Poles)} := \frac{2 \cdot \pi}{(\text{Poles} \cdot m_{\text{total}})} \quad \text{Slot_Arc(Poles)} = 15 \cdot \text{deg}$$

$$\text{Slot_Cord(Poles)} := 2 \cdot R_{\text{Outer_Stator}} \cdot \sin\left(\frac{\text{Slot_Arc(Poles)}}{2}\right) \quad \text{Slot_Cord(Poles)} = 0.683 \cdot \text{in}$$

b. Tooth: Set tooth width to a portion of the slot width... optimize for maximum efficiency

$$\text{Tooth_Width(Poles)} := \frac{m_q}{m_{\text{total}}} \cdot \frac{\text{Pole_Pitch(Poles)} \cdot B_d_{\text{Airgap}}}{2 \cdot B_d_{\text{Tooth}}} \quad \text{Tooth_Width(Poles)} = 0.226 \cdot \text{in}$$

c. Slot Opening: The slot opening is the area between the stator teeth.

$$\text{Slot_Opening_Width_Top(Poles)} := \text{Slot_Cord(Poles)} - \text{Tooth_Width(Poles)}$$

$$\text{Slot_Opening_Width_Top(Poles)} = 0.457 \cdot \text{in}$$

$$\text{Slot_Depth} := \frac{D_{\text{Outer_Stator}}}{2} - 1.35 \text{in} \quad \text{Slot_Depth} = 1.268 \cdot \text{in}$$

4) Determining Slot Area

$$\text{Slot_Cord_Bottom(Poles)} := 2 \cdot (R_{\text{Outer_Stator}} - \text{Slot_Depth}) \cdot \sin\left(\frac{\text{Slot_Arc(Poles)}}{2}\right)$$

$$\text{Slot_Cord_Bottom(Poles)} = 0.352 \cdot \text{in}$$

$$\text{Slot_Opening_Bottom(Poles)} := \text{Slot_Cord_Bottom(Poles)} - \text{Tooth_Width(Poles)}$$

$$\text{Slot_Opening_Bottom(Poles)} = 0.126 \cdot \text{in}$$

$$\text{Slot_Opening_Area(Poles)} := \text{Slot_Depth} \cdot \frac{\left(\begin{array}{l} \text{Slot_Opening_Width_Top(Poles)} \\ + \text{Slot_Opening_Bottom(Poles)} \end{array} \right)}{2}$$

$$\text{Slot_Opening_Area(Poles)} = 0.37 \cdot \text{in}^2$$

5) Determining Chevron Parameters:

Pole arc and pole pitch in the direct axis is defined as the area under the direct axis of the machine or magnetic pole. The fraction of the arc and pitch under the magnetic pole of the machine is equal to the ratio of quadrature axis coils to the total number of coils. This is due to the fact that the flux induced in the direct axis of the machine is due to the coils in the inner pole region, the direct axis coils. The coils under the pole of the machine or in the outer pole region, are the quadrature axis coils. The physical placement of the direct axis coils are off 90 degrees electrical from the direct axis magnetic pole. The same is true for the quadrature axis.

Rotor Chevron Arcs

$$\text{Pole_Arc}_d(\text{Poles}) := \frac{m_q}{m_{\text{total}}} \cdot \text{Pole_Arc}(\text{Poles}) \quad \text{Pole_Arc}_d(\text{Poles}) = 30 \cdot \text{deg}$$

$$\text{Pole_Arc}_q(\text{Poles}) := \frac{m_d}{m_{\text{total}}} \cdot \text{Pole_Arc}(\text{Poles}) \quad \text{Pole_Arc}_q(\text{Poles}) = 60 \cdot \text{deg}$$

$$\text{Pole_Pitch}_d(\text{Poles}) := \frac{m_q}{m_{\text{total}}} \cdot \text{Pole_Pitch}(\text{Poles}) \quad \text{Pole_Pitch}_d(\text{Poles}) = 1.371 \cdot \text{in}$$

$$\text{Pole_Pitch}_q(\text{Poles}) := \frac{m_d}{m_{\text{total}}} \cdot \text{Pole_Pitch}(\text{Poles}) \quad \text{Pole_Pitch}_q(\text{Poles}) = 2.742 \cdot \text{in}$$

$$\text{Chevron_Width}(\text{Poles}) := \frac{\text{Pole_Pitch}_d(\text{Poles})}{2} \quad \text{Chevron_Width}(\text{Poles}) = 0.685 \cdot \text{in}$$

$$\text{Area_Pole}_d(\text{Poles}) := \text{Pole_Pitch}_d(\text{Poles}) \cdot \text{Effective_Length} \quad \text{Area_Pole}_d(\text{Poles}) = 2.638 \cdot \text{in}^2$$

Calculate the cross-sectional areas of the q axis flux paths:

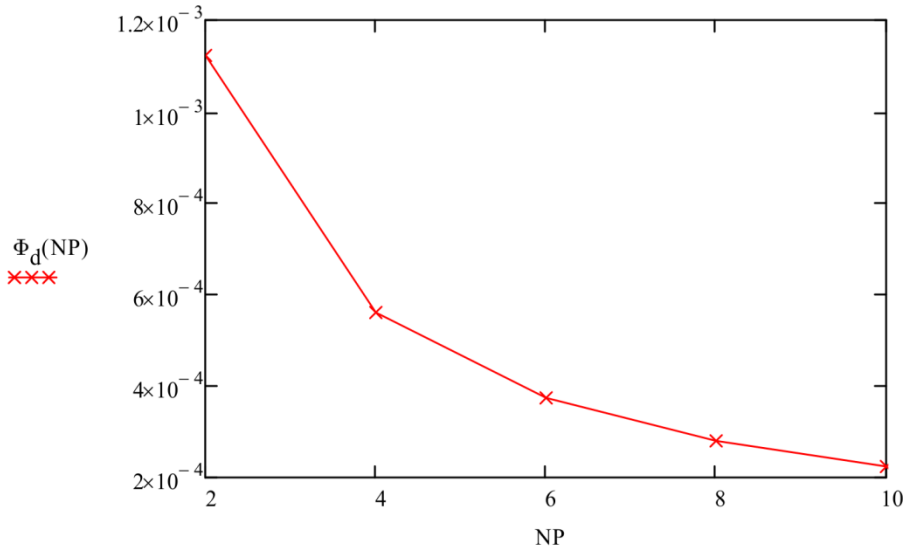
$$\text{Area_Pole}_q(\text{Poles}) := \frac{\text{Area_Pole}_d(\text{Poles})}{4} \quad \text{Area_Pole}_q(\text{Poles}) = 0.659 \cdot \text{in}^2$$

C. Determine Quadrature Axis Current:

$$I_q(\text{Poles}) := \frac{\text{Power}}{\text{Voltage} \cdot m_q \cdot \text{Poles}} \quad I_q(\text{Poles}) = 4.167 \text{ A} \quad \text{mWb} := 10^{-3} \cdot \text{Wb}$$

D. Determining Direct Axis Flux:

$$\Phi_d(\text{Poles}) := \text{Area_Pole}_d(\text{Poles}) \cdot B_{d_Airgap} \quad \Phi_d(\text{Poles}) = 0.562 \cdot \text{mWb}$$



E. Determining MMFs:

$$\text{Permeability Free Space: } \mu_0 = 1.257 \times 10^{-6} \cdot \frac{\text{H}}{\text{m}}$$

1) Determining MMF due to Air gap:

$$B_{d\text{-Airgap}} = 0.33 \text{ T}$$

$$H_{\text{Airgap}_d} := \frac{B_{d\text{-Airgap}}}{\mu_0} \quad H_{\text{Airgap}_d} = 262.606 \cdot \frac{\text{kA}}{\text{m}}$$

$$b_0(\text{Poles}) := \text{Slot_Opening_Width_Top}(\text{Poles})$$

$$\text{DEN_term}(\text{Poles}) := b_0(\text{Poles}) \cdot \text{atan}\left(\frac{b_0(\text{Poles})}{2 \cdot \text{Airgap}}\right) - \text{Airgap} \cdot \ln\left[1 + \left(\frac{b_0(\text{Poles})}{2 \cdot \text{Airgap}}\right)^2\right]$$

$$\text{Carter_Factor}(\text{Poles}) := \frac{\text{Slot_Pitch}(\text{Poles})}{\left[\text{Slot_Pitch}(\text{Poles}) - \left(\frac{2}{\pi}\right) \cdot \text{DEN_term}(\text{Poles})\right]} \quad \text{Carter_Factor}(\text{Poles}) = 1.869$$

$$\text{MMF}_{\text{Airgap_d}}(\text{Poles}) := \text{Carter_Factor}(\text{Poles}) \cdot 2 \cdot \text{Airgap} \cdot H_{\text{Airgap}_d} \quad \text{MMF}_{\text{Airgap_d}}(\text{Poles}) = 0.982 \cdot \text{kA}$$

2) Determining Total MMF in the direct axis:

Note: The MMF drops across the iron (stator back iron, stator teeth, and rotor chevrons) is negligible compared to the airgap because we are not saturating the iron and have a relatively large airgap.

$$\text{MMF}_{\text{Total_d}}(\text{Poles}) := \text{MMF}_{\text{Airgap_d}}(\text{Poles})$$

$$\text{MMF}_{\text{Total_d}}(\text{Poles}) = 0.982 \cdot \text{kA}$$

F. Calculate number of turns and quadrature axis flux:

1) Calculate the quadrature axis flux

*Write Voltage and MMF equations in terms of number of turns

*Set equations equal to each other and solve using a given-find block

$$V = \frac{N \cdot (\Phi_d + \Phi_q) \cdot \omega_m \cdot \text{Poles}}{\frac{m_q}{(m_q + m_d)} \cdot \pi \cdot 2}$$

$$\text{MMF} = \frac{m_q \cdot N_f \cdot I_q}{2} = \sum_k (H_k \cdot L_k)$$

$$B_{q\text{-Airgap}} = \frac{\Phi_q}{A_{\text{Airgap_q}}}$$

$$H_{q\text{-Airgap}} = \frac{B_{q\text{-Airgap}}}{\mu_0}$$

$$\text{Initial Guess for the q axis flux: } \mu\text{Wb} := 10^{-6} \cdot \text{Wb} \quad \Phi_{q\text{-guess}} := 60 \mu\text{Wb}$$

Given

$$\begin{aligned} & \frac{\text{Voltage} \cdot \left[\frac{m_q}{(m_q + m_d)} \cdot 2 \cdot \pi \right]}{\left[(\Phi_d(\text{Poles}) + \Phi_{q\text{-guess}}) \cdot \omega_m \cdot \text{Poles} \right]} \dots \\ & + \frac{-2}{I_q(\text{Poles}) \cdot m_q} \cdot \left(\frac{\Phi_{q\text{-guess}}}{\text{Area_Pole}_q(\text{Poles}) \cdot \mu_0} \cdot 2 \cdot \text{Carter_Factor}(\text{Poles}) \cdot \text{Airgap} \right) = 0 \end{aligned}$$

$$\Phi_q(\text{Poles}) := \text{Find}(\Phi_{q\text{-guess}}) \quad \Phi_q(\text{Poles}) = 33.384 \mu\text{Wb}$$

2) Calculate the number of turns:

$$N_t(\text{Poles}) := \frac{\text{Voltage} \cdot \left[\frac{m_q}{(m_q + m_d)} \cdot 2 \cdot \pi \right]}{\left[(\Phi_d(\text{Poles}) + \Phi_q(\text{Poles})) \cdot \omega_m \cdot \text{Poles} \right]}$$

$N_t(\text{Poles}) = 56.021$

3) Determining Field Current:

$$I_d(\text{Poles}) := \frac{\text{MMF}_{\text{Total_d}}(\text{Poles})}{\left[N_t(\text{Poles}) \cdot (m_d) \right]}$$

$I_d(\text{Poles}) = 4.381 \cdot A$

4) Calculate Q-Axis MMF's

$$B_{q\text{-Airgap}}(\text{Poles}) := \frac{\Phi_q(\text{Poles})}{\text{Area_Pole}_q(\text{Poles})}$$

$B_{q\text{-Airgap}}(\text{Poles}) = 0.078 T$

$$H_{q\text{-Airgap}}(\text{Poles}) := \frac{B_{q\text{-Airgap}}(\text{Poles})}{\mu_0}$$

$H_{q\text{-Airgap}}(\text{Poles}) = 62.44 \cdot \frac{kA}{m}$

$$\text{MMF}_{\text{Airgap_q}}(\text{Poles}) := H_{q\text{-Airgap}}(\text{Poles}) \cdot 2 \cdot \text{Carter_Factor}(\text{Poles}) \cdot \text{Airgap}$$

$\text{MMF}_{\text{Airgap_q}}(\text{Poles}) = 233.421 A$

$$\text{MMF}_{\text{Total_q}}(\text{Poles}) := \text{MMF}_{\text{Airgap_q}}(\text{Poles})$$

$\text{MMF}_{\text{Total_q}}(\text{Poles}) = 233.421 A$

G. Copper Losses

$$\text{Calculate Fill Factor } \rho := 2.1 \cdot 10^{-8} \cdot \Omega \cdot m$$

Actual Fill Factor based on selected AWG parameters and # of turns.

$$\text{Area_wire} := 2 N_t(\text{Poles}) (.0403 \text{in})^2 \cdot \frac{\pi}{4} = 0.143 \cdot \text{in}^2$$

$\text{Fill Factor} := \frac{\text{Area_wire}}{\text{Slot_Opening_Area}(\text{Poles})} = 0.386$

1) Calculation of Current Densities:

$$S_{\text{Current_q}}(\text{Poles}) := \frac{m_q}{m_{\text{total}}} \cdot I_q(\text{Poles})^2$$

$S_{\text{Current_q}}(\text{Poles}) = 5.787 A^2$

$$S_{\text{Current_d}}(\text{Poles}) := \frac{m_d}{m_{\text{total}}} \cdot I_d(\text{Poles})^2$$

$S_{\text{Current_d}}(\text{Poles}) = 12.795 A^2$

$$S_{\text{Current}}(\text{Poles}) := S_{\text{Current_q}}(\text{Poles}) + S_{\text{Current_d}}(\text{Poles})$$

$S_{\text{Current}}(\text{Poles}) = 18.582 A^2$

$$\text{RMS_Current(Poles)} := \sqrt{\text{S_Current(Poles)}}$$

$$\text{RMS_Current(Poles)} = 4.311 \text{ A}$$

$$\text{MA} := 10^6 \cdot \text{A}$$

$$\text{Current_Density(Poles)} := \frac{\text{N}_t(\text{Poles}) \cdot \text{RMS_Current(Poles)}}{\text{Fill_Factor} \cdot \text{Slot_Opening_Area(Poles)}}$$

$$\text{Current_Density(Poles)} = 2.619 \cdot \frac{\text{MA}}{\text{m}^2}$$

$$\text{Surface_Current_Density(Poles)} := \frac{\text{N}_t(\text{Poles}) \cdot \text{Poles} \cdot \text{m}_{\text{total}} \cdot \text{RMS_Current(Poles)}}{(\pi \cdot \text{D_Outer_Stator})}$$

$$\text{Surface_Current_Density(Poles)} = 13.871 \cdot \frac{\text{kA}}{\text{m}}$$

2) Calculation of Power Losses:

$$\text{Length_Wire_Slot} := 2 \cdot \text{Length}$$

$$\text{Length_Wire_Slot} = 4.009 \cdot \text{in}$$

$$\text{Length_Wire_End(Poles)} := 2 \cdot \left(\frac{\pi}{2} \cdot \text{Pole_Pitch(Poles)} + 0.025 \cdot \text{m} \right)$$

$$\text{Length_Wire_End(Poles)} = 14.888 \cdot \text{in}$$

The 0.025 m is because we would cut the insulation on the wire if we bent it right at the end of the machine. Not a function of the length of the machine.

$$\text{Resistance_Slot(Poles)} := \frac{\text{N}_t(\text{Poles})^2 \cdot \rho \cdot \text{Length_Wire_Slot}}{\text{Slot_Opening_Area(Poles)} \cdot \text{Fill_Factor}}$$

$$\text{Resistance_Slot(Poles)} = 0.073 \cdot \Omega$$

$$\text{Resistance_End(Poles)} := \frac{\text{N}_t(\text{Poles})^2 \cdot \rho \cdot \text{Length_Wire_End(Poles)}}{\text{Slot_Opening_Area(Poles)} \cdot \text{Fill_Factor}}$$

$$\text{Resistance_End(Poles)} = 0.27 \cdot \Omega$$

$$\text{Resistance_Total(Poles)} := \text{Resistance_Slot(Poles)} + \text{Resistance_End(Poles)}$$

$$\text{Resistance_Total(Poles)} \cdot \text{S_Current(Poles)} \cdot \frac{\text{Poles}}{2} = 12.751 \text{ W}$$

$$\text{Resistance_Total(Poles)} = 0.343 \Omega$$

End Winding Power Losses

$$\text{Power_Loss_End_d(Poles)} := \text{m}_{\text{total}} \cdot \text{Poles} \cdot \text{Resistance_End(Poles)} \cdot \text{S_Current_d(Poles)}$$

$$\text{Power_Loss_End_d(Poles)} = 83.007 \text{ W}$$

$$\text{Power_Loss_End_q(Poles)} := \text{m}_{\text{total}} \cdot \text{Poles} \cdot \text{Resistance_End(Poles)} \cdot \text{S_Current_q(Poles)}$$

$$\text{Power_Loss_End_q(Poles)} = 37.542 \text{ W}$$

$$\text{Power_Loss_End(Poles)} := \text{m}_{\text{total}} \cdot \text{Poles} \cdot \text{S_Current(Poles)} \cdot \text{Resistance_End(Poles)}$$

$$\text{Power_Loss_End(Poles)} = 120.549 \text{ W}$$

Slot Winding Power Losses

$$\text{Power_Loss_Slot_d(Poles)} := m_{\text{total}} \cdot \text{Poles} \cdot \text{Resistance_Slot(Poles)} \cdot S_{\text{Current_d(Poles)}}$$

$$\text{Power_Loss_Slot_d(Poles)} = 22.351 \text{ W}$$

$$\text{Power_Loss_Slot_q(Poles)} := m_{\text{total}} \cdot \text{Poles} \cdot \text{Resistance_Slot(Poles)} \cdot S_{\text{Current_q(Poles)}}$$

$$\text{Power_Loss_Slot_q(Poles)} = 10.109 \text{ W}$$

$$\text{Power_Loss_Slot(Poles)} := m_{\text{total}} \cdot \text{Poles} \cdot S_{\text{Current(Poles)}} \cdot \text{Resistance_Slot(Poles)}$$

$$\text{Power_Loss_Slot(Poles)} = 32.46 \text{ W}$$

Direct and Quadrature Axis Losses

$$\text{Power_Loss_d(Poles)} := m_{\text{total}} \cdot \text{Resistance_Total(Poles)} \cdot S_{\text{Current_d(Poles)}} \cdot \text{Poles}$$

$$\text{Power_Loss_d(Poles)} = 105.358 \text{ W}$$

$$\text{Power_Loss_q(Poles)} := m_{\text{total}} \cdot \text{Resistance_Total(Poles)} \cdot S_{\text{Current_q(Poles)}} \cdot \text{Poles}$$

$$\text{Power_Loss_q(Poles)} = 47.651 \text{ W}$$

Total Losses

$$\text{Power_Loss_Total(Poles)} := \text{Power_Loss_d(Poles)} + \text{Power_Loss_q(Poles)}$$

$$\text{Power_Loss_Total(Poles)} = 153.009 \text{ W}$$

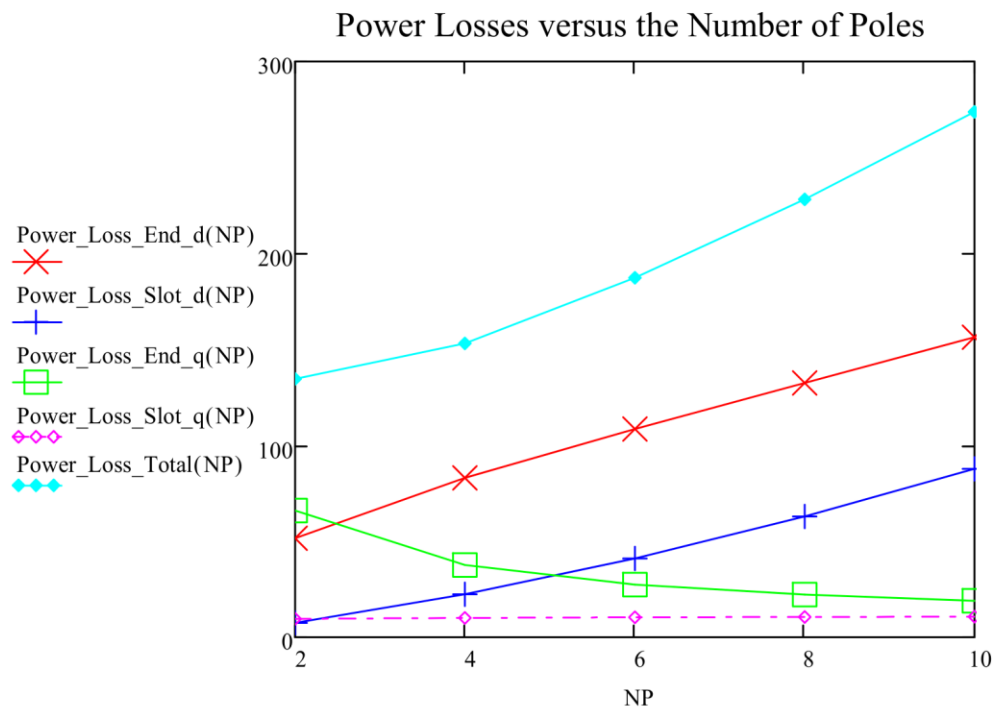
$$\eta(\text{Poles}) := \frac{\text{Power}}{\text{Power} + \text{Power_Loss_Total(Poles)}} \quad \begin{aligned} \eta(2) &= 74.819\% & \eta(4) &= 72.332\% \\ \eta(6) &= 68.101\% & N_t(4) &= 56.021 \end{aligned}$$

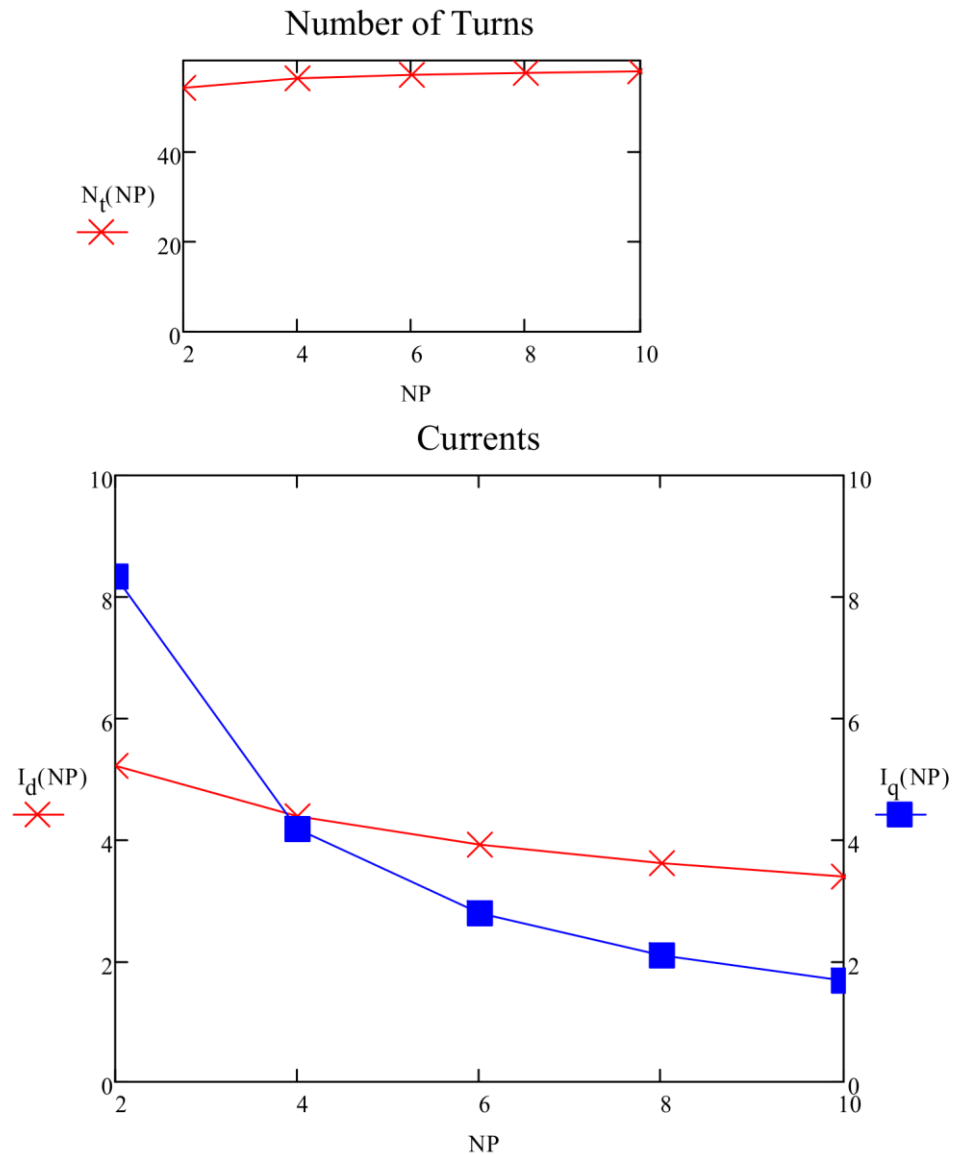
Calculate Maximum Wire Diameter

$$\text{Wire_Diameter(Poles)} := \left(\frac{4}{\pi} \cdot \frac{\text{Slot_Opening_Area(Poles)} \cdot \text{Fill_Factor}}{2 N_t(\text{Poles})} \right)^{\frac{1}{2}} \quad \text{Wire_Diameter(Poles)} = 1.024 \cdot \text{mm}$$

$$R_{\text{Middle_Rotor}} := 3.75 \text{ in} - \text{Chevron_Width(Poles)} \quad R_{\text{Middle_Rotor}} = 3.065 \cdot \text{in}$$

$$R_{\text{Tooth_Bottom}} := R_{\text{Outer_Stator}} - \text{Slot_Depth} \quad R_{\text{Tooth_Bottom}} = 1.35 \cdot \text{in}$$




Part E: Verify Dimensions

$$\eta(\text{Poles}) = 72.332\%$$

$$\Phi_q(\text{Poles}) = 33.384 \cdot \mu\text{Wb}$$

$$\Phi_d(\text{Poles}) = 561.616 \cdot \mu\text{Wb}$$

$$\frac{\Phi_d(\text{Poles})}{\Phi_q(\text{Poles})} = 16.823$$

Would like as high of a saliency ratio as possible

$$\frac{I_d(\text{Poles})}{I_q(\text{Poles})} = 1.051$$

Optimal design has ratio about equal to 1

Where are the MMF drops?

$$\text{MMF}_{\text{Airgap}_q}(\text{Poles}) = 233.421 \text{ A}$$

$$\text{MMF}_{\text{Total}_q}(\text{Poles}) = 233.421 \text{ A}$$

$$\frac{\text{MMF}_{\text{Total}_d}(\text{Poles})}{\text{MMF}_{\text{Total}_q}(\text{Poles})} = 4.206$$

$$\text{MMF}_{\text{Airgap}_d}(\text{Poles}) = 981.707 \text{ A}$$

$$\text{MMF}_{\text{Total}_d}(\text{Poles}) = 981.707 \text{ A}$$

Values below should equal total MMF in the d and q-axis

$$N_t(\text{Poles}) \cdot I_q(\text{Poles}) \cdot \frac{m_q}{2} = 233.421 \text{ A}$$

$$N_t(\text{Poles}) \cdot I_d(\text{Poles}) \cdot m_d = 981.707 \text{ A}$$

$$\Phi_q(\text{Poles}) = 3.338 \times 10^{-5} \text{ Wb}$$

$$\Phi_d(\text{Poles}) = 5.616 \times 10^{-4} \text{ Wb}$$

Reluctance in the d- and q-axis calculated using two different methods:

$$\text{Reluctance}_q(\text{Poles}) := \frac{2 \cdot \text{Carter Factor}(\text{Poles}) \cdot \text{Airgap}}{\mu_0 \cdot \text{Area Pole}_q(\text{Poles})}$$

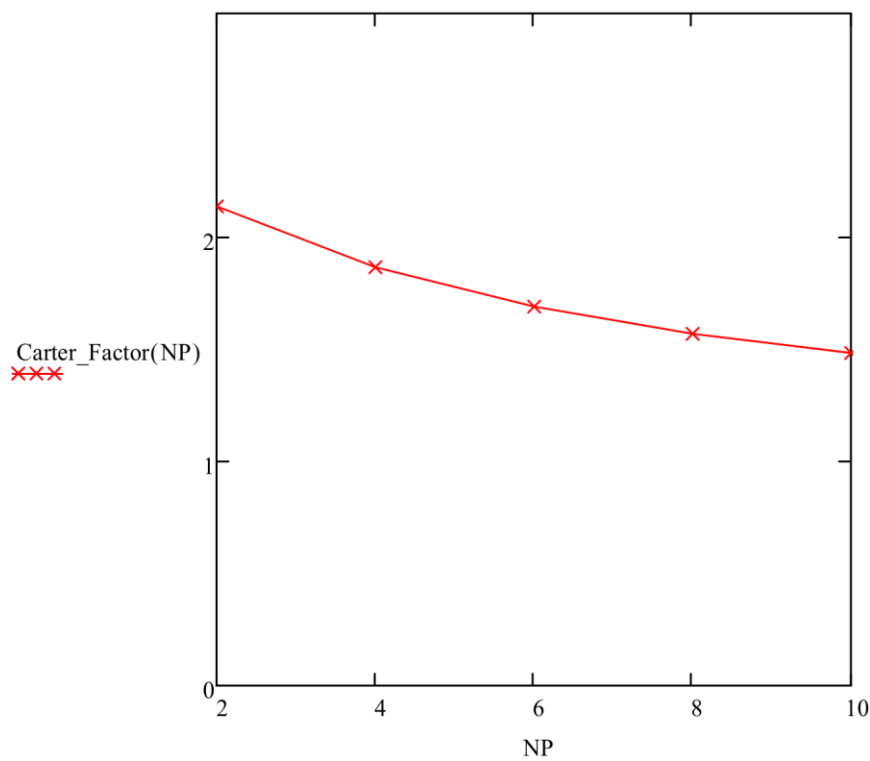
$$\text{Reluctance}_q(\text{Poles}) = 6.992 \times 10^6 \frac{1}{\text{H}}$$

$$\text{Reluctance}_d(\text{Poles}) := \frac{2 \cdot \text{Carter Factor}(\text{Poles}) \cdot \text{Airgap}}{\mu_0 \cdot \frac{\text{Area Pole}_d(\text{Poles})}{2}}$$

$$\text{Reluctance}_d(\text{Poles}) = 3.496 \times 10^6 \frac{1}{\text{H}}$$

$$\frac{N_t(\text{Poles}) \cdot I_q(\text{Poles}) \cdot \frac{m_q}{2}}{\Phi_q(\text{Poles})} = 6.992 \times 10^6 \frac{1}{\text{H}}$$

$$\frac{N_t(\text{Poles}) \cdot I_d(\text{Poles}) \cdot m_d}{\left(\frac{\Phi_d(\text{Poles})}{2} \right)} = 3.496 \times 10^6 \frac{1}{\text{H}}$$



Appendix B: Rotor Assembly Moment of Inertia Calculations

Last Date Modified: March 31st, 2014. **Title:** Rotor Assembly MOI Calculations. **Authors:** Bridget Wimer and Brent Kisling. **Page Count:** 14

Part 1: Center of Mass (COM) equations for the rotor assembly components:

Definitions:

- 1) Fill Material Density (four non-magnetic materials were explored initially):

$$\rho_a := \frac{.0376\text{lbm}}{\text{in}^3} \quad \text{ABS Plastic}$$

$$\rho_b := \frac{.0419\text{lbm}}{\text{in}^3} \quad \text{Acrylic}$$

$$\rho_c := \frac{.051\text{lbm}}{\text{in}^3} \quad \text{Nylon}$$

$$\rho_{st} := \frac{.26\text{lbm}}{\text{in}^3} \quad \text{Steel}$$

$$\rho_{Lam} := \frac{.284\text{lbm}}{\text{in}^3} \quad \begin{array}{l} \text{Density of the Laminations (M36, 26GA Steel} \\ \text{Density) - matches the material used in CATIA.} \end{array}$$

- 2) Define the inner and outer radius of each section (these were already set):

$$\begin{aligned} r_{mid_DB} &:= 3.065\text{in} & r_{outer_DB} &:= 3.75\text{in} & r_{inner_DB} &:= 2.657\text{in} & r_{hole_DB} &:= .138\text{in} \\ r_{inner_mag_plate} &:= 2.675\text{in} & r_{outer_mag_plate} &:= 4\text{in} \\ r_{inner_top_plate} &:= 2.657\text{in} & r_{outer_top_plate} &:= 4\text{in} \end{aligned}$$

The stabilizing bearing and fill section radii were assumed to be the following to match the DB design:

$$r_{inner_SB} := r_{inner_DB} \quad r_{outer_SB} := r_{outer_DB} \quad r_{inner_fill} := r_{inner_DB} \quad r_{outer_fill} := r_{outer_DB}$$

- 3) Heights of the top and bottom plates (the other heights will be varied and therefore the equations will be functions of these heights)

$$h_{Mag_plate} := 1.5\text{in} \quad h_{Top_plate} := 1\text{in} \quad \text{Top plate height based on sensors.}$$

Step 1: Calculate the areas of each component of the rotor assembly:

$$A_{Mag_plate} := \pi \cdot \left(r_{outer_mag_plate}^2 - r_{inner_mag_plate}^2 \right) \quad A_{Mag_plate} = 27.785 \cdot \text{in}^2$$

$$A_{Top_plate} := \pi \cdot \left(r_{outer_top_plate}^2 - r_{inner_top_plate}^2 \right) \quad A_{Top_plate} = 28.087 \cdot \text{in}^2$$

$$A_{Fill} := \pi \cdot \left(r_{outer_fill}^2 - r_{inner_fill}^2 \right) \quad A_{Fill} = 22 \cdot \text{in}^2$$

The SB area calculation currently assumes it will be a solid ring.

$$A_{SB_lams} := \pi \cdot (r_{outer_SB}^2 - r_{inner_SB}^2) \quad A_{SB_lams} = 22 \cdot \text{in}^2$$

The DB area calculation takes into account the saliency:

$$\begin{aligned} A_{DB_outer} &:= \pi \cdot (r_{outer_DB}^2 - r_{mid_DB}^2) & A_{DB_outer} &= 14.666 \cdot \text{in}^2 \\ A_{DB_hole} &:= \pi \cdot r_{hole_DB}^2 & A_{DB_hole} &= 0.06 \cdot \text{in}^2 \\ A_{DB_saliency} &:= \pi \cdot (r_{mid_DB}^2 - r_{inner_DB}^2) \cdot \frac{1}{3} & A_{DB_saliency} &= 2.445 \cdot \text{in}^2 \\ A_{DB_lams} &:= A_{DB_outer} + A_{DB_saliency} - 4 \cdot A_{DB_hole} & A_{DB_lams} &= 16.871 \cdot \text{in}^2 \end{aligned}$$

(1/3) Explanation: Due to the saliency on the DB rotor, the pole face area needed to be taken into account and they encompass 4*30deg / 360deg of the circle perimeter.

Step 2: Calculate the masses of each section:

Governing Equations:

$$M \cdot x_{CM} = \sum_{i=1}^N (m_i \cdot x_i) \quad \text{Where } m_i \text{ is the mass of each individual piece and } x_i \text{ is the center of mass of each individual piece.}$$

$$m_i = \text{Volume} \cdot \rho \quad \text{Volume} = \text{Area} \cdot \text{Height}$$

$$m_{Mag_plate} := \rho_{st} \cdot A_{Mag_plate} \cdot h_{Mag_plate} \quad m_{Mag_plate} = 10.836 \cdot \text{lbm}$$

$$m_{Top_plate} := \rho_{st} \cdot A_{Top_plate} \cdot h_{Top_plate} \quad m_{Top_plate} = 7.303 \cdot \text{lbm}$$

$$m_{DB}(Length_{DB}) := Length_{DB} \cdot A_{DB_lams} \cdot \rho_{Lam}$$

$$m_{SB}(Length_{SB}) := Length_{SB} \cdot A_{SB_lams} \cdot \rho_{Lam}$$

$$m_{Fill}(h_{Fill}, \rho_{Fill}) := h_{Fill} \cdot A_{Fill} \cdot \rho_{Fill}$$

$$m_{Total}(Length_{DB}, Length_{SB}, h_{Fill}, \rho_{Fill}) := \left(m_{Mag_plate} + m_{Top_plate} + m_{DB}(Length_{DB}) \dots \right. \\ \left. + m_{SB}(Length_{SB}) + m_{Fill}(h_{Fill}, \rho_{Fill}) \dots \right)$$

Step 3: Calculate the Center of Mass location of each section:

Define the center of mass heights of each object using the bottom of the mag plate as the reference point:

NOTE: This height assumes that the magnets that will be placed in the holes in the magnetic plate have a similar density to the material of the magnetic plate. This is not the case so these calculations will not match up perfectly with the CATIA results.

$$z_{Mag_plate} := \frac{h_{Mag_plate}}{2} \quad z_{Mag_plate} = 0.75 \cdot \text{in} \quad z_{Mag_plate} = .845 \text{in} \quad \text{CATIA output - difference.}$$

$$z_{DB}(Length_{DB}) := h_{Mag_plate} + \frac{Length_{DB}}{2}$$

$$z_{Fill}(Length_{DB}, h_{Fill}) := h_{Mag_plate} + Length_{DB} + \frac{h_{Fill}}{2}$$

$$z_{SB}(Length_{DB}, Length_{SB}, h_{Fill}) := h_{Mag_plate} + Length_{DB} + h_{Fill} + \frac{Length_{SB}}{2}$$

$$z_{Top_plate}(Length_{DB}, Length_{SB}, h_{Fill}) := h_{Mag_plate} + Length_{SB} + h_{Fill} + Length_{DB} + \frac{h_{Top_plate}}{2}$$

$$z_{CM}(Length_{DB}, Length_{SB}, h_{Fill}, \rho_{Fill}) := \frac{\left(m_{Mag_plate} \cdot z_{Mag_plate} + m_{DB}(Length_{DB}) \cdot z_{DB}(Length_{DB}) \dots \right) + m_{SB}(Length_{SB}) \cdot z_{SB}(Length_{DB}, Length_{SB}, h_{Fill}) \dots + m_{Fill}(h_{Fill}, \rho_{Fill}) \cdot z_{Fill}(Length_{DB}, h_{Fill}) \dots + m_{Top_plate} \cdot z_{Top_plate}(Length_{DB}, Length_{SB}, h_{Fill})}{m_{Total}(Length_{DB}, Length_{SB}, h_{Fill}, \rho_{Fill})}$$

$$\text{Total_rotor_height}(Length_{DB}, Length_{SB}, h_{Fill}) := h_{Fill} + h_{Top_plate} + Length_{DB} + Length_{SB} \dots + h_{Mag_plate}$$

Step 4: Calculate the MOI Ratio:

Governing equations:

Parallel Axis Theorem (where r is the perpendicular distance between the axis of rotation and the axis that would pass through the center of mass). This was only needed for the x -axis.

$$I_z = I_{COM} + m \cdot r^2$$

References:

http://en.wikipedia.org/wiki/List_of_moments_of_inertia
(under thick-walled cylindrical tube) for the I_z and I_x
calculations where mass = (density * area * height) and

$$I_z = \frac{1}{2} \cdot \rho \cdot \text{Area} \cdot \text{height} \cdot (r_{inner}^2 + r_{outer}^2) = \frac{1}{2} \cdot \pi \cdot \rho \cdot \text{height} \cdot (r_{outer}^4 - r_{inner}^4)$$

$$I_x = \frac{1}{12} \cdot \rho \cdot \text{Area} \cdot \text{height} \cdot [3 \cdot (r_{inner}^2 + r_{outer}^2) + \text{height}^2] \quad I_y = I_x$$

$$I_{z_mag_plate} := \frac{1}{2} \cdot \rho_{st} \cdot A_{Mag_plate} \cdot h_{Mag_plate} \cdot (r_{outer_mag_plate}^2 + r_{inner_mag_plate}^2)$$

$$I_{z_mag_plate} = 125.461 \cdot \text{lbm} \cdot \text{in}^2$$

$$I_{z_top_plate} := \frac{1}{2} \cdot \rho_{st} \cdot A_{Top_plate} \cdot h_{Top_plate} \cdot (r_{outer_top_plate}^2 + r_{inner_top_plate}^2)$$

$$I_{z_top_plate} = 84.198 \cdot \text{lbm} \cdot \text{in}^2$$

$$I_{z_SB}(Length_{SB}) := \frac{1}{2} \cdot \rho_{st} \cdot A_{SB_lams} \cdot Length_{SB} \cdot \left(r_{outer_SB}^2 + r_{inner_SB}^2 \right)$$

Note: Iz fill calculation assumes that the fill area will be a solid ring.

$$I_{z_fill}(\rho_{Fill}, h_{Fill}) := \frac{1}{2} \cdot \rho_{Fill} \cdot A_{Fill} \cdot h_{Fill} \cdot \left(r_{outer_fill}^2 + r_{inner_fill}^2 \right)$$

$$d_{hole_COG} := 2.927 \text{ in}$$

$$\begin{aligned} I_{z_DB}(Length_{DB}) := & \frac{1}{2} \cdot \rho_{st} \cdot \pi \cdot Length_{DB} \cdot \left(r_{outer_DB}^4 - r_{mid_DB}^4 \right) \dots \\ & + \left(\frac{1}{2} \rho_{st} \cdot 4\pi \cdot Length_{DB} \cdot r_{hole_DB}^4 + \pi \cdot \rho_{st} \cdot Length_{DB} \cdot r_{hole_DB}^2 \cdot d_{hole_COG}^2 \right) \dots \\ & + \frac{1}{3} \frac{1}{2} \cdot \rho_{st} \cdot \pi \cdot Length_{DB} \cdot \left(r_{mid_DB}^4 - r_{inner_DB}^4 \right) \end{aligned}$$

*For the "holes" the parallel axis theorem needed to be applied since the centroidal axes of the hole features does not line up with the centroidal axis of the flywheel. That is why the holes portion has the additional m*d^2 part where mass is area*height*density.*

$$\begin{aligned} I_{z_rotor_total}(Length_{DB}, Length_{SB}, h_{Fill}, \rho_{Fill}) := & I_{z_mag_plate} + I_{z_top_plate} + I_{z_SB}(Length_{SB}) \dots \\ & + I_{z_fill}(\rho_{Fill}, h_{Fill}) + I_{z_DB}(Length_{DB}) \end{aligned}$$

MOI through the local center of mass (Parallel Axis Theorem will be applied at the end):

$$I_{x_mag_plate} := \frac{1}{12} \cdot \rho_{st} \cdot A_{Mag_plate} \cdot h_{Mag_plate} \cdot \left[3 \left(r_{outer_mag_plate}^2 + r_{inner_mag_plate}^2 \right) + h_{Mag_plate}^2 \right]$$

$$I_{x_top_plate} := \frac{1}{12} \cdot \rho_{st} \cdot A_{Top_plate} \cdot h_{Top_plate} \cdot \left[3 \left(r_{outer_top_plate}^2 + r_{inner_top_plate}^2 \right) + h_{Top_plate}^2 \right]$$

$$I_{x_fill}(\rho_{Fill}, h_{Fill}) := \frac{1}{12} \cdot \rho_{Fill} \cdot A_{Fill} \cdot h_{Fill} \cdot \left[3 \left(r_{outer_fill}^2 + r_{inner_fill}^2 \right) + h_{Fill}^2 \right]$$

$$I_{x_SB}(Length_{SB}) := \frac{1}{12} \cdot \rho_{st} \cdot A_{SB_lams} \cdot Length_{SB} \cdot \left[3 \left(r_{outer_SB}^2 + r_{inner_SB}^2 \right) + Length_{SB}^2 \right]$$

$$I_{x_mag_plate} = 64.762 \cdot \text{lbm} \cdot \text{in}^2 \quad I_{x_top_plate} = 42.707 \cdot \text{lbm} \cdot \text{in}^2$$

This equation was derived from the CATIA model and a relationship between the number of laminations and the Ix was determined as a line with a slope of .519. Therefore, this will need to be changed if the number of laminations or the geometry of these bottom lams is adjusted. This route proved to be valid and was also used to determine Iz.

$$I_{x_DB} := .519494 \cdot \text{lbm} \cdot \text{in}^2 \cdot 108 \quad I_{x_DB} = 56.105 \cdot \text{lbm} \cdot \text{in}^2$$

Need to define distances from the centroid of the rotor to the centroid of the each section in order to apply the parallel axis theorem. The centroids of each section were already found above.

$$d_{Mag_CM}(Length_{DB}, Length_{SB}, h_{Fill}, \rho_{Fill}) := |z_{Mag_plate} - z_{CM}(Length_{DB}, Length_{SB}, h_{Fill}, \rho_{Fill})|$$

$$d_{DB_CM}(Length_{DB}, Length_{SB}, h_{Fill}, \rho_{Fill}) := |z_{DB}(Length_{DB}) - z_{CM}(Length_{DB}, Length_{SB}, h_{Fill}, \rho_{Fill})|$$

$$d_{Fill_CM}(Length_{DB}, Length_{SB}, h_{Fill}, \rho_{Fill}) := |z_{Fill}(Length_{DB}, h_{Fill}) - z_{CM}(Length_{DB}, Length_{SB}, h_{Fill}, \rho_{Fill})|$$

$$d_{SB_CM}(Length_{DB}, Length_{SB}, h_{Fill}, \rho_{Fill}) := \left| z_{SB}(Length_{DB}, Length_{SB}, h_{Fill}) \dots + -z_{CM}(Length_{DB}, Length_{SB}, h_{Fill}, \rho_{Fill}) \right|$$

$$d_{Top_CM}(Length_{DB}, Length_{SB}, h_{Fill}, \rho_{Fill}) := \left| z_{Top_plate}(Length_{DB}, Length_{SB}, h_{Fill}) \dots + -z_{CM}(Length_{DB}, Length_{SB}, h_{Fill}, \rho_{Fill}) \right|$$

$$\begin{aligned} Y(Length_{DB}, Length_{SB}, h_{Fill}, \rho_{Fill}) := & I_{x_mag_plate} + I_{x_top_plate} + I_{x_SB}(Length_{SB}) \dots \\ & + I_{x_fill}(\rho_{Fill}, h_{Fill}) + I_{x_DB} \dots \\ & + d_{Mag_CM}(Length_{DB}, Length_{SB}, h_{Fill}, \rho_{Fill})^2 \cdot m_{Mag_plate} \dots \\ & + d_{DB_CM}(Length_{DB}, Length_{SB}, h_{Fill}, \rho_{Fill})^2 \cdot m_{DB}(Length_{DB}) \dots \\ & + d_{Fill_CM}(Length_{DB}, Length_{SB}, h_{Fill}, \rho_{Fill})^2 \cdot m_{Fill}(h_{Fill}, \rho_{Fill}) \dots \\ & + d_{SB_CM}(Length_{DB}, Length_{SB}, h_{Fill}, \rho_{Fill})^2 \cdot m_{SB}(Length_{SB}) \dots \\ & + d_{Top_CM}(Length_{DB}, Length_{SB}, h_{Fill}, \rho_{Fill})^2 \cdot m_{Top_plate} \end{aligned}$$

$$I_{x_rotor_total}(Length_{DB}, Length_{SB}, h_{Fill}, \rho_{Fill}) := Y(Length_{DB}, Length_{SB}, h_{Fill}, \rho_{Fill})$$

$$MOI_Ratio(Length_{DB}, Length_{SB}, h_{Fill}, \rho_{Fill}) := \frac{I_{z_rotor_total}(Length_{DB}, Length_{SB}, h_{Fill}, \rho_{Fill})}{I_{x_rotor_total}(Length_{DB}, Length_{SB}, h_{Fill}, \rho_{Fill})}$$

Note: MOI should not be within .9-1.1 and the further away from 1 the better.
Design Feature

Part 2: SB and DB force and moment calculations.

Given Parameters:

Spacer (fill material) dimensions:

$$W_{\text{winding_triangular}} := 0.822 \text{ in} \quad \text{Based on the SB design.}$$

$$h_{\text{Fill_min}} := W_{\text{winding_triangular}} + 2 \text{ in} \quad h_{\text{Fill_min}} = 2.822 \cdot \text{in}$$

added approx. 0.5 in to ensure adequate spacing between both bearings

$$h_{\text{Fill}} := h_{\text{Fill_min}} + .428 \text{ in} \quad h_{\text{Fill}} = 3.25 \cdot \text{in}$$

$$\rho_{\text{Fill}} := 0.051 \frac{\text{lb}}{\text{in}^3} \quad \text{Density for nylon fill material - final design decision based on cost.}$$

DB additional dimensions:

$$N_{\text{turnsDB}} := 55$$

Machine (drive bearing) length:

$$Length_{\text{DB}} := 2 \text{ in} \quad \text{Decision made based on initial machine design.}$$

Parameters to vary to adjust COM:

$$Length_{\text{SB}} := 0.75 \text{ in} \quad \text{SB Height was varied.}$$

Adjust the bearing currents to change the bearing forces and correct for the worse case tilt scenario.

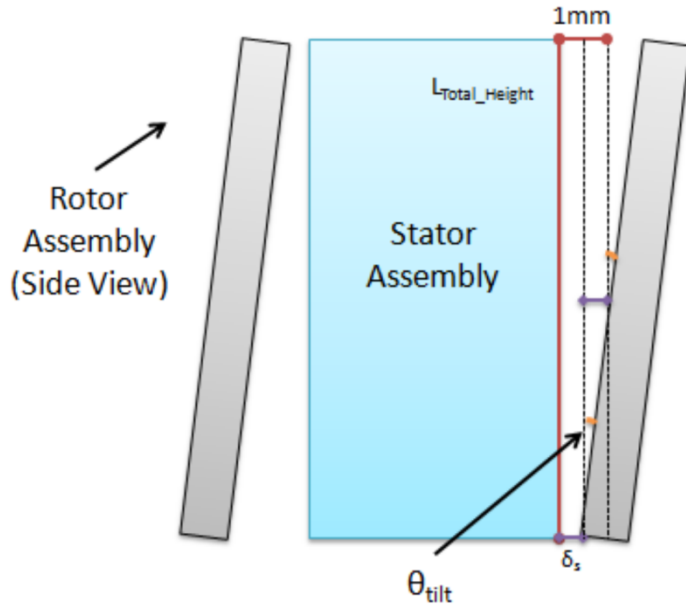
$$I_{\text{SB_bias}} := 2.6 \text{ A} \quad I_{\text{DB_bias}} := 1.75 \text{ A} \quad \Delta I_{\text{SB}} := 1.35 \text{ A} \quad \Delta I_{\text{DB}} := .651 \text{ A}$$

$$I_{\text{DB_left}} := I_{\text{DB_bias}} + \Delta I_{\text{DB}} = 2.401 \text{ A} \quad I_{\text{DB_right}} := I_{\text{DB_bias}} - \Delta I_{\text{DB}} = 1.099 \text{ A}$$

$$I_{\text{SB_left}} := I_{\text{SB_bias}} - \Delta I_{\text{SB}} = 1.25 \text{ A} \quad I_{\text{SB_right}} := I_{\text{SB_bias}} + \Delta I_{\text{SB}} = 3.95 \text{ A}$$

$$\Delta \sec := 0.0001 \text{ in} \quad \text{Used to find the total force for both bearings when tilt occurs. (vertical height)}$$

Worse Case Rotor Tilt (Static Case):



$$\text{Min_Separation_bottom} := 1\text{mm}$$

$$\text{rotor_height_overlapping_stator} := \text{Length}_{DB} + \text{Length}_{SB} + h_{Fill}$$

$$\frac{\text{rotor_height_overlapping_stator}}{2} = 3.\text{in}$$

$$\delta_s := .5\text{mm}$$

$$\theta_t := \arcsin\left(\frac{\delta_s}{\frac{\text{rotor_height_overlapping_stator}}{2}}\right) = 0.376\cdot\text{deg}$$

COM Location and MOI Calculation Check:

$$z_{CM}(\text{Length}_{DB}, \text{Length}_{SB}, h_{Fill}, \rho_{Fill}) = 3.955\cdot\text{in}$$

$$\text{MOI_Ratio}(\text{Length}_{DB}, \text{Length}_{SB}, h_{Fill}, \rho_{Fill}) = 0.768$$

Avoid MOI Ratio between .9 - 1.1.

$$\text{Length}_{DB_below} := z_{CM}(\text{Length}_{DB}, \text{Length}_{SB}, h_{Fill}, \rho_{Fill}) - h_{Mag_plate}$$

$$\text{Length}_{DB_below} = 2.455\cdot\text{in}$$

$$\text{Total_rotor_height}(\text{Length}_{DB}, \text{Length}_{SB}, h_{Fill}) = 8.5\cdot\text{in}$$

$$C_1 := \begin{cases} \text{check_COM} \leftarrow 1 & \text{if } h_{\text{Mag_plate}} < z_{\text{CM}}(\text{Length}_{\text{DB}}, \text{Length}_{\text{SB}}, h_{\text{Fill}}, \rho_{\text{Fill}}) < (\text{Length}_{\text{DB}} + h_{\text{Mag_plate}}) \\ \text{check_COM} \leftarrow -1 & \text{if } z_{\text{CM}}(\text{Length}_{\text{DB}}, \text{Length}_{\text{SB}}, h_{\text{Fill}}, \rho_{\text{Fill}}) > (\text{Length}_{\text{DB}} + h_{\text{Mag_plate}}) \\ \text{check_COM} \leftarrow 2 & \text{if } z_{\text{CM}}(\text{Length}_{\text{DB}}, \text{Length}_{\text{SB}}, h_{\text{Fill}}, \rho_{\text{Fill}}) < h_{\text{Mag_plate}} \\ \text{check_COM} & \end{cases}$$

Check_COM_Location := C₁

Check_COM_Location = -1

If this is equal to -1, then the COM is located in the spacer region of the rotor, as desired.

Bearing force equations

B_{Fe_sat} := 1.6T Based on BH Curve for the selected lamination material.

Final Parameters taken from the SB stator design:

arc_pole_face := 1.383in A_{cs}(Δsec) := arc_pole_face·Δsec θ₁ := 25.9deg N_{turnsSB} := 183

W_{pole} := .407in A_{PoleFaceSB}(L_{SB_iron}) := W_{pole}·L_{SB_iron}

Step 1: Determine the magnetic forces based on the flux density from the DB (for all 16 coils energized) and SB.

$$B_{fe_DB}(airgap_section, I_{DBx}) := \frac{4 \mu_0 \cdot 2 \cdot N_{turnsDB} \cdot I_{DBx}}{2 airgap_section}$$

$$F_{DB}(B_{fe_section}, \Delta sec) := \frac{1}{2\mu_0} \cdot A_{cs}(\Delta sec) \cdot (B_{fe_section})^2$$

$$B_{fe_SB}(airgap_section, I_{SB_current}) := \frac{\mu_0 \cdot N_{turnsSB} \cdot I_{SB_current}}{airgap_section}$$

$$F_{SB}(B_{fe_section}, \Delta sec) := \frac{1}{\mu_0} \cdot A_{PoleFaceSB}(\Delta sec) \cdot (B_{fe_section})^2$$

$$F_{DB_check}(airgap, Length_{DB_section}, I_{DBx}) := \frac{1}{2\mu_0} \cdot A_{cs}(Length_{DB_section}) \cdot \left(\frac{4 \cdot 2 \mu_0 \cdot N_{turnsDB} \cdot I_{DBx}}{2 airgap} \right)^2$$

$$F_{DB_check}(1\text{mm}, Length_{DB}, 1.75A) = 166.196 \text{N} \quad \text{Matches calculations done later on in the project.}$$

$$F_{SB_check}(airgap, Length_{SB}, I_{SB_current}) := \frac{1}{\mu_0} \cdot A_{PoleFaceSB}(Length_{SB}) \cdot \left(\frac{\mu_0 \cdot N_{turnsSB} \cdot I_{SB_current}}{airgap} \right)^2$$

$$F_{SB_check}(1\text{mm}, Length_{SB}, 2.6A) = 56.025 \text{N} \quad \text{Matches calculations done later on in the project.}$$

Step 2: Determine the moments for the DB and SB based on COM location of the rotor assembly.

Drive bearing right side (located below COM):

$k := 1$

$$n := \frac{\text{Length}_{\text{DB}}}{\Delta \text{sec}} = 2 \times 10^4 \quad \text{Number of iterations over the height of the bearing}$$

NOTE: X = 0 at the bottom of the DB for the DB programming loops.

$$\begin{pmatrix} \text{Force}_{\text{DBR}} \\ \text{Moment}_{\text{DBR}} \\ \text{airgap_length} \end{pmatrix} := \left| \begin{array}{l} \text{while } k \leq n \\ \quad X \leftarrow X + \Delta \text{sec} \\ \quad \text{airgap_section} \leftarrow \left(X - \frac{\Delta \text{sec}}{2} \right) \cdot \tan(\theta_t) + \frac{\text{Min_Separation_bottom}}{2} \\ \quad B_{fe_section} \leftarrow B_{fe_DB}(\text{airgap_section}, I_{DB_right}) \\ \quad B_{fe_section} \leftarrow B_{Fe_sat} \text{ if } B_{fe_section} > B_{Fe_sat} \\ \quad \text{Force}_{\text{DB_below}} \leftarrow F_{DB}(B_{fe_section}, \Delta \text{sec}) \\ \quad \text{Force_Sum}_{\text{DB_below}} \leftarrow \text{Force_Sum}_{\text{DB_below}} + \text{Force}_{\text{DB_below}} \\ \quad \text{Moment_Sum}_{\text{DB_below}} \leftarrow \text{Moment_Sum}_{\text{DB_below}} \\ \quad \quad + \text{Force}_{\text{DB_below}} \cdot \left[\text{Length}_{\text{DB_below}} - \left(X - \frac{\Delta \text{sec}}{2} \right) \right] \\ \quad k \leftarrow k + 1 \end{array} \right| \begin{pmatrix} \text{Force_Sum}_{\text{DB_below}} \cdot m \\ \text{Moment_Sum}_{\text{DB_below}} \\ \text{airgap_section} \cdot N \end{pmatrix}$$

$$\text{Force}_{\text{DB_below_right}} := \text{Force}_{\text{DBR}} \cdot \frac{1}{m} \quad \text{Need to convert to make units work.}$$

$$\text{Airgap_Final_Value} := \text{airgap_length} \cdot \frac{1}{N}$$

$$\text{Force}_{\text{DB_below_right}} = 157.307 \text{ N}$$

$$\text{Moment}_{\text{DBR}} = 6.487 \cdot \text{N}\cdot\text{m}$$

$$\text{Airgap_Final_Value} = 0.833 \cdot \text{mm} \quad \text{Final airgap is less than 1mm since the DB height is below the total rotor height/2.}$$

$$\left(\frac{\Delta \text{sec}}{2} \right) \cdot \tan(\theta_t) + \frac{\text{Min_Separation_bottom}}{2} = 0.5 \cdot \text{mm} \quad \text{Initial Airgap at the bottom of the right side of the DB.}$$

Check when θ_t is zero: $\text{LeverArm}_{\text{DB_below}} := \frac{\text{Length}_{\text{DB_below}}}{2}$ $\text{LeverArm}_{\text{DB_below}} = 1.227 \cdot \text{in}$

$$F_{\text{DB_check}}(1 \cdot \text{mm}, \text{Length}_{\text{DB_below}}, I_{\text{DB_bias}}) \cdot \text{LeverArm}_{\text{DB_below}} = 6.359 \cdot \text{N} \cdot \text{m}$$

Drive bearing left side:

$$n := \frac{\text{Length}_{\text{DB}}}{\Delta \text{sec}} = 2 \times 10^4 \quad \text{Number of iterations}$$

$$\begin{pmatrix} \text{Force}_{\text{DBL}} \\ \text{Moment}_{\text{DBL}} \\ \text{airgap_length_left} \end{pmatrix} := \begin{cases} \text{while } k \leq n \\ \quad X \leftarrow X + \Delta \text{sec} \\ \quad \text{airgap_section} \leftarrow \text{Min_Separation_bottom} \dots \\ \quad \quad \quad + \frac{\text{Min_Separation_bottom}}{2} - \left(X - \frac{\Delta \text{sec}}{2} \right) \cdot \tan(\theta_t) \\ \quad B_{\text{fe_section}} \leftarrow B_{\text{fe_DB}}(\text{airgap_section}, I_{\text{DB_left}}) \\ \quad B_{\text{fe_section}} \leftarrow B_{\text{Fe_sat}} \text{ if } B_{\text{fe_section}} > B_{\text{Fe_sat}} \\ \quad \text{Force}_{\text{DB_below}} \leftarrow F_{\text{DB}}(B_{\text{fe_section}}, \Delta \text{sec}) \\ \quad \text{Force_Sum}_{\text{DB_below}} \leftarrow \text{Force_Sum}_{\text{DB_below}} + \text{Force}_{\text{DB_below}} \\ \quad \text{Moment_Sum}_{\text{DB_below}} \leftarrow \text{Moment_Sum}_{\text{DB_below}} \dots \\ \quad \quad \quad + \text{Force}_{\text{DB_below}} \cdot \left[\text{Length}_{\text{DB_below}} - \left(X - \frac{\Delta \text{sec}}{2} \right) \right] \\ \quad k \leftarrow k + 1 \\ \end{cases} \begin{pmatrix} \text{Force_Sum}_{\text{DB_below}} \cdot \text{m} \\ \text{Moment_Sum}_{\text{DB_below}} \\ \text{airgap_section} \cdot N \end{pmatrix}$$

$$\text{Force}_{\text{DB_below_left}} := \text{Force}_{\text{DBL}} \cdot \frac{1}{m} \quad \text{Need to convert to make units work out.}$$

$$\text{Force}_{\text{DB_below_left}} = 178.77 \text{ N}$$

$$\text{Moment}_{\text{DBL}} = 6.226 \cdot \text{N} \cdot \text{m}$$

$$\text{airgap_final_value_left} := \text{airgap_length_left} \cdot \frac{1}{N} \quad \text{airgap_final_value_left} = 1.167 \cdot \text{mm}$$

$$\text{Min_Separation_bottom} + \frac{\text{Min_Separation_bottom}}{2} - \left(\frac{\Delta\text{sec}}{2} \right) \cdot \tan(\theta_t) = 1.5 \cdot \text{mm}$$

Check: First iteration - correct airgap on the right hand side since at bottom it should be at the maximum.

$$\text{Length}_{\text{DB_below}} - \left(\frac{\Delta\text{sec}}{2} \right) = 2.455 \cdot \text{in} \quad \text{Max lever arm at bottom as well.}$$

Check when θ_t is zero:

$$F_{\text{DB_check}}(1 \cdot \text{mm}, \text{Length}_{\text{DB_below}}, I_{\text{DB_bias}}) \cdot \text{LeverArm}_{\text{DB_below}} = 6.359 \cdot \text{N} \cdot \text{m}$$

Stabilization Bearing (right side)

$$\text{Dist}_{\text{SB_above}} := h_{\text{Mag_plate}} + \text{Length}_{\text{DB}} + h_{\text{Fill}} + \text{Length}_{\text{SB}} = 7.5 \cdot \text{in}$$

$$\text{Lever_arm_top_SB} := \text{Dist}_{\text{SB_above}} - z_{\text{CM}}(\text{Length}_{\text{DB}}, \text{Length}_{\text{SB}}, h_{\text{Fill}}, \rho_{\text{Fill}}) = 3.545 \cdot \text{in}$$

$$n := \frac{\text{Length}_{\text{SB}}}{\Delta\text{sec}} = 7.5 \times 10^3 \quad \text{NOTE: X = 0 at the top of the SB for the stabilization bearing loops.}$$

$$\begin{pmatrix} \text{Force}_{\text{SBR}} \\ \text{Moment}_{\text{SBR}} \\ \text{airgap_length}_{\text{SB_r}} \end{pmatrix} := \begin{cases} \text{while } k \leq n \\ \quad X \leftarrow X + \Delta\text{sec} \\ \quad \text{airgap_section} \leftarrow \text{Min_Separation_bottom} ... \\ \quad \quad \quad + \frac{\text{Min_Separation_bottom}}{2} - \left(X - \frac{\Delta\text{sec}}{2} \right) \cdot \tan(\theta_t) \\ \quad \quad \quad B_{\text{fe_section}} \leftarrow B_{\text{fe_SB}}(\text{airgap_section}, I_{\text{SB_right}}) \\ \quad \quad \quad B_{\text{fe_section}} \leftarrow B_{\text{Fe_sat}} \text{ if } B_{\text{fe_section}} > B_{\text{Fe_sat}} \\ \quad \quad \quad \text{Force}_{\text{SB}} \leftarrow F_{\text{SB}}(B_{\text{fe_section}}, \Delta\text{sec}) \\ \quad \quad \quad \text{Force}_{\text{Sum}_{\text{SB}}} \leftarrow \text{Force}_{\text{Sum}_{\text{SB}}} + \text{Force}_{\text{SB}} \\ \quad \quad \quad \text{Moment}_{\text{Sum}_{\text{SB}}} \leftarrow \text{Moment}_{\text{Sum}_{\text{SB}}} ... \\ \quad \quad \quad \quad \quad + \text{Force}_{\text{SB}} \cdot \left[\text{Lever_arm_top_SB} - \left(X - \frac{\Delta\text{sec}}{2} \right) \right] \\ \quad \quad \quad k \leftarrow k + 1 \\ \end{cases} \begin{pmatrix} \text{Force}_{\text{Sum}_{\text{SB}}} \cdot m \\ \text{Moment}_{\text{Sum}_{\text{SB}}} \\ \text{airgap_section} \cdot N \end{pmatrix}$$

$$\text{Force}_{\text{SB_right}} := \text{Force}_{\text{SBR}} \cdot \frac{1}{m} \quad \text{Force}_{\text{SB_right}} = 62.686 \text{ N}$$

$$\text{Moment}_{\text{SBR}} = 5.031 \cdot \text{N} \cdot \text{m}$$

$$\text{airgap_length_SB_Right} := \text{airgap_length_SB_r} \cdot \frac{1}{N} \quad \text{airgap_length_SB_Right} = 1.375 \cdot \text{mm}$$

Initial airgap: Should be equal to 1.5mm since X = 0 at the top of the SB for this loop.

$$\text{Min_Separation_bottom} + \frac{\text{Min_Separation_bottom}}{2} - \left(\frac{\Delta \text{sec}}{2} \right) \cdot \tan(\theta_t) = 1.5 \cdot \text{mm}$$

$$\text{LeverArm}_{\text{SB}} := \text{Lever_arm_top_SB} - \left(\frac{\text{Length}_{\text{SB}}}{2} \right) = 3.17 \cdot \text{in}$$

$$F_{\text{SB_check}}(1 \text{ mm}, \text{Length}_{\text{SB}}, I_{\text{SB_bias}}) \cdot \text{LeverArm}_{\text{SB}} = 4.512 \cdot \text{N} \cdot \text{m}$$

Stabilization Bearing (left side)

$$\begin{pmatrix} \text{Force}_{\text{SBL}} \\ \text{Moment}_{\text{SBL}} \\ \text{airgap_length_SB_l} \end{pmatrix} := \begin{cases} \text{while } k \leq n \\ \quad X \leftarrow X + \Delta \text{sec} \\ \quad \text{airgap_section} \leftarrow \left(X - \frac{\Delta \text{sec}}{2} \right) \cdot \tan(\theta_t) + \frac{\text{Min_Separation_bottom}}{2} \\ \quad B_{fe_section} \leftarrow B_{fe_SB}(\text{airgap_section}, I_{\text{SB_left}}) \\ \quad B_{fe_section} \leftarrow B_{Fe_sat} \text{ if } B_{fe_section} > B_{Fe_sat} \\ \quad \text{Force}_{\text{SB}} \leftarrow F_{\text{SB}}(B_{fe_section}, \Delta \text{sec}) \\ \quad \text{Force_Sum}_{\text{SB}} \leftarrow \text{Force_Sum}_{\text{SB}} + \text{Force}_{\text{SB}} \\ \quad \text{Moment_Sum}_{\text{SB}} \leftarrow \text{Moment_Sum}_{\text{SB}} \\ \quad \quad + \text{Force}_{\text{SB}} \left[\text{Lever_arm_top_SB} - \left(X - \frac{\Delta \text{sec}}{2} \right) \right] \\ \quad k \leftarrow k + 1 \\ \end{cases} \begin{pmatrix} \text{Force_Sum}_{\text{SB}} \cdot m \\ \text{Moment_Sum}_{\text{SB}} \\ \text{airgap_section} \cdot N \end{pmatrix}$$

$$\text{Force}_{\text{SB_left}} := \text{Force}_{\text{SBL}} \cdot \frac{1}{m} \quad \text{Force}_{\text{SB_left}} = 41.434 \text{ N}$$

$$\text{Moment}_{\text{SBL}} = 3.366 \cdot \text{N} \cdot \text{m}$$

$$\text{airgap_length_SB_Left} := \text{airgap_length_SB_l} \cdot \frac{1}{\text{N}} \quad \text{airgap_length_SB_Left} = 0.625 \cdot \text{mm}$$

$$\left(\frac{\Delta \text{sec}}{2} \right) \cdot \tan(\theta_t) + \frac{\text{Min_Separation_bottom}}{2} = 0.5 \cdot \text{mm} \quad \begin{aligned} &\text{Initial airgap, should be equal to .5mm} \\ &\text{since X = 0 at top of SB.} \end{aligned}$$

$$F_{\text{SB_check}}(1 \cdot \text{mm}, \text{Length}_{\text{SB}}, I_{\text{SB_bias}}) \cdot \text{LeverArm}_{\text{SB}} = 4.512 \cdot \text{N} \cdot \text{m}$$

Step 3: Sum the SB and DB forces and moments to determine if the combination can correct for the worst case tilt scenario.

Total Moment Summation

Positive Moment = CCW rotation and positive force points towards the right. Since everything defined as positive will take into account signs below.

$$\text{Moment_Sum} := (\text{Moment}_{\text{DBL}} + \text{Moment}_{\text{SBR}}) - (\text{Moment}_{\text{SBL}} + \text{Moment}_{\text{DBR}})$$

$$\text{Moment}_{\text{DBL}} = 6.226 \cdot \text{N} \cdot \text{m}$$

$$\text{Moment}_{\text{SBL}} = 3.366 \cdot \text{N} \cdot \text{m}$$

$$\text{Moment}_{\text{DBR}} = 6.487 \cdot \text{N} \cdot \text{m}$$

$$\text{Moment}_{\text{SBR}} = 5.031 \cdot \text{N} \cdot \text{m}$$

$$\text{Moment_Sum} = 1.404 \cdot \text{N} \cdot \text{m} \quad \text{Positive value corrects tilt for the given scenario.}$$

$$\text{Force_Sum} := (\text{Force}_{\text{DB_below_left}} + \text{Force}_{\text{SB_left}}) - (\text{Force}_{\text{DB_below_right}} + \text{Force}_{\text{SB_right}})$$

$$\text{Force}_{\text{DB_below_left}} = 178.77 \text{ N}$$

$$\text{Force}_{\text{SB_left}} = 41.434 \text{ N}$$

$$\text{Force}_{\text{DB_below_right}} = 157.307 \text{ N}$$

$$\text{Force}_{\text{SB_right}} = 62.686 \text{ N}$$

$$F_{\text{DB_Sum}} := \text{Force}_{\text{DB_below_left}} - \text{Force}_{\text{DB_below_right}} \quad F_{\text{DB_Sum}} = 21.463 \text{ N}$$

$$F_{\text{SB_Sum}} := \text{Force}_{\text{SB_left}} - \text{Force}_{\text{SB_right}} \quad F_{\text{SB_Sum}} = -21.252 \text{ N}$$

$$\text{Force_Sum} = 0.21 \text{ N}$$

Negative value moves rotor right,
Positive value moves rotor left,
Zero Force Desired to prevent translation
when correct for the symmetrical rotor tilt.

Results:

$$\text{Moment_Sum} = 1.404 \cdot \text{N} \cdot \text{m} \quad \text{MOI_Ratio}(\text{Length}_{\text{DB}}, \text{Length}_{\text{SB}}, h_{\text{Fill}}, \rho_{\text{Fill}}) = 0.768$$

$$z_{\text{CM}}(\text{Length}_{\text{DB}}, \text{Length}_{\text{SB}}, h_{\text{Fill}}, \rho_{\text{Fill}}) = 3.955 \cdot \text{in}$$

$$m_{\text{Total}}(\text{Length}_{\text{DB}}, \text{Length}_{\text{SB}}, h_{\text{Fill}}, \rho_{\text{Fill}}) = 36.054 \cdot \text{lb}$$

Checks:

Check_COM_Location = -1

If 1: COM within the middle of the drive bearing

If -1: COM above the height of the drive bearing

If 2: COM below the drive bearing (within the magnetic plate)

$\theta_t = 0.376 \cdot \text{deg}$ Max Tilt Angle

$h_{\text{Fill_min}} = 2.822 \cdot \text{in}$ hfill exceeds this minimum.

CATIA Results for final design:

$$\text{MOI_Ratio_CATIA} := \frac{406.698 \cdot \text{lb}\cdot\text{in}^2}{509.28 \cdot \text{lb}\cdot\text{in}^2}$$

Close to results above. Results will vary since the heights/density of the materials from the sources online versus CATIA will differ.

MOI_Ratio_CATIA = 0.799

$z_{\text{CM_CATIA}} := 3.977 \text{in}$

mass_total_CATIA := 36.089 lb

Final Bearing/Spacer Parameters:

$h_{\text{Fill}} = 3.25 \cdot \text{in}$

$$\rho_{\text{Fill}} = 0.051 \cdot \frac{\text{lb}}{\text{in}^3}$$

Nylon Fill Material selected for spacer.

Length_{DB} = 2 · in

Length_{SB} = 0.75 · in

$r_{\text{inner_SB}} = 2.657 \cdot \text{in}$

$r_{\text{outer_SB}} = 3.75 \cdot \text{in}$

$r_{\text{inner_fill}} = 2.657 \cdot \text{in}$

$r_{\text{outer_fill}} = 3.75 \cdot \text{in}$

$I_{\text{DB_bias}} = 1.75 \text{ A}$

$I_{\text{SB_bias}} = 2.6 \text{ A}$

Appendix C: Modified Winding Approach Calculations

Last Date Modified: March 19th, 2014. **Title:** Modified Winding Approach for the FRRM and MCM Approach for the SB. **Author:** Bridget Wimer. **Page Count:** 21. **References:** See references in Chapter 7 of my thesis - MWA Section.

General Information for the Field Regulated Reluctance Machine (FRRM) or DB:

$$\text{Pole} := 4 \quad \text{Coils} := 24$$

$$\text{Pole Pitch: angular distance between 2 poles.} \quad \text{Pole_Pitch} := \frac{360\text{deg}}{\text{Pole}} \quad \text{Pole_Pitch} = 90\text{-deg}$$

Coil Pitch: Coil is fully pitched if the stator coil stretches across the same angle as the pole pitch.

$$\text{Coil_Pitch} := \frac{\text{Coils}}{\text{Pole}} \quad \text{Coil_Pitch} = 6$$

Winding Explanation:

North and South Poles: At the south pole, the flux enters the rotor and leaves the stator and at the north pole, the flux exits the rotor to the stator. This is valid for the inside-out configuration of the FRRM.

The inner pole region will all have the same polarity for both layers for the direct axis currents. The pole region will have the same polarity as the previous d-axis coils.

There is 1 coil/pole/phase (there aren't multiple phases per pole). A dot denotes a negative polarity and the current is coming out of the page, while an x denotes a positive polarity and the current is going into the page. There are 6 phases.

Winding Function Theory Information (assumptions all in thesis main body):



Modified Winding Approach to determine the X and Y Total Forces for the FRRM:

NOTE: The MWA calculations below are only valid when the machine is not saturated. Therefore, if all the DB direct axis coils exceed approximately 2.25 A, the DB experiences severe saturation. Saturation was determined by simulating the DB in FEMM.

Machine Definitions: $N := 55$ Number of Turns/Coil - Design Parameter (N=55)

$$\frac{360}{24} = 15 \quad \beta := \frac{\pi}{12} \quad \beta = 15\text{-deg} \quad \frac{\beta}{2} = 7.5\text{-deg} \quad \text{Beta is equal to the angle between the center of two slots}$$

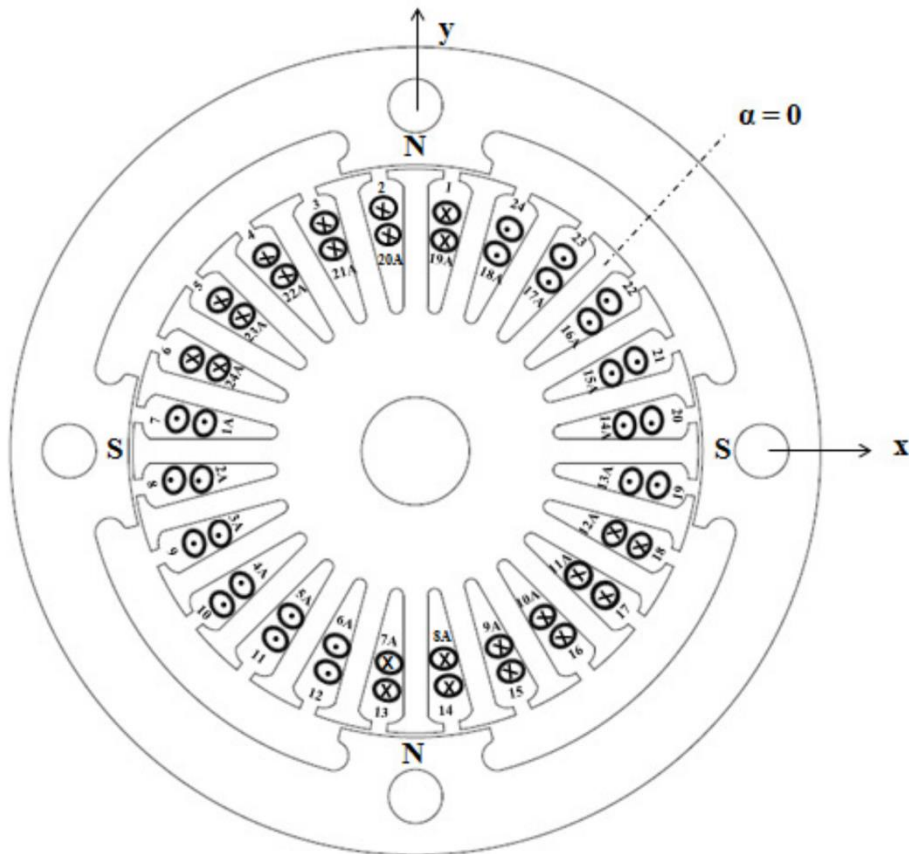
Determine MMF assuming that the rotor is stationary initially. Therefore, let $\theta=0$ (θ is the rotor position angle) and only have the functions below vary with α (varies from 0 to 2π).

$$\omega_m := 188.5 \frac{\text{rad}}{\text{sec}} \quad 1800 \text{ RPMs (FRRM Design Input)}$$

$$\omega_e := \frac{\text{Pole}}{2} \cdot \omega_m$$

$$\theta_e = \frac{\text{Pole}}{2} \cdot \theta_m \quad \theta_m(t) := \omega_m \cdot t$$

Winding Schematic for the Field Regulated Reluctance Machine (will be used for the MWA and the coil numbers correspond with the numbering used below):



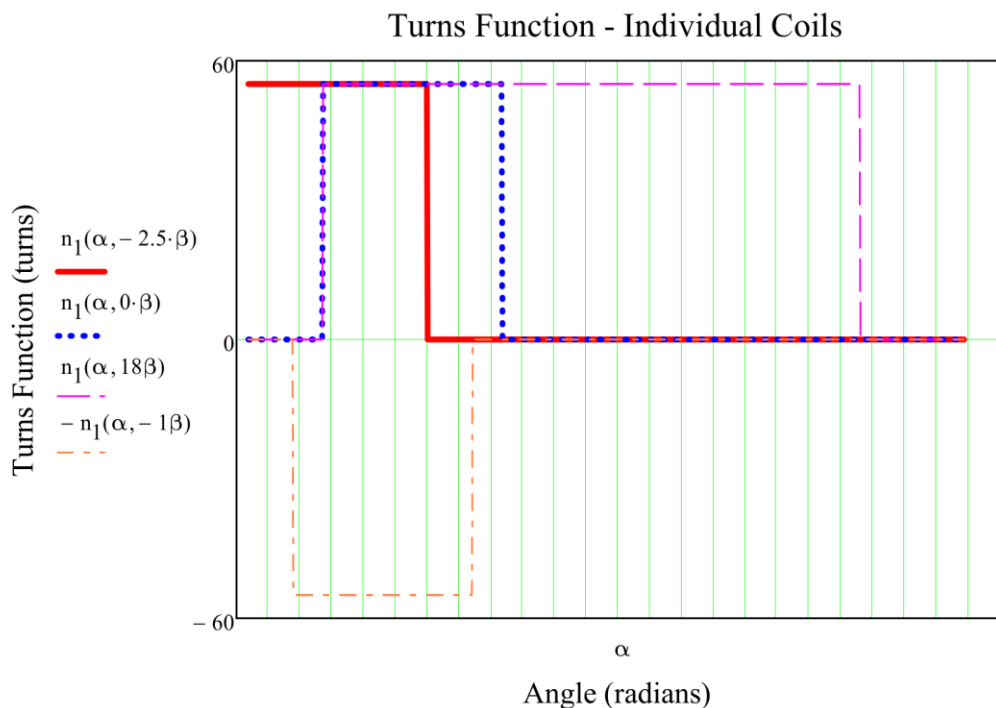
1) Find the Turns Function for each coil:

Instead of developing 24 turns functions, define the turns function for coil #1 and make it a function of ζ to find the remaining turns function by shifting the turns function for coil #1.

ζ = Turns_Function_Shift_Variable

Note that coil #1 is located under a pole face and will be operated as a quadrature axis coil. Keeping the current polarity definition in the winding function and operating it the way I originally had it. Kevin and Brent agreed with this winding schematic.

$$n_1(\alpha, \zeta) := \begin{cases} \text{if } \zeta < 16\beta \\ \begin{cases} 0 & \text{if } 0 \leq \alpha < \frac{\beta}{2} + 2\cdot\beta + \zeta \\ N & \text{if } \frac{\beta}{2} + 2\cdot\beta + \zeta \leq \alpha < \frac{\beta}{2} + 8\cdot\beta + \zeta \\ 0 & \text{if } \frac{\beta}{2} + 8\cdot\beta + \zeta \leq \alpha < 2\cdot\pi \end{cases} \\ \text{otherwise} \\ \begin{cases} 0 & \text{if } 0 \leq \alpha < \frac{\beta}{2} + \zeta - 16\beta \\ N & \text{if } \frac{\beta}{2} + \zeta - 16\beta \leq \alpha < \frac{\beta}{2} + 2\cdot\beta + \zeta \\ 0 & \text{if } \frac{\beta}{2} + 2\cdot\beta + \zeta \leq \alpha < 2\cdot\pi \end{cases} \end{cases}$$



$$n_{1_avg} := \frac{1}{2\cdot\pi} \left(\int_0^{2\cdot\pi} n_1(\alpha, 0) d\alpha \right) \quad n_{1_avg} = 13.75$$

Now, define the turns function for coils #2-24 using the shifting variable.

$$n_2(\alpha) := n_1(\alpha, 1\beta) \quad n_3(\alpha) := n_1(\alpha, 2\beta) \quad n_4(\alpha) := n_1(\alpha, 3\beta) \quad n_5(\alpha) := n_1(\alpha, 4\beta)$$

$$n_6(\alpha) := n_1(\alpha, 5\beta) \quad n_7(\alpha) := -n_1(\alpha, 6\beta) \quad n_8(\alpha) := -n_1(\alpha, 7\beta) \quad n_9(\alpha) := -n_1(\alpha, 8\beta)$$

$$n_{10}(\alpha) := -n_1(\alpha, 9\beta) \quad n_{11}(\alpha) := -n_1(\alpha, 10\beta) \quad n_{12}(\alpha) := -n_1(\alpha, 11\beta) \quad n_{13}(\alpha) := n_1(\alpha, 12\beta)$$

$$n_{14}(\alpha) := n_1(\alpha, 13\beta) \quad n_{15}(\alpha) := n_1(\alpha, 14\beta) \quad n_{16}(\alpha) := n_1(\alpha, 15\beta) \quad n_{17}(\alpha) := -n_1(\alpha, 16\beta)$$

$$n_{18}(\alpha) := -n_1(\alpha, 17\beta) \quad n_{19}(\alpha) := n_1(\alpha, 18\beta) \quad n_{20}(\alpha) := n_1(\alpha, 19\beta) \quad n_{21}(\alpha) := n_1(\alpha, 20\beta)$$

$$n_{22}(\alpha) := n_1(\alpha, 21\beta) \quad n_{23}(\alpha) := -n_1(\alpha, -2\beta) \quad n_{24}(\alpha) := -n_1(\alpha, -1\beta) \quad n_y(\alpha) := n_1(\alpha, -2.5\beta)$$

$n_x(\alpha) := n_1(\alpha, 15.5\beta)$ n_x and n_y were defined as turn functions symmetric about the x and y axes for quick checks.

$$n_{avg} := \frac{1}{2\cdot\pi} \left(\int_0^{2\cdot\pi} n_{17}(\alpha) d\alpha \right) \quad n_{avg} = -41.251 \quad n_{1_avg} \cdot 3 = 41.25$$

Note: A few of the coils will have a larger average value. As expected, this is three times that of coil #1.

2) Define the Airgap Function (for a symmetric rotor with/without eccentricity):

Step 1: Define the airgap function assuming no eccentricity:

Note: I will make approximations to make the geometry easier since the poles are curved at the end. I will assume the corners of the poles are at right angles. Used the same reference as the turns function of where $\alpha=0$.

I have used the measured values instead of the design parameters to improve accuracy.

$$d_{mid_actual} := 155.03\text{mm} \quad \frac{d_{mid_actual}}{2} = 3.052\text{-in} \quad r_{mid} := 3.052\text{in}$$

$$d_{inner_actual} := 134.92\text{mm} \quad \frac{d_{inner_actual}}{2} = 2.656\text{-in} \quad r_{inner} := 2.656\text{in}$$

$$\text{gap}_{innerpole} := (r_{mid} - r_{inner}) + 1\text{mm} \quad \text{gap}_{innerpole} = 11.058\text{-mm} \quad \text{gap}_{pole} := 1\text{mm}$$

$$g_1(\alpha) := \begin{cases} \text{gap}_{\text{innerpole}} & \text{if } 0 \leq \alpha < 30\text{deg} \\ \text{gap}_{\text{pole}} & \text{if } 30\text{deg} \leq \alpha < 60\text{deg} \\ \text{gap}_{\text{innerpole}} & \text{if } 60\text{deg} \leq \alpha < 120\text{deg} \\ \text{gap}_{\text{pole}} & \text{if } 120\text{deg} \leq \alpha < 150\text{deg} \\ \text{gap}_{\text{innerpole}} & \text{if } 150\text{deg} \leq \alpha < 210\text{deg} \\ \text{gap}_{\text{pole}} & \text{if } 210\text{deg} \leq \alpha < 240\text{deg} \\ \text{gap}_{\text{innerpole}} & \text{if } 240\text{deg} \leq \alpha < 300\text{deg} \\ \text{gap}_{\text{pole}} & \text{if } 300\text{deg} \leq \alpha < 330\text{deg} \\ \text{gap}_{\text{innerpole}} & \text{if } 330\text{deg} \leq \alpha < 360\text{deg} \end{cases}$$

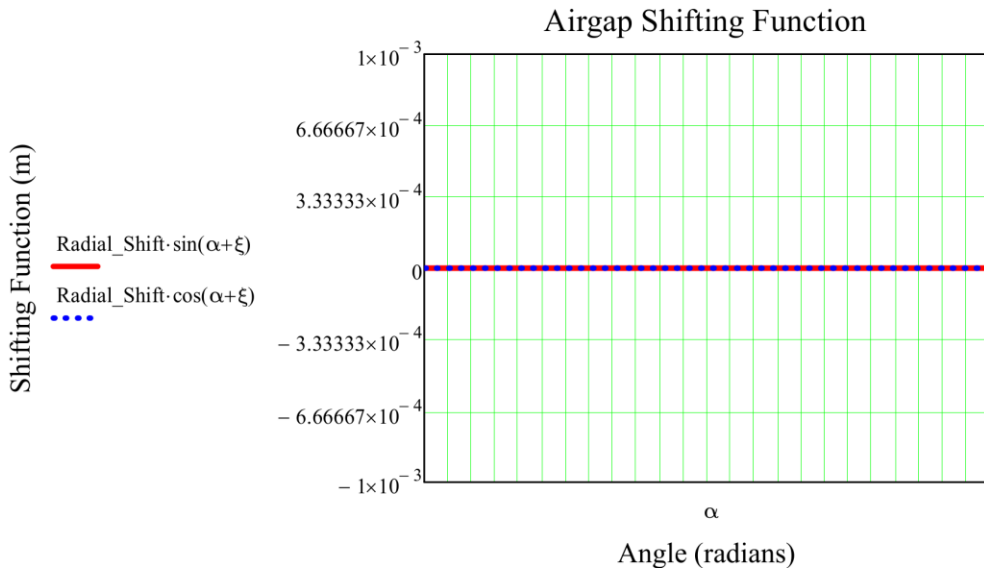
Step 2: Include static eccentricities in the airgap function to include non-ideal cases in the radial direction. Initially, I will use a quick approximation by adding a sinusoidal function to the airgap function to properly model that the airgap increases on one side of the machine and then decreases 180 degrees opposite of it.

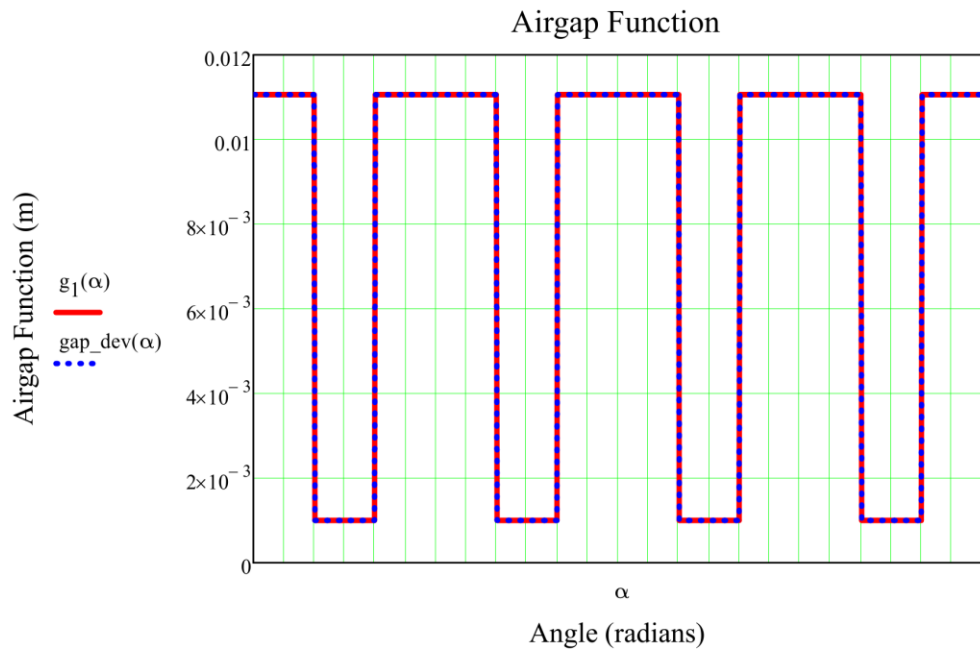
This modified airgap function includes small deviations in the airgap for either the y or x direction depending on what sinusoidal function the Radial Shift is multiplied by. The angle ξ is added to α to vary where the deviation is applied. So for example, if $\xi = 45\text{deg}$, this will either apply the force directly in the x or y-axis.

$$\text{Radial_Shift} := 0\text{mm} \quad \xi := 45\text{deg}$$

$$\text{gap_dev}(\alpha) := g_1(\alpha) - \text{Radial_Shift} \sin(\alpha + \xi)$$

To cause a shift in the y-direction, add a $k \cdot \sin(\alpha)$. The $\sin(\alpha)$ will shift the rotor along the y-axis.
To cause a shift in the x-direction, add a $k \cdot \cos(\alpha)$. The $\cos(\alpha)$ will shift the rotor along the x-axis.

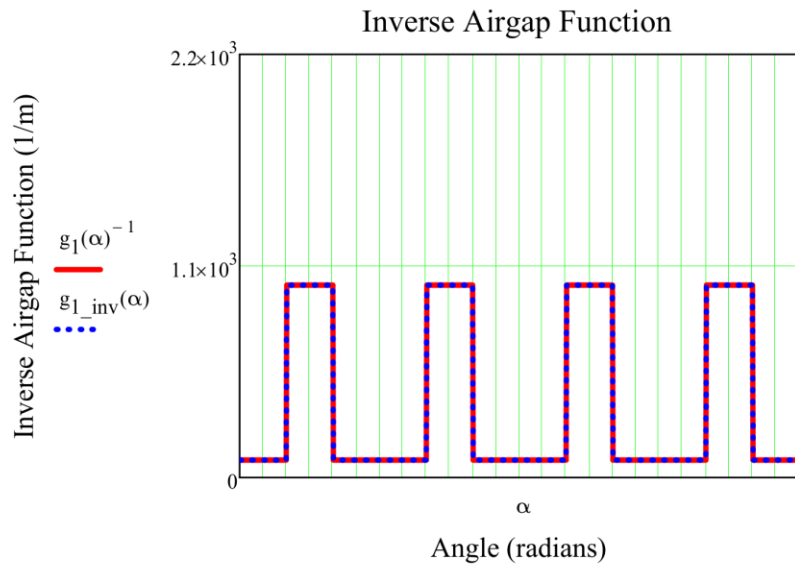




$$gap_dev(270\text{deg}) = 11.058 \cdot \text{mm} \quad gap_dev(225\text{deg}) = 1 \cdot \text{mm}$$

3) Calculate the Inverse Airgap Function:

$$g_{1_inv}(\alpha) := gap_dev(\alpha)^{-1} \quad g_{1_inv}(30\text{deg}) = 1 \times 10^3 \frac{1}{\text{m}} \quad g_{1_inv}(0\text{deg}) = 90.429 \frac{1}{\text{m}}$$



4) Find the average value of the inverse airgap function.

Route #1: Discretize the inverse airgap function to find the average value.



Route #2: Take the integral of the inverse airgap function without discretizing to see if it will solve.

$$g_{1_inv_avg} := \frac{1}{2\pi} \left(\int_0^{2\pi} g_{1_inv}(\alpha) d\alpha \right)$$

$g_{1_inv_avg} = 393.619 \frac{1}{m}$

$\text{avg_inv_gap} = 393.619 \frac{1}{m}$

Average method used the airgap with no shifts. This shows how the average value changes with a shift in x or y.

5) Solve for the component of the modified winding function (for each coil). This component is only a function of θ and not a .

Route #1: Use integration to find the component of the Modified function:

$$M_{comp_1} := \frac{1}{2\pi \cdot g_{1_inv_avg}} \cdot \int_0^{2\pi} g_{1_inv}(\alpha) \cdot n_1(\alpha, 0) d\alpha$$

Should be unitless and simply a number as expected.

$$M_{comp_1} = 13.75 \quad n_{1_avg} = 13.75 \quad \text{Will match } n_{1_avg} \text{ without eccentricities.}$$

When there is no eccentricity, the component of the modified winding function (M_{comp}) will be equal to the average of the turns function. Since there is no eccentricity for this problem, the two match as expected. As stated in "A Novel Method for Modeling Dynamic Air-Gap Eccentricity in Synchronous Machines Based on Modified Winding Function Theory": "if the rotor is eccentric, i.e. the air-gap is symmetric, and the north and south poles of the salient-pole machine are identical, then the inverse air-gap function has only even harmonics including a dc value. Therefore, in cases where the air-gap is has only even harmonics, i.e. non-eccentric rotor, the $\langle M(\alpha) \rangle$ reduces to $\langle n \rangle$ " (158).

$$M_{comp_2} := \frac{1}{2\pi \cdot g_{1_inv_avg}} \cdot \int_0^{2\pi} g_{1_inv}(\alpha) \cdot n_2(\alpha) d\alpha \quad M_{comp_2} = 13.75$$

$$M_{comp_3} := \frac{1}{2\pi \cdot g_{1_inv_avg}} \cdot \int_0^{2\pi} g_{1_inv}(\alpha) \cdot n_3(\alpha) d\alpha \quad M_{comp_3} = 13.75$$

$$M_{comp_4} := \frac{1}{2\pi \cdot g_{1_inv_avg}} \cdot \int_0^{2\pi} g_{1_inv}(\alpha) \cdot n_4(\alpha) d\alpha \quad M_{comp_4} = 13.75$$

$$M_{comp_5} := \frac{1}{2\pi \cdot g_{1_inv_avg}} \cdot \int_0^{2\pi} g_{1_inv}(\alpha) \cdot n_5(\alpha) d\alpha \quad M_{comp_5} = 13.75$$

$$M_{comp_6} := \frac{1}{2\cdot\pi\cdot g_{1_inv_avg}} \cdot \int_0^{2\cdot\pi} g_{1_inv}(\alpha) \cdot n_6(\alpha) d\alpha$$

M_{comp_6} = 13.75

$$M_{comp_7} := \frac{1}{2\cdot\pi\cdot g_{1_inv_avg}} \cdot \int_0^{2\cdot\pi} g_{1_inv}(\alpha) \cdot n_7(\alpha) d\alpha$$

M_{comp_7} = -13.75

$$M_{comp_8} := \frac{1}{2\cdot\pi\cdot g_{1_inv_avg}} \cdot \int_0^{2\cdot\pi} g_{1_inv}(\alpha) \cdot n_8(\alpha) d\alpha$$

M_{comp_8} = -13.75

$$M_{comp_9} := \frac{1}{2\cdot\pi\cdot g_{1_inv_avg}} \cdot \int_0^{2\cdot\pi} g_{1_inv}(\alpha) \cdot n_9(\alpha) d\alpha$$

M_{comp_9} = -13.75

$$M_{comp_10} := \frac{1}{2\cdot\pi\cdot g_{1_inv_avg}} \cdot \int_0^{2\cdot\pi} g_{1_inv}(\alpha) \cdot n_{10}(\alpha) d\alpha$$

M_{comp_10} = -13.75

$$M_{comp_11} := \frac{1}{2\cdot\pi\cdot g_{1_inv_avg}} \cdot \int_0^{2\cdot\pi} g_{1_inv}(\alpha) \cdot n_{11}(\alpha) d\alpha$$

M_{comp_11} = -13.75

$$M_{comp_12} := \frac{1}{2\cdot\pi\cdot g_{1_inv_avg}} \cdot \int_0^{2\cdot\pi} g_{1_inv}(\alpha) \cdot n_{12}(\alpha) d\alpha$$

M_{comp_12} = -13.75

$$M_{comp_13} := \frac{1}{2\cdot\pi\cdot g_{1_inv_avg}} \cdot \int_0^{2\cdot\pi} g_{1_inv}(\alpha) \cdot n_{13}(\alpha) d\alpha$$

M_{comp_13} = 13.75

$$M_{comp_14} := \frac{1}{2\cdot\pi\cdot g_{1_inv_avg}} \cdot \int_0^{2\cdot\pi} g_{1_inv}(\alpha) \cdot n_{14}(\alpha) d\alpha$$

M_{comp_14} = 13.75

$$M_{comp_15} := \frac{1}{2\cdot\pi\cdot g_{1_inv_avg}} \cdot \int_0^{2\cdot\pi} g_{1_inv}(\alpha) \cdot n_{15}(\alpha) d\alpha$$

M_{comp_15} = 13.75

$$M_{comp_16} := \frac{1}{2\cdot\pi\cdot g_{1_inv_avg}} \cdot \int_0^{2\cdot\pi} g_{1_inv}(\alpha) \cdot n_{16}(\alpha) d\alpha$$

M_{comp_16} = 13.75

$$M_{comp_17} := \frac{1}{2\pi \cdot g_{l_inv_avg}} \cdot \int_0^{2\pi} g_{l_inv}(\alpha) \cdot n_{17}(\alpha) d\alpha \quad M_{comp_17} = -41.273$$

$$M_{comp_18} := \frac{1}{2\pi \cdot g_{l_inv_avg}} \cdot \int_0^{2\pi} g_{l_inv}(\alpha) \cdot n_{18}(\alpha) d\alpha \quad M_{comp_18} = -41.25$$

$$M_{comp_19} := \frac{1}{2\pi \cdot g_{l_inv_avg}} \cdot \int_0^{2\pi} g_{l_inv}(\alpha) \cdot n_{19}(\alpha) d\alpha \quad M_{comp_19} = 41.25$$

$$M_{comp_20} := \frac{1}{2\pi \cdot g_{l_inv_avg}} \cdot \int_0^{2\pi} g_{l_inv}(\alpha) \cdot n_{20}(\alpha) d\alpha \quad M_{comp_20} = 41.25$$

$$M_{comp_21} := \frac{1}{2\pi \cdot g_{l_inv_avg}} \cdot \int_0^{2\pi} g_{l_inv}(\alpha) \cdot n_{21}(\alpha) d\alpha \quad M_{comp_21} = 41.25$$

$$M_{comp_22} := \frac{1}{2\pi \cdot g_{l_inv_avg}} \cdot \int_0^{2\pi} g_{l_inv}(\alpha) \cdot n_{22}(\alpha) d\alpha \quad M_{comp_22} = 41.273$$

$$M_{comp_23} := \frac{1}{2\pi \cdot g_{l_inv_avg}} \cdot \int_0^{2\pi} g_{l_inv}(\alpha) \cdot n_{23}(\alpha) d\alpha \quad M_{comp_23} = -13.75$$

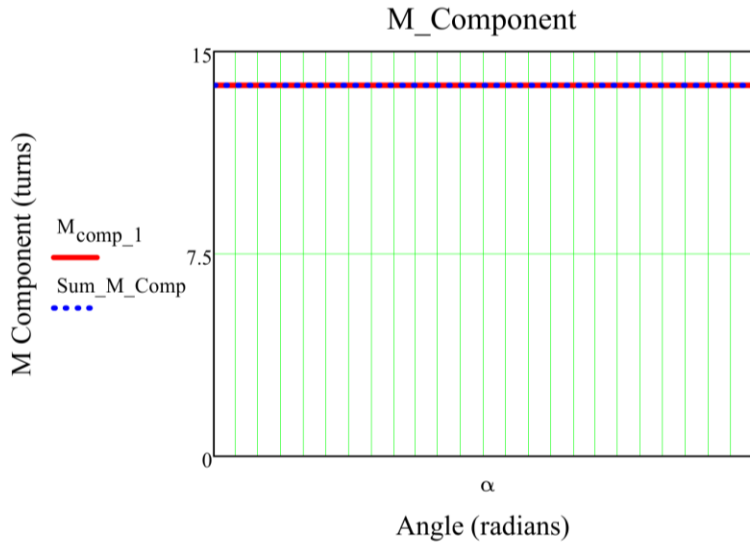
$$M_{comp_24} := \frac{1}{2\pi \cdot g_{l_inv_avg}} \cdot \int_0^{2\pi} g_{l_inv}(\alpha) \cdot n_{24}(\alpha) d\alpha \quad M_{comp_24} = -13.75$$

Results Explanation: There is a minor difference in M_{comp17} and M_{comp22} due to the turns function calculation. They are both defined correctly and for some reason are off a decimal place for the average value and this small error carries through. Otherwise, the rest of the M components come out to the expected values.

Results with Eccentricities: When the Radial_Shift = .5mm and is multiplied by sin this results in a shift in the y-direction with an increase in the airgap under the pole face located at $\alpha=45\text{deg}$ and a decrease in the airgap under the pole face located at $\alpha=225\text{deg}$.

Route #2: Discretize to find this component to see if the two routes match.





6) Find the Modified Winding Function for each coil:

$$M(\alpha, \theta) = n(\alpha, \theta) - M_{\text{comp}}(\theta)$$

Modified Winding Function Equation #11 from SRC.

$$M_1(\alpha) := n_1(\alpha, 0) - M_{\text{comp}}_1$$

$$M_{\text{Route}2}(\alpha) := n_1(\alpha, 0) - \text{Sum}_M_{\text{Comp}}$$

$$M_2(\alpha) := n_2(\alpha) - M_{\text{comp}}_2$$

$$M_3(\alpha) := n_3(\alpha) - M_{\text{comp}}_3$$

$$M_4(\alpha) := n_4(\alpha) - M_{\text{comp}}_4$$

$$M_5(\alpha) := n_5(\alpha) - M_{\text{comp}}_5$$

$$M_6(\alpha) := n_6(\alpha) - M_{\text{comp}}_6$$

$$M_7(\alpha) := n_7(\alpha) - M_{\text{comp}}_7$$

$$M_8(\alpha) := n_8(\alpha) - M_{\text{comp}}_8$$

$$M_9(\alpha) := n_9(\alpha) - M_{\text{comp}}_9$$

$$M_{10}(\alpha) := n_{10}(\alpha) - M_{\text{comp}}_{10}$$

$$M_{11}(\alpha) := n_{11}(\alpha) - M_{\text{comp}}_{11}$$

$$M_{12}(\alpha) := n_{12}(\alpha) - M_{\text{comp}}_{12}$$

$$M_{13}(\alpha) := n_{13}(\alpha) - M_{\text{comp}}_{13}$$

$$M_{14}(\alpha) := n_{14}(\alpha) - M_{\text{comp}}_{14}$$

$$M_{15}(\alpha) := n_{15}(\alpha) - M_{\text{comp}}_{15}$$

$$M_{16}(\alpha) := n_{16}(\alpha) - M_{\text{comp}}_{16}$$

$$M_{17}(\alpha) := n_{17}(\alpha) - M_{\text{comp}}_{17}$$

$$M_{18}(\alpha) := n_{18}(\alpha) - M_{\text{comp}}_{18}$$

$$M_{19}(\alpha) := n_{19}(\alpha) - M_{\text{comp}}_{19}$$

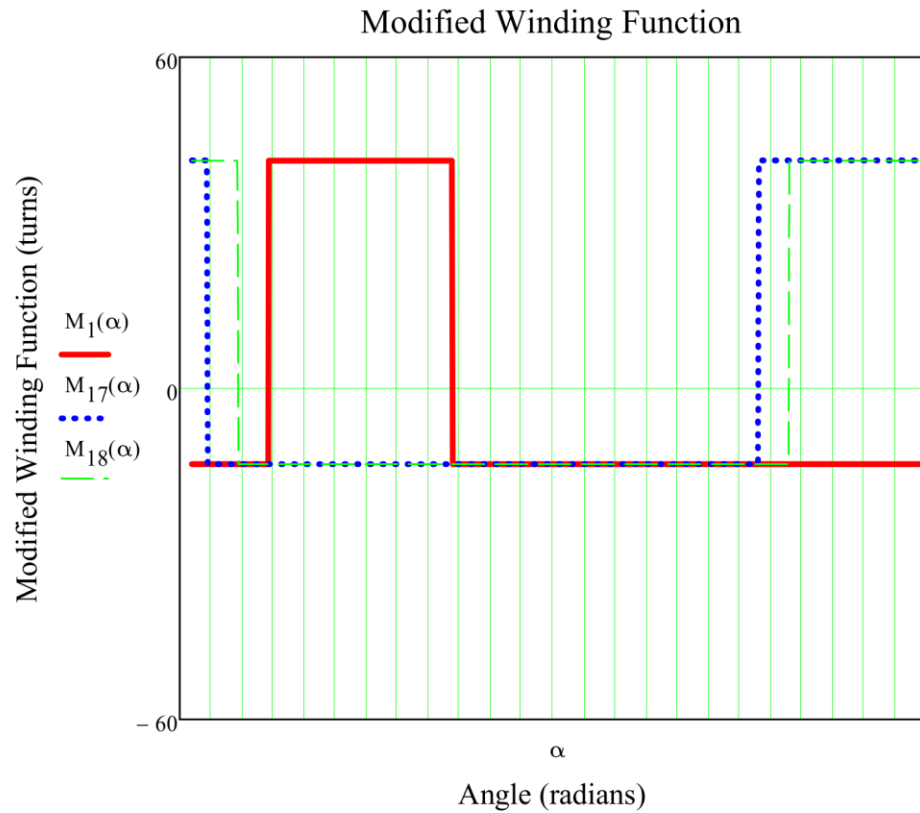
$$M_{20}(\alpha) := n_{20}(\alpha) - M_{\text{comp}}_{20}$$

$$M_{21}(\alpha) := n_{21}(\alpha) - M_{\text{comp}}_{21}$$

$$M_{22}(\alpha) := n_{22}(\alpha) - M_{\text{comp}}_{22}$$

$$M_{23}(\alpha) := n_{23}(\alpha) - M_{\text{comp}}_{23}$$

$$M_{24}(\alpha) := n_{24}(\alpha) - M_{\text{comp}}_{24}$$



7) Find the MMF for each coil:

$$i_d := 1.75A \quad i_q := 0A \quad \Delta i_x := 0A \quad \Delta i_y := 0A$$

Assuming this current for now, since we are developing a winding function for each individual coil, we can still assume that the windings enclosed by the path carry the same current to make the simplification from eqn 2 in "A Novel Method for Modeling Dynamic Aig-Gap Eccentricity in Synchronous Machines Based on Modified Winding Function Theory".

$$F_{cd}(\alpha, \theta) = \left(n(\alpha, \theta) - \frac{1}{2\pi \cdot g_{inv_avg}(\alpha, \theta)} \cdot \int_0^{2\pi} g_{inv}(\alpha, \theta) \cdot n(\alpha, \theta) d\alpha \right) \cdot i \quad \text{Equation #10 from SRC.}$$

Define the currents depending on whether they are operated as a quadrature or direct axis coil:

$$i_1 := i_q \quad i_2 := i_q \quad i_7 := i_q \quad i_8 := i_q \quad i_{13} := i_q \quad i_{14} := i_q \quad i_{19} := i_q \quad i_{20} := i_q$$

Currents associated with the "X-Axis":

$i_3 := i_d - \Delta i_x$	$i_4 := i_3$	$i_5 := i_3$	$i_6 := i_3$
$i_{15} := i_d + \Delta i_x$	$i_{16} := i_{15}$	$i_{17} := i_{15}$	$i_{18} := i_{15}$

4 Coils will be altered at the same amount together and the same amount added to one side will be subtracted from the 4 coils on the opposing side.

Currents associated with the "Y-Axis":

$$\begin{array}{llll} i_9 := i_d - \Delta iy & i_{10} := i_9 & i_{11} := i_9 & i_{12} := i_9 \\ i_{21} := i_d + \Delta iy & i_{22} := i_{21} & i_{23} := i_{21} & i_{24} := i_{21} \end{array}$$

Now, define the MMFs for each coil:

$$\text{MMF}_1(\alpha) := M_1(\alpha) \cdot i_1 \quad \text{MMF}_1(0\text{deg}) = 0 \quad \text{MMF}_1(45\text{deg}) = 0$$

$$\text{MMF}_{1_Route2}(\alpha) := M_{\text{Route2}}(\alpha) \cdot i_1 \quad \text{MMF}_{1_Route2}(0\text{deg}) = 0$$

$$\text{MMF}_2(\alpha) := M_2(\alpha) \cdot i_2 \quad \text{MMF}_3(\alpha) := M_3(\alpha) \cdot i_3$$

$$\text{MMF}_4(\alpha) := M_4(\alpha) \cdot i_4 \quad \text{MMF}_5(\alpha) := M_5(\alpha) \cdot i_5$$

$$\text{MMF}_6(\alpha) := M_6(\alpha) \cdot i_6 \quad \text{MMF}_7(\alpha) := M_7(\alpha) \cdot i_7$$

$$\text{MMF}_8(\alpha) := M_8(\alpha) \cdot i_8 \quad \text{MMF}_9(\alpha) := M_9(\alpha) \cdot i_9$$

$$\text{MMF}_{10}(\alpha) := M_{10}(\alpha) \cdot i_{10} \quad \text{MMF}_{11}(\alpha) := M_{11}(\alpha) \cdot i_{11}$$

$$\text{MMF}_{12}(\alpha) := M_{12}(\alpha) \cdot i_{12} \quad \text{MMF}_{13}(\alpha) := M_{13}(\alpha) \cdot i_{13}$$

$$\text{MMF}_{14}(\alpha) := M_{14}(\alpha) \cdot i_{14} \quad \text{MMF}_{15}(\alpha) := M_{15}(\alpha) \cdot i_{15}$$

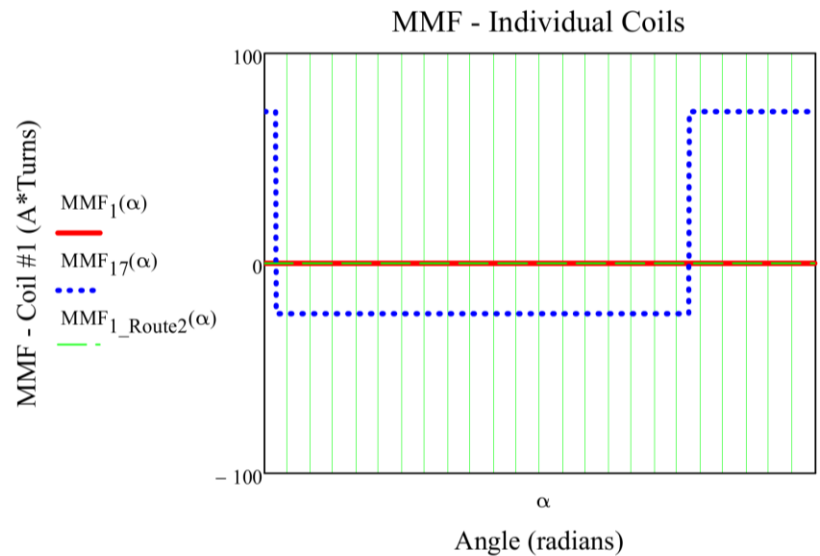
$$\text{MMF}_{16}(\alpha) := M_{16}(\alpha) \cdot i_{16} \quad \text{MMF}_{17}(\alpha) := M_{17}(\alpha) \cdot i_{17}$$

$$\text{MMF}_{18}(\alpha) := M_{18}(\alpha) \cdot i_{18} \quad \text{MMF}_{19}(\alpha) := M_{19}(\alpha) \cdot i_{19}$$

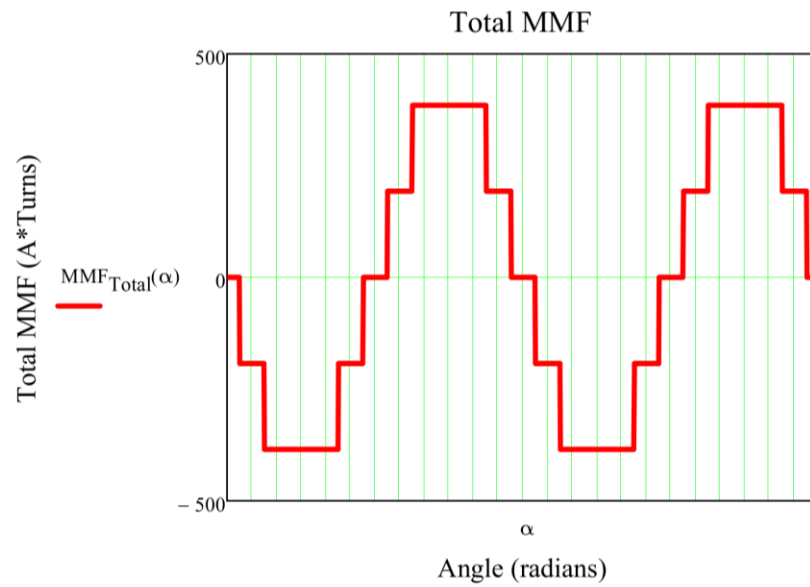
$$\text{MMF}_{20}(\alpha) := M_{20}(\alpha) \cdot i_{20} \quad \text{MMF}_{21}(\alpha) := M_{21}(\alpha) \cdot i_{21}$$

$$\text{MMF}_{22}(\alpha) := M_{22}(\alpha) \cdot i_{22} \quad \text{MMF}_{23}(\alpha) := M_{23}(\alpha) \cdot i_{23}$$

$$\text{MMF}_{24}(\alpha) := M_{24}(\alpha) \cdot i_{24}$$



$$\begin{aligned}
 MMF_{\text{Total}}(\alpha) := & MMF_1(\alpha) + MMF_2(\alpha) + MMF_3(\alpha) + MMF_4(\alpha) + MMF_5(\alpha) + MMF_6(\alpha) \dots \\
 & + MMF_7(\alpha) + MMF_8(\alpha) + MMF_9(\alpha) + MMF_{10}(\alpha) + MMF_{11}(\alpha) + MMF_{12}(\alpha) \dots \\
 & + MMF_{13}(\alpha) + MMF_{14}(\alpha) + MMF_{15}(\alpha) + MMF_{16}(\alpha) + MMF_{17}(\alpha) + MMF_{18}(\alpha) \dots \\
 & + MMF_{19}(\alpha) + MMF_{20}(\alpha) + MMF_{21}(\alpha) + MMF_{22}(\alpha) + MMF_{23}(\alpha) + MMF_{24}(\alpha)
 \end{aligned}$$



$$MMF_{\text{Total}}(225\text{deg}) = -385 \text{ A}$$

8) Find the Field Intensity:

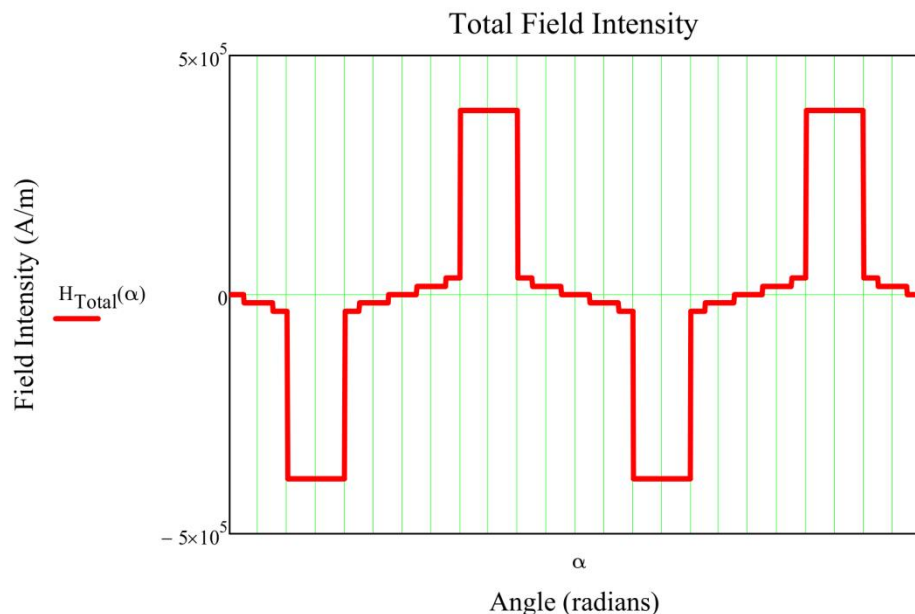
$$\text{MMF} = H \cdot g$$

Coil #1 Field Intensity & Flux Density (still wanted to show an individual coil):



Find the total field intensity based on the MMF Total:

$$H_{\text{Total}}(\alpha) := \text{MMF}_{\text{Total}}(\alpha) \cdot g_{l_inv}(\alpha) \quad H_{\text{Total}}(225\text{deg}) = -3.85 \times 10^5 \frac{\text{A}}{\text{m}}$$



9) Find the Flux Density - Check to see if Gauss's Law holds for the results found above.

$$\int_S B \cdot ds = 0 \quad \int_0^{2\pi} \int_0^L \mu_0 \cdot H(\alpha) r dl d\alpha = 0 \quad \mu_0 = 1.257 \times 10^{-6} \frac{\text{H}}{\text{m}}$$

Gauss Law check for total MMF...not sure if this is valid or if needs to be done for each coil:

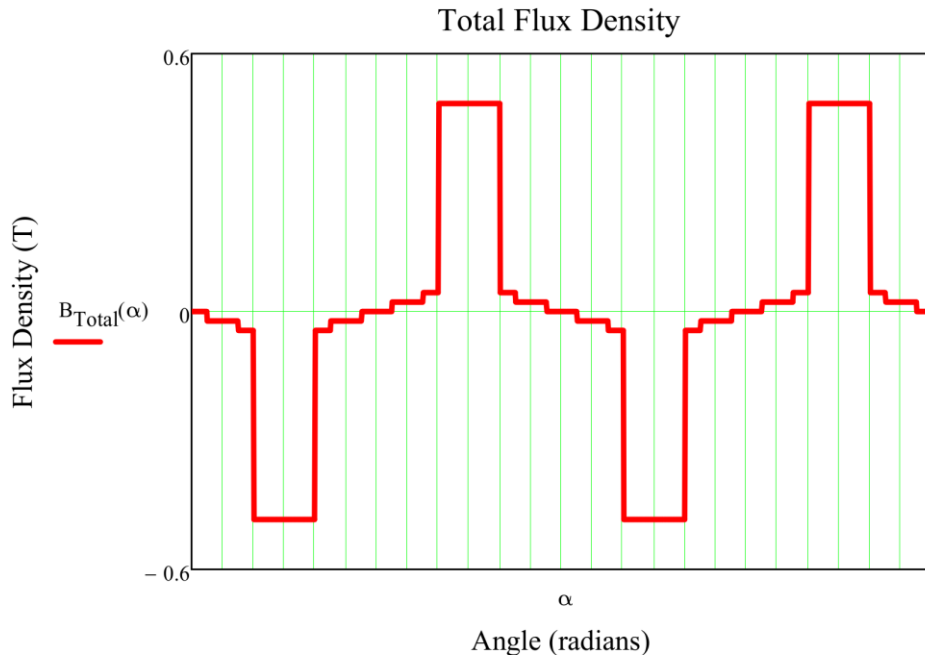
$$B_{\text{Total}}(\alpha) := \begin{cases} \mu_0 \cdot H_{\text{Total}}(\alpha) & \text{if } 0\text{deg} \leq \alpha \leq 2\pi \\ \mu_0 \cdot H_{\text{Total}}(\alpha + 2\pi) & \text{if } \alpha < 0\text{deg} \\ \mu_0 \cdot H_{\text{Total}}(\alpha - 2\pi) & \text{if } \alpha \geq 2\pi \end{cases}$$

Define the flux density over a range of values since we know that it will repeat for the force calculations.

$$B_{\text{Total}}(225\text{deg}) = -0.484 \text{ T}$$

$$\text{Guass_Law_Check1} := \int_0^{2\pi} \mu_0 \cdot H_{\text{Total}}(\alpha) d\alpha \quad \boxed{\text{Guass_Law_Check1} = 0 \text{ T}}$$

Due to rounding errors, Gauss's Law doesn't result in zero exactly but this is close enough. Since the integral simplifies down to only integrating field intensity, this is what I show above since the remaining coefficients can be divided through.



10) Calculate the Forces produced by each coil:



Key Equations:

$$W_a = \frac{1}{2} \cdot B_a \cdot H_a \cdot V_a = \frac{1}{2} \cdot B_a \cdot H_a \cdot A_a \cdot s$$

$$\text{Force} = -\frac{\partial W_a}{\partial s} = \frac{B_a^2 \cdot A_a}{2\mu_0}$$

Energy stored in the volume of the airgap equation. "The force acting on the ferromagnetic body is generated by a change in the field energy in the air gap, as a function of the body displacement. For small displacements ds the magnetic flux $B_a A_a$ remains constant. When the airgap s increased by ds , the Volume $V_a = s A_a$ increases, and the energy W_a in the field increases by dW_a " (77, Schweitzer)

For this model, the volume increases by $1sA_a$ since there are multiple point forces per each airgap path.

To find the force in the x-direction, I will take the derivative of each side of the main equation above and then integrate to find the force. **Assume that the x-axis reference point is 45 degrees offset of where $\alpha=0$. This will allow the x and y-axis to be aligned with the poles initially.**

$$\frac{d}{d\alpha} F(\alpha) = \frac{d}{d\alpha} \left(\frac{B(\alpha)^2 \cdot A}{2\mu_0} \right) \quad F_x(\alpha) = F(\alpha) \cdot \cos(\alpha) \quad F_y(\alpha) = F(\alpha) \cdot \sin(\alpha)$$

$$F_x = \int_0^{2\pi} \frac{B(\alpha)^2 \cdot A}{2\mu_0} \cdot \cos(\alpha) d\alpha \quad dA = r \cdot dl \cdot d\alpha \quad dA = r \cdot L_{eff} \cdot d\alpha \quad r = \text{Stator_Outer_Radius}$$

Since it doesn't vary axially.

$$r_{outer_stator} := r_{inner} - 1 \text{ mm} \quad r_{outer_stator} = 2.617 \cdot \text{in} \quad L_{eff} = 1.96 \cdot \text{in}$$

Assuming that we are taking the surface S to be a cylindrical volume located just outside the stator outer surface (for Gauss's Law).

Force Calculations - Coil #1 (expect both x and y forces due to coil location):



Total Resulting Forces:

$$F_{x_Total}(\varepsilon) := - \int_0^{2\pi} \frac{B_{Total}(\alpha)^2 \cdot r_{outer_stator} \cdot L_{eff}}{2\mu_0} \cdot \cos(\alpha + \varepsilon) d\alpha$$

$$F_{y_Total}(\varepsilon) := - \int_0^{2\pi} \frac{B_{Total}(\alpha)^2 \cdot r_{outer_stator} \cdot L_{eff}}{2\mu_0} \cdot \sin(\alpha + \varepsilon) d\alpha$$

$$F_{x_P}(\varepsilon) := - \int_{-\pi/2}^{\pi/2} \frac{B_{Total}(\alpha)^2 \cdot r_{outer_stator} \cdot L_{eff}}{2\mu_0} \cdot \cos(\alpha + \varepsilon) d\alpha$$

$$F_{x_N}(\varepsilon) := - \int_{\pi/2}^{3\pi/2} \frac{B_{Total}(\alpha)^2 \cdot r_{outer_stator} \cdot L_{eff}}{2\mu_0} \cdot \cos(\alpha + \varepsilon) d\alpha$$

Note: The x and y total forces are multiplied by a negative to denote the correct direction of the force vectors since the force vectors will always be point from the rotor towards the stator in terms of forces on the rotor.

$$F_{x_P}(45\text{deg}) = -160.428 \text{ N} \quad F_{x_N}(45\text{deg}) = 160.428 \text{ N}$$

$$F_{y_P}(\varepsilon) := - \int_{-\pi}^0 \frac{B_{Total}(\alpha)^2 \cdot r_{outer_stator} \cdot L_{eff}}{2\mu_0} \cdot \sin(\alpha + \varepsilon) d\alpha$$

$$F_{y_N}(\varepsilon) := - \int_0^\pi \frac{B_{Total}(\alpha)^2 \cdot r_{outer_stator} \cdot L_{eff}}{2\mu_0} \cdot \sin(\alpha + \varepsilon) d\alpha$$

$$F_{y_P}(45\text{deg}) = 160.428 \text{ N} \quad F_{y_N}(45\text{deg}) = -160.428 \text{ N} \quad F_{y_P}(45\text{deg}) + F_{y_N}(45\text{deg}) = 2.842 \times 10^{-14} \text{ N}$$

I am finding the x and y forces at $\varepsilon = 45$ degrees so that they are aligned with the actual x and y axes.

$$F_{x_P}(45\text{deg}) + F_{x_N}(45\text{deg}) = 2.842 \times 10^{-14} \text{ N}$$

$$F_{x_Total}(45\text{deg}) = 9.173 \times 10^{-6} \text{ N}$$

$$F_{y_P}(45\text{deg}) + F_{y_N}(45\text{deg}) = 2.842 \times 10^{-14} \text{ N}$$

$$F_{y_Total}(45\text{deg}) = 9.173 \times 10^{-6} \text{ N}$$

$$\frac{F_{y_Total}(45\text{deg})}{F_{x_Total}(45\text{deg})} = 1$$

$$B_{Total}(225\text{deg}) = -0.484 \text{ T}$$

$$B_{Total}(315\text{deg}) = 0.484 \text{ T}$$

$$B_{Total}(45\text{deg}) = -0.484 \text{ T}$$

$$B_{Total}(135\text{deg}) = 0.484 \text{ T}$$

Total Force Explanations:

When there are no eccentricities, the total forces in the x and y direction are approximately equal to zero as expected. When eccentricities are added in the positive y-direction, there is a larger force in the y direction versus the x direction.

Instead of using the other way to verify the forces, I can let $Iq=0$ (since the quadrature axis coils will only be producing torque and not force) to do a quick check of the forces when eccentricities are added into the picture. For no eccentricities, the total forces in the x and y direction are equal to zero. For an eccentricity of .1mm, The forces in the y direction = -738N (the gap is increasing in the positive y direction and decreasing in the negative y direction) and the forces in the x direction = 0N.

For an eccentricity of -.1mm, the forces in the y direction = 738N (the gap is decreasing in the positive y direction) and the forces in the x direction = 0N.

Stabilizing Bearing Force Calculations - MCM Approach:

Major Assumptions for Stabilizing Bearing:

- 1) Assume that the innerpole region airgap is very larger compared to the pole region airgaps so that we can ignore the flux paths through here. Also, the leakage flux will be neglected.
- 2) The permeability of the iron core compared to the air is infinite.
- 3) The magnetic circuit model can be used versus winding theory due to initially neglecting the innerpole regions (the FEM analysis proved this assumption was valid).

Note that there will be four groups of two windings connected in series due to how the Stabilizing Bearing is being operated to maximize the force.

Governing Equations (same as equations in AMB for 2 airgaps):

$$B = \frac{2\mu_0 \cdot N \cdot I}{2 \cdot s} \quad F = \frac{B^2 \cdot A}{\mu_0} \cdot \cos(\sigma)$$

For a real radial bearing, the forces are directed in the middle of each coil pair and not along the flux paths and therefore the forces of the magnetic poles will affect the rotor with an angle σ . For the stabilizing bearing with eight poles, σ will equal

$$\sigma := \frac{36.09\text{deg}}{2} + \frac{8.91\text{deg}}{2} \quad \sigma = 22.5\cdot\text{deg}$$

Stabilizing Bearing Parameters (actual):

$$N_{SB} := 183 \quad I_{SB} := 2.6A \quad g_{SB_ideal} := 1\text{mm} \quad \text{Area}_{Gap_SB} := .407\text{in}\cdot.76\text{in} \quad \text{Area}_{Gap_SB} = 199.561\cdot\text{mm}^2$$

Define the currents for the 8 coils (note that due to the series connection the following coil pairs will have the same current flowing through them: coils 5&6 - I_SB56, coils 7&8 - I_SB78, coils 1&2 - I_SB12, and coils 3&4 - I_SB34).

$$\Delta ix_{_SB} := 0A \quad \Delta iy_{_SB} := 0A$$

Currents associated with the "X-Axis":

$$I_{SB12} := I_{SB} + \Delta ix_{_SB} \quad I_{SB56} := I_{SB} - \Delta ix_{_SB} \quad I_{SB12} = 2.6A \quad I_{SB56} = 2.6A$$

Currents associated with the "Y-Axis":

$$I_{SB78} := I_{SB} + \Delta iy_{_SB} \quad I_{SB34} := I_{SB} - \Delta iy_{_SB} \quad I_{SB78} = 2.6A \quad I_{SB34} = 2.6A$$

Ideal Case - Force Calculations (negative signs so force vector points from rotor to stator):

$$F_{x_pos_SB} := -\frac{\left[\frac{2N_{SB} \cdot I_{SB12} \cdot \mu_0}{2 \cdot (g_{SB_ideal})} \right]^2 \cdot Area_{Gap_SB}}{\mu_0} \cdot \cos(\sigma)$$

$$F_{x_neg_SB} := -\frac{\left[\frac{2N_{SB} \cdot I_{SB56} \cdot \mu_0}{2 \cdot (g_{SB_ideal})} \right]^2 \cdot Area_{Gap_SB}}{\mu_0} \cdot \cos(\sigma)$$

$$F_{X_SB} := F_{x_pos_SB} - F_{x_neg_SB} \quad F_{X_SB} = 0 \text{ N}$$

$$F_{y_pos_SB} := -\frac{\left[\frac{2N_{SB} \cdot I_{SB78} \cdot \mu_0}{2 \cdot (g_{SB_ideal})} \right]^2 \cdot Area_{Gap_SB}}{\mu_0} \cdot \cos(\sigma)$$

$$F_{y_neg_SB} := -\frac{\left[\frac{2N_{SB} \cdot I_{SB34} \cdot \mu_0}{2 \cdot (g_{SB_ideal})} \right]^2 \cdot Area_{Gap_SB}}{\mu_0} \cdot \cos(\sigma)$$

$$F_{Y_SB} := F_{y_pos_SB} - F_{y_neg_SB} \quad F_{Y_SB} = 0 \text{ N}$$

Note: These forces are located along the stabilizing bearing x and y axes (where the sensors are located) and the current stiffness matched with the FEMM results.

Non-Ideal Case - Force Calculations (based on same shift as DB):

$$\xi_{SB} := 67.5\text{deg}$$

Purely adding shift along SB x or y axes if $\xi_{SB} = 67.5$ degrees.
Can change to match the shift applied above for the DB.

$$\xi = 45\text{-deg} \quad \text{Radial_Shift} = 0\text{-mm}$$

$$g_{SB}(\alpha) := \begin{cases} g_{SB_ideal} & \text{if } 0 \leq \alpha < 360\text{deg} \\ 0 & \text{otherwise} \end{cases}$$

$$gap_dev_SB(\alpha) := g_{SB}(\alpha) - \text{Radial_Shift} \cos(\alpha + \xi_{SB})$$

Airgap directly along the x and y axes:

$$gap_dev_SB(22.5\text{deg}) = 1\text{-mm}$$

$$gap_dev_SB(22.5\text{deg} + 180\text{deg}) = 1\text{-mm}$$

$$gap_dev_SB(22.5\text{deg} + 90\text{deg}) = 1\text{-mm}$$

$$gap_dev_SB(22.5\text{deg} + 270\text{deg}) = 1\text{-mm}$$

Airgaps associated with the x and y axes:

$$\text{gap_dev_SB}(360\text{deg} - 67.5\text{deg}) = 1 \cdot \text{mm}$$

$$\text{gap_dev_SB}(360\text{deg} - 45\text{deg}) = 1 \cdot \text{mm}$$

$$\text{gap_dev_SB}(360\text{deg} - 90\text{deg}) = 1 \cdot \text{mm}$$

Matches my expectations if the shift is placed right along the x-axis. Decreases on the positive x side and increases by the same amount on the negative x side. **NOTE: $\xi_{\text{SB}} = 67.5 \text{ deg}$ to be valid.**

$$\text{gap_dev_SB}(135\text{deg}) = 1 \cdot \text{mm}$$

$$\text{gap_dev_SB}(90\text{deg}) = 1 \cdot \text{mm}$$

$$\text{gap_dev_SB}(90\text{deg} + 22.5\text{deg}) = 1 \cdot \text{mm}$$

Define the 8 airgaps associated with each pole (these are the airgaps used to calculate the forces):

$$s_1 := \text{gap_dev_SB}(315\text{deg}) \quad s_2 := \text{gap_dev_SB}(270\text{deg})$$

$$s_3 := \text{gap_dev_SB}(225\text{deg}) \quad s_4 := \text{gap_dev_SB}(180\text{deg})$$

$$s_5 := \text{gap_dev_SB}(135\text{deg}) \quad s_6 := \text{gap_dev_SB}(90\text{deg})$$

$$s_7 := \text{gap_dev_SB}(45\text{deg}) \quad s_8 := \text{gap_dev_SB}(0\text{deg})$$

Airgaps associated with the X direction:

$$s_1 = 1 \cdot \text{mm} \quad s_2 = 1 \cdot \text{mm} \quad s_5 = 1 \cdot \text{mm} \quad s_6 = 1 \cdot \text{mm}$$

Airgaps associated with the Y direction:

$$s_7 = 1 \cdot \text{mm} \quad s_8 = 1 \cdot \text{mm} \quad s_4 = 1 \cdot \text{mm} \quad s_3 = 1 \cdot \text{mm}$$

Define the SB forces in terms of the eight airgaps:

$$F_{x_pos_SB1} := -\frac{\left(\frac{2N_{SB} \cdot I_{SB12} \cdot \mu_0}{s_1 + s_2}\right)^2 \cdot \text{Area}_{\text{Gap_SB}}}{\mu_0} \cdot \cos(\sigma)$$

$$F_{x_neg_SB1} := -\frac{\left(\frac{2N_{SB} \cdot I_{SB56} \cdot \mu_0}{s_5 + s_6}\right)^2 \cdot \text{Area}_{\text{Gap_SB}}}{\mu_0} \cdot \cos(\sigma)$$

$$F_{X_SB1} := F_{x_pos_SB1} - F_{x_neg_SB1}$$

$$F_{X_SB1} = 0 \text{ N}$$

$$F_{x_pos_SB1} = -52.45 \text{ N} \quad F_{x_neg_SB1} = -52.45 \text{ N}$$

$$F_{y_pos_SB1} := -\frac{\left(\frac{2N_{SB} \cdot I_{SB78} \cdot \mu_0}{s_7 + s_8}\right)^2 \cdot \text{Area}_{Gap_SB}}{\mu_0} \cdot \cos(\sigma)$$

$$F_{y_neg_SB1} := -\frac{\left(\frac{2N_{SB} \cdot I_{SB34} \cdot \mu_0}{s_3 + s_4}\right)^2 \cdot \text{Area}_{Gap_SB}}{\mu_0} \cdot \cos(\sigma)$$

$$F_{Y_SB1} := F_{y_pos_SB1} - F_{y_neg_SB1} \quad F_{Y_SB1} = 0 \text{ N}$$

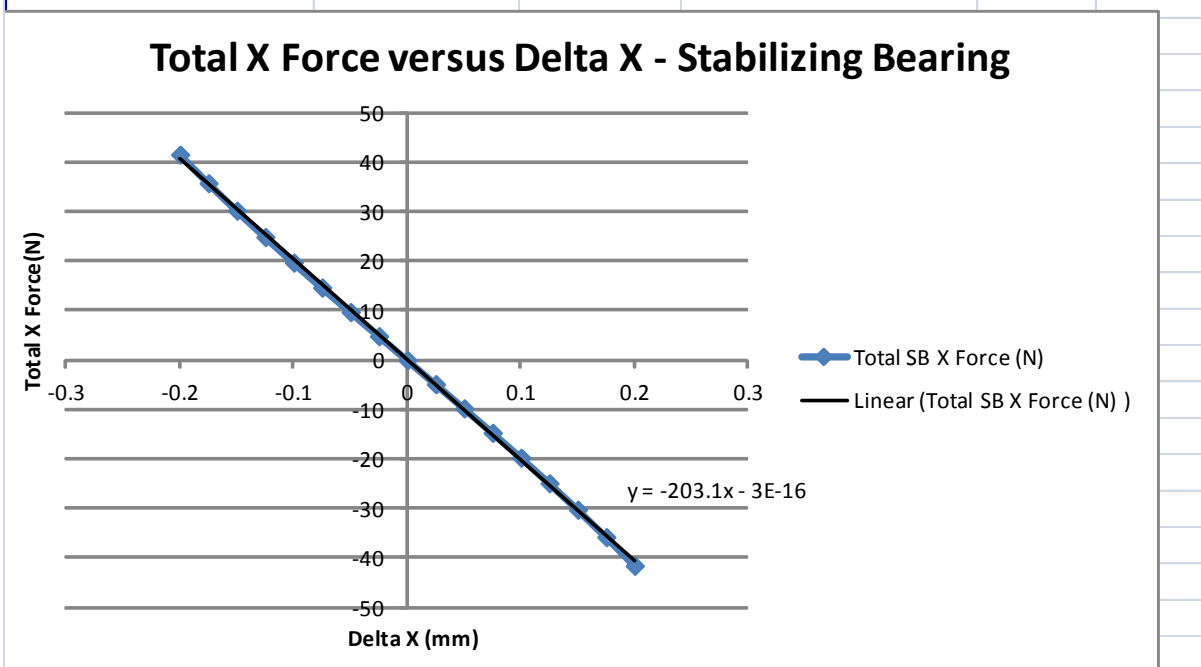
$$F_{y_pos_SB1} = -52.45 \text{ N} \quad F_{y_neg_SB1} = -52.45 \text{ N}$$

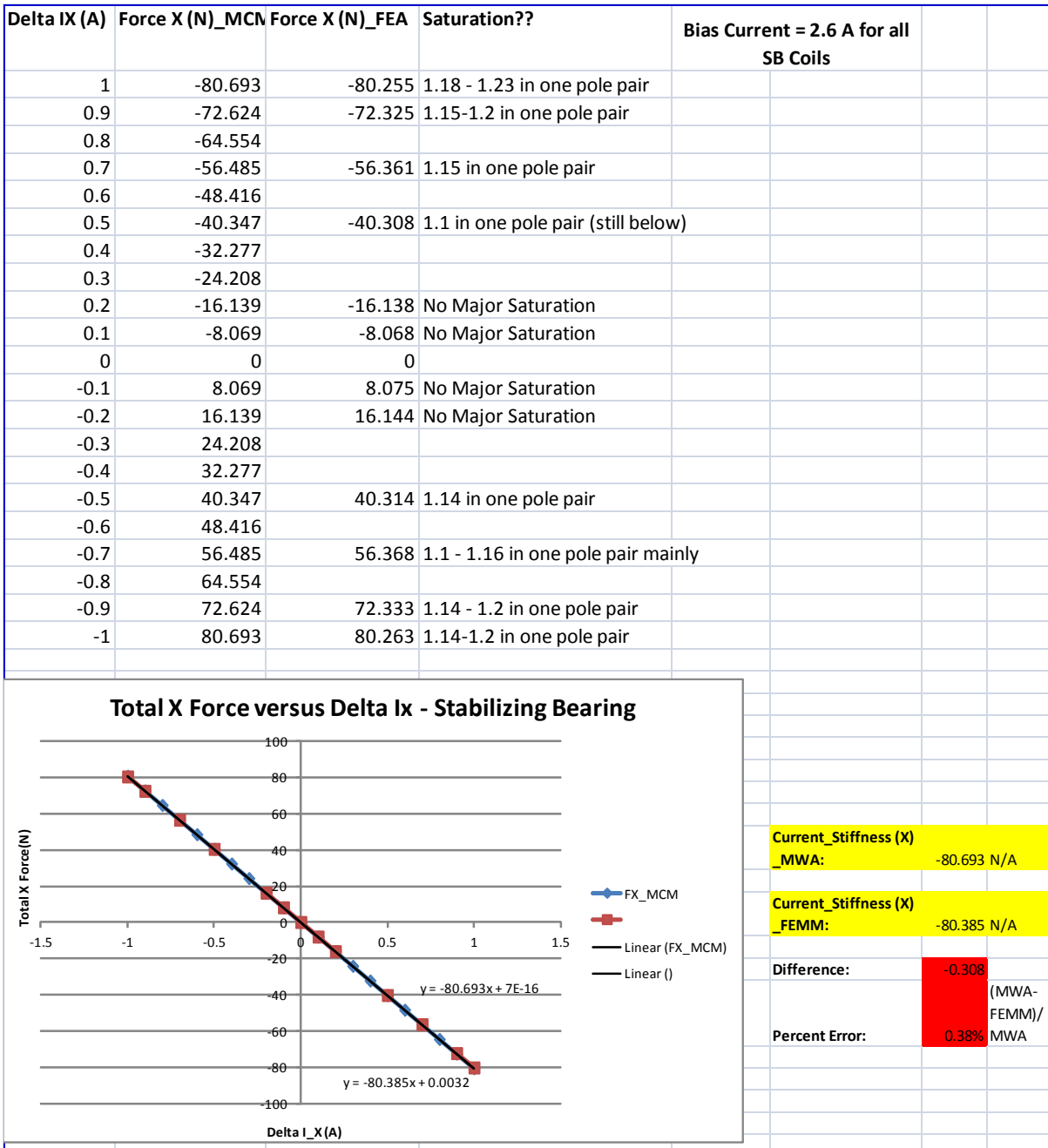
Appendix D: Bearing Stiffness and Current/Force Graphs

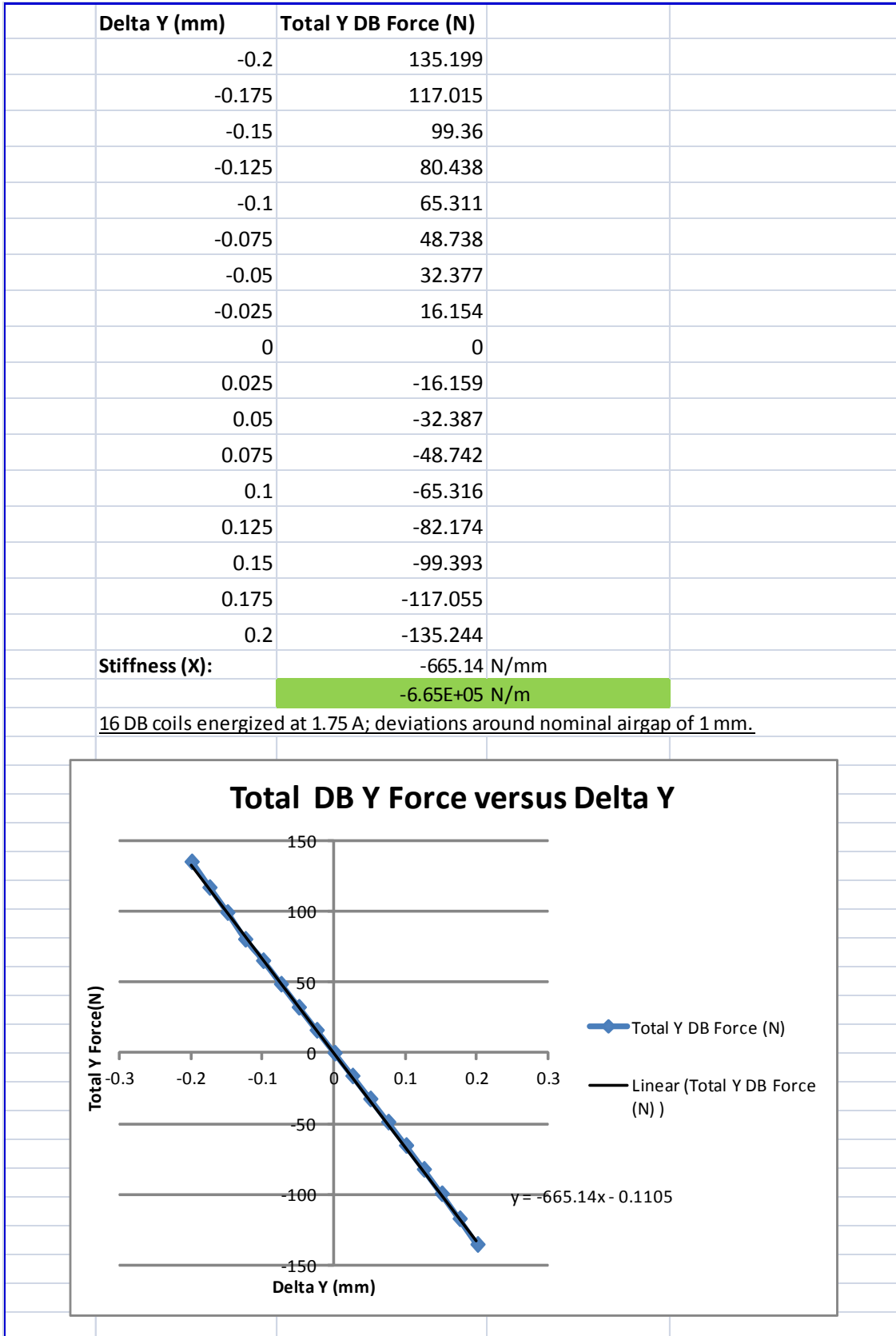
Delta X (mm)	Total SB X Force (N)			
-0.2	41.555			
-0.175	35.766			
-0.15	30.225			
-0.125	24.888			
-0.1	19.718			
-0.075	14.678			
-0.05	9.733			
-0.025	4.851			
0	0			
0.025	-4.851			
0.05	-9.733			
0.075	-14.678			
0.1	-19.718			
0.125	-24.888			
0.15	-30.225			
0.175	-35.766			
0.2	-41.555			

SB Coils energized at SB Bias Current of 2.6 A; deviations around 1mm nominal airgap.

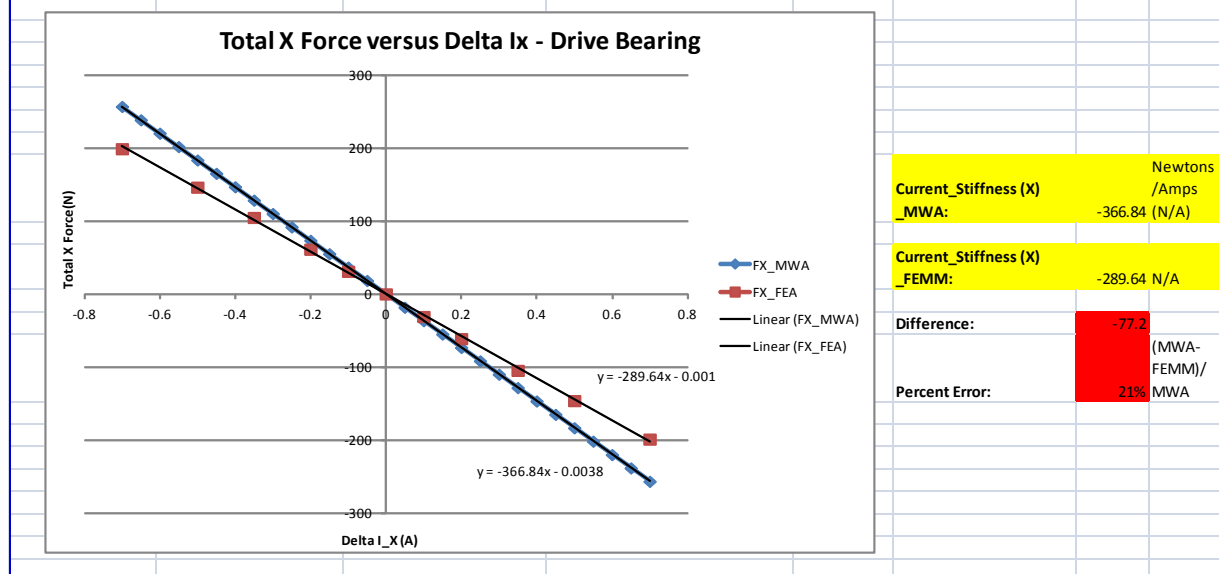
Stiffness (X):	-203.1 N/mm
	-2.03E+05 N/m

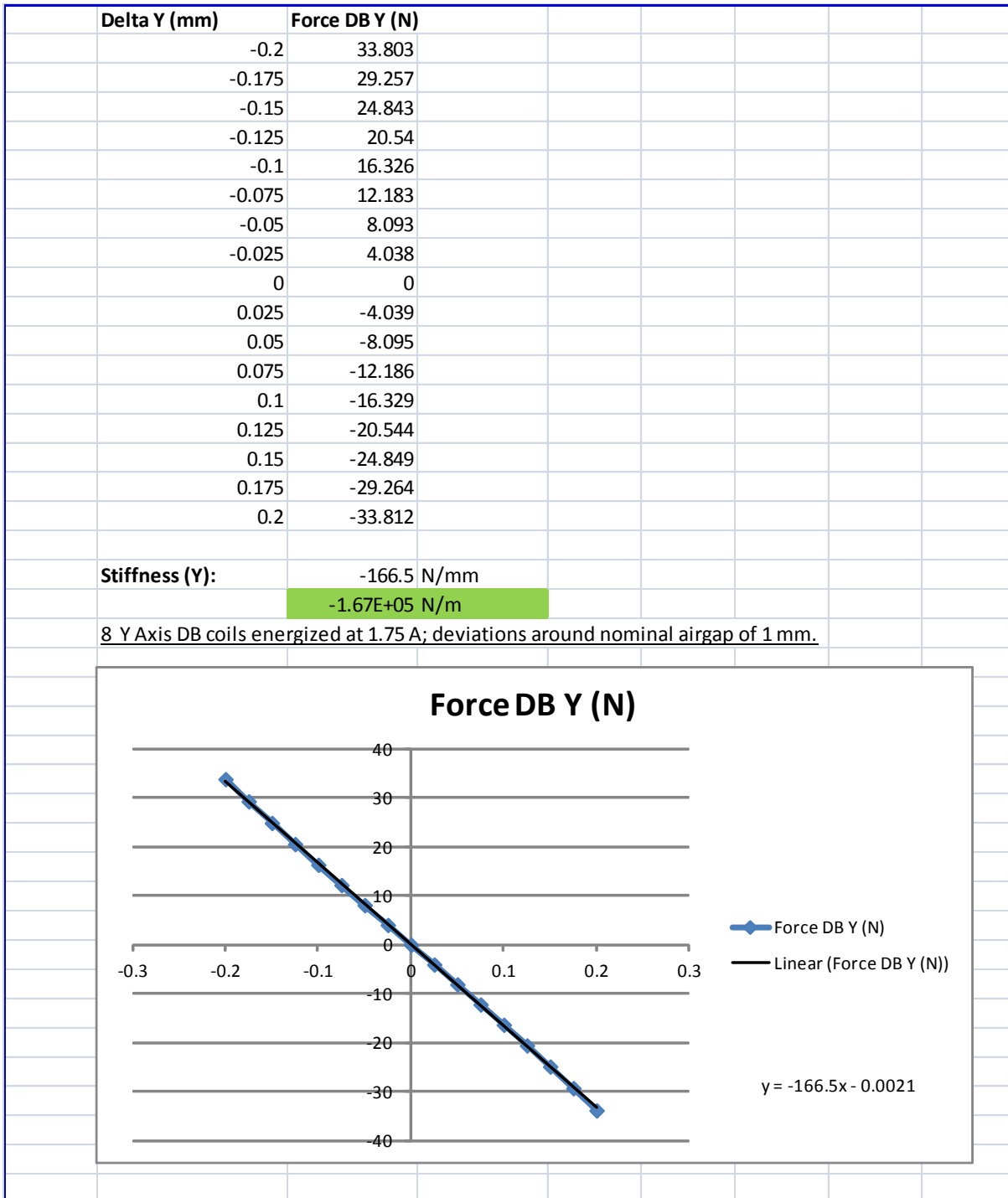






Delta IX (A)	Force X (N)_MWA	Force X (N)_FEMM	Saturation??	Bias Current = 1.75 A for all 16 Direct Axis Coils
0.7	-256.799	-198.849	Middle Tooth = 1.47T (other teeth = 1.2T)	
0.65	-238.456			
0.6	-220.112			
0.55	-201.769			
0.5	-183.426	-146.21	Middle Tooth = 1.44T	
0.45	-165.083			
0.4	-146.74			
0.35	-128.397	-104.73	Middle Tooth = 1.4T	
0.3	-110.054			
0.25	-91.711			
0.2	-73.369	-61.242	Middle Tooth = 1.35T	
0.15	-55.027			
0.1	-36.684	-30.973		
0.05	-18.342			
0	0	0		
-0.05	18.342			
-0.1	36.684	30.973	Middle Tooth = 1.3 T	
-0.15	55.026			
-0.2	73.367	61.242		
-0.25	91.709			
-0.3	110.05			
-0.35	128.392	104.73		
-0.4	146.733			
-0.45	165.074			
-0.5	183.415	146.21		
-0.55	201.756			
-0.6	220.096			
-0.65	238.438			
-0.7	256.778	198.838	Middle Tooth = 1.47T (other teeth = 1.2T)	





Appendix E: Magnetic Circuit Model – Drive Bearing Calculations

Last Date Modified: January 29th, 2014. **Title:** Magnetic Circuit Model Approach for Determining the DB Stiffness for 8 Coils Energized. **Author:** Bridget Wimer. **Page Count:** 8

Stiffness Characterization (X OR Y) - ignore effects of iron:

$$N_{DB} := 55 \quad I_{d,DB} := 1.75A \quad \text{Area}_{Gap,DB} := .0017m^2 \quad \text{airgap} := 1mm$$

$$n_{coils} := 4 \quad \text{Area}_{Gap,DB} = 17\cdot cm^2$$

Primary Equations:

Assuming no rotation currently to characterize stiffness. Therefore, no q axis current. Look at the 8 direct axis coils associated with a delta x first to find the stiffness in the x-direction.

Magnetic Circuit Model Approach:

Primary Equations:

$$\int H dl = \int J dS \quad \text{Ampere's Law}$$

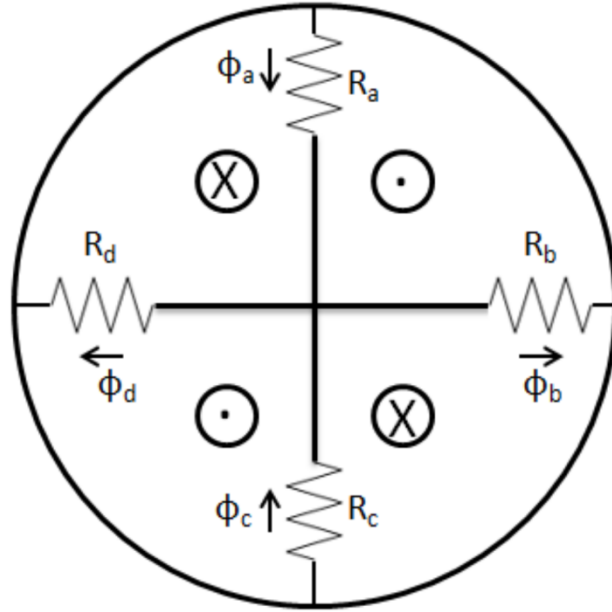
$$\int B dS = 0 \quad \text{Gauss's Law}$$

Problem Explanation: The magnetic circuit will only include the 8 direct axis coils that will result in a force in the X direction. Due to the right hand convention for the 4 pole machine, the flux will flow from the North pole on the rotor to the South pole on the rotor. This will result in 4 flux paths. The permeability of the iron is assumed to be infinite compared to the permeability of the air. Therefore, the reluctances of the iron are neglected in the magnetic circuit and replaced with shorts, but the reluctances of the airgaps are still taken into account.

Instead of looking at the magnetic circuit in terms the individual fluxes that flow through each of the 4 loops, I will analyze the circuit in terms of branch fluxes. Since the forces at the airgap are desired, the branch flux will directly relate to these forces. Since the iron is neglected, branch fluxes can be used since there are not unique paths defined for the flux flowing through the iron paths without iron reluctances. Ampere's Law can be applied to the four loops.

Gauss's Law is needed for the fourth equation so that the problem can be solved and the matrix is no longer singular. By taking into account both Ampere's and Gauss's law, this will directly relate to the winding theory route as well. Below are the 4 equations (3 are based on Ampere's law and 1 is based on Gauss's Law which was applied at the center node) and the magnetic circuit from which these were derived:

Equivalent Magnetic Circuit Model for 8 DB Coils:



$$\text{Eqn #1: } \phi_a \cdot R_a + \phi_b \cdot R_b = 4 \cdot N \cdot I$$

$$\text{Eqn #2: } \phi_c \cdot R_c + \phi_b \cdot R_b = 4 \cdot N \cdot I$$

$$\text{Eqn #3: } \phi_d \cdot R_d + \phi_c \cdot R_c = 4 \cdot N \cdot I$$

$$\text{Eqn #4: } \phi_a + \phi_c = \phi_b + \phi_d$$

Now put these into matrix form to solve for the unknowns, for the ideal case, all of the airgap reluctances are equal and therefore all of the fluxes should be equal as shown below:

$$R_a := \frac{\text{airgap}}{\mu_0 \cdot \text{Area}_{\text{Gap_DB}}}$$

$$R_b(\Delta x) := \frac{\text{airgap} - \Delta x}{\mu_0 \cdot \text{Area}_{\text{Gap_DB}}}$$

Increased R_d by Δx and decreased R_b by Δx to include eccentricities in the same direction as the winding theory route.

$$R_c := \frac{\text{airgap}}{\mu_0 \cdot \text{Area}_{\text{Gap_DB}}}$$

$$R_d(\Delta x) := \frac{\text{airgap} + \Delta x}{\mu_0 \cdot \text{Area}_{\text{Gap_DB}}}$$

$$\text{Reluctance}(\Delta x) := \begin{pmatrix} R_a & R_b(\Delta x) & 0 \cdot \frac{1}{H} & 0 \cdot \frac{1}{H} \\ 0 \cdot \frac{1}{H} & R_b(\Delta x) & R_c & 0 \cdot \frac{1}{H} \\ 0 \cdot \frac{1}{H} & 0 \cdot \frac{1}{H} & R_c & R_d(\Delta x) \\ \frac{1}{H} & \frac{-1}{H} & \frac{1}{H} & \frac{-1}{H} \end{pmatrix}$$

$$\text{Reluctance}(0\text{mm})^{-1} = \begin{pmatrix} 1.602 \times 10^{-6} & -1.068 \times 10^{-6} & 5.341 \times 10^{-7} & 0.25 \\ 5.341 \times 10^{-7} & 1.068 \times 10^{-6} & -5.341 \times 10^{-7} & -0.25 \\ -5.341 \times 10^{-7} & 1.068 \times 10^{-6} & 5.341 \times 10^{-7} & 0.25 \\ 5.341 \times 10^{-7} & -1.068 \times 10^{-6} & 1.602 \times 10^{-6} & -0.25 \end{pmatrix} H$$

Ensure that this is solvable.

$$\text{MMF} := \begin{pmatrix} 4 \cdot N_{DB} \cdot I_{d,DB} \\ 4 \cdot N_{DB} \cdot I_{d,DB} \\ 4 \cdot N_{DB} \cdot I_{d,DB} \\ 0 \end{pmatrix} \quad \text{MMF} = \begin{pmatrix} 385 \\ 385 \\ 385 \\ 0 \end{pmatrix} A$$

$$\text{Flux}(\Delta x) := \text{Reluctance}(\Delta x)^{-1} \cdot \text{MMF}$$

Ideal Case Results:

$$\text{Flux}(0\text{mm}) = \begin{pmatrix} 4.112 \times 10^{-4} \\ 4.112 \times 10^{-4} \\ 4.112 \times 10^{-4} \\ 4.112 \times 10^{-4} \end{pmatrix} \text{Wb}$$

As expected, when there are no eccentricities, all of the fluxes are equal to one another...this satisfies Gauss's Law.

$$\text{Reluctance}(0\text{mm}) \cdot \text{Flux}(0\text{mm}) = \begin{pmatrix} 385 \\ 385 \\ 385 \\ 0 \end{pmatrix} A$$

Check - this matches the MMF matrix above!

Eccentricities Case Results:

For an eccentricity (only in the x-direction) of 0.01 mm, this should result in an increase in flux through Rb and a decrease in flux through Rd. This matches the result (as shown below).

$$\text{Flux}(0\text{mm}) = \begin{pmatrix} 4.112 \times 10^{-4} \\ 4.112 \times 10^{-4} \\ 4.112 \times 10^{-4} \\ 4.112 \times 10^{-4} \end{pmatrix} \text{Wb}$$

$$\text{Flux}(0.01\text{mm}) = \begin{pmatrix} 4.113 \times 10^{-4} \\ 4.154 \times 10^{-4} \\ 4.113 \times 10^{-4} \\ 4.071 \times 10^{-4} \end{pmatrix} \text{Wb}$$

Now relate the fluxes to flux density so that the forces can be determined in the airgap for the positive and negative x directions:

$$\phi = \mathbf{B} \cdot \mathbf{A}$$

$$\text{Flux_Density}(\Delta x) := \frac{\text{Flux}(\Delta x)}{\text{Area}_{\text{Gap_DB}}}$$

Solve for the flux densities associated with each airgap:

$$\text{Flux_Density}(0\text{mm})_0 = 0.242 \text{ T} \quad \text{Flux_Density}(0\text{mm})_1 = 0.242 \text{ T} \quad \text{All should match without any eccentricities.}$$

$$\text{Flux_Density}(0\text{mm})_2 = 0.242 \text{ T} \quad \text{Flux_Density}(0\text{mm})_3 = 0.242 \text{ T}$$

$$\text{Flux_Density}(0.01\text{mm})_0 = 0.242 \text{ T}$$

$$\text{Flux_Density}(0.01\text{mm})_1 = 0.244 \text{ T}$$

The flux densities associated with the reluctances B and D will vary (1 and 3) - as shown. One should increase and one should decrease.

Force Equations:

$$W_a = \frac{1}{2} \cdot B_a \cdot H_a \cdot V_a = \frac{1}{2} \cdot B_a \cdot H_a \cdot A_a \cdot l \cdot g$$

$$\text{Force} = \frac{d}{dg} W_a = B_a \cdot H_a \cdot A_a = \frac{B_a^2 \cdot A_a}{2\mu_0}$$

X Force Calculations:

Determine the forces for an eccentricity Δx ; therefore the airgap increases on one side and decreases on the opposing side. **Assume coils are energized with the DB Bias Current of 1.75 A.**

$$F_{X_Positive}(\Delta x) := -\frac{(Flux_Density(\Delta x)_1)^2 \cdot Area_{Gap_DB}}{2\mu_0}$$

$$F_{X_Negative}(\Delta x) := -\frac{(Flux_Density(\Delta x)_3)^2 \cdot Area_{Gap_DB}}{2\mu_0}$$

$$F_X(\Delta x) := F_{X_Positive}(\Delta x) - F_{X_Negative}(\Delta x)$$

Results for no eccentricities (the forces should sum to zero):

$$F_{X_Positive}(0mm) = -39.581 \text{ N}$$

$$F_{X_Negative}(0mm) = -39.581 \text{ N}$$

$$F_X(0mm) = 0 \text{ N}$$

Results for eccentricities (no longer equal to zero, depending on Δx , will produce a positive or negative force in the x-direction):

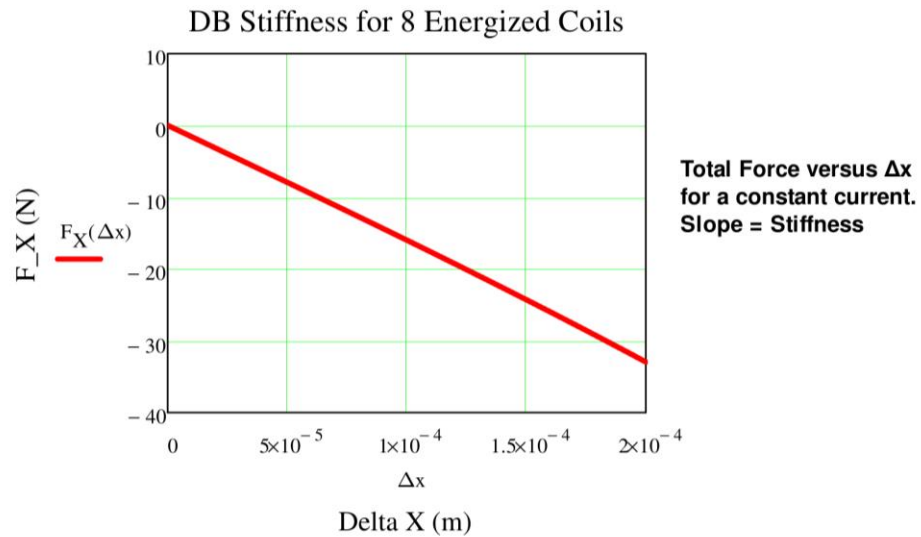
$$F_{X_Positive}(.01mm) = -40.381 \text{ N}$$

$$F_{X_Negative}(.01mm) = -38.798 \text{ N}$$

$$F_X(.01mm) = -1.583 \text{ N}$$

X Stiffness Calculations (ideal case without adding in other reluctances for non-ideal case):

The range for Δx can go from 0mm to 1mm. At 0mm, the distance between the stator and rotor is equal to the initial airgap (1mm) and at 1mm, this would result in a collision between the rotor and stator and the force would then have a divide by zero resulting in errors and an equation that cannot be solved. I will vary it from 0 to .2mm since after this point the controllers will not be able to control the airgap correctly.



$$\Delta x := .001\text{mm}, 0.01\text{mm}..2\text{mm}$$

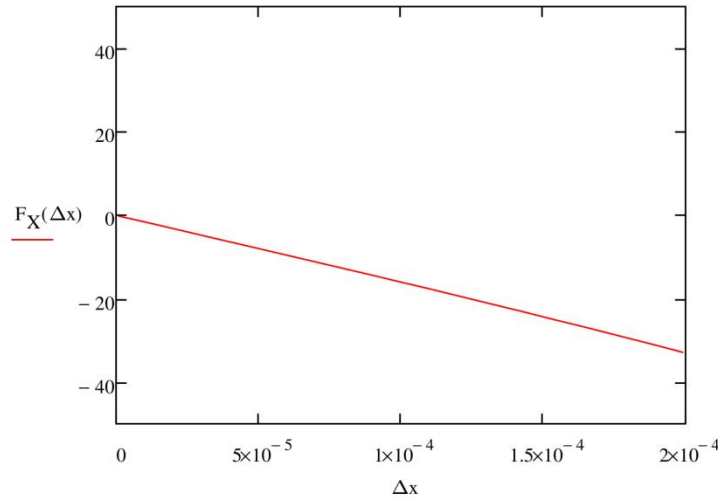
$$X1 := \Delta x$$

$$Y1_new(X1) := F_X(X1)$$

Data for Excel:

$$\begin{aligned}
 X1 &= \begin{array}{|c|} \hline 1 \cdot 10^{-6} \\ \hline 1 \cdot 10^{-5} \\ \hline 1.9 \cdot 10^{-5} \\ \hline 2.8 \cdot 10^{-5} \\ \hline 3.7 \cdot 10^{-5} \\ \hline 4.6 \cdot 10^{-5} \\ \hline 5.5 \cdot 10^{-5} \\ \hline 6.4 \cdot 10^{-5} \\ \hline 7.3 \cdot 10^{-5} \\ \hline 8.2 \cdot 10^{-5} \\ \hline 9.1 \cdot 10^{-5} \\ \hline 1 \cdot 10^{-4} \\ \hline 1.09 \cdot 10^{-4} \\ \hline 1.18 \cdot 10^{-4} \\ \hline 1.27 \cdot 10^{-4} \\ \hline \dots \\ \hline \end{array} \text{ m} \\
 Y1_new(X1) &= \begin{array}{|c|} \hline -0.158 \\ \hline -1.583 \\ \hline -3.009 \\ \hline -4.437 \\ \hline -5.866 \\ \hline -7.298 \\ \hline -8.734 \\ \hline -10.174 \\ \hline -11.62 \\ \hline -13.07 \\ \hline -14.528 \\ \hline -15.992 \\ \hline -17.464 \\ \hline -18.945 \\ \hline -20.436 \\ \hline \dots \\ \hline \end{array} \text{ N} \\
 Y_actual &:= -15.992 \quad \cdot \text{N} \quad X_actual := 1 \cdot 10^{-4} \quad \cdot \text{m} \\
 &\quad \left(\begin{array}{c} -0.158 \\ -1.583 \\ -3.009 \\ -4.437 \\ -5.866 \\ -7.298 \\ -8.734 \\ -10.174 \\ -11.62 \\ -13.07 \\ -14.528 \\ -15.992 \\ -17.464 \\ -18.945 \\ -20.436 \\ -21.936 \\ -23.448 \\ -24.971 \\ -26.507 \\ -28.056 \\ -29.619 \\ -31.198 \\ -32.792 \end{array} \right) \\
 &\quad \left(\begin{array}{c} 1 \times 10^{-6} \\ 1 \times 10^{-5} \\ 1.9 \times 10^{-5} \\ 2.8 \times 10^{-5} \\ 3.7 \times 10^{-5} \\ 4.6 \times 10^{-5} \\ 5.5 \times 10^{-5} \\ 7.3 \times 10^{-5} \\ 8.2 \times 10^{-5} \\ 9.1 \times 10^{-5} \\ 1.09 \times 10^{-4} \\ 1.18 \times 10^{-4} \\ 1.27 \times 10^{-4} \\ 1.36 \times 10^{-4} \\ 1.45 \times 10^{-4} \\ 1.54 \times 10^{-4} \\ 1.63 \times 10^{-4} \\ 1.72 \times 10^{-4} \\ 1.81 \times 10^{-4} \\ 1.9 \times 10^{-4} \\ 1.99 \times 10^{-4} \end{array} \right)
 \end{aligned}$$

Plot the resulting forces versus Δx and determine the slope of the line below. This will be equal to the stiffness associated with the electromagnetic forces in the x direction.



$m_1 := \text{slope}(X_{\text{actual}}, Y_{\text{actual}})$

$$m_1 = -1.642 \times 10^5 \frac{\text{N}}{\text{m}} \quad \text{-- Stiffness Result (Negative as expected)}$$

Now solve for the slope at each point, then find the average stiffness and the standard deviation:

$i := 0, 1..21$

$$\text{slope_it}_i := \frac{Y_{\text{actual}}_{i+1} - Y_{\text{actual}}_i}{X_{\text{actual}}_{i+1} - X_{\text{actual}}_i}$$

$\text{Avg_Stiffness} := \text{mean}(\text{slope_it})$

$$\text{Avg_Stiffness} = -1.648 \times 10^5 \frac{\text{N}}{\text{m}} \quad m_1 = -1.642 \times 10^5 \frac{\text{N}}{\text{m}} \quad \text{Very close.}$$

$\text{Std_Dev_Stiffness} := \text{stdev}(\text{slope_it})$

$$\text{Std_Dev_Stiffness} = 5.835 \times 10^3 \frac{\text{N}}{\text{m}}$$

Appendix F: CATIA Model Outputs

Product : Motor Assembly		Area[in ²]	Volume[in ³]	Density[lb_in ³]
Date : Friday, 31 January 2014 17:26:40				
Author : Rolo1561				
"Only main bodies" option : Unchecked				
Component	Sub-Component	Area[in ²]	Volume[in ³]	Density[lb_in ³]
Top Plate.1		100.574	27.53	0.26
SB Rotor Lamination.1		77.73	16.091	0.284
Rotor Stack Spacer.1		190.066	62.832	0.051
DB Rotor Lamination.1		137.473	32.159	0.284
MagPlate.1		186.296	34.778	0.26
RotorStandoff.1		14.921	0.914	0.284
RotorStandoff.2		14.921	0.914	0.284
RotorStandoff.3		14.921	0.914	0.284
RotorStandoff.4		14.921	0.914	0.284
Rotor Bolts.1		5.877	0.361	0.284
Rotor Bolts.2		5.877	0.361	0.284
Rotor Bolts.3		5.877	0.361	0.284
Rotor Bolts.4		5.877	0.361	0.284
92994A029.1		1.154	0.048	0.284
92994A029.2		1.154	0.048	0.284
92994A029.3		1.154	0.048	0.284
92994A029.4		1.154	0.048	0.284
Magnets.1		82.5	5.625	0.267
Rotor Assembly		862.45	184.31	Not uniform

Mass[lb]	Gx[in]	Gy[in]	Gz[in]	M1[lbxin2]	M2[lbxin2]
7.151	1.60E-16	-5.32E-16	7.959	42.034	42.034
4.575	-5.21E-17	-6.68E-17	7.079	24.4	24.4
3.178	-2.40E-16	-6.90E-17	5.099	19.925	19.925
9.144	-1.94E-15	-3.64E-16	2.5	54.766	54.766
9.034	1.11E-15	2.55E-16	0.845	54.095	54.095
0.26	3.205	4.06E-17	4.504	0.01	0.839
0.26	-4.24E-16	-3.205	4.504	0.01	0.839
0.26	-3.95E-16	3.205	4.504	0.01	0.839
0.26	-3.205	4.33E-16	4.504	0.01	0.839
0.103	-8.43E-16	-3.205	4.904	0.000801252	0.463
0.103	3.205	5.37E-16	4.904	0.000801252	0.463
0.103	-3.205	-8.13E-16	4.904	0.000801252	0.463
0.103	-7.03E-16	3.205	4.904	0.000801252	0.463
0.014	-0.000126662	-3.205	8.656	0.000379982	0.000385501
0.014	3.205	-5.32E-06	8.656	0.000379982	0.000385501
0.014	-3.205	-5.32E-06	8.656	0.000379982	0.000385501
0.014	-0.000126662	3.205	8.656	0.000379982	0.000385501
1.504	0.000103956	-0.000489074	0.25	8.446	8.446
36.089	4.14E-06	-2.04E-05	3.977	406.698	0

M3[Ibxin2]	IoxG[Ibxin2]	IoyG[Ibxin2]	IozG[Ibxin2]	IxyG[Ibxin2]	IxzG[Ibxin2]
82.88	42.034	42.034	82.88	0	0
48.362	24.4	24.4	48.362	0	0
34.426	19.925	19.925	34.426	0	0
103.441	54.766	54.766	103.441	0	0
105.274	54.095	54.095	105.274	0	0
0.839	0.839	0.839	0.01	-7.14E-50	-5.14E-33
0.839	0.839	0.839	0.01	-7.14E-50	-5.14E-33
0.839	0.839	0.839	0.01	-7.14E-50	-5.14E-33
0.839	0.839	0.839	0.01	-7.14E-50	-5.14E-33
0.463	0.463	0.463	8.01E-04	1.23E-16	-1.80E-17
0.463	0.463	0.463	8.01E-04	1.23E-16	-1.80E-17
0.463	0.463	0.463	8.01E-04	1.23E-16	-1.80E-17
0.463	0.463	0.463	8.01E-04	1.23E-16	-1.80E-17
0.000385524	3.86E-04	3.86E-04	3.80E-04	-1.19E-08	-1.40E-08
0.000385524	3.86E-04	3.86E-04	3.80E-04	-1.19E-08	-1.40E-08
0.000385524	3.86E-04	3.86E-04	3.80E-04	-1.19E-08	-1.40E-08
0.000385524	3.86E-04	3.86E-04	3.80E-04	-1.19E-08	-1.40E-08
16.829	8.446	8.446	16.829	-1.34E-15	-3.62E-16
0	509.28	509.28	406.698	2.58E-08	6.15E-04

Appendix G: Rotor Dynamic Simulink[®] Model

Dynamic Open-Loop Model Inputs:

4/6/14 4:52 PM H:\Matlab\DynamicMdlInputs.m

1 of 1

```

clc;
clear;
%-----Define Constants-----
s0 = 1*(10^-3); %Ideal airgap (m)
%z_lev = 4; %Levitation Height (in mm for levitation equation)- Axial Input

%-----Dynamic Model Inputs = Sensor Measurements-----

x1_m = 1*(10^-3); %x1 sensor measurement (converted from a measurement in mm to m)
x2_m = 1*(10^-3); %x2 sensor measurement (converted from mm to m)
y1_m = 1.2*(10^-3); %y1 sensor measurement (converted from mm to m)
y2_m = 1.2*(10^-3); %y2 sensor measurement (converted from mm to m)

%-----Radial Model Constants-----

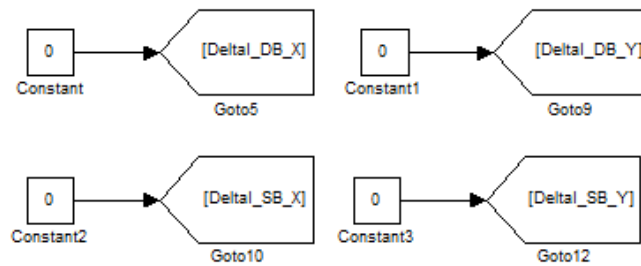
%L1,L2,l1, and l2 represent distances between two points and will all be positive

I_T = .149 %I_x0 from Catia Model (kg*m^2)
I_P = .119; %I_z0 from Catia Model (kg*m^2)
m = 16.343; %Measured Rotor Mass(Kg)
l1 = .08; %Axial distance of position sensor plane #1 to COM (m) - ASSUMING at center of ↵
mag plate
%l2 = .101; %Axial distance of position sensor plane #2 to COM (m) - ASSUMING at center of ↵
top plate
l2 = l1;
L1 = .038; %Axial distance of "motor #1's center" to COM (m) - Based on CATIA results
%L2 = .079; %Axial distance of "motor #2's center" to COM (m) - Based on CATIA results
L2 = L1;
%k1 = -6.65*10^5; %Negative Stiffness of motor #1 (N/m) - drive bearing - 16 coils excited
k2 = -2.03*10^5; %Negative Stiffness of motor #2 (N/m) - stabilizing bearing
k1 = k2;
%k1i = -366.84; %Current Stiffness of motor #1 (N/A) - drive bearing - 16 coils excited
k2i = -80.69; %Current Stiffness of motor #2 (N/A) - stabilizing bearing
k1i = k2i;
w = 188.5; %angular velocity of rotor (rad/sec) = 1800 RPM
%w = 10; %Angular velocity of rotor for low speeds (rad/sec) = 100 RPM
%w = 0; %Initially, no rotation - enables a static model.
Theta_r_M = 0; %Measured angle (degrees) between sensor locations and rotor poles ↵
(positive - CCW)
Theta_r = (Theta_r_M*pi())/180 % Angle between the rotating and stationary rotor axes ↵
(rads)
eu = 0; %radial distance between geo center and COM (m) = 0 initially, so no ↵
unbalance!!!; eu = e1+e2

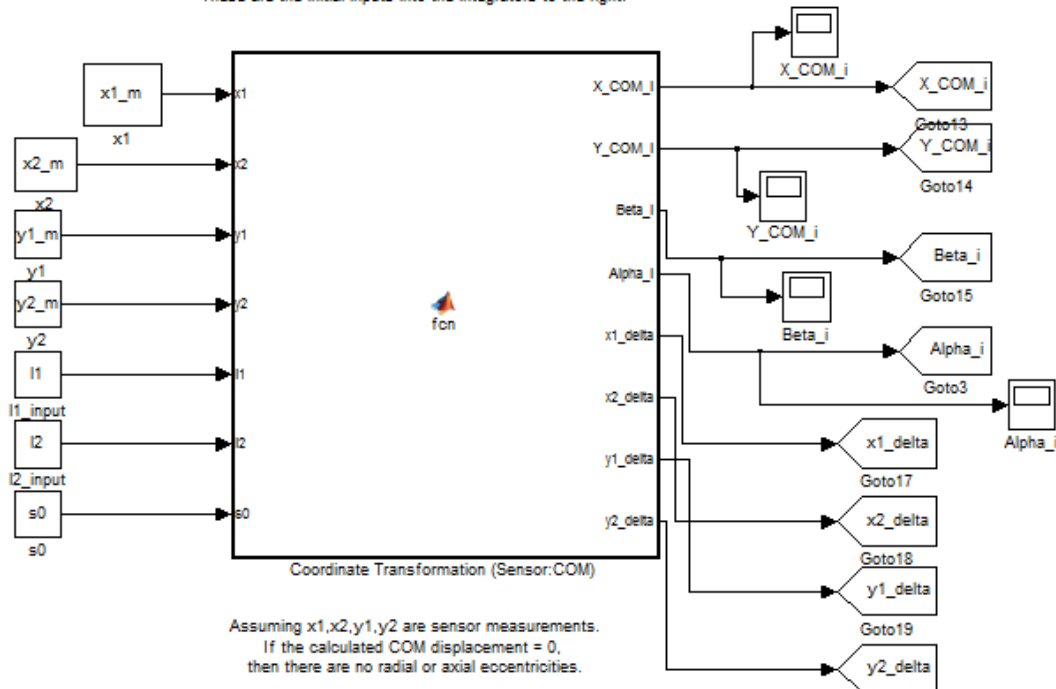
```

Open-Loop Simulink Dynamic Model:

Model Inputs - Delta I and Delta X based on sensor measurements:

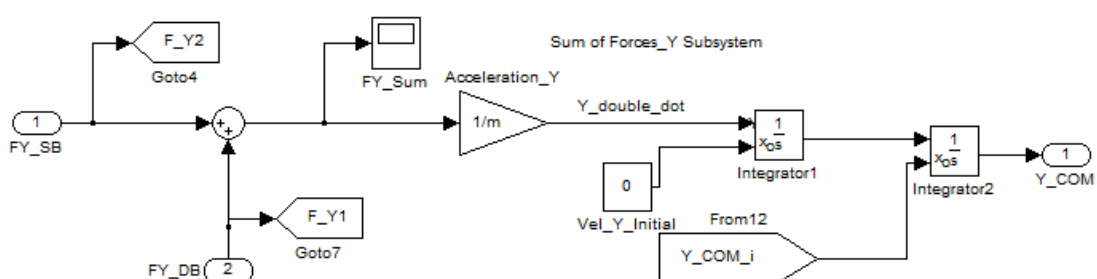
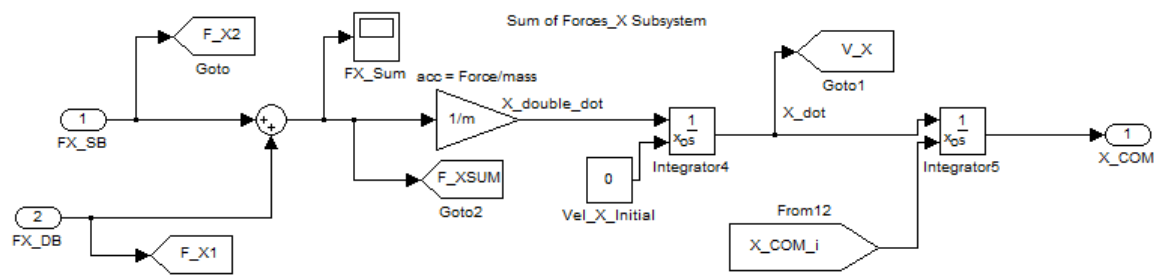
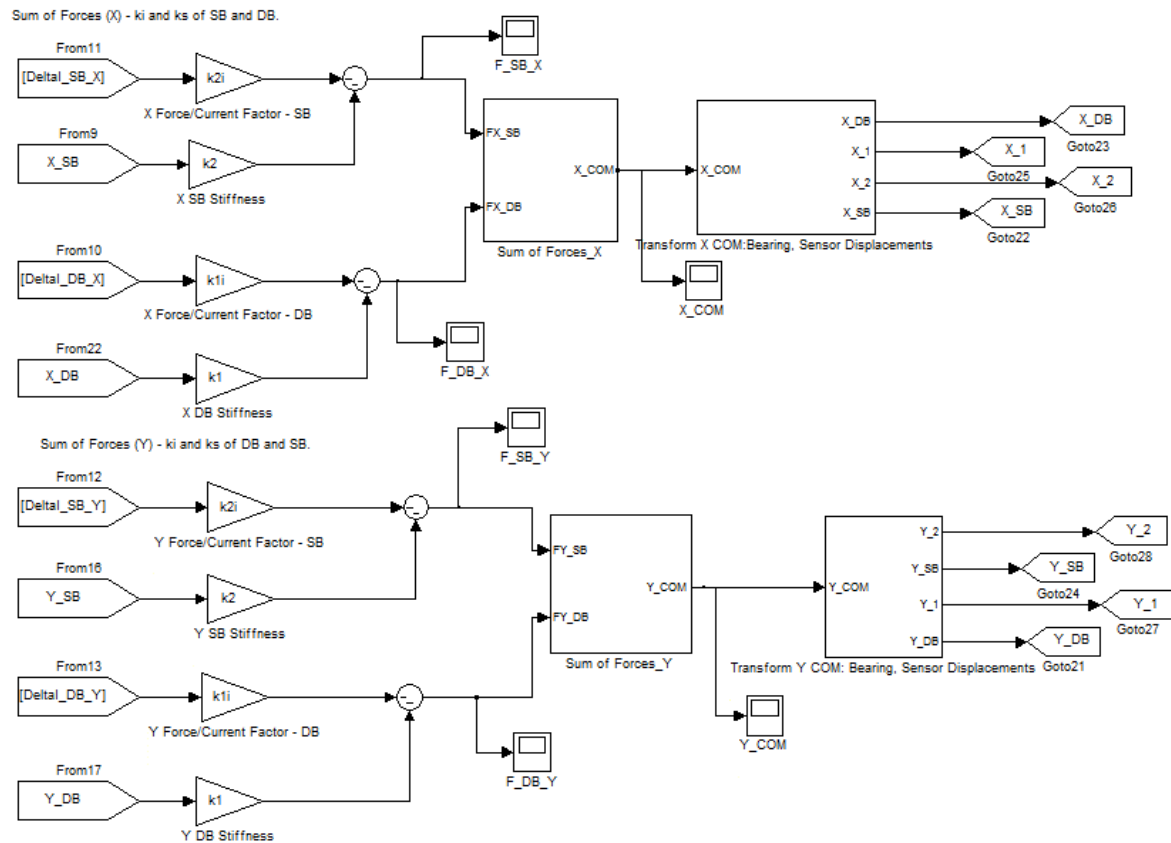


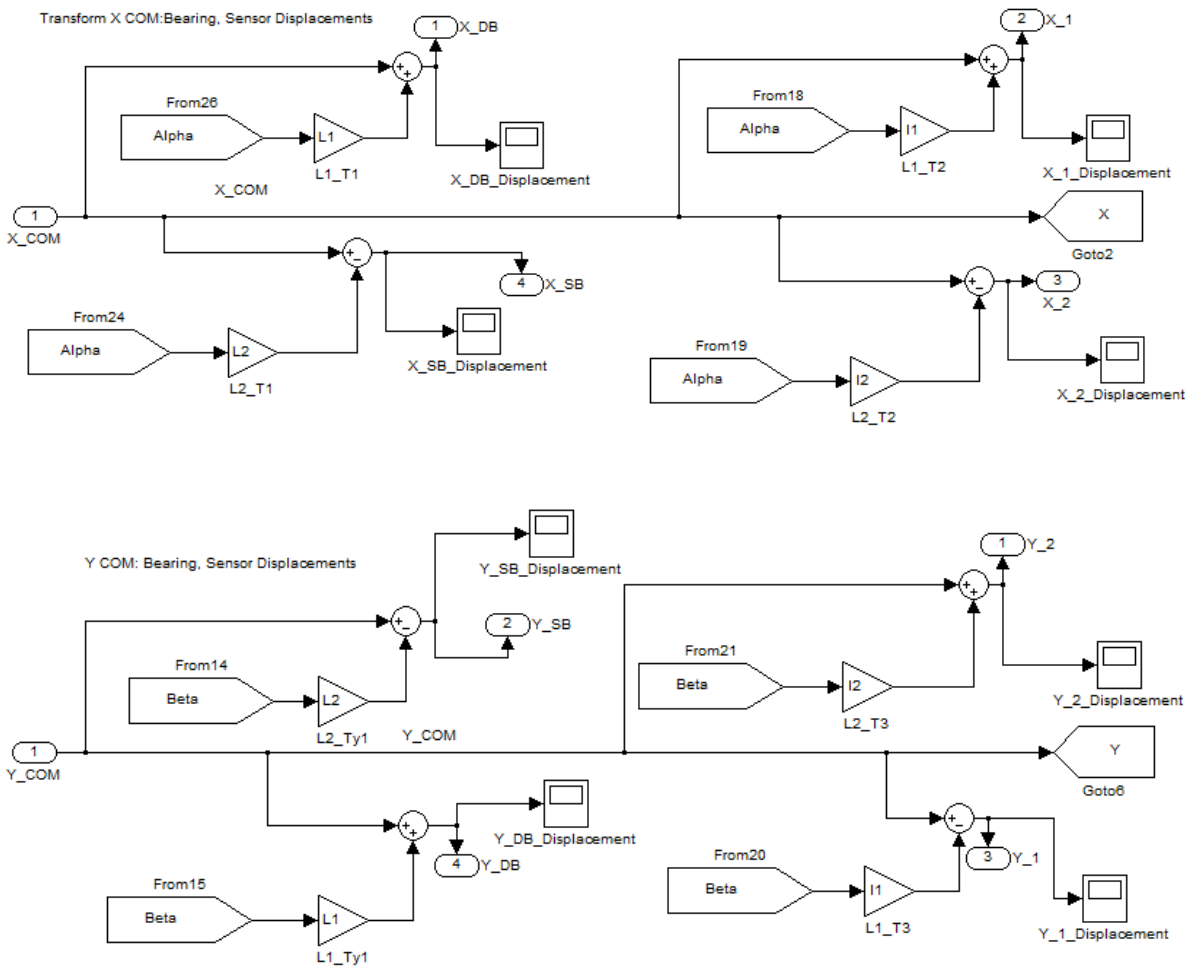
The following function will transform the measured sensor distances into the displacements at the COM.
These are the initial inputs into the integrators to the right.

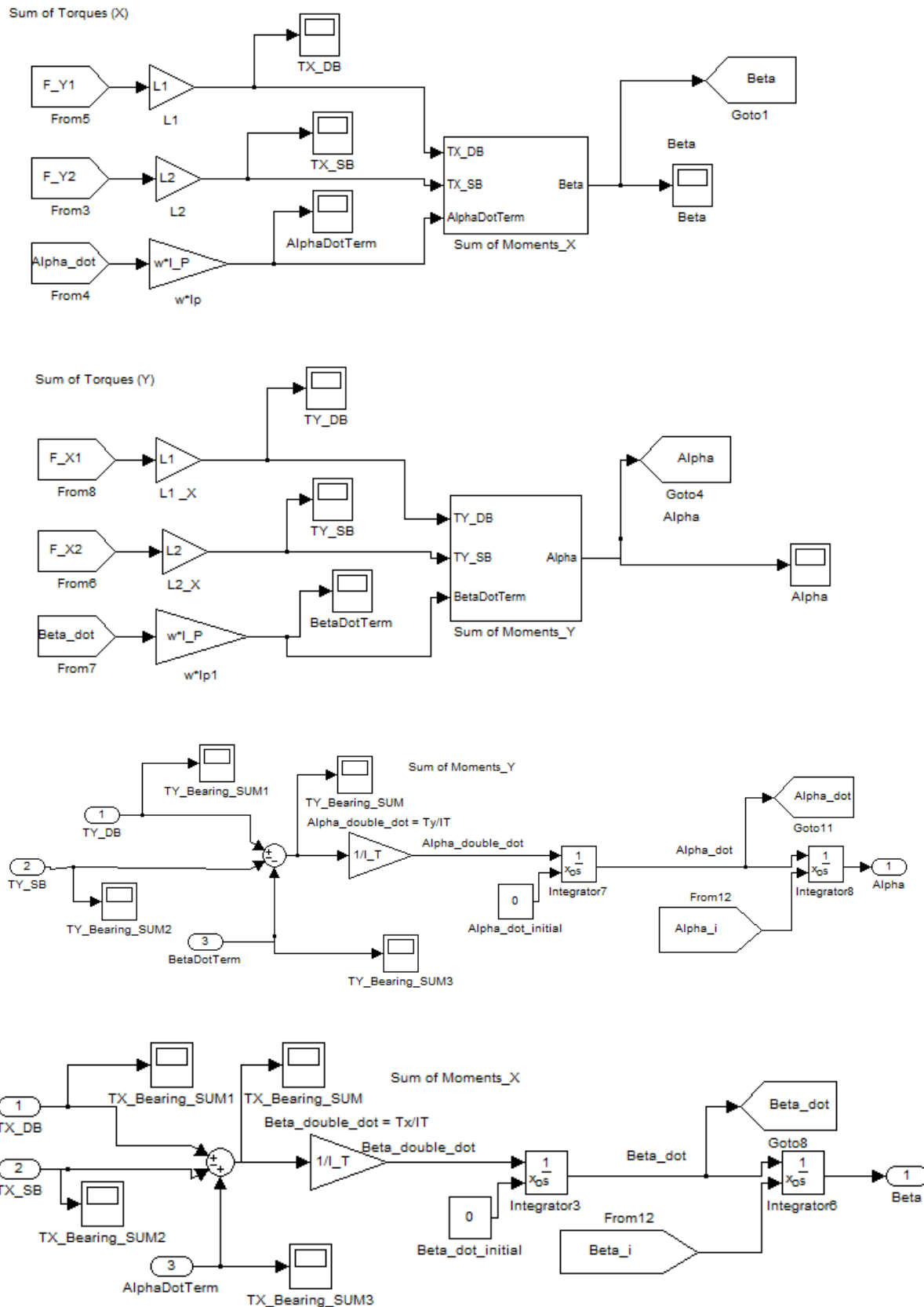


4/6/14 5:02 PM B.../Coordinate Transformation (Sensor:COM) 1 of 1

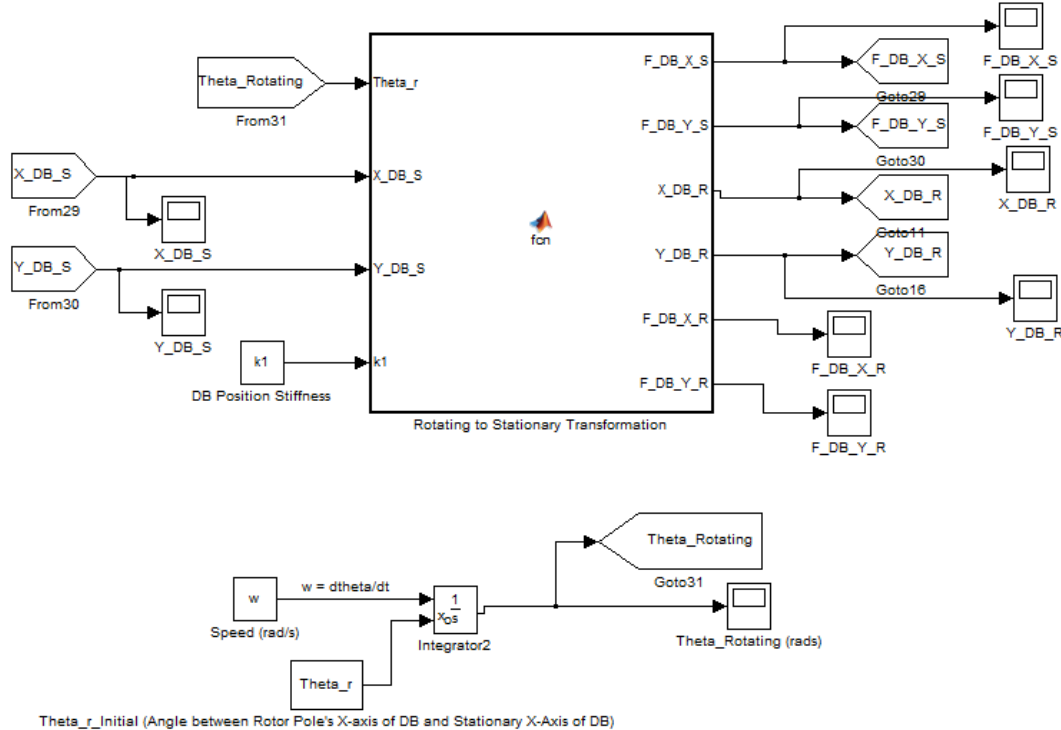
```
function [X_COM_i,Y_COM_i,Beta_i,Alpha_i, x1_delta,x2_delta,y1_delta,y2_delta] = fcn(x1,  
x2,y1,y2,l1,l2,s0)  
 %#codegen  
  
%Calculate the delta x and y values and the tilt angles  
%These are based on the sensor measurements (x1,x2,y1,y2)  
%The lever arms l1 & l2 are inputs from 'DynamicMdlInputs.m'  
%These are the distance between the sensor planes and COM  
  
l = l1+l2  
  
X_prime = (x2 - x1)/l;  
Y_prime = (y2 - y1)/l;  
  
%Calculate the sensor displacements based on the measurements  
x1_delta = s0 - x1  
x2_delta = s0 - x2  
y1_delta = s0 - y1  
y2_delta = s0 - y2  
  
%Calculate COM displacements based on sensor displacements  
  
X_COM_i = ((l2*x1_delta)+(l1*x2_delta))/l  
Y_COM_i = ((l2*y1_delta)+(l1*y2_delta))/l  
  
%Include the following to set the values to zero due to machine tolerance  
  
if abs(X_COM_i)<(10^-16)  
    X_COM_i = 0;  
end  
if abs(Y_COM_i)<(10^-16)  
    Y_COM_i = 0;  
end  
  
%Calculate Euler angles using small angle approximations  
  
Beta_i = Y_prime;  
Alpha_i = X_prime;  
  
%End of file
```







Open-Loop Simulink Model with Rotational to Stationary Transformation:



4/6/14 5:37 PM Bl.../Rotating to Stationary Transformation 1 of 1

```

function [F_DB_X_S,F_DB_Y_S,X_DB_R,Y_DB_R,F_DB_X_R,F_DB_Y_R] = fcn(Theta_r, X_DB_S,%
Y_DB_S, k1)
 %#codegen

%Transform the stationary DB displacements into rotating DB displacements
%These rotating displacements are located at the rotor poles

Matrix_Trans = [(cos(Theta_r)) (sin(Theta_r)); (-sin(Theta_r)) (cos(Theta_r))]

%Include the following to set the values to zero due to machine tolerance

X_DB_R = Matrix_Trans(1,1:2)*[X_DB_S; Y_DB_S];
Y_DB_R = Matrix_Trans(2,1:2)*[X_DB_S; Y_DB_S];

Matrix_Inv = inv(Matrix_Trans)

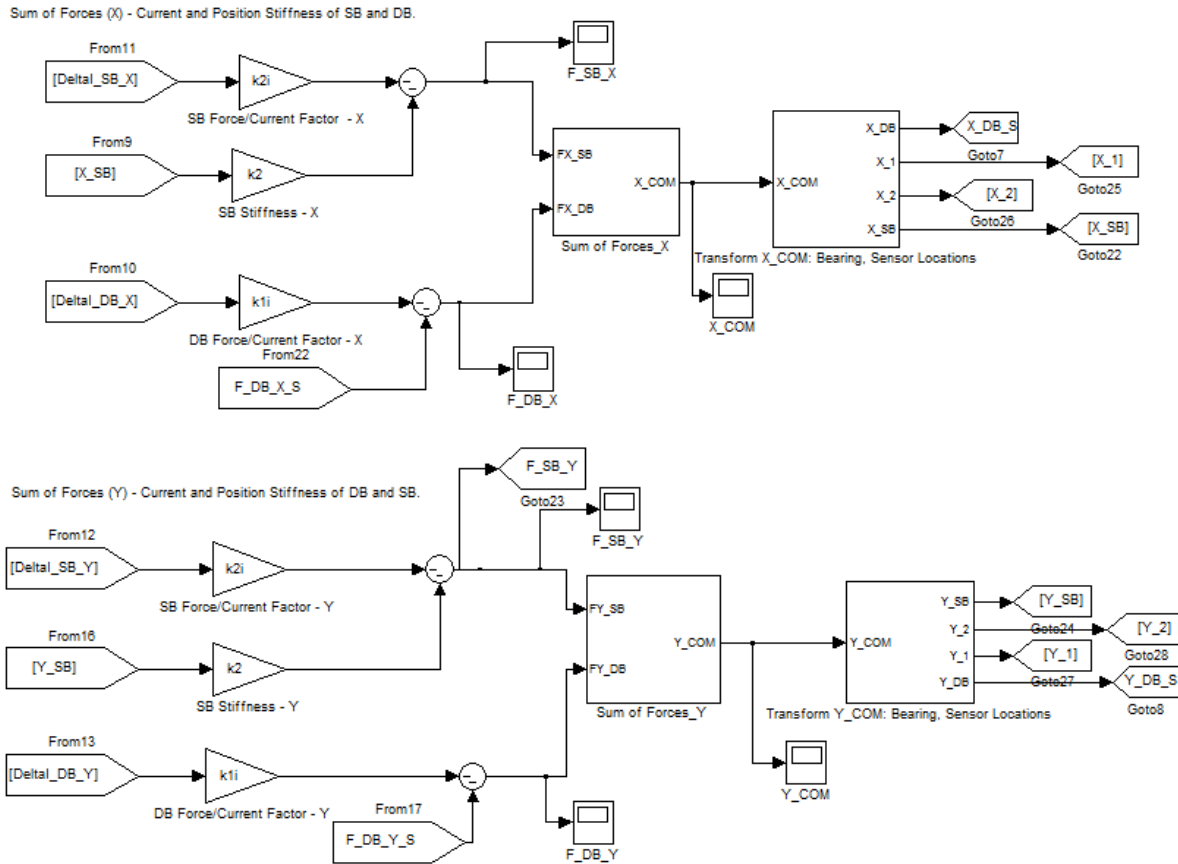
%Determine the DB Forces associated with the DB displacements

F_DB_X_R = k1*X_DB_R;
F_DB_Y_R = k1*Y_DB_R;

%Transform these to stationary Forces for the eqns. of motion

F_DB_X_S = Matrix_Inv(1,1:2)*[F_DB_X_R; F_DB_Y_R];
F_DB_Y_S = Matrix_Inv(2,1:2)*[F_DB_X_R; F_DB_Y_R];

```



Note: The rest of the Simulink model was identical to the open-loop dynamic model subsystems already shown. These two models resulted in identical results and therefore the stationary to rotating transformation wasn't included in the closed-loop model.

Closed-Loop Dynamic Model Inputs (no constraints):

4/6/14 5:52 PM C:\Users\User...\DynamicMdlInputs PIDTest.m 1 of 1

```

clc;
clear;
%-----Define Constants-----
s0 = 1*(10^-3); %Ideal airgap (m)

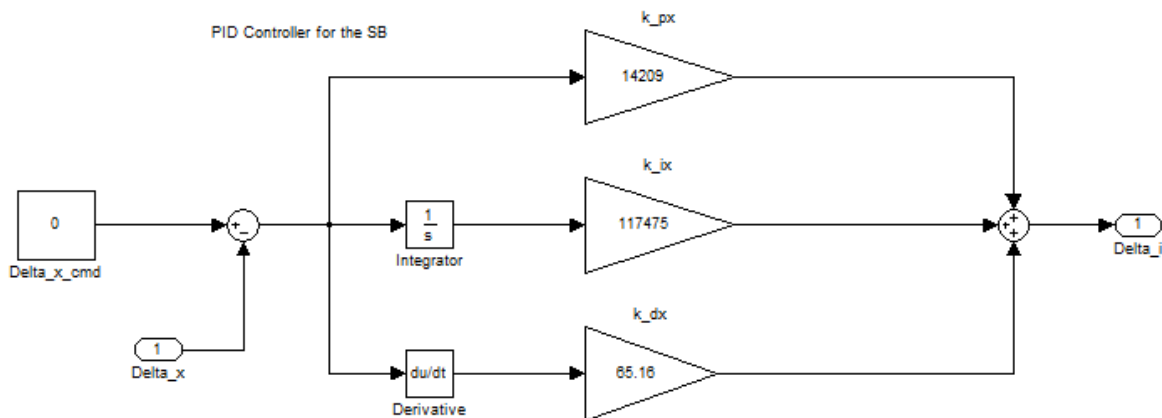
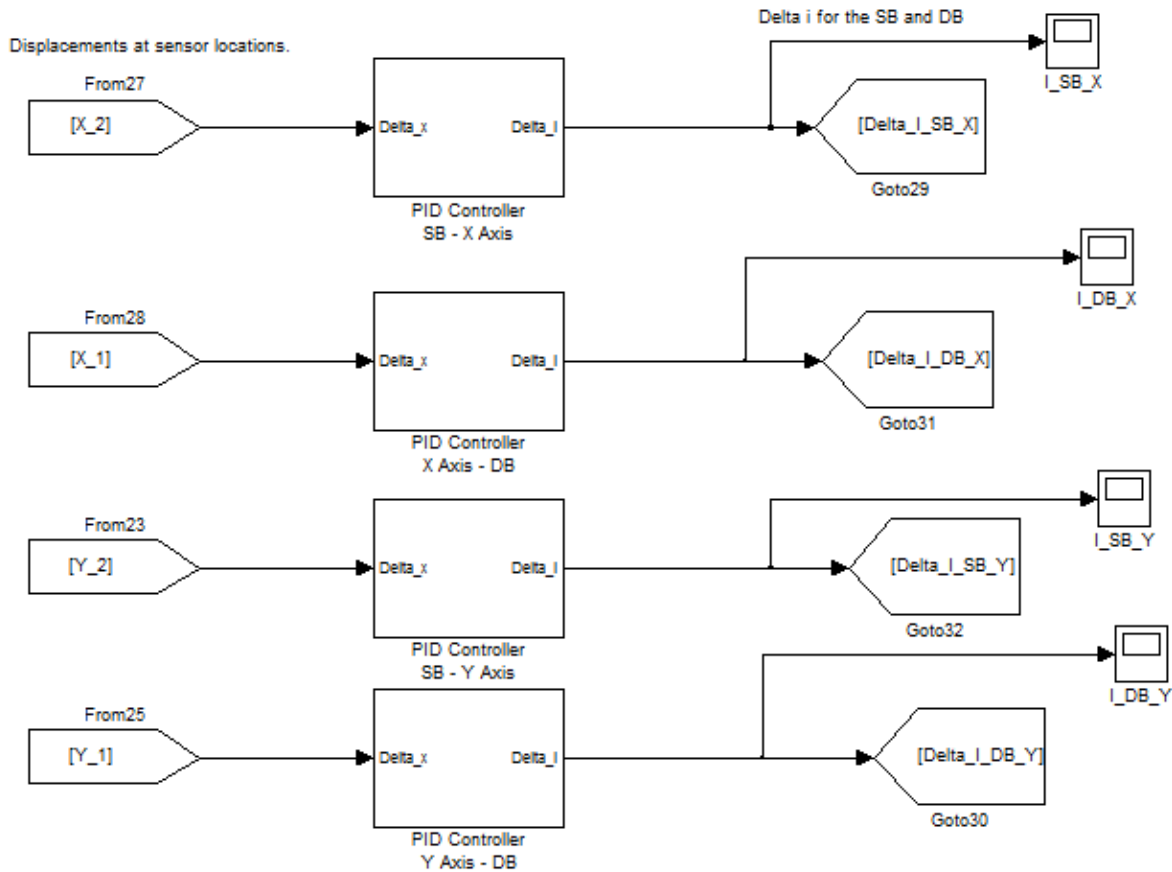
%-----Dynamic Model Inputs = Sensor Measurements-----
x1_m = .8*(10^-3); %x1 sensor measurement (converted from a measurement in mm to m)
x2_m = 1.2*(10^-3); %x2 sensor measurement (converted from mm to m)
y1_m = 1.2*(10^-3); %y1 sensor measurement (converted from mm to m)
y2_m = 1.2*(10^-3); %y2 sensor measurement (converted from mm to m)

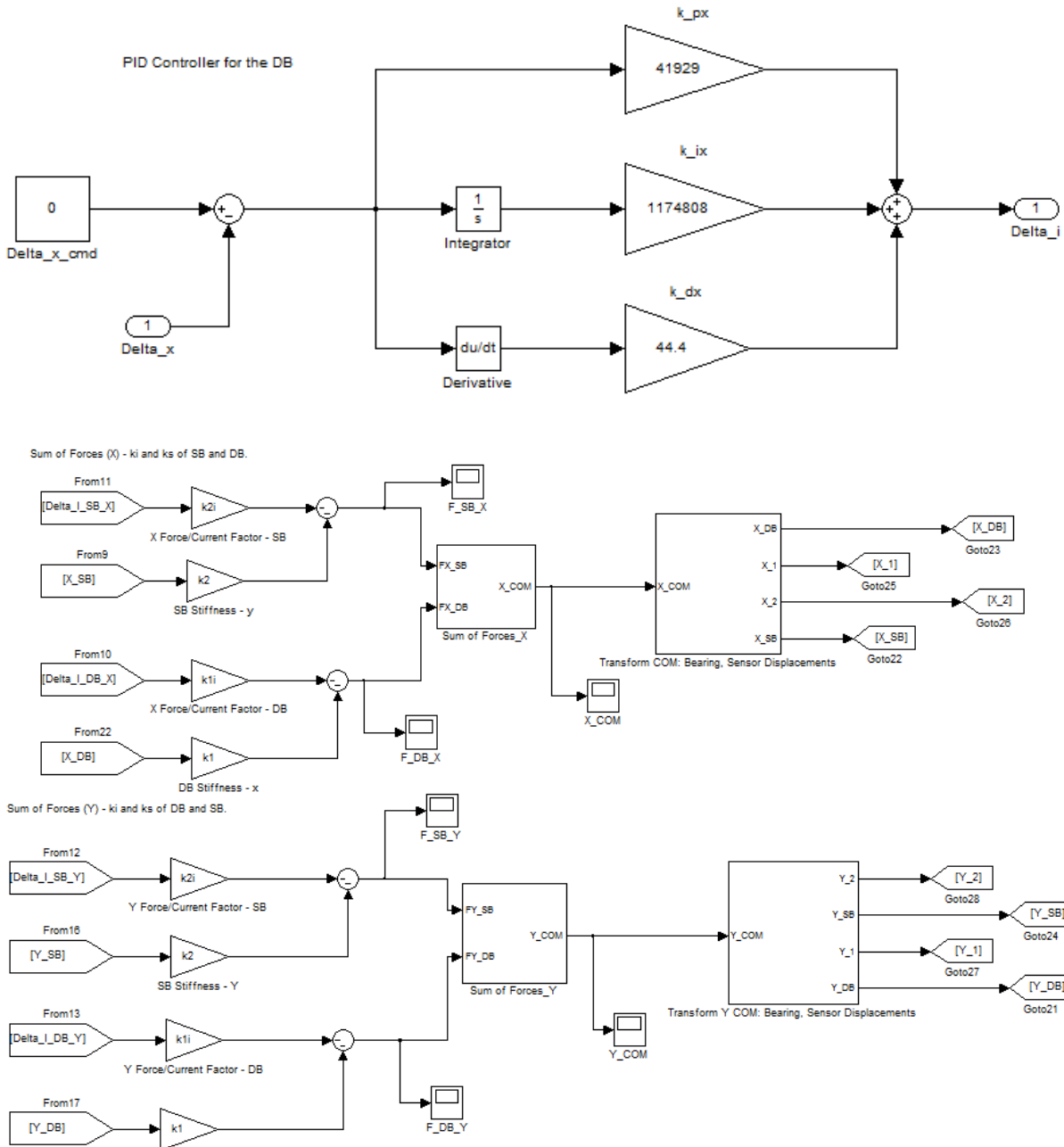
%-----Radial Model Constants-----
%L1,L2,l1, and l2 represent distances between two points and will all be positive

I_T = .149 %I_x0 from Catia Model (kg*m^2)
I_P = .119; %I_z0 from Catia Model (kg*m^2)
m = 16.343; %Measured Rotor Mass(Kg)
l1 = .08; %Axial distance of position sensor plane #1 to COM (m)- ASSUMING at center of ↘
mag plate
l2 = .101; %Axial distance of position sensor plane #2 to COM (m)- ASSUMING at center of ↘
top plate
L1 = .038; %Axial distance of "motor #1's center" to COM (m)- Based on CATIA results
L2 = .079; %Axial distance of "motor #2's center" to COM (m)- Based on CATIA results
k1 = -6.65*10^5; %Negative Stiffness of motor #1 (N/m)- drive bearing - 16 coils excited
k2 = -2.03*10^5; %Negative Stiffness of motor #2 (N/m) - stabilizing bearing NEW
k1i = -366.84; %Current Stiffness of motor #1 (N/A)- drive bearing - 16 coils excited
k2i = -80.69; %Current Stiffness of motor #2 (N/A)- stabilizing bearing
w = 188.5 %angular velocity of rotor (rad/sec) = 1800 RPM
%w = 10; %Angular velocity of rotor for low speeds (rad/sec) = 100 RPM
%w = 0; %Initially, no rotation - enables a static model.

```

Closed-Loop Simulink Dynamic Model:





Note: The rest of the Simulink model was identical to the open-loop dynamic model subsystems already shown and were not duplicated here.